Mechanical Loading of Engineered Heart Muscle Tissues for Disease Modeling and Repair of the Human Heart

Submitted in partial fulfillment of the requirements for the

degree of

Doctor of Philosophy

in

Biomedical Engineering

Jacqueline M. Bliley

B.S., Health Management Systems, Duquesne University
M.S., Medical Sciences, Boston University

Carnegie Mellon University
Pittsburgh, PA

August 2021

DEDICATION

When I was five years old, my father took my siblings and I to the ocean to teach us how to fish. It was a dreary day and the dark grey ocean stretched as far as my eye could see. My dad set us all up, showing us how to bait our hooks and cast our fishing poles.

The red and white bobber attached to the fishing line floated on the surface, he explained, “If the bobber sinks, you know that you have a bite.”

“But, how long will it take?” my siblings groaned, already eager to have a snack as it had taken my father awhile to get us settled.

He smiled, “It can be very quick, or it can take all day, really depends.”

For us, it seemed like it was the latter. A couple hours passed by and nothing, the bobber gently floating on the grey ocean surface.

“I am hungry,” my brother grumbled and so they all went in to the cabin to enjoy some sandwiches.

“But how will we know if we have a bite if no one is watching?”, I asked.

“We won’t,” my father said, “we can just continue after lunch.”

I sat on my perch, just staring at the bobber as it gently floated on the waves. “I think I will stay and wait,” I said.

“Okay,” my father smiled, and I watched as he turned around to enter the cabin where my siblings were eager to eat their sandwiches.

Later, I could hear laughter coming from the cabin interior as they all sat and ate lunch. I briefly looked inside, but then abruptly turned my head. I was determined and wanted to be ready to catch a fish.

More time went by and I could hear they had now moved onto the cookies. My stomach grumbled, but still I sat and watched the bobber sway up and down with the waves.

“Fishing requires patience”, I heard my dad say, as he came out to check on my progress. Still the bobber floated on the surface.

Then, in a flash, I saw it. The bobber gently dipped for a split second and came back to the surface. Unsure if this was a fluke, I stared at the bobber. A second or two goes by and it dips below the surface again. The fishing pole began to bow as I held onto it, “I think I got one”, I screamed.

My dad came running out with a big smile on his face, “Now you have to slowly reel it in.” As I turned the reel, I could feel the fish and could see it darting just below the surface.

I smiled and turned to my dad as the fish breached, “I really got one.”

Like the story above, I would not have completed this dissertation without those who instilled patience, hard work, and determination in me, and without the love, guidance and support of many people. I would like to dedicate this dissertation to:

My father, Christopher Bliley, who along with the help of my mother, really showed me the value of hard work, determination, and dedication. My mother, Jeannene, and him worked tirelessly to not only run their own business but to also raise four children, and to them I am forever grateful. When my father passed away, my mother didn’t stop. She worked hard to support us, attended every school event (with four of us there were a lot), while also simultaneously going back to school to get her nursing degree. Even to this day, she hasn't stopped pushing, and in fact, might have the most degrees and certificates out of anyone I

know. She always told me I could do anything I put my mind to and you know, after hearing that so much, you start to believe it. Her curiosity, support and never-ending quest for knowledge has always inspired me and truly made me the person I am today.

My mother was also not alone. My grandmother, Marguerite DeRudder, and my grandfather, Albert DeRudder, were always a constant source of support. It is here when you look back over generations that you realize how ideals are imparted on the following generation. My grandfather grew up on the Lower East Side in New York City. His father was a merchant marine who passed away when a German U-Boat sunk the ship he was on in World War II. He attended school until 8th grade but then took multiple jobs to support his family. He worked hard and never complained, building a life for himself and for his future family. I even got to see first-hand his capacity for hard work, as we worked together in a Hardware store during a summer. He was retired, but he still worked every day, and even still works to this day. I have always admired his strong work ethic. His wife, my grandmother, was a beautiful soul and through her I developed an appreciation for all the wonderful things in life. It was impossible to feel unsupported by her and to this day I miss her immensely.

My mother also met a kind, crazy, and stubborn man, Bob Weichbrodt, who for some reason, thought it was a great idea to marry a woman with four children. Bob was also an extremely hard worker (if you are starting to see the theme here). When he took us in, he was retired, but prior to that, he worked his way up, saving money, and eventually running his own marina. Like my grandfather, retired life did not mean there was no work. To my brother and sister's dismay, his hard work ideals extended into yard work and chores, but from this I learned that some amount of discomfort is necessary to reach common goals. Bob also taught me to enjoy life and treasure your family, where even after him and my mother split, we would often visit and go on vacations together. Bob passed away this past year and he will be forever missed.

My mother was also fortunate to remarry a wonderful, compassionate and smart man, Howard Fritz, who for some reason thought it was a good idea to get with a woman with four teenagers (yikes, probably the worst part). Despite all this, Howard helped support and guide my siblings and I through our teenage years. Howard is also an extremely hard worker (see theme). Prior to "retirement", Howard was a doctor where he would spend long hours dictating, taking call, and showing compassion to all his patients. In "retirement", Howard became Chief Medical Officer of Glens Falls Hospital before and during the COVID-19 pandemic (seems like an easy retirement job, right?). Howard's compassion and hard work has always inspired me. Howard also has an M.S. in Neuroscience and I frequently ask him to review my scientific writing. I appreciate his willingness to read pretty much everything I write (except for this section because I wanted it to be a surprise). Hopefully the writing isn't too terrible.

During all of this, I was also not alone, where I have had the constant support of my siblings- Katie, Chris and Nicole. My sisters, Nicole and Katie, are my best friends and have honestly made my whole life more enjoyable, especially during this whole PhD process, which has had its fair share of rough events. My brother, Chris, has also always been there, always ready to make me laugh and listen to me cry (cue "MallRats" and tissues) and for that I am very grateful.

I was also fortunate to meet the love of my life, Greg Wittmer, prior to applying to graduate school. Greg has been a continuous source of support, from when I was initially applying to graduate schools to the late nights and weekends in the lab. He was understanding when I applied to graduate schools across the country, even if it meant I could potentially move away. In all honesty, I was never worried, I knew we would make it work, no matter what the obstacles were. Luckily, Carnegie Mellon was the best fit and we didn't have to experience the hardship of living far away from each other. Greg has always been understanding (even with me working late at night and on the weekends) and made sure that I was well fed. He also didn't call me crazy when I wanted to get married during my PhD. Greg, I am so happy that we met and that I am able to share this life with you.

Greg's parents, my mother and father in-law, Eileen and Ralph Wittmer, and Greg's grandmother, Anna Mae, have also been the incredibly supportive throughout this entire PhD. I am incredibly grateful for them welcoming me into their family with open arms and for always being so understanding when it comes to the craziness of my PhD schedule.

ACKNOWLEDGEMENTS

I would like to personally thank all of my friends, mentors, collaborators, and funding sources that made it possible for me to pursue my PhD studies.

Thank you to Adam for bringing me into the group and allowing me to perform amazing research. Throughout the years, you really pushed me when I needed to be challenged and allowed me to learn more than I could have ever imagined. Thank you the most for challenging me and making me a better scientist in the process.

I would also like to thank my committee members – Professors Yu-li Wang, Chris Bettinger, Adam Kwiatkowski, and Zev Gartner. To Yu-li Wang, for your tremendous insights into biomechanics and also for the curiosity you display in your own research - it is truly inspiring and I hope that I am similarly able to be as involved in the lab when I become a PI. To Chris Bettinger, for always coming up with unique and interesting questions that really make me think and have contributed immensely to this dissertation. To Adam Kwiatkowski – for offering your amazing insights into cardiomyocyte coupling and how this relates to heart tissue function. To Zev Gartner for your tough questions and influential fibroblast compaction paper and for inspiring me to use a similar approach to program heart tube bending.

I would also like to thank my funding sources that made it possible for me to do this research, including Additional Ventures [to A.W.F], the Human Frontier Science Program [grant number RGY 0071/2014 to P.v.d.M. and A.W.F.], the National Institutes of Health [grant number DP2HL117750 to A.W.F.], the Office of Naval Research [grant number N00014-17-1-2566 to A.W.F.], and the Dowd Fellowship and Presidential Fellowship, Carnegie Mellon University [to J.M.B.]. and in part by the European Research Council [grant number: ERC-2016-StG – 715732 to P.v.d.M].

I truly believe the Biomedical Engineering Department at Carnegie Mellon is so great because of all the wonderful people. Thank you Professor Yu-li Wang for talking with me about the environment in the department. Since our initial conversations, I could not imagine being in any other department, at any other institution, for my PhD. It is clear that all the professors and staff truly care about the students and I am very grateful that I was able to perform my dissertation research in such a supportive community. Thank you to all the administrative staff (Maryia, Keri, Mike, and Bryce). In particular, thank you Misti- you make the 3rd floor Collaboratory such a welcoming environment and you are always there to help whether it be regarding laboratory equipment or talking with me about my life. Both of these things are equally needed during the grueling PhD process and I know I speak for everyone in saying that we truly appreciate your support.

To my current and previous female mentors- Drs. Kacey Marra, Lauren Kokai, Rachelle Palchesko, Anne Argenta, Rebecca Duffy, Tara Grahovac, Jolene Valentin, Debra Bourne, and Sarah Woodley. They say that it is difficult for someone to perceive their abilities until they see someone like themselves in that position. For me, this was seeing strong women leaders as scientists. Thank you for taking the time to mentor me and inspiring me to pursue a career in research. I would not be here without your support and time dedicated to mentoring me.

To the females within the biomedical engineering department at CMU (especially those in the Feinberg lab-Maria Stang, Erica Comber, Anne Behre, Neeha Arun, and Emily Sevcik): Sometimes it is tough being a female in science and I want to thank you all for being there for me during my successes but also being there for me when I was frustrated. I could not have done this without you guys and your support. Thank you all for making the lab such a supportive and inclusive environment.

To my former and previous lab mates:

Anna Kalmykov: Thank you for being such a good friend. You were always there to listen to my frustrations. You let me vent when I wanted to quit and helped me gain a better understanding of when and how I should speak up for myself. I know you will be successful with anything you do in life and I hope we get the opportunity to catch up soon.

Andrew Lee: You are still such a great friend and I really treasure our moments when we get to periodically catch up. I still remember the first time you helped me image on the MP at 10 pm at night. You took the time to explain everything when undoubtedly, you had so much other stuff going on. Your willingness to help, teach and listen, really helped me better understand how a true mentor teaches. We had some great times together, whether it be in the Stem Cell room, or at ISSCR. I know you will keep crushing it at FluidForm and doing amazing things.

Ivan Batalov: I am happy that you are back in Pittsburgh and that we get to go climbing and spend time together. Thank you so much for taking the time to teach me about stem cells and for all your coding expertise that has contributed immensely to this dissertation. You are so smart and an amazing researcher, I know that you will undoubtedly create something like the iPhone someday.

Maria Stang: You are such an amazing friend (TEAM CANADA!). I have always treasured my discussions with you and can't wait to see all the amazing things you do in your future career. My only hope is that you begin to see just how amazing a researcher you are and that you begin to share that knowledge and power with those around you.

Anne Behre: You are truly a great friend and such a great person to be around. I truly enjoy spending time with you outside of the lab (doing yoga or whatever other crazy workout class we want to try) and in the lab (making never-ending batches of slurry). You are super smart and motivated and I can't wait to see what you do with your time in the lab and in your future career.

Erica Comber: I have really enjoyed all of our conversations and working with you in the lab. You are an amazing researcher with such a high attention to detail. I can't wait to see what you do with your research and really look forward to continue our work together.

Santiago Carrasquilla: We started in the lab at the same time and it is crazy that we are now at the end of our PhD studies. Thank you for teaching me how to make more appealing figures and slides and also for reminding me that I need to take time to enjoy my life. If it weren't for you, I would have delayed my honeymoon even longer. I am excited to see what you do in your future career where there is no doubt in my mind that you will have great impact on scientific research and policy.

Emily Sevcik: Thank you so much for being such a good friend and guiding me through the lab and teaching me how to be a tissue engineering TA. I have always admired how hard-working and detailed oriented you are.

Neeha Dev Arun: I am super impressed with all that you have done in the lab: from your Masters until now. It has been really fun helping you with cell culture and imaging. I also really enjoyed serving with you on the SFB student board: from organizing our first Biomaterials Day to 3D printing frosting on cookies-I have really enjoyed our times together.

Brian Coffin: It has been such a pleasure to work with you on the stem cell team! I am so excited to see where your research and life (new addition) take you!

Josh Tashman: You are an incredible researcher. I feel lucky that I got to learn tips and tricks of bioprinting from you. Thank you for taking the time to teach me. There is no doubt in my mind that you will do amazing things as you have already have some pretty amazing accomplishments!

Sam and Caner: I am lumping you guys together because you are new, but I have really appreciated getting to know both of you. You guys are both so hard-working and I can't wait to see what you two do in the lab.

Collagen Paper Group (Andrew Lee, Andrew Hudson, TJ Hinton, Josh Tashman, Dan Shiwarski, Sai Gopalkrishna Yerneni): There were some points during this process that I wish I could block out of my mind, but overall, I am happy how everything turned out. I am truly grateful that I got to work with and learn from all of you.

Collaborators in other Labs (Peter, Mathilde, Tzahi, Sahil, Anna, Sam, Yingqiao, Charlie, Wai Hoe, Barbie, and others): If I had any advice to early career researchers, get out and discuss your techniques and findings with other researchers. I am the scientist that I am today because of my willingness to work with and take time with other researchers. Because of this, I have been exposed to some pretty amazing things and this has only furthered my excitement for research.

To my former undergraduate trainees- Sabrina Liu, Madison Stiefbold, Xining Gao, Mohamed Eltaeb, Sanjana Shah and Kristina Kim. Being your mentor taught me more than I could have ever imagined and allowed me to grow as a scientist. It is my hope that you carry on this tradition of mentoring and teaching to your future trainees.

To the stem cell team (Ivan Batalov, Andrew Lee, Yan Sun, Maria Stang, and Brian Coffin). Few people understand the time and effort it takes care for stem cells. Thank you for always putting in the time and energy to make sure that I had cells to do my studies. Without everyone on this list, this dissertation (and pretty much every single paper I published during my PhD studies) would not be possible and I truly appreciate all the effort and dedication.

ABSTRACT

Heart failure, a condition where the heart muscle loses its ability to effectively contract and pump blood throughout the body, is often the result following significant cardiac damage. Though medication and lifestyle changes can delay heart failure progression, other factors, like the changes in mechanical loads on the tissue, are often not taken into account, and many of these patients will go on to need a heart transplant. In fact, nearly half of those patients diagnosed with heart failure will die within 5 years of their diagnosis, which is mainly attributed to a poor understanding of the factors that drive disease progression (mechanical load, genetic factors, etc.) and the lack of available donor hearts suitable for transplantation. Tissue engineered heart muscle has recently emerged as a tool to test drug toxicity, to model disease, and to eventually repair and replace the human heart. However, current heart muscle tissue models are hampered by their limited ability to mimic physiologic mechanical loading, which precludes their use as models for drug screening or disease modeling. Further, many of these models also lack the geometric complexity to support advanced functions of the human heart, such as pumping fluid, which are necessary when we consider using these models to repair or replace the human heart. In this work, I first engineered a system that can be used to mimic physiologic hemodynamic loading conditions, including the preload (load that stretches heart muscle during chamber filling) and afterload (pressure that the heart must contract against to eject blood). Dynamic loading of healthy control engineered heart tissues (EHTs) in this model (dyn-EHT) led to adaptive heart muscle remodeling and increases in heart muscle function, including contractile stress generation, myofibrillar alignment, and electrical excitability. In contrast, dyn-EHTs generated from a patient with a desmoplakin mutation, a mutation that clinically results in arrhythmogenic cardiomyopathy, displayed maladaptive remodeling with excessive tissue

lengthening and reduced contractile stress generation. These results are consistent with the clinical course of disease progression observed in human patients, including ventricular dilation and reduced cardiac output. As a first step towards producing engineered heart muscle with more advanced geometric complexity, I also manufactured a bioinspired, contractile human heart tube using Freeform Reversible Embedding of Suspended Hydrogels (FRESH) bioprinting. Heart tubes displayed dense layers of interconnected cardiomyocytes, unidirectional calcium wave propagation, and displacement of fluorescent beads with increased pressure generation during contraction. Finally, I used heart tube morphogenesis as a template to demonstrate that mechanical loading is critical in engineering more complex heart muscle structures. Here, I used 3D printing to insert structural asymmetries in prints, causing them to bend in a specified direction when a force was applied. Heart tube bending resulted in region-specific changes in myofibrillar alignment and calcium conduction. These findings suggest that mechanical loading is critical to engineered heart muscle formation, from manufacturing patient-specific disease models to personalized tissues and organs for heart repair and replacement.

TABLE OF CONTENTS

LIST OF TABLES

LIST OF FIGURES

LIST OF ACRONYMS

Engineered heart tissue	EHT
Freeform Reversible Embedding of Suspended Hydrogels	FRESH
Dynamic engineered heart tissue	dyn-EHT
Polydimethylsiloxane	PDMS
Arrhythmogenic cardiomyopathy	ACM
Cardiovascular disease	CVD
Myocardial Infarction	MI
Left ventricle	LV
Extracellular Matrix	ECM
Organoid Building Blocks	OBBs
Embryonic Stem Cells	ESCs
Induced pluripotent stem cells	iPSCs
Essential 8	E8
Normal human cardiac ventricular fibroblasts	NHCF-V
Time to 50% contraction	t50
Time to 90% contraction	t90
Phosphate Buffered Saline	PBS
4′,6-diamidino-2-phenylindole	DAPI
Human Embryonic stem cell	hESC
Human induced pluripotent stem cell	hiPSC
Bovine serum albumin	BSA
Action Potential Duration	APD
Maximum Upstroke Velocity	Vmax
Complementary DNA	cDNA
Polymerase chain reaction	pCR
poly n-isopropyl acrylamide	PIPAAm
fibronectin	FN

Chapter 1

Introduction

The heart is responsible for pumping blood throughout the body and it must maintain sufficient cardiac output by adapting to differences in mechanical loads, including stretch during chamber filling (preload), and the pressure the heart must work against to eject blood (afterload). These physiological loads are critical to normal heart function, for example, during development they contribute to heart muscle maturation resulting in increased cardiomyocyte alignment and hypertrophy[60]. However, abnormal forces due to disease and injury can lead to altered ventricular loads, resulting in maladaptive changes in structure and function, including disorganization of heart muscle cells (cardiomyocytes), dilation of heart muscle chambers, and reduced contractile force[49]. Thus, the heart can undergo dramatic remodeling with loading, however, it is not well understood how these forces specifically contribute to either maladaptive or adaptive changes in heart structure and function.

Recent developments in cardiac tissue engineering and stem cell technologies have made it possible to generate engineered heart muscle tissues (EHTs), which can serve as tools to study how heart muscle forms, as a platform to study disease, and as a potential therapeutic to repair or replace damaged heart muscle. However, current tissue engineered heart muscles are not exposed to physiologic mechanical loading regimes, which contribute to heart muscle structure and function, limiting their use as a surrogates for *in vivo* heart muscle. Further, current engineered heart muscle tissues are fabricated into simplified geometries[95], like strips, rings and sheets, and lack the geometric complexity to perform advanced functions of the human heart, such as pumping, which also limits their applicability as therapeutic strategies to repair or replace the

damaged heart. Thus, a greater understanding of how specifically mechanical loading and geometry influences heart structure and function could significantly aid in our ability to not only generate more physiologic tissues for *in vitro* screening but also significantly aid in our ability to generate tissues for repair and replacement.

In this thesis, I first provide an extensive background on heart muscle structure and function and its relation to mechanical loading under various health and disease states. I then discuss the current strategies to engineer heart muscle and current mechanical loading strategies to yield EHTs for *in vitro* screening platforms and therapeutic use. In chapter 3, I created an improved dynamic mechanical loading platform (dyn-EHT) by incorporating EHTs with elastic polydimethylsiloxane (PDMS) strip, which is used to simulate the physiologic mechanical loads on heart muscle. I demonstrate that this platform can increase EHT function in control tissues, while also driving a disease phenotype in tissues with a genetic mutation that results in arrhythmogenic cardiomyopathy (ACM) in human patients. Next, I use 3D printing to create an engineered heart muscle tissue platform with a more intricate geometry capable of performing complex functions of the heart, such as pumping fluid. Later, I incorporate mechanical loads through structural transitions observed in the heart morphogenesis and show that this is important in developing regional variations in heart muscle tissue structure and function.

1.2. Dissertation Organization

This dissertation is organized into several vignettes designed to gain a further understanding of how mechanical load influences heart muscle structure and function. Specifically, in chapter 3, I examine the development of a dynamic mechanical loading platform, which can be used to increase the functional of control engineered heart muscle tissues. In chapter

4, I then use this dynamic mechanical loading platform to better understand disease progression in an *in vitro* model of ACM. In our progress to develop a more accurate 3D representation of heart muscle, chapter 5 focuses on engineering a contractile, bioprinted linear heart tube reminiscent of early heart morphogenesis. To better understand how mechanical loading influences the organization of heart muscle in a more complex three-dimensional system, I use the linear heart tube and apply a mechanical load that is observed during the tube bending portion of heart morphogenesis and observe the effects that this has on the structure and function of the heart tube. Overall, in this work, I show the important role mechanical load plays in guiding heart structure and function in both health and disease.

1.3. Chapter 2: Background on Heart Muscle Tissue Engineering and Mechanical Loading

In this chapter, I discuss the structure and function of heart muscle and its relation to physiological mechanical loads observed during health, disease, and heart development. An extensive literature review is then performed to discuss current 2D and 3D engineered cardiac tissue fabrication strategies and mechanical loading techniques.

1.4. Chapter 3: Dynamic Loading of Human Engineered Heart Tissue Enhances Contractile Function

In this chapter, I create a simplified model of physiologic mechanical loading on engineered heart muscle (dynamic EHT or dyn-EHT) with the intent of gaining further insight into those mechanical loads which drive healthy cardiac tissue function. Here, I show that dynamic loading with a threshold load leads to improved tissue function, including contractility, structural

organization, and electrophysiology.

1.5. Chapter 4: Dynamic Loading Drives a Desmosome-Linked Disease Phenotype

In Chapter 4, I use the previously developed dyn-EHT system to investigate a disease known to be exacerbated by increased mechanical loading on heart muscle, namely a desmosomal associated ACM. Under a dynamic loading regime that increased function in control engineered heart muscle tissues, I found that ACM patient derived EHTs displayed reduced tissue function, including reduced contractile shortening, and stress generation.

1.6. Chapter 5: Creation of 3D bioprinted heart tube model

I aimed to use our findings of mechanical loads that drive increases in tissue function and apply them to tissues with more intricate geometries that are capable of performing complex functions of the heart, such as pumping fluid. To do this, I used Freeform Reversible Embedding of Suspended Hydrogels (FRESH) 3D bioprinting to create a model of the linear embryonic heart tube. Here, I demonstrate that the heart tube model has dense layers of cardiomyocytes on its surface, displays unidirectional calcium wave propagation, and can be electrically paced up to 3 Hz. Finally, I was also able to demonstrate that engineered heart tubes can displace fluorescent beads from their tube lumen via increased pressure generation with tissue contraction.

1.7. Chapter 6: Programmed Tube Bending Morphogenesis of a 3D Bioprinted Heart Tube

The goal of this chapter was to investigate mechanical loading observed during heart morphogenesis in an engineered system. During morphogenesis, the heart first starts as a linear tube that then bends, loops, and septates to form its mature 4-chambered structure. This complex

change in shape is accompanied by changes in tissue loads, which can contribute to later heart structure and function. In this chapter, I sought to replicate the tissue morphogenesis process by inserting structural and mechanical asymmetries with 3D printing to drive heart tube bending upon the application of cardiac fibroblast compaction forces. Interestingly, bent tubes displayed regional differences in cardiomyocyte alignment, conduction velocity and conduction patterns when compared to linear tubes.

1.8. Appendices

Appendices A and B contain chapters that are not directly related to this thesis work but are necessary to consider in engineering heart muscle. In appendix A, I introduce and discuss a technique to deliver extracellular matrix "shrink-wrapped" functional units of contractile heart muscle to damaged heart muscle tissue with the ultimate goal of restoring tissue function. In appendix B, I evaluated 3D bioprinted tubes as vasculature to support the viability of large, volumetric tissues.

Chapter 2

Background on Heart Muscle Tissue Engineering and Mechanical Loading

2.1. Cardiovascular Disease Prevalence, Current Treatments, and Tissue Engineering

Cardiovascular diseases (CVDs) are a group of disorders that affect the heart and associated blood vessels. CVDs are the leading cause of death worldwide and have a number of contributing causes, including behavioral risk factors (tobacco and alcohol use), infection (rheumatic fever), and genetics[91]. However, the leading cause of CVDs is myocardial infarction (MI), a condition where heart muscle dies following coronary artery occlusion.

Unfortunately, heart muscle cells, or cardiomyocytes, display poor regenerative capacity and are unable to repair the damaged muscle[88]. In many, this leads to a slow degenerative disease that results in structural and functional remodeling of the remaining heart muscle termed heart failure. While lifestyle modifications and medicines have been beneficial in slowing disease progression, those patients with severe heart failure will go on to require a heart transplant. Unfortunately, donor heart organs are in limited supply with only ~ 3,000 heart transplants being performed in the United States each year[20]. This lack of donor organ supply also contributes to high patient mortality with more than half of the patients diagnosed with heart failure dying within 5 years of their diagnosis[91]. Thus, there is an urgent need to better understand the structural and functional remodeling that occurs in heart disease and to develop clinical alternatives for heart repair and replacement.

Cardiac tissue engineering has emerged as a tool to study how heart muscle forms, a platform to model disease and injury, and a potential therapeutic approach to create contractile

tissues to repair or replace the damaged heart. In fact, cardiomyocytes can now be generated extensively from both embryonic and induced pluripotent stem cells and even through direct trans-differentiation of blood cells or fibroblasts[23,42]. However, cardiomyocytes obtained from these protocols have immature characteristics with underdeveloped structural (sarcomeres, t-tubules, etc.) and functional maturation (calcium storage, expression of ion channels, etc.) compared to their adult counterparts[47]. Thus, one significant challenge is being able to engineer cardiac tissues with adult level function that can provide insights into disease and are capable of repairing the damaged heart.

2.2. Macroscale Heart Anatomy and Function

The heart is composed of 3 distinct layers: the outer epicardium, the middle myocardium, and the inner endocardium. Cardiac muscle, which is responsible for the contractile behavior of the heart, is found within the myocardium and will be the focus of this dissertation. Cardiac muscle requires a precise hierarchical organization which is intimately linked to its function. Thus, a primary requirement in the cardiac muscle engineering field is to understand the organization of cardiac muscle and the factors that drive this organization.

The primary function of the heart is transporting oxygenated blood and nutrients to all tissues and organs in the body. This function is achieved through its macroscale organization, which consists of muscular walls surrounding hollow chambers. In brief, the heart consists of two smaller chambers (the atria) and two larger chambers (the ventricles) which are separated by valve structures to facilitate pumping and unidirectional blood flow. The atria and ventricles form a two pump system with different objectives: (i) to deliver oxygenated blood and nutrients to the body and (ii) to deliver deoxygenated blood to the lungs for reoxygenation and removal of carbon

dioxide. The right side of the heart, which consists of the right atria and right ventricle, is responsible for pumping deoxygenated blood to the lungs, whereas the left side of the heart (the left atrium and left ventricle), receives reoxygenated blood and transports it to the systemic circulation.

2.3. Supporting Vasculature and Nerves

Though not the direct investigation of this thesis, it is important to note that there are other important tissue components within the heart besides the musculature, including vessels and nerves. For the vasculature component, the heart is supplied by the coronary arteries and veins, which deliver nutrients and remove wastes from the actively contracting heart muscle. Given the high metabolic activity of the heart, it is crucial that heart muscle has a constant supply of nutrients and oxygen and that wastes are efficiently removed. For this reason, heart muscle cells, or cardiomyocytes, are surrounded by a dense capillary network with about 20 μm spacing[7]. For the nervous component, the heart receives autonomic inputs, which can either speed up (sympathetic) or slow down (parasympathetic) the heart rate. These autonomic inputs are received by nodal cells, which are able to generate spontaneous depolarizations in the absence of nervous input, leading to the initiation of contraction throughout the heart.

2.4. Heart Muscle Architecture

The ability of the heart to pump fluid is not only accomplished by its macroscale organization of chambers and valves, but also through its internal muscular organization. The heart is composed of laminar sheets of cardiac muscle which wrap in a defined helical pattern (Figure 2.1). This characteristic wrapping of aligned heart muscle layers is important for heart pumping

function as it allows the heart muscle to decrease its chamber volume and increase pressure, facilitating blood flow.

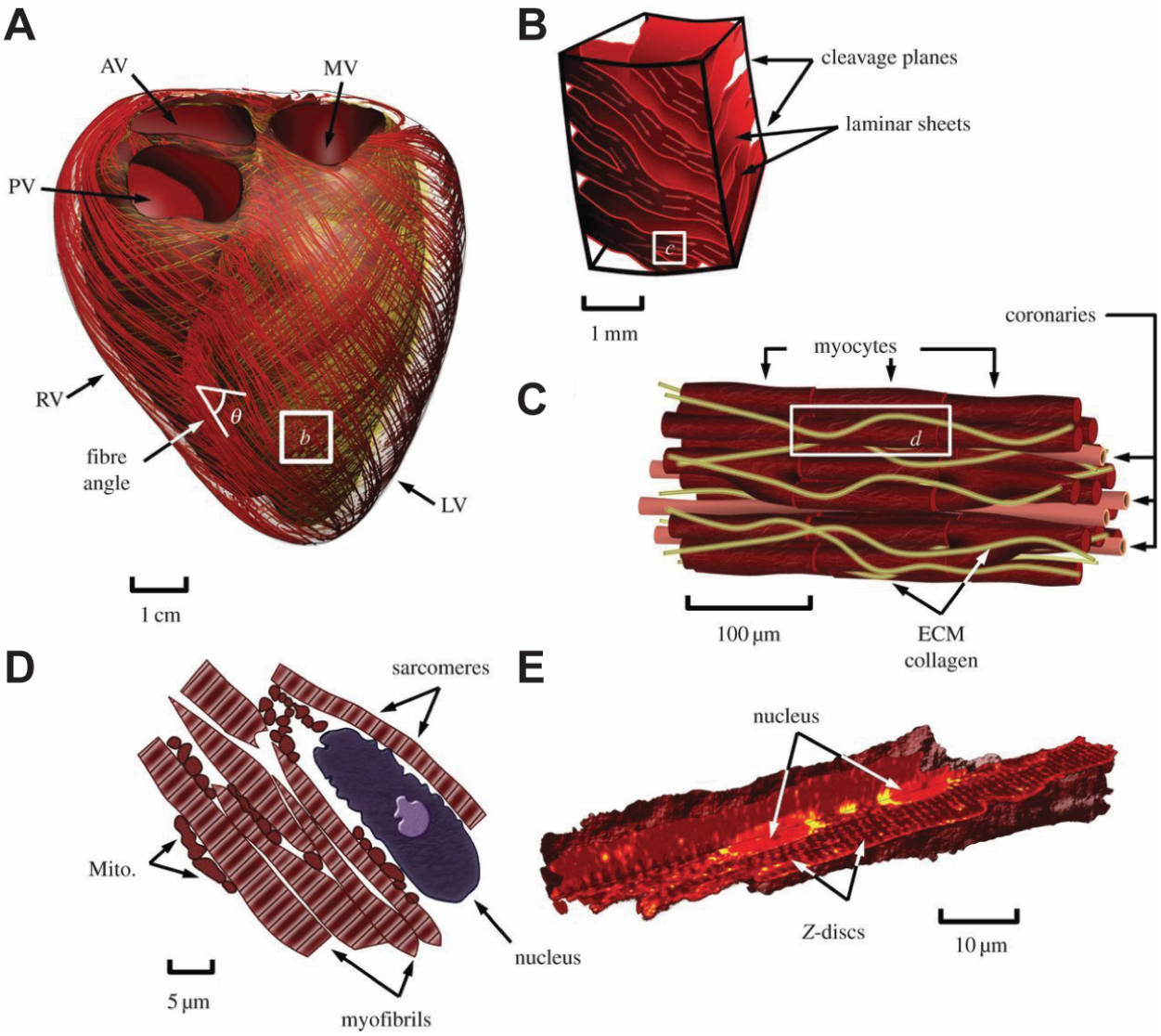

Fig 2.1: Multiscale Architecture of Heart Muscle. (A) Whole heart schematic with streamlines showing orientation of cardiac muscle fibers. (B) Heart muscle section showing muscle fiber bundles arranged in lamellar sheets with separated cleavage planes. (C) Zoomed in version of lamellar sheets showing cardiac myocytes surrounded by extracellular matrix and coronary capillaries. (D) Internal view of cardiomyocyte showing aligned internal sarcomeres and numerous mitochondria. (E) Cardiomyocyte anatomy showing nuclei and z discs, which anchor the ends of individual sarcomeres. Figure adapted from[17]. right ventricle (RV); left ventricle (LV); pulmonary valve (PV); aortic valve (AV); mitral valve (MV); extracellular matrix (ECM); mitochondria (Mito). Creative commons license.

On the tissue scale, these laminar sheets are composed of anisotropically aligned cardiomyocytes connected from end to end via important cellular junctions called intercalated discs. These intercalated discs (Figure 2.2) house critical components of the heart muscle machinery, linking together adjacent cardiomyocytes with gap junctions, adherens junctions and desmosomes. Gap junctions are important electrical connections between cardiomyocytes that allow for the depolarizing ions to flow freely between adjacent cells resulting in a coordinated muscle contraction (a syncytium). Desmosomes, which link intermediate filaments of adjacent cells together, are important mechanical linkages between cardiomyocytes and are responsible for preventing separation of cardiomyocytes during the contraction and relaxation. Adherens junctions are also critical structural components of the intercalated disc, which connect actin filaments to the closest sarcomere, the contractile unit of heart muscle cells.

Within individual cardiomyocytes, sarcomeres have precise orientations that dictate the direction of cardiomyocyte contraction. The sarcomere consists of parallel thin (actin) and thick (myosin) filaments, whereby myosin is able to pull on the actin filaments resulting in cellular shortening upon exposure to an appropriate depolarizing stimulus. In adult heart muscle cells, depolarization is initiated by spontaneous depolarizations in adjoining pacemaker (nodal) cells. Depolarization of a cardiomyocyte results in activation of voltage-gated Ca^{2+} channels and release of Ca^{2+} from the sarcoplasmic reticulum. This is important because, at rest and in the absence of Ca^{2+}, cross-bridge cycling and sarcomere shortening is blocked via the troponin-tropomyosin complex. However, upon sarcoplasmic release, Ca^{2+} binds to the troponin-tropomyosin complex which exposes myosin active sites and leads to cross-bridge cycling between actin and myosin filaments and coordinated shortening of sarcomeres. It is important to note that the combined shortening of sarcomeres in parallel and in series results in macroscopic muscle shortening. Thus,

the organization and alignment of sarcomeres are critical to observed macroscopic heart pumping function.

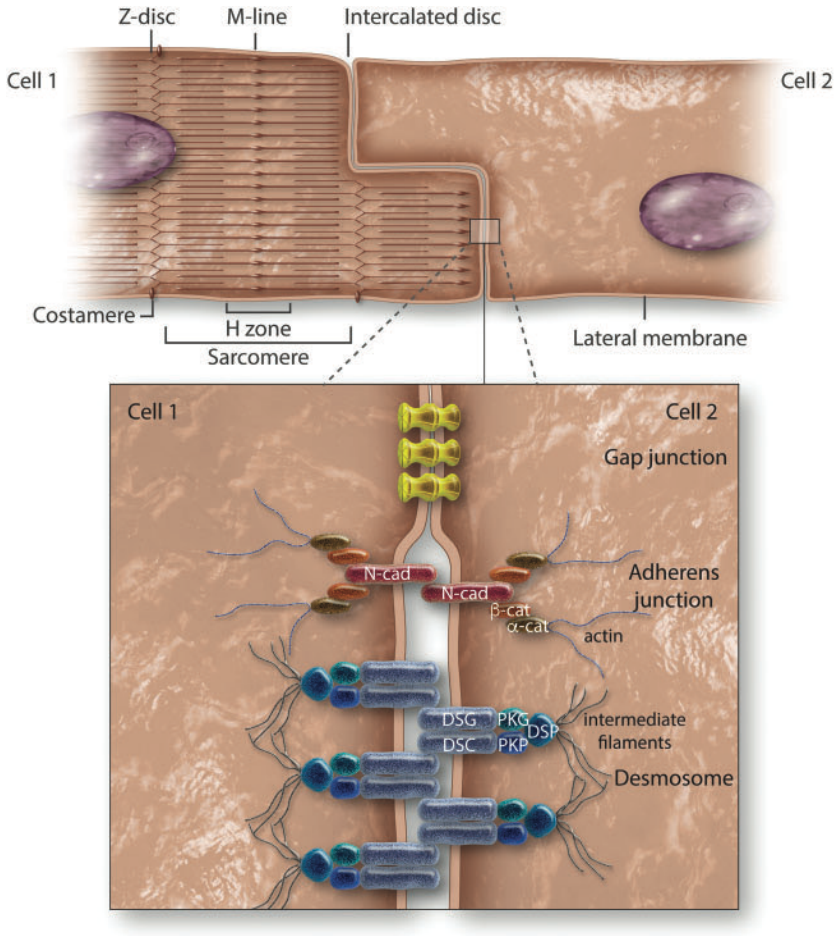

Fig 2.2: Schematic of the intercalated disc. Intercalated discs are found between adjacent cardiomyocytes and house essential junctions, including gap junctions, adherens junctions, and desmosomes. Figure from[90]. N-cadherin (N-cad), Beta-catenin (β-cat), Alpha-catenin (α-catenin. Desmoglein (DSG), plakophilin (PKP), plakoglobin (PKG), Desmoplakin (DSP).

2.2 Mechanical Forces in the Heart

Given that structure of the heart is so intricately linked with its function, it is perhaps unsurprising that the heart can respond to changing hemodynamic loads and adapt its structure and hence its function, to respond to changing loading conditions. On the short time scale, the heart is responsible for pumping blood throughout the body and it must maintain sufficient cardiac output by adapting to differences in mechanical loads, including stretch during chamber filling (preload) and pressure the heart must work against to eject blood (afterload). In the long term, this means that heart muscle cells can physically remodel to respond to these changing loading conditions, including hypertrophy (an increase in cell size) or rearranging their sarcomeres. It is important to

note that these responses are critical to normal heart function and formation, where during development they contribute to heart muscle maturation resulting in increased cardiomyocyte alignment and hypertrophy[60]. However, these loads can also result in maladaptive remodeling, such as ventricular dilation, and reduced function of the heart as is the case in heart disease[49]. In the following sections, we will discuss what is known about the about the heart's structural and functional adaptations to loading in two separate case conditions, heart development and cardiac disease.

2.2.1. Mechanical Forces in Cardiac Development

Mechanical loads play a critical role in heart formation and development. Thus, an understanding of how these loads guide heart muscle formation is critical for the scientist who is attempting to engineer the heart.

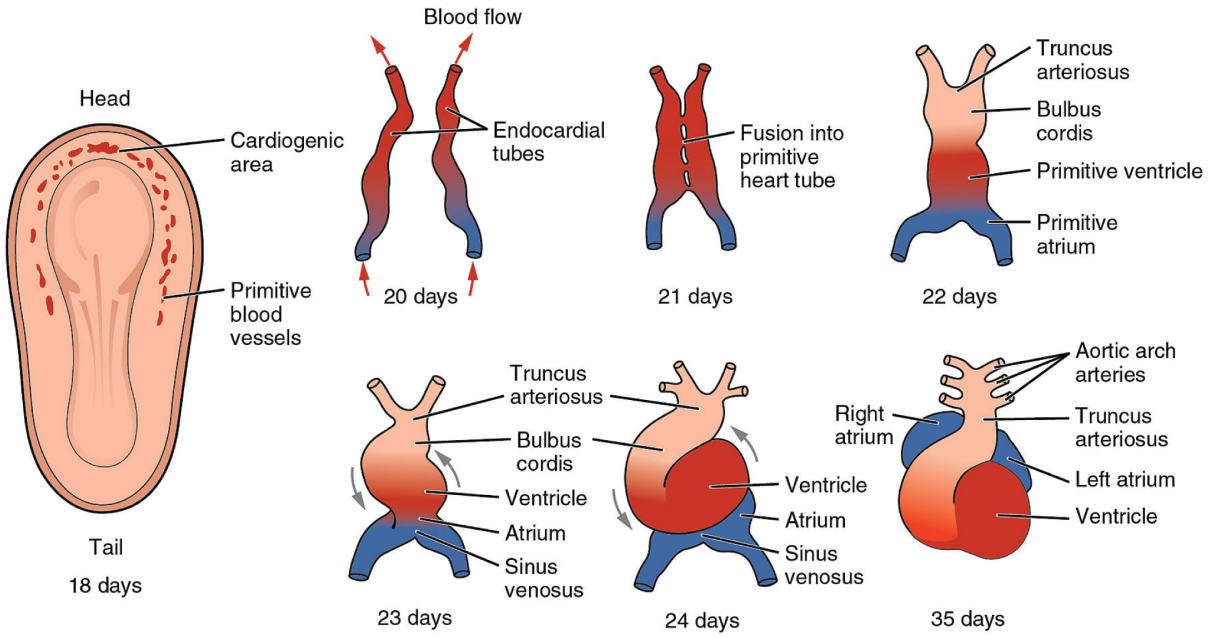

Fig 2.3: Overview of Heart Development. The heart forms from mesodermal cells derived from the cardiogenic region near the head of the embryo. The cardiogenic region then begins to form cardiogenic cords which form lumens and paired endocardial tubules. These endocardial tubules then fuse to form the primitive heart tube, which then undergoes a complex bending and looping process to form its more mature three-dimensional fetal heart structure. Creative commons license. Illustration from Anatomy & Physiology, Connexions Web site. http://cnx.org/content/col11496/1.6/, Jun 19, 2013.

The heart is the first organ to form during development as it is needed to pump nutrients to a rapidly developing embryo[32]. To enable this, the heart must undergo morphogenesis (drastic changes in its structure and function), first starting as a linear tube then bending and looping to transition to its more mature chambered-structure[50] (Figure 2.3). During this morphogenesis process, it is proposed that changes in mechanical loads drive cellular and molecular responses that coordinate heart tissue remodeling through a process called mechanotransduction. Mechanotransduction is the translation of mechanical forces into chemical/electrical signals that initiate structural and functional changes within cells and tissues. The primary mechanical forces responsible for this are the afterload (the pressure cardiomyocytes must contract against to expel blood out of the heart), the preload (stretch during heart muscle relaxation due to blood filling), and fluid shear stress (the frictional force parallel to the blood vessel wall due to fluid flow). Further, as the heart tube is undergoing the bending and looping process there are also changes in loading conditions along the length of the heart tube, which will be subsequently referred to as the morphogenetic load. Shear stress has been shown to impact valve morphogenesis, trabeculation, and chamber septation, however, the purpose of this thesis is to more thoroughly investigate the effects of preload, afterload, and morphogenetic loads on heart muscle function. Literature on the effects of shear stress on heart development can be reviewed elsewhere[32].

So how do these loads ultimately influence heart muscle function? In cardiomyocytes, increased mechanical loading contributes to either increases in proliferation (an increase in the number of cardiomyocytes) or hypertrophy (an increase in the size of cardiomyocytes via contractile protein synthesis and sarcomere number and organization). Embryonic cardiomyocytes display a high rate of proliferation when exposed to increases in mechanical load with the highest rate of DNA synthesis being observed during cardiac morphogenesis, which is necessary to

increase myocardial mass[85]. Later in development, embryonic cardiomyocytes display hypertrophy, with increased organization and number of myofibrils, in response to increased afterload[18]. The organization and alignment of myofibrils and cardiomyocytes is also significantly impacted by changes in loading conditions[67,97]. In fact, during morphogenesis, there is an increased alignment and elongation of cells on the outer curvature of the bent heart tube[5]. Cardiomyocyte phenotype is also significantly impacted by loading where changes in isoforms and amounts of electrical, mechanical, and metabolic proteins is commonly observed[35]. There is also evidence that extracellular matrix composition in the developing heart is modulated by mechanical loading with increases in afterload creating stiffer heart muscle through both increased collagen content and organization[33].

There are several additional lines of evidence that suggest mechanical loading of heart muscle is critical during morphogenesis and affects structure and function of later heart muscle. First, the initiation of the heart beat starts prior to the embryo requiring substantial nutrients and oxygenation. For instance, ligation of the cardiac outflow tract[15] or partial banding of the conotruncus[14] after the bending and looping process has occurred does not significantly affect oxygen consumption or body mass accumulation suggesting that there are alternative reasons for the initiation of heart muscle contraction, like mechanotransduction. Second, altering mechanical loading during heart muscle development leads to formation of congenital heart defects, or problems in the structure and function of the heart that are present at birth. For example, left atrial ligation[80] in chick embryos reduces left ventricular preload resulting in a condition similar to that observed in human patients called hypoplastic left heart syndrome, where the left ventricle is severely underdeveloped and unable to effectively pump blood. In addition, occlusion of either the heart tube inflow or outflow tract causes defects in heart tube looping, valve and chamber

formation[40]. Third, while genetic mutations associated with congenital heart defects have been the focus of investigations, specific genetic defects are often associated with a variety of congenital heart malformations. For example, family members that carry the same mutation often have a diverse set of heart malformations, including tetralogy of fallot, ventricular septal defects, or even atrial septal defects[13]. Further, there is increasing evidence that heart malformations occur primarily in families with no history of disease, and that only 2-4% of all congenital heart defects are present in families with a history of congenital heart defects[73]. These findings suggest that hemodynamic alterations, rather than sole genetic mutations, are the primary cause of these heart malformations.

2.2.2. Mechanical Forces in Cardiac Disease

Mechanical loads can also lead to maladaptive remodeling of heart structure and function in the adult, as is the case in heart disease. In the heart, tissue mechanical properties are largely determined by the cells (mainly cardiomyocytes and fibroblasts) and their associated extracellular matrix. Perhaps then, it is not surprising that cardiac diseases that alter the density or distribution of either cells or the extracellular matrix contribute to large changes in the mechanical properties of the heart and thus, its response to mechanical loads. One case example of this is the remodeling observed following death to the heart muscle wall or myocardial infarction (MI). Following MI, there is a prominent wound healing response that leads to inflammation and remodeling[39]. These processes are considerably impacted by mechanical loads on the tissue and can lead to variations in the structural and functional remodeling observed in the ventricle (Figure 2.4). MI leads to loss of cellular structure and focal thinning of the ventricle, which locally increases tissue stress[34]. When the damage is significant, this results in two predominant outcomes, either diastolic or

systolic heart failure. For example, diastolic heart failure, which is characterized by increased ventricular stiffness and reduced ventricular filling, results from excessive fibrosis as well as heart muscle hypertrophy during tissue remodeling[92]. Here, it has been suggested that mechanical stress contributes to the regulation and production of new ECM materials within the infarct area through various mechanotransduction pathways[10,22]. Alternatively, systolic heart failure can also occur post-MI, where the ventricle displays reduced ability to contract and is often associated with tissue lengthening and ventricular dilation[92].

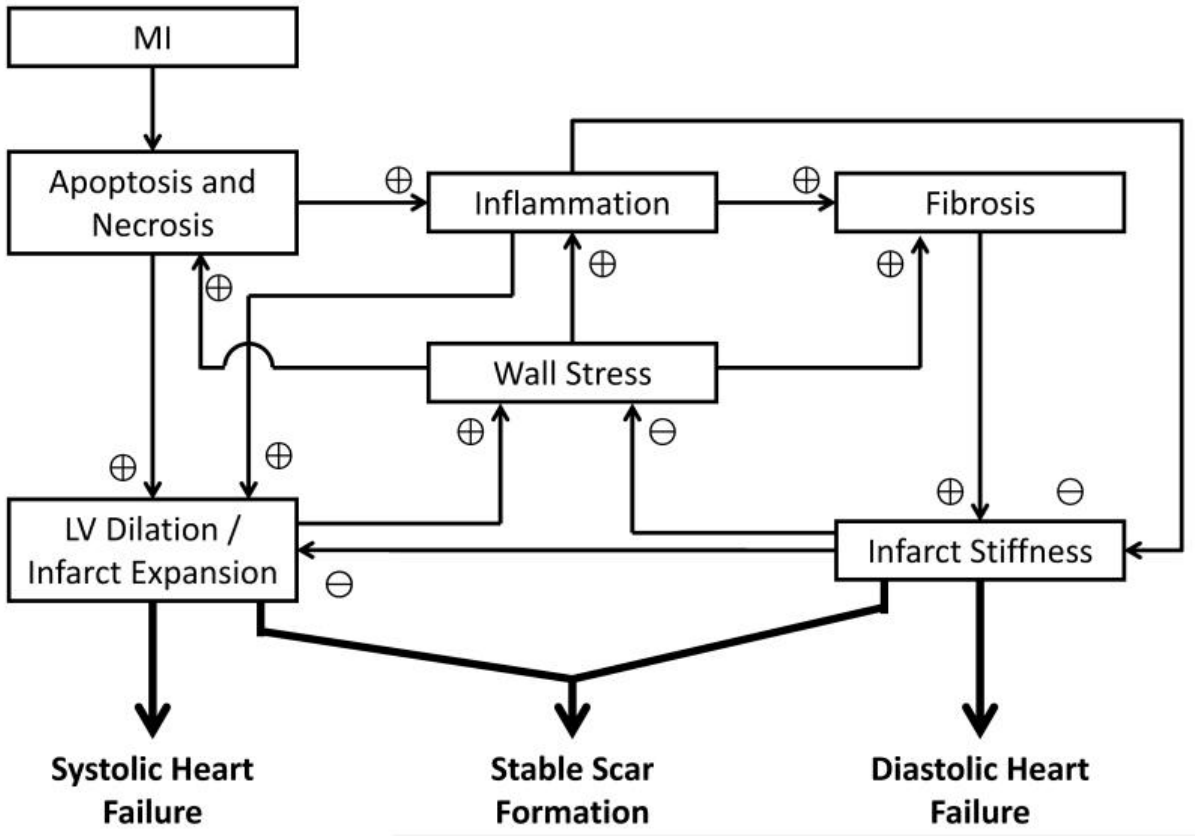

Fig 2.4: Mechanical Regulation of Heart Muscle Remodeling. Chart demonstrating the effects of myocardial infarction on tissue remodeling, wall stress, and heart failure. The positive (+) symbol represents a positive association between these factors [i.e. apoptosis and necrosis contributes to left ventricle (LV) dilation and infarct expansion] while a negative (-) symbol represents a negative association between the two factors (i.e. infarct stiffness decreases wall stress). Figure from [92].

Additional support for load-driven remodeling following heart muscle damage has been demonstrated by those who have seen more favorable remodeling post-MI with strategies developed to reduce ventricular wall stress. For instance, D'Amore et al. reduced tissue stress and subsequent left ventricular wall thinning after myocardial infarction by attaching a bi-layered polyurethane-extracellular matrix patch over the infarct[19]. Similarly, approaches aimed at thickening the ventricle wall through injection of materials has also proved successful in ameliorating the maladaptive remodeling after myocardial infarction[63]. However, though it is clear that tissue mechanics drives remodeling, more research needs to be performed to better understand the extent and duration of mechanical loading and how that contributes to heart failure.

2.3. Guiding Heart Muscle Formation in 2D Systems

Now that we have a good understanding of the structure and function of the heart and how mechanical loading contributes, it is necessary to discuss the techniques used to engineer heart muscle tissues *in vitro*. As previously described, cardiomyocyte alignment is critical to heart muscle function. Here, two dimensional (2D) *in vitro* systems have been used extensively to study the extracellular matrix (ECM) and topographical cues that govern heart muscle cell alignment.

2.3.1. Topographical and Extracellular Matrix Cues

Traditional 2D culture of cardiomyocytes (i.e. isotropic organization on 2D plastic dishes) has served as a reference for drug screening and disease modelling. However, researchers have quickly learned that the environment of monolayer 2D culture is different than that observed in the human heart. For instance, *in vivo* cardiomyocytes in the heart are arranged in highly aligned lamellar sheets. Thus, many researchers have focused their investigations on creating highly

aligned cardiomyocyte platforms through several techniques, such as incorporation of either topographical[4,16,66,74] or extracellular matrix[6,77] cues. In particular, nanoscale topographical cues on the order of 400 and 800 nm ridges on a polyethylene glycol hydrogels (Figure 2.5A) have demonstrated efficacy in creating highly aligned cardiomyocyte monolayers (Figure 2.5B-D) with anisotropic calcium wave propagation (Figure 2.5E)[51]. Since these ridges are much smaller than the size of the cell, the researchers were also able to demonstrate that this alignment was due to organization of focal adhesions (integrin-containing structures within the cell) that attach the extracellular matrix to intracellular actin cytoskeleton.

In the same vein, extensive research has been performed on using the ECM to drive cardiomyocyte alignment in 2D culture. Here, researchers have used a technique termed microcontact printing[75] to create extracellular matrix patterns that cardiomyocytes can be cultured on. For example, line patterns (20 μm width and 20 μm spacing) made from the ECM protein fibronectin are particularly adept at aligning both primary and stem cell-derived cardiomyocytes[6,77]. However, though these platforms have provided expanded capability in drug and disease modelling, a major limitation in these 2D platforms is the inability to assess contractile function of these cardiomyocytes.

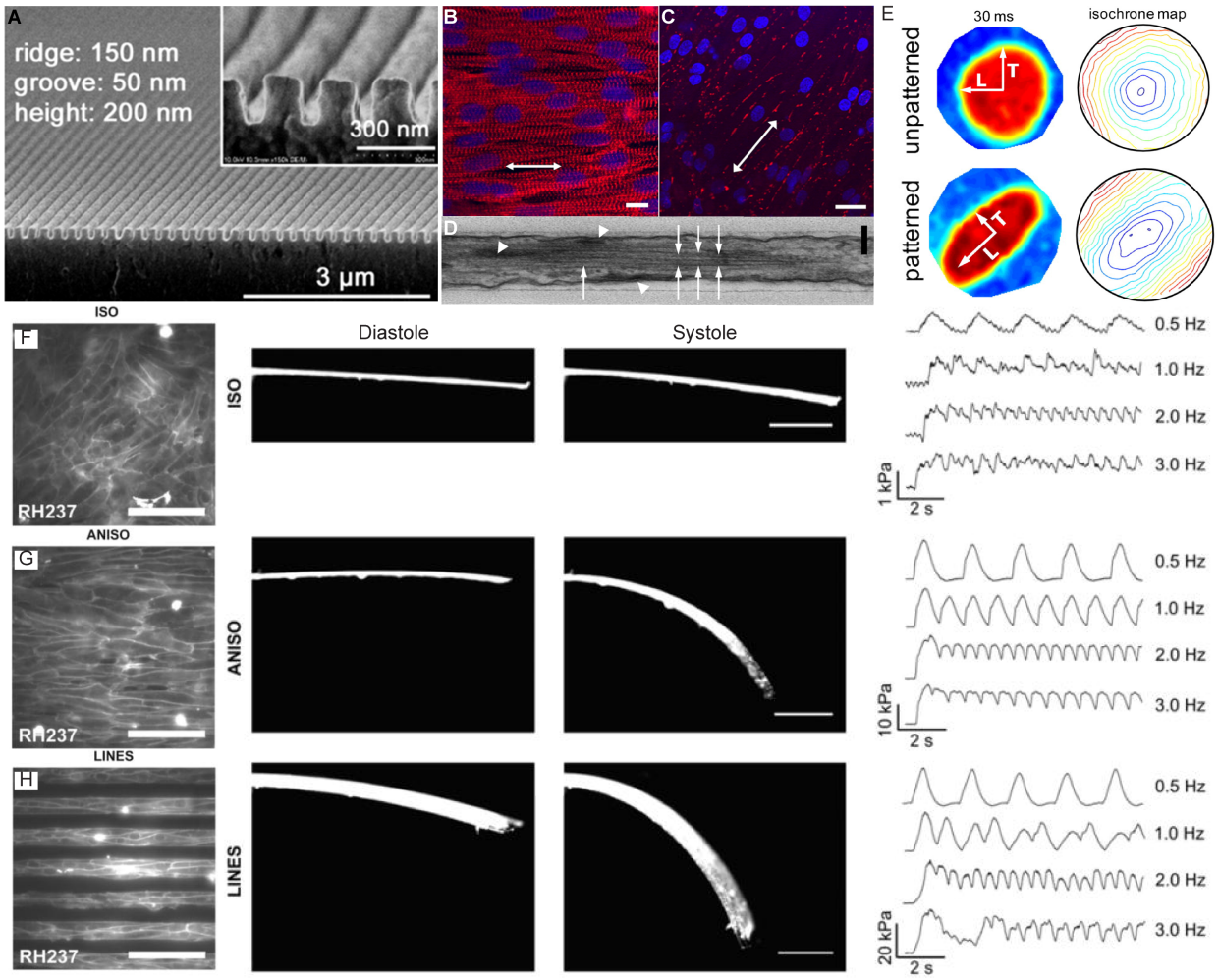

Fig 2.5: 2D Engineered Heart Muscle Tissues. (A) Topographical ridges created in polyethylene glycol hydrogels. **(B)** Cardiomyocyte culture on these hydrogels leads to highly aligned cardiomyocytes with z lines in register. Arrow indicates direction of ridge longitudinal axis. Red (alpha actinin), blue (nuclei). **(C)** Immunohistochemistry for gap junction (red) in cardiomyocytes cultured on ridges. Blue (nuclei). Arrow indicates direction of ridge longitudinal axis. **(D)** Transmission electron microscopy image showing that cells protrude into the ridge and have highly alignment myofilaments (white arrows) and focal adhesions (white arrowheads). **(E)** Electrophysiological characteristics of unpatterned (no ridges) and patterned (ridges) shown with isochrones. Patterned substrates showed a higher conduction in the direction of the longitudinal axis of the ridges. **(F)** Row from left to right. Cardiomyocyte alignment on unpatterned substrates results in isotropic organization leading to little contractility of the muscular thin film (MTF). Representative contractile stress plots at different stimulation frequencies for isotropic MTF (right) **(G)** Row from left to right. Confluent aligned monolayer on MTF leads to higher levels of deformation of the MTF. Representative contractile stress plots for anisotropic monolayer MTFs (far right). **(H)** Highly aligned cardiomyocytes on fibronectin line patterns show similar levels of contractile deformation despite lower levels of surface coverage suggesting if corrected for surface area then line MTFs would display higher levels of contractile stress (compared to ANISO). Representative contractile stress plots for line monolayer MTFs (far right).

2.3.2. 2D Muscular Thin Films

To improve upon these aligned 2D platforms, investigators have combined these with flexible films. These muscular thin films (MTFs) allow for the measurement of cardiac tissue contractility based on the degree of film bending that occurs with cardiomyocyte contraction. In fact, Feinberg et al. incorporated the microcontact printing of fibronectin lines on flexible PDMS films, and demonstrated increased cardiomyocyte and electrical anisotropy, as well as greater contractile forces (Figure 2.5F-H)[27]. Further, the authors could pattern the ECM in order to direct film bending, and even create films that could swim in a unidirectional manner[28]. Using a similar approach, McCain et al. molded topographical ridges on flexible gelatin films to align the cardiomyocytes and was able to showed increased alignment and improved contractility and metabolic function[65]. Given the combination of increased cardiac tissue anisotropy and improved measurements of contractile function, MTFs have also been utilized for drug screening[59] and for cardiac disease modelling[94].

2.4. Building Contractile 3D Heart Muscle Tissues

A clear advantage of these previously described 2D systems is greater control over the microenvironmental cues that drive cardiomyocyte organization, however, 2D culture does not accurately represent the 3D environment of the human heart[84] leading many researchers to investigate various 3D engineered heart muscle tissue systems.

2.4.1. Cardiac Spheroids and Self Assembly

In an effort to build systems that more accurately replicate the 3D nature of the heart, a number of cardiomyocyte self-assembly approaches have been developed to model drug toxicity, disease, and even, early cardiac development. For instance, cardiac spheroids, which consist of a

random assembly of cardiomyocytes potentially combined with endothelial cells and fibroblasts, have been manufactured through self-aggregation via hanging drop[76] or in aggreWells[12]. While these systems have demonstrated improved structure and function over age-match 2D controls[12], they still do not replicate the highly anisotropic nature of the human heart with spheroid structures displaying disorganized sarcomeres and extracellular matrix deposition compared to the adult human heart (Figure 2.6).

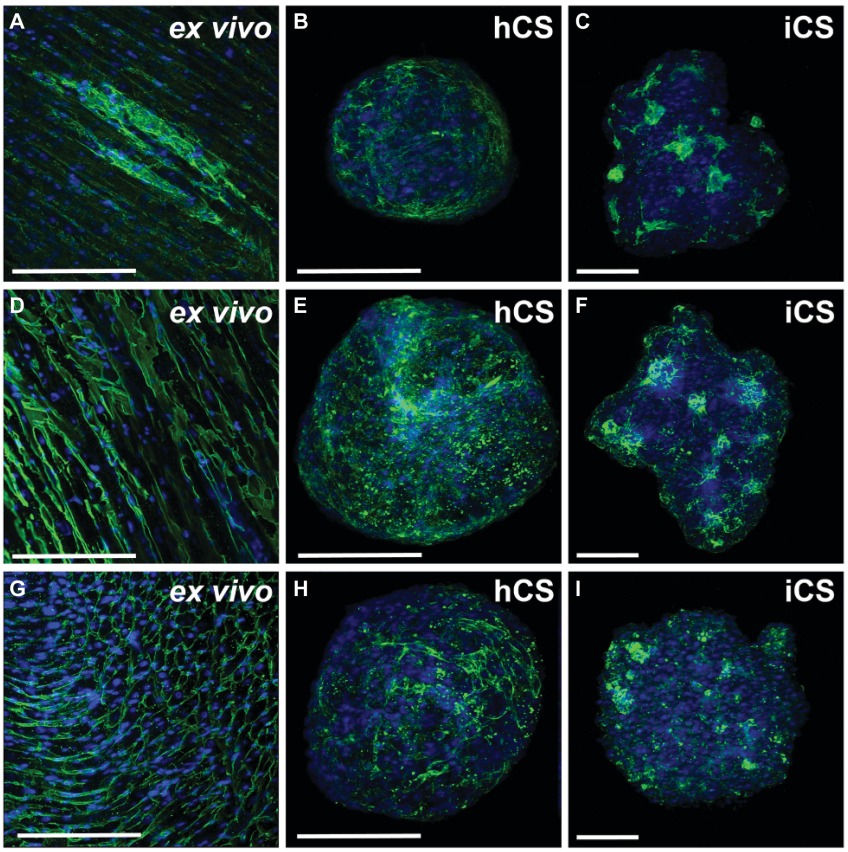

Fig 2.6: Extracellular matrix (ECM) deposition in human heart sections (ex vivo), human cardiac spheroids (hCS) and induced pluripotent cardiac spheroids (iCS). (A-C) Fibronectin, (D-F) collagen type IV and (G-I) laminin deposition within human heart sections, hCSs and iCSs (green). Nuclei were stained with Hoechst stain (blue). Scale bars: 200 μm. Figure adapted from [76].

Another interesting self-assembly approach that has been developed to study early cardiac morphogenesis are cardioids. Cardioids are aggregates of pluripotent stem cells that are induced

to differentiate and can undergo "self-morphogenesis" to create structures reminiscent of early heart development, such as primitive endocardial tubes[21] and even early heart chambers[38]. These platforms are also able to replicate some aspects of early heart defect formation using knockouts of genes that are known to be drivers in heart formation (NKX2.5 and Hand1)[21,38]. However, more research needs to be performed to confirm that the "self-morphogenesis" observed in these systems accurately depicts *in vivo* heart morphogenesis. Similar to previous spheroid systems, there still remains challenges in being able to use this cardioid technology to create heart structures with aligned microarchitectures, likely due to lack of mechanical cues that are known to drive cardiomyocyte organization.

2.4.2. 3D Heart Muscle Hydrogel-Based Casting Approaches

Building off the previously described self-assembly approaches, a number of groups have used hydrogel-based casting techniques by embedding cardiomyocytes as well as other cell types (fibroblasts and endothelial cells) within a liquid hydrogel that undergoes gelation, encasing the cells within the matrix[95]. These approaches are often accompanied by a mechanical support, like Velcro [26], pillars [56,58], frames [81], wires [29,93], and sutures [70], which can be used to generate tension within the tissue during fibroblast compaction of the matrix (Figure 2.7). This tension is critical in driving the uniaxial cardiomyocyte alignment as well as increasing the contractile function of 3D engineered heart muscle tissues[2,11]. This technology has been appropriated to also create highly aligned heart muscle sheets that are either suspended between a flexible frame[81] or have embedded pillars, to control tension and alignment throughout the tissue[58]. To create more advanced structures like that observed in ventricular chambers, Li et al. used a hydrogel casting approach around balloon catheters to generate a primitive heart muscle chamber[57]. Despite this, there are

limited examples of using casting-based approaches to generate heart muscles with more advanced structure, suggesting that there are challenges in using a casting-based technique alone to achieve geometric complexity.

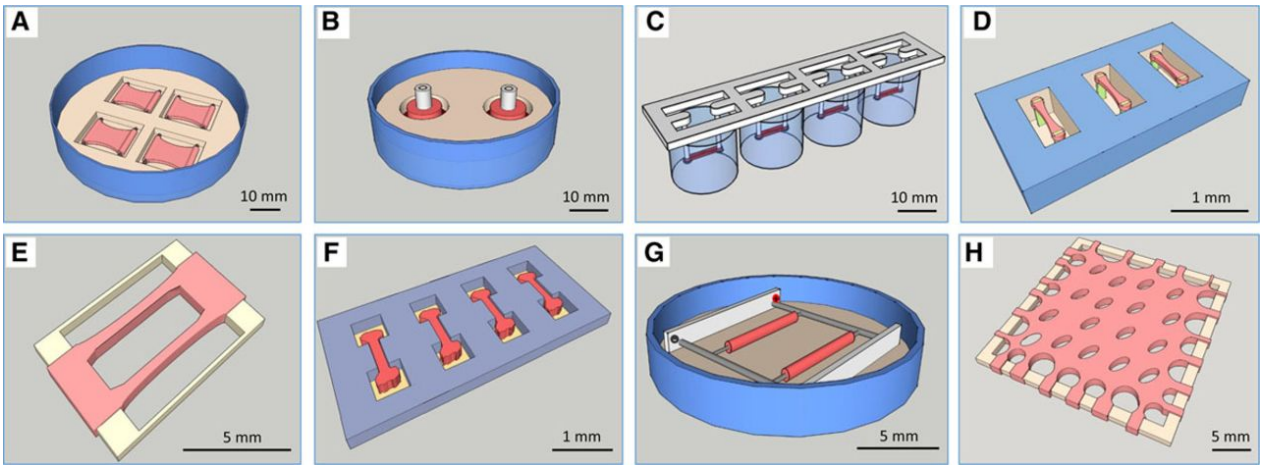

Fig 2.7: Casting Based Approaches to Engineer Heart Muscle Tissues. (A) Engineered heart muscle tissue cultured between velcro[26]. **(B)** Ring EHT cast around single post[99]. **(C)** EHTs cast around PDMS posts[36]. **(D)** Linear EHT cast around flexible posts with embedded fluorescent material for tracking[11]. **(E)** EHT sheet cultured on PDMS frame[44]. **(F)** Micro-heart muscles attached to the flexible PDMS surface[41]. **(G)** Cardiac biowires cast around suture template[70]. **(H)** Cardiac patch where individual holes result from posts designed to align cardiomyocytes throughout the patch[9].

2.4.3. Advanced 3D Biofabrication Approaches

Though more difficult to fabricate, there are several examples of creating structures that are reminiscent of the human heart using more advanced 3D biofabrication methods. For instance, tissue decellularization approaches have yielded ECM scaffolds from whole organs and tissues, such as hearts[61,72,79] (Figure 2.8A-B), skeletal muscle[98], lungs[71] and liver[64], with unmatched structural preservation. However, one major concern is repopulating these dense ECM scaffolds with cells. In fact, decellularized hearts that have been reseeded with cardiomyocytes have achieved only modest recellularizations per cross-sectional area (ranging from 10~35%)[61,72].

Building off of previous studies showing the importance of topography in guiding cardiomyocyte alignment, Parker and colleagues created 3D ventricle-like structures out of

electrospun aligned polycaprolactone/gelatin nanofibers (Figure 2.8C). This resulted in anisotropic cardiomyocyte alignment in the direction of the nanofibers[62] (Figure 2.8D). These small ventricles displayed ejection fractions of ~1% for neonatal rat ventricles and ~0.2% from human iPSC-CM ventricles, which is approximately 50-250 times and 10^4–10^8 times smaller than that observed in either neonatal rat and adult human ventricles, respectively. This is likely due to limited cardiomyocyte infiltration into the dense nanofiber scaffold during cellular seeding.

In contrast to these approaches of creating a dense scaffold followed by cellular reconstitution, others have developed strategies to 3D print both cells and ECM directly. In particular, a 3D printing technique termed Freeform Reversible Embedding of Suspended Hydrogels (FRESH) has received dramatic attention for its ability to allow the printing of a wide range of soft materials, including extracellular matrix (ECM), by embedding them within a sacrificial support bath. With this technique, researchers can print complex structures, such as trabeculated embryonic hearts, coronary arteries, and even miniature brains[37]. Dvir and colleagues similarly capitalized on a variation of this technique to print endothelial cells and cardiomyocytes into miniature whole heart and blood vessel structures. However, these whole heart structures did not display contractile activity, which is likely due to either the rounded morphology of the cardiomyocytes or the limited post-printing culture time (1 day)[69]. In contrast, Ogle's group was able to combine the printing of advanced structures with contractile cardiomyocytes into a simplified version of a whole heart that was able to achieve nominal ejection fractions of ~0.7%[53] (Figure 2.8E-I). As an alternative strategy, the authors printed a bioink consisting of pluripotent stem cells and various ECM factors, and subsequently initiated cardiomyocyte differentiation in 3D. However, despite increased contractile function compared to the early Dvir paper, their current strategy is limited in generating different cell types in distinct spatial positions. Further, the

researchers were unable to create dense muscular walls, as a perfusion bioreactor was not used to maintain cellular viability throughout the entire construct.

In another method to create highly cellular dense heart-like structures, Skylar-Scott et al. printed a sacrificial pluronics hydrogel within a support bath composed of cardiac derived organ building blocks (OBBs) that had similar rheological properties to that observed in the FRESH support baths[83] (Figure 2.8J-M). With this technique, the pluronics could later be removed to form vasculature within the construct. Printed cardiac structures derived with this technique had a high degree of cellularity which was comparable to that observed in the human myocardium (~10^8 cells per mL), but one limitation is that the OBBs had to be cast within specially designed molds to create the outward surface of the print. Finally, combining the ability to print advanced ECM structures with the printing of cells, Lee et al. was able to demonstrate printing of contractile ventricles using a collagen-based bioink for the ventricle wall and a dense cardiomyocyte bioink as the cellular component[54](Figure 2.8N-Q). Printed cardiomyocytes appeared to display conduction in the direction of the print path indicating that it may be possible to create anisotropic cardiac tissues via print path optimization.

Despite these tremendous developments in the field of heart muscle tissue biofabrication, it is clear that challenges still exist in being able to manufacture cardiac tissues with the appropriate structural and functional requirements of that observed in the adult human heart. Thus, the following sections will focus on mechanical bioreactor strategies aimed at increasing the function of engineered heart muscle tissues.

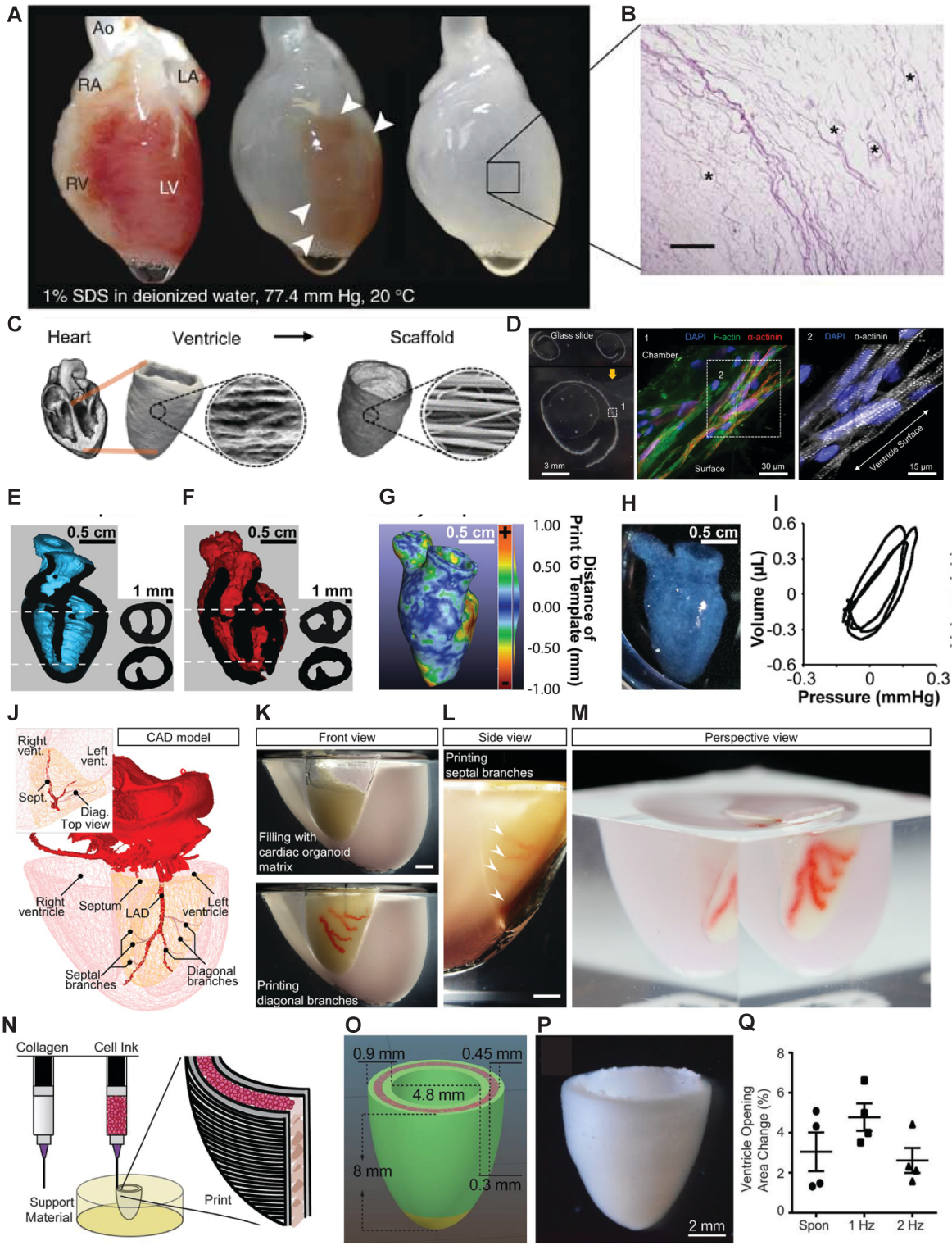
A
Ao
RA
LA
RV
LV
1% SDS in deionized water, 77.4 mm Hg, 20 °C
B
C
Heart
Ventricle
Scaffold
D
Glass slide
Chamber
DAPI F-actin α-actinin
DAPI α-actinin
Surface
Ventricle Surface
3 mm
30 μm
15 μm
E
F
G
H
I
0.5 cm
1 mm
Distance of Print to Template (mm)
1.00
0.50
0.00
-0.50
-1.00
Volume (μL)
Pressure (mmHg)
J
CAD model
Right vent.
Left vent.
Sept.
Diag.
Top view
Right ventricle
Septum
LAD
Left ventricle
Septal branches
Diagonal branches
K
Front view
Filling with cardiac organoid matrix
Printing diagonal branches
L
Side view
Printing septal branches
M
Perspective view
N
Collagen
Cell Ink
Support Material
Print
O
0.9 mm
0.45 mm
4.8 mm
8 mm
0.3 mm
P
2 mm
Q
Ventricle Opening Area Change (%)
Spon
1 Hz
2 Hz

Fig 2.8: Advanced 3D Biofabrication Approaches for Heart Muscle. (A) Rat heart decellularization process where the heart becomes translucent as cellular material is removed. Aorta (A); Right Atrium (RA); Right Ventricle (RV); left ventricle (LV); left atrium (LA).[72] **(B)** H&E staining showing that SDS decellularization method removes all cellular material and retains large vascular conduits (indicated by asterisks).[72] **(C)** Bioinspired scaffold derived from circumferential alignment of ECM fibers within the native heart. Ventricular scaffold was created by electrospinning PCL/gelatin nanofibers.[62] **(D)** Cardiomyocytes seeded on these scaffolds showed uniaxial alignment in the direction of the aligned nanofibers.[62] **(E)** Ventricular model used for printing stem cells in gelatin mathacrylate (GelMA) based scaffold.[52] **(F)** Print derived from model.[52] **(G)** Gauging performed on print showing the difference in dimensions compared to the model.[53] **(H)** Brightfield image of the print.[52] **(I)** Pressure-volume loop obtained from spontaneous beating of heart construct.[52] **(J)** 3D CAD model of human heart with a segmented of the left ventricle including the left anterior descending artery (LAD).[83] **(K-M)** A PDMS mold is created using the CAD model and filled with cardiac OBBs and the LAD vasculature is printed in (red).[83] **(N)** Schematic of printing simplified ventricle model with two outer walls consisting of collagen and the medial wall consisting of a cardiomyocyte-based cellular ink.[55] **(O)** CAD model of ventricle with collagen (green) and cell ink (pink).[55] **(P)** Brightfield image of ventricle print.[55] **(Q)** Percent area change of ventricle with contraction under spontaneous, and 1 and 2 Hz field stimulation.[55]

2.5. Mechanical Loading Strategies in Heart Muscle Tissue Engineering

Given the abundance of previous evidence suggesting mechanical loading drives heart muscle tissue function, tissue engineers have sought to utilize mechanical loading strategies to build engineered cardiac tissues that more closely mimic the function observed in the adult human heart. In the following sections, we will discuss the predominant methods of mechanical loading in both 2D and 3D *in vitro* systems.

2.5.1. 2D Models of Mechanical Load

To alter mechanical loading conditions in 2D cardiomyocytes cultures, investigators have either i) altered the stiffness of the substrate the cells are cultured on or ii) incorporated either stepwise or dynamic stretching of cells. Previous *in vivo* work suggests that cardiac tissue stiffness increases significantly during embryonic development[8,45,48] and that during this time period, cardiomyocytes drastically increase their contractile force generation and myofibrillar alignment

and organization. Thus, many investigators have tried to experimentally manipulate stiffness of materials cardiomyocytes are cultured on in order to either increase their contractile function or in an effort to better model disease (i.e. increased tissue stiffness associated with fibrosis). Here, neonatal cardiomyocytes cultured on gels much stiffer than the embryonic heart (>50 kPa) displayed stress fibers whereas those cultured on softer gels with a comparable stiffness to the embryonic heart (~10 kPa) had defined sarcomeric striations[45]. Cardiomyocytes also adapt their contractility based on the stiffness of the material[31] they are cultured on, where soft gels allow deformation of the underlying material and stiff materials only permit deformation of the cardiomyocyte itself[24]. Similarly, cardiomyocytes cultured on substrates that shown time-varying stiffening (similar to that observed during embryonic cardiac development) showed increased cardiac troponin T and NKX2.5 expression, as well as an increase in sarcomere length compared to cardiomyocytes cultured on substrates in which the stiffness did not change[25]. All in all, the predominant findings have been that embryonic cardiomyocytes display increased function on matrices with a similar stiffness and time varying stiffening to that observed in embryonic development.

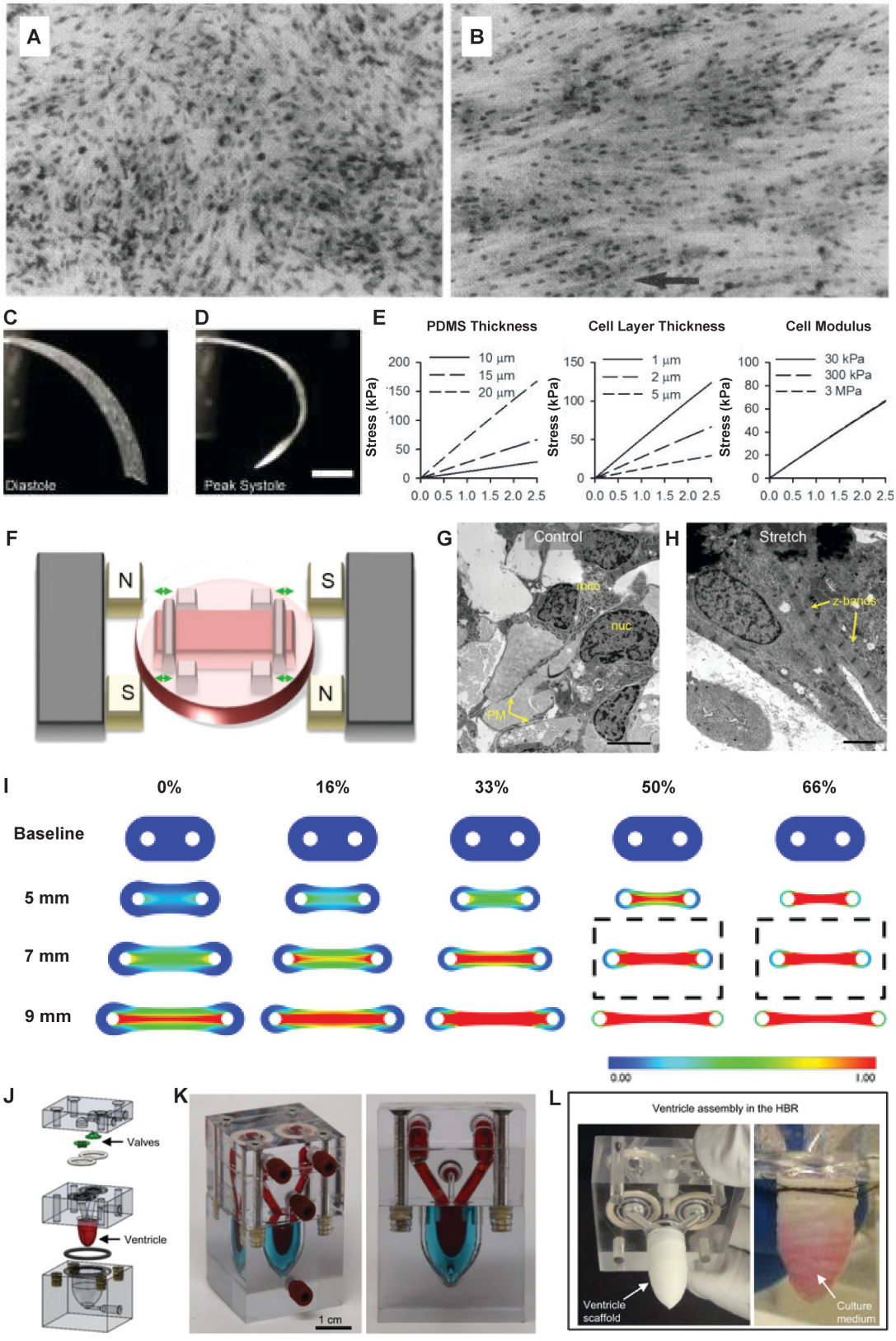
A
B
C
Diastole
D
Peak Systole
E
PDMS Thickness
Cell Layer Thickness
Cell Modulus
Stress (kPa)
10 µm
15 µm
20 µm
1 µm
2 µm
5 µm
30 kPa
300 kPa
3 MPa
0.0 0.5 1.0 1.5 2.0 2.5
F
N
S
S
N
G
Control
nucl
nuc
PM
H
Stretch
z-bands
I
0%
16%
33%
50%
66%
Baseline
5 mm
7 mm
9 mm
0.00
1.00
J
Valves
Ventricle
K
1 cm
L
Ventricle assembly in the HBR
Ventricle scaffold
Culture medium

Fig 2.9: 2D and 3D Mechanical Loading Strategies. (A) Cardiomyocytes grown on PDMS under static culture display random alignment and rounded shape[89]. **(B)** Upon 25% increase in stretch for a period of 4 days, cardiomyocytes begin to display highly aligned and rod-shaped morphology in the direction of applied stretch (indicated by the arrow)[89]. **(C-D)** Brightfield image of MTF bending in diastole **(C)** and systole[3] **(D)**. **(E)** Calculated stress for a given curvature of the MTF is based on PDMS thickness, cell layer thickness and cell modulus[3]. **(F)** Magnet-driven cardiac tissue stretching device provided dynamic stretching (12% increase in length at 1.25 Hz)[68]. **(G-H)** TEM images of control samples and those that were dynamic stretched with magnet device[68]. **(G)** Unstretched control cardiomyocytes displayed rounded structure. **(H)** Stretched samples had uniaxial aligned cardiomyocytes with defined sarcomeric striations. **(I)** Finite element modeling of maximum principal stresses in engineered heart muscle tissues based on degree of compaction (indicated by percentages) and distance between PDMS posts[2]. **(J-L)** Advanced bioreactor built to show potential of long-term culture of fabricated ventricles. **(J)** Bioreactor CAD model. **(K)** Front and **(L)** Isometric view of assembled bioreactor. **(L)** High magnification view of fabricated ventricle inside the bioreactor assembly[62].

Since preload is also known to contribute immensely to *in vivo* cardiomyocyte function, several groups have attempted to provide preload in a 2D setting through the stretching of cardiomyocyte cultures. Cardiomyocytes in 2D cultures that are exposed to progressive uniaxial stretch were more likely to be binucleated and demonstrated increased alignment and expression of myosin heavy chains (Figure 2.9A-B)[89]. Building off of models involving step-wise static increases in stretch, others have incorporated dynamic stretching in order to mimic the cyclic stretch during the cardiomyocyte contractile cycle. Here, Bannerjee et al. showed that stretching of the substrate increased cardiomyocyte proliferation, myofibril content, and cardiac specific gene expression compared to static 2D controls[43] suggesting that a cyclic mechanical loading platform can result in increased cardiomyocyte maturation. However, because these cardiomyocytes are adhered to a 2D surface, there is limited applicability in being able to use these models to represent the complex 3D heart muscle tissue environment.

As previously mentioned, MTFs have been created to measure the contractility of 2D engineered cardiac muscle, where the dimensions of the muscular thin film, including MTF thickness/modulus, cell modulus and stiffness, can be changed to modulate the afterload the MTF must contract against (Figure 2.9C-E)[1]. Further, the preload on the MTF, can be determined by the

resting curvature of the film when the cardiomyocytes are not actively contracting. However, because the cardiomyocytes are constrained and physically adhered to the film, the preload is limited and the true contractile shortening that the cells can undergo is <1%[3], which does not mimic the stretch and contractile shortening observed in the human heart of about 10-20%[46].

2.5.2. 3D Models of Mechanical Load

As previously mentioned, 3D engineered heart muscle tissues have been produced by casting cardiomyocytes in combination with fibroblasts and other cell types in a hydrogel solution formed around anchor points, such as frames[82], pillars[36,86], posts[99], pinned substrates[41], or even wires[70]. Here, the purpose of these anchor points is to provide both an afterload and passive tension ("preload") to the tissue. The afterload can be modulated by increasing the stiffness of the incorporated anchor points by either changing their physical dimensions or material properties[11]. The anchor points also create a passive tension to the cardiomyocytes as fibroblasts compact the tissue around them. This passive tension creates anisotropic alignment of the cardiomyocytes between anchor points and this passive tension can be modulated by the placement of these anchor points [for example, by increasing the distance between two posts(Figure 2.9I)[2]]. However, because these rely on tension generated during fibroblast compaction, it is difficult to create very large, aligned tissues with just two anchor points. Thus, investigators have created large arrays of posts in order to modulate the tension, and thus, cardiomyocyte alignment throughout the interior of the tissue[9]. However, this type of prestress is distinct from the preload in the heart, where chamber filling provides an active cardiomyocyte stretch and sarcomere lengthening, which can be altered depending on the physiological demands of the body, such as exercise.

In order to more accurately model preload, others have designed linear motors[30,78,87,96] or used magnets (Figure 2.9F-H)[68] to cyclically stretch the engineered cardiac tissue after fabrication. While this better mimics the physiologic strain during preload, it fails to accurately recapitulate physiologic loads that cardiomyocytes experience during this process. Further, these systems fail to recapitulate the dynamic loading of heart tissue, where the contraction of the heart muscle leads to the volume displacement of blood that further leads to diastolic filling and preload on the heart muscle.

It should be noted that almost all previous attempts to mechanically load tissues has been performed on simplified tissue geometries, such as sheets or linear muscle strips. Several papers have incorporated perfusion bioreactor systems (Figure 2.9J-L)[52,62] that could potentially pressurize tissues with more advanced structures, such as ventricles, or even whole hearts. While some studies have been performed using bioreactor systems to modulate mechanical loading in advanced tissue systems[72], more comprehensive studies on the effects of mechanical loading in advanced tissue systems should be performed.

Further, little research has been performed to understand the contributions that loads observed during embryonic development (morphogenetic loads) have on heart structure and function in 3D engineered systems. Thus, although tremendous progress has been made in engineering cardiac tissues, there is still an unmet need to create engineered heart muscle structures with advanced geometries that accurately replicate physiologic mechanical loading. In this thesis work, I look to expand on the previous literature by developing a more physiologically relevant 3D mechanical loading platform, while also demonstrating the importance of incorporating mechanical loading in the fabrication of engineered heart muscle tissues with more advanced 3D structure.

2.6 References for Chapters 1 and 2

1. A. W. Feinberg, A. Feigel, S. S. Shevkoplyas, S. Sheehy, G. M. Whitesides, and K. K. Parker. Muscular thin films for building actuators and powering devices. *Science (80-.).* , 2007.
2. Abilez, O. J., E. Tzatzalos, H. Yang, M. T. Zhao, G. Jung, A. M. Zöllner, M. Tiburcy, J. Riegler, E. Matsa, P. Shukla, Y. Zhuge, T. Chour, V. C. Chen, P. W. Burridge, I. Karakikes, E. Kuhl, D. Bernstein, L. A. Couture, J. D. Gold, W. H. Zimmermann, and J. C. Wu. Passive Stretch Induces Structural and Functional Maturation of Engineered Heart Muscle as Predicted by Computational Modeling. *Stem Cells* 36:265–277, 2018.
3. Alford, P. W., A. W. Feinberg, S. P. Sheehy, and K. K. Parker. Biohybrid thin films for measuring contractility in engineered cardiovascular muscle. *Biomaterials* , 2010.doi:10.1016/j.biomaterials.2010.01.079
4. Au, H. T. H., I. Cheng, M. F. Chowdhury, and M. Radisic. Interactive effects of surface topography and pulsatile electrical field stimulation on orientation and elongation of fibroblasts and cardiomyocytes. *Biomaterials* , 2007.doi:10.1016/j.biomaterials.2007.06.001
5. Auman, H. J., H. Coleman, H. E. Riley, F. Olale, H. J. Tsai, and D. Yelon. Functional modulation of cardiac form through regionally confined cell shape changes. *PLoS Biol.* 5:0604–0615, 2007.
6. Batalov, I., Q. Jallerat, S. Kim, J. Bliley, and A. W. Feinberg. Engineering aligned human cardiac muscle using developmentally inspired fibronectin micropatterns. *Sci. Rep.* 11:1–14, 2021.
7. Batra, S., and K. Rakusan. Capillary Length, Tortuosity, and Spacing in Rat Myocardium During Cardiac Cycle. *Society* , 1992.
8. Bhana, B., R. K. Iyer, W. L. K. Chen, R. Zhao, K. L. Sider, M. Likhitpanichkul, C. A. Simmons, and M. Radisic. Influence of substrate stiffness on the phenotype of heart cells. *Biotechnol. Bioeng.* , 2010.doi:10.1002/bit.22647
9. Bian, W., C. P. Jackman, and N. Bursac. Controlling the structural and functional anisotropy of engineered cardiac tissues. *Biofabrication* , 2014.doi:10.1088/1758-5082/6/2/024109
10. Boccafoschi, F., C. Mosca, M. Ramella, G. Valente, and M. Cannas. The effect of mechanical strain on soft (cardiovascular) and hard (bone) tissues: Common pathways for different biological outcomes. *Cell Adhes. Migr.* 7:165–173, 2013.
11. Boudou, T., W. R. Legant, A. Mu, M. A. Borochin, N. Thavandiran, M. Radisic, P. W. Zandstra, J. A. Epstein, K. B. Margulies, and C. S. Chen. A microfabricated platform to measure and manipulate the mechanics of engineered cardiac microtissues. *Tissue Eng. - Part A* , 2012.doi:10.1089/ten.tea.2011.0341
12. Branco, M. A., J. P. Cotovio, C. A. V. Rodrigues, S. H. Vaz, T. G. Fernandes, L. M. Moreira, J. M. S. Cabral, and M. M. Diogo. Transcriptomic analysis of 3D Cardiac Differentiation of Human Induced Pluripotent Stem Cells Reveals Faster Cardiomyocyte Maturation Compared to 2D Culture. *Sci. Rep.* 9:1–13, 2019.
13. Bruneau, B. G. The developmental genetics of congenital heart disease. *Nature* 451:943–948, 2008.
14. Burggren, W., S. Khorrami, A. Pinder, and T. Sun. Body, eye, and chorioallantoic vessel growth are not dependent on cardiac output level in day 3-4 chicken embryos. *Am. J. Physiol. - Regul. Integr. Comp. Physiol.* 287:1399–1406, 2004.
15. Burggren, W. W., S. J. Warburton, and M. D. Slivkoff. Interruption of cardiac output does not affect short-term growth and metabolic rate in day 3 and 4 chick embryos. *J. Exp. Biol.* 203:3831–3838, 2000.
16. Carson, D., M. Hnilova, X. Yang, C. L. Nemeth, J. H. Tsui, A. S. T. Smith, A. Jiao, M. Regnier, C. E. Murry, C. Tamerler, and D. H. Kim. Nanotopography-Induced Structural Anisotropy and Sarcomere Development in Human Cardiomyocytes Derived from Induced Pluripotent Stem Cells. , 2016.doi:10.1021/acsami.5b11671
17. Chabiniok, R., V. Y. Wang, M. Hadjicharalambous, L. Asner, J. Lee, M. Sermesant, E. Kuhl, A. A. Young, P. Moireau, M. P. Nash, D. Chapelle, and D. A. Nordsletten. Multiphysics and multiscale modelling, data–model fusion and integration of organ physiology in the clinic: Ventricular cardiac mechanics. *Interface Focus* 6:, 2016.
18. Clark, E. B., N. Hu, P. Frommelt, G. K. Vandekieft, J. L. Dummett, and R. J. Tomanek. Effect of increased pressure on ventricular growth in stage 21 chick embryos. *Am. J. Physiol. - Hear. Circ. Physiol.* 257:, 1989.
19. D'Amore, A., T. Yoshizumi, S. K. Luketich, M. T. Wolf, X. Gu, M. Cammarata, R. Hoff, S. F. Badylak, and W. R. Wagner. Bi-layered polyurethane – Extracellular matrix cardiac patch improves ischemic ventricular wall remodeling in a rat model. *Biomaterials* , 2016.doi:10.1016/j.biomaterials.2016.07.039

20. Deng, M. Cardiac Transplantation. *Heart* 87:177–184, 2002.
21. Drakhlis, L., S. Biswanath, C. M. Farr, V. Lupanow, J. Teske, K. Ritzenhoff, A. Franke, F. Manstein, E. Bolesani, H. Kempf, S. Liebscher, K. Schenke-Layland, J. Hegermann, L. Nolte, H. Meyer, J. de la Roche, S. Thiemann, C. Wahl-Schott, U. Martin, and R. Zweigerdt. Human heart-forming organoids recapitulate early heart and foregut development. *Nat. Biotechnol.* 39:737–746, 2021.
22. Duscher, D., Z. N. Maan, V. W. Wong, R. C. Rennert, M. Rodrigues, M. Hu, A. J. Whitmore, J. Alexander, M. T. Longaker, and G. C. Gurtner. Mechanotransduction and fibrosis. 47:1997–2005, 2015.
23. Ebert, A. D., S. Diecke, I. Y. Chen, and J. C. Wu. Reprogramming and transdifferentiation for cardiovascular development and regenerative medicine: where do we stand? *EMBO Mol. Med.* 7:1090–1103, 2015.
24. Engler, A. J., C. Carag-Krieger, C. P. Johnson, M. Raab, H. Y. Tang, D. W. Speicher, J. W. Sanger, J. M. Sanger, and D. E. Discher. Embryonic cardiomyocytes beat best on a matrix with heart-like elasticity: Scar-like rigidity inhibits beating. *J. Cell Sci.* 121:3794–3802, 2008.
25. Engler, J. L. Y. and A. J. Hydrogels with Time-Dependent Material Properties Enhance Cardiomyocyte Differentiation In Vitro. *Bone* 23:1–7, 2006.
26. Eschenhagen, T., C. Fink, U. Remmers, H. Scholz, J. Wattchow, J. Weil, W. Zimmermann, H. H. Dohmen, H. Schäfer, N. Bishopric, T. Wakatsuki, and E. L. Elson. Three-dimensional reconstitution of embryonic cardiomyocytes in a collagen matrix: a new heart muscle model system. *FASEB J.* 11:683–694, 1997.
27. Feinberg, A. W., P. W. Alford, H. Jin, C. M. Ripplinger, A. A. Werdich, S. P. Sheehy, A. Grosberg, and K. K. Parker. Controlling the contractile strength of engineered cardiac muscle by hierarchal tissue architecture. *Biomaterials* , 2012.doi:10.1016/j.biomaterials.2012.04.043
28. Feinberg, A. W., A. Feigel, S. S. Shevkoplyas, S. Sheehy, G. M. Whitesides, and K. K. Parker. Muscular thin films for building actuators and powering devices. *Science (80-.).* , 2007.doi:10.1126/science.1146885
29. Feric, N. T., I. Pallotta, R. Singh, D. R. Bogdanowicz, M. M. Gustilo, K. W. Chaudhary, R. N. Willette, T. P. Chendrimada, X. Xu, M. P. Graziano, and R. Aschar-Sobbi. Engineered Cardiac Tissues Generated in the Biowire II: A Platform for Human-Based Drug Discovery. *Toxicol. Sci.* , 2019.doi:10.1093/toxsci/kfz168
30. Fink, C., S. Ergün, D. Kralisch, U. Remmers, J. Weil, and T. Eschenhagen. Chronic stretch of engineered heart tissue induces hypertrophy and functional improvement. *FASEB J.* 14:669–679, 2000.
31. Galie, P. A., N. Khalid, K. E. Carnahan, M. V. Westfall, and J. P. Stegemann. Substrate stiffness affects sarcomere and costamere structure and electrophysiological function of isolated adult cardiomyocytes. *Cardiovasc. Pathol.* 22:219–227, 2013.
32. Granados-Riveron, J. T., and J. D. Brook. The impact of mechanical forces in heart morphogenesis. *Circ. Cardiovasc. Genet.* 5:132–142, 2012.
33. Gregory M. Fomovsky, MS1, Stavros Thomopoulos, PhD2, and Jeffrey W. Holmes, M. P. Contribution of Extracellular Matrix to the Mechanical Properties of the Heart. *Bone* 23:1–7, 2014.
34. Guccione, J. M., S. M. Moonly, P. Moustakidis, K. D. Costa, M. J. Moulton, M. B. Ratcliffe, and M. K. Pasque. Mechanism underlying mechanical dysfunction in the border zone of left ventricular aneurysm: A finite element model study. *Ann. Thorac. Surg.* 71:654–662, 2001.
35. Guo, Y., and W. T. Pu. Cardiomyocyte maturation: New phase in development. *Circ. Res.* 1086–1106, 2020.doi:10.1161/CIRCRESAHA.119.315862
36. Hansen, A., A. Eder, M. Bönstrup, M. Flato, M. Mewe, S. Schaaf, B. Aksehirlioglu, A. Schwörer, J. Uebeler, and T. Eschenhagen. Development of a drug screening platform based on engineered heart tissue. *Circ. Res.* , 2010.doi:10.1161/CIRCRESAHA.109.211458
37. Hinton, T. J., Q. Jallerat, R. N. Palchesko, J. H. Park, M. S. Grodzicki, H. J. Shue, M. H. Ramadan, A. R. Hudson, and A. W. Feinberg. Three-dimensional printing of complex biological structures by freeform reversible embedding of suspended hydrogels. *Sci. Adv.* 1:, 2015.
38. Hofbauer, P., S. M. Jahnel, N. Papai, M. Giesshammer, A. Deyett, C. Schmidt, M. Penc, K. Tavernini, N. Grdseloff, C. Meledeth, L. C. Ginistrelli, C. Ctortecka, Š. Šalic, M. Novatchkova, and S. Mendjan. Cardioids reveal self-organizing principles of human cardiogenesis. *Cell* 184:3299-3317.e22, 2021.
39. Holmes, J. W., T. K. Borg, and J. W. Covell. Structure and mechanics of healing myocardial infarcts. *Annu. Rev. Biomed. Eng.* 7:223–253, 2005.
40. Hove, J. R., R. W. Köster, A. S. Forouhar, G. Acevedo-Bolton, S. E. Fraser, and M. Gharib. Intracardiac fluid forces are an essential epigenetic factor for embryonic cardiogenesis. *Nature* 421:172–177, 2003.
41. Huebsch, N., P. Loskill, N. Deveshwar, C. I. Spencer, L. M. Judge, M. A. Mandegar, C. B. Fox, T. M. A. Mohamed, Z. Ma, A. Mathur, A. M. Sheehan, A. Truong, M. Saxton, J. Yoo, D. Srivastava, T. A. Desai, P. L. So, K. E. Healy, and B. R. Conklin. Miniaturized iPS-Cell-Derived Cardiac Muscles for Physiologically

Relevant Drug Response Analyses. *Sci. Rep.* , 2016.doi:10.1038/srep24726
42. Ieda, M., J. D. Fu, P. Delgado-Olguin, V. Vedantham, Y. Hayashi, B. G. Bruneau, and D. Srivastava. Direct reprogramming of fibroblasts into functional cardiomyocytes by defined factors. *Cell* 142:375–386, 2010.
43. Indroneal Banerjee, PhDa, Katrina Carrion, B.Sb, Ricardo Serrano, MEng, M.S.c, Jeffrey Dyo, M.S.b, Roman Sasik, PhDd, Sean Lund, B.S.e, Erik Willems, PhDf, Seema Aceves, M.D. PhDe,g,h, Rudolph Meili, PhDc,i, Mark Mercola, PhDf, Ju Chen, PhDa, Alexander Za, and V. N. Cyclic stretch of Embryonic Cardiomyocytes Increases Proliferation, Growth, and Expression While Repressing Tgf-β Signaling. *Bone* 23:1–7, 2006.
44. Jackman, C. P., A. L. Carlson, and N. Bursac. Dynamic culture yields engineered myocardium with near-adult functional output. *Biomaterials* 66–79, 2017.doi:10.1016/j.biomaterials.2016.09.024.Dynamic
45. Jeffrey G. Jacot1, 2, Jody C. Martin3, and D. L. H. Mechanobiology of Cardiomyocyte Development. *Bone* 23:1–7, 2006.
46. Jeung, M. Y., P. Germain, P. Croisille, S. El Ghannudi, C. Roy, and A. Gangi. Myocardial tagging with MR imaging: Overview of normal and pathologic findings. *Radiographics* 32:1381–1398, 2012.
47. Jiang, Y., P. Park, S. M. Hong, and K. Ban. Maturation of cardiomyocytes derived from human pluripotent stem cells: Current strategies and limitations. *Mol. Cells* 41:613–621, 2018.
48. Joshua R. Gershlak1,*, Joshua IN Resnikoff1,*, Kelly E Sullivan1, Corin Williams1, R., and 2 M. Wang1, and Lauren D. Black III1. Mesenchymal stem cells ability to generate traction stress in response to substrate stiffness is modulated by the changing extracellular matrix composition of the heart during development. *Bone* 23:1–7, 2014.
49. Katz, A. M. Maladaptive growth in the failing heart: The cardiomyopathy of overload. , 2002.doi:10.1023/A:1020604623427
50. Kelly, R. G., M. E. Buckingham, and A. F. Moorman. Heart fields and cardiac morphogenesis. *Cold Spring Harb. Perspect. Med.* 4:1–10, 2014.
51. Kim, D. H., E. A. Lipke, P. Kim, R. Cheong, S. Thompson, M. Delannoy, K. Y. Suh, L. Tung, and A. Levchenko. Nanoscale cues regulate the structure and function of macroscopic cardiac tissue constructs. *Proc. Natl. Acad. Sci. U. S. A.* , 2010.doi:10.1073/pnas.0906504107
52. Kupfer, M. E., W.-H. Lin, V. Ravikumar, K. Qiu, L. Wang, L. Gao, D. Bhuiyan, M. Lenz, J. Ai, R. R. Mahutga, D. Townsend, J. Zhang, M. C. McAlpine, E. G. Tolkacheva, and B. M. Ogle. In Situ Expansion, Differentiation and Electromechanical Coupling of Human Cardiac Muscle in a 3D Bioprinted, Chambered Organoid . *Circ. Res.* , 2020.doi:10.1161/circresaha.119.316155
53. Kupfer, M. E., W. H. Lin, V. Ravikumar, K. Qiu, L. Wang, L. Gao, D. B. Bhuiyan, M. Lenz, J. Ai, R. R. Mahutga, D. W. Townsend, J. Zhang, M. C. McAlpine, E. G. Tolkacheva, and B. M. Ogle. In Situ Expansion, Differentiation, and Electromechanical Coupling of Human Cardiac Muscle in a 3D Bioprinted, Chambered Organoid. *Circ. Res.* , 2020.doi:10.1161/CIRCRESAHA.119.316155
54. Lee, A., A. R. Hudson, D. J. Shiwarski, J. W. Tashman, T. J. Hinton, S. Yerneni, J. M. Bliley, P. G. Campbell, and A. W. Feinberg. 3D bioprinting of collagen to rebuild components of the human heart. *Science (80-.).* , 2019.doi:10.1126/science.aav9051
55. Lee, A., A. R. Hudson, D. J. Shiwarski, J. W. Tashman, T. J. Hinton, S. Yerneni, J. M. Bliley, P. G. Campbell, and A. W. Feinberg. 3D bioprinting of collagen to rebuild components of the human heart. *Science (80-.).* , 2019.doi:10.1126/science.aav9051
56. Legant, W. R., A. Pathak, M. T. Yang, V. S. Deshpande, R. M. McMeeking, and C. S. Chen. Microfabricated tissue gauges to measure and manipulate forces from 3D microtissues. *Proc. Natl. Acad. Sci. U. S. A.* 106:10097–10102, 2009.
57. Li, R. A., W. Keung, T. J. Cashman, P. C. Backeris, B. V. Johnson, E. S. Bardot, A. O. T. Wong, P. K. W. Chan, C. W. Y. Chan, and K. D. Costa. Bioengineering an electro-mechanically functional miniature ventricular heart chamber from human pluripotent stem cells. *Biomaterials* , 2018.doi:10.1016/j.biomaterials.2018.02.024
58. Liau, B., N. Christoforou, K. W. Leong, and N. Bursac. Pluripotent stem cell-derived cardiac tissue patch with advanced structure and function. *Biomaterials* , 2011.doi:10.1016/j.biomaterials.2011.08.050
59. Lind, J. U., M. Yadid, I. Perkins, B. B. O'Connor, F. Eweje, C. O. Chantre, M. A. Hemphill, H. Yuan, P. H. Campbell, J. J. Vlassak, and K. K. Parker. Cardiac microphysiological devices with flexible thin-film sensors for higher-throughput drug screening. *Lab Chip* 17:3692–3703, 2017.
60. Lindsey, S. E., J. T. Butcher, and H. C. Yalcin. Mechanical regulation of cardiac development. *Front. Physiol.* 5 AUG:1–15, 2014.
61. Lu, T. Y., B. Lin, J. Kim, M. Sullivan, K. Tobita, G. Salama, and L. Yang. Repopulation of decellularized

mouse heart with human induced pluripotent stem cell-derived cardiovascular progenitor cells. *Nat. Commun.* , 2013.doi:10.1038/ncomms3307
62. Macqueen, L. A., S. P. Sheehy, C. O. Chantre, J. F. Zimmerman, F. S. Pasqualini, X. Liu, J. A. Goss, P. H. Campbell, G. M. Gonzalez, S. J. Park, A. K. Capulli, J. P. Ferrier, T. Fettah Kosar, L. Mahadevan, W. T. Pu, and K. K. Parker. A tissue-engineered scale model of the heart ventricle. *Nat. Biomed. Eng.* , 2018.doi:10.1038/s41551-018-0271-5
63. Matsumura, Y., Y. Zhu, H. Jiang, A. D'Amore, S. K. Luketich, V. Charwat, T. Yoshizumi, H. Sato, B. Yang, T. Uchibori, K. E. Healy, and W. R. Wagner. Intramyocardial injection of a fully synthetic hydrogel attenuates left ventricular remodeling post myocardial infarction. *Biomaterials* , 2019.doi:10.1016/j.biomaterials.2019.119289
64. Mazza, G., K. Rombouts, A. Rennie Hall, L. Urbani, T. Vinh Luong, W. Al-Akkad, L. Longato, D. Brown, P. Maghsoudlou, A. P. Dhillon, B. Fuller, B. Davidson, K. Moore, D. Dhar, P. De Coppi, M. Malago, and M. Pinzani. Decellularized human liver as a natural 3D-scaffold for liver bioengineering and transplantation. *Sci. Rep.* 5:1–15, 2015.
65. Megan L. McCain1,2, Ashutosh Agarwal1,3, Haley W. Nesmith1, Alexander P. Nesmith1, and K. K. P. Micromolded Gelatin Hydrogels for Extended Culture of Engineered Cardiac Tissues. *Biomaterials* 23:1–7, 2010.
66. Mengsteab, P. Y., K. Uto, A. S. T. Smith, S. Frankel, E. Fisher, Z. Nawas, J. Macadangdang, M. Ebara, and D. H. Kim. Spatiotemporal control of cardiac anisotropy using dynamic nanotopographic cues. *Biomaterials* , 2016.doi:10.1016/j.biomaterials.2016.01.062
67. Midgett, M., C. S. López, L. David, A. Maloyan, and S. Rugonyi. Increased hemodynamic load in early embryonic stages alters myofibril and mitochondrial organization in the myocardium. *Front. Physiol.* 8:1–15, 2017.
68. Mihic, A., J. Li, Y. Miyagi, M. Gagliardi, S. H. Li, J. Zu, R. D. Weisel, G. Keller, and R. K. Li. The effect of cyclic stretch on maturation and 3D tissue formation of human embryonic stem cell-derived cardiomyocytes. *Biomaterials* 35:2798–2808, 2014.
69. Noor, N., A. Shapira, R. Edri, I. Gal, L. Wertheim, and T. Dvir. 3D Printing of Personalized Thick and Perfusable Cardiac Patches and Hearts. *Adv. Sci.* , 2019.doi:10.1002/advs.201900344
70. Nunes, S. S., J. W. Miklas, J. Liu, R. Aschar-Sobbi, Y. Xiao, B. Zhang, J. Jiang, S. Massé, M. Gagliardi, A. Hsieh, N. Thavandiran, M. A. Laflamme, K. Nanthakumar, G. J. Gross, P. H. Backx, G. Keller, and M. Radisic. Biowire: A platform for maturation of human pluripotent stem cell-derived cardiomyocytes. *Nat. Methods* , 2013.doi:10.1038/nmeth.2524
71. Ohata, K., and H. C. Ott. Human-scale lung regeneration based on decellularized matrix scaffolds as a biologic platform. *Surg. Today* 50:633–643, 2020.
72. Ott, H. C., T. S. Matthiesen, S. K. Goh, L. D. Black, S. M. Kren, T. I. Netoff, and D. A. Taylor. Perfusion-decellularized matrix: Using nature's platform to engineer a bioartificial heart. *Nat. Med.* 14:213–221, 2008.
73. Øyen, N., G. Poulsen, H. A. Boyd, J. Wohlfahrt, P. K. A. Jensen, and M. Melbye. Recurrence of congenital heart defects in families. *Circulation* 120:295–301, 2009.
74. Patel, A. A., M. G. Chown, R. G. Thakar, T. A. Desai, and S. Kumar. Control of Cardiomyocyte Adhesion and Organization by Microscale Topographical Cues. *Biophys. J.* , 2010.doi:10.1016/j.bpj.2009.12.2183
75. Perl, A., D. N. Reinhoudt, and J. Huskens. Microcontact printing: Limitations and achievements. *Adv. Mater.* 21:2257–2268, 2009.
76. Polonchuk, L., M. Chabria, L. Badi, J. C. Hoflack, G. Figtree, M. J. Davies, and C. Gentile. Cardiac spheroids as promising in vitro models to study the human heart microenvironment. *Sci. Rep.* 7:1–12, 2017.
77. Pong, T., W. J. Adams, M. A. Bray, A. W. Feinberg, S. P. Sheehy, A. A. Werdich, and K. K. Parker. Hierarchical architecture influences calcium dynamics in engineered cardiac muscle. *Exp. Biol. Med.* , 2011.doi:10.1258/ebm.2010.010239
78. Rogers, A. J., R. Kannappan, H. Abukhalifeh, M. Ghazal, J. M. Miller, A. El-Baz, V. G. Fast, and P. Sethu. Hemodynamic Stimulation Using the Biomimetic Cardiac Tissue Model (BCTM) Enhances Maturation of Human Induced Pluripotent Stem Cell-Derived Cardiomyocytes. *Cells Tissues Organs* 206:82–94, 2019.
79. Sánchez, P. L., M. E. Fernández-Santos, S. Costanza, A. M. Climent, I. Moscoso, M. A. Gonzalez-Nicolas, R. Sanz-Ruiz, H. Rodríguez, S. M. Kren, G. Garrido, J. L. Escalante, J. Bermejo, J. Elizaga, J. Menarguez, R. Yotti, C. Pérez del Villar, M. A. Espinosa, M. S. Guillem, J. T. Willerson, A. Bernad, R. Matesanz, D. A. Taylor, and F. Fernández-Avilés. Acellular human heart matrix: A critical step toward whole heart grafts. *Biomaterials* 61:279–289, 2015.
80. Sedmera, D., T. Pexieder, V. Rychterova, N. Hu, and E. B. Clark. Remodeling of chick embryonic

ventricular myoarchitecture under experimentally changed loading conditions. *Anat. Rec.* 254:238–252, 1999.
81. Shadrin, I. Y., B. W. Allen, Y. Qian, C. P. Jackman, A. L. Carlson, M. E. Juhas, and N. Bursac. Cardiopatch platform enables maturation and scale-up of human pluripotent stem cell-derived engineered heart tissues. *Nat. Commun.* 8:, 2017.
82. Shadrin, I. Y., B. W. Allen, Y. Qian, C. P. Jackman, A. L. Carlson, M. E. Juhas, and N. Bursac. Cardiopatch platform enables maturation and scale-up of human pluripotent stem cell-derived engineered heart tissues. *Nat. Commun.* , 2017.doi:10.1038/s41467-017-01946-x
83. Skylar-Scott, M. A., S. G. M. Uzel, L. L. Nam, J. H. Ahrens, R. L. Truby, S. Damaraju, and J. A. Lewis. Biomanufacturing of organ-specific tissues with high cellular density and embedded vascular channels. *Sci. Adv.* 5:, 2019.
84. Soares, C. P., V. Midlej, M. E. W. de Oliveira, M. Benchimol, M. L. Costa, and C. Mermelstein. 2D and 3D-Organized Cardiac Cells Shows Differences in Cellular Morphology, Adhesion Junctions, Presence of Myofibrils and Protein Expression. *PLoS One* 7:e38147, 2012.
85. Soonpaa, M. H., and L. J. Field. Survey of studies examining mammalian cardiomyocyte DNA synthesis. *Circ. Res.* 83:15–26, 1998.
86. Stoehr, A., C. Neuber, C. Baldauf, I. Vollert, F. W. Friedrich, F. Flenner, L. Carrier, A. Eder, S. Schaaf, M. N. Hirt, B. Aksehirlioglu, C. W. Tong, A. Moretti, T. Eschenhagen, and A. Hansen. Automated analysis of contractile force and Ca2+ transients in engineered heart tissue. *Am. J. Physiol. - Hear. Circ. Physiol.* 306:1353–1363, 2014.
87. Tulloch, N. L., V. Muskheli, M. V. Razumova, F. S. Korte, M. Regnier, K. D. Hauch, L. Pabon, H. Reinecke, and C. E. Murry. Growth of engineered human myocardium with mechanical loading and vascular coculture. *Circ. Res.* 109:47–59, 2011.
88. Tzahor, E., and K. D. Poss. Cardiac regeneration strategies: Staying young at heart. *Science (80-.).* 356:1035–1039, 2017.
89. Vandenburgh, H. H., R. Solerssi, J. Shansky, J. W. Adams, and S. A. Henderson. Mechanical stimulation of organogenic cardiomyocyte growth in vitro. *Am. J. Physiol. - Cell Physiol.* 270:, 1996.
90. Vermij, S. H., H. Abriel, and T. A. B. Van Veen. Refining the molecular organization of the cardiac intercalated disc. *Cardiovasc. Res.* 113:259–275, 2017.
91. Virani, S. S. *et al.* Heart disease and stroke statistics—2020 update: A report from the American Heart Association. , 2020.doi:10.1161/CIR.0000000000000757
92. Voorhees, A. P., and H. C. Han. Biomechanics of cardiac function. *Compr. Physiol.* , 2015.doi:10.1002/cphy.c140070
93. Wang, E. Y., N. Rafatian, Y. Zhao, A. Lee, B. F. L. Lai, R. X. Lu, D. Jekic, L. Davenport Huyer, E. J. Knee-Walden, S. Bhattacharya, P. H. Backx, and M. Radisic. Biowire Model of Interstitial and Focal Cardiac Fibrosis. *ACS Cent. Sci.* 5:1146–1158, 2019.
94. Wang, G., M. L. McCain, L. Yang, A. He, F. S. Pasqualini, A. Agarwal, H. Yuan, D. Jiang, D. Zhang, L. Zangi, J. Geva, A. E. Roberts, Q. Ma, J. Ding, J. Chen, D. Z. Wang, K. Li, J. Wang, R. J. A. Wanders, W. Kulik, F. M. Vaz, M. A. Laflamme, C. E. Murry, K. R. Chien, R. I. Kelley, G. M. Church, K. K. Parker, and W. T. Pu. Modeling the mitochondrial cardiomyopathy of Barth syndrome with induced pluripotent stem cell and heart-on-chip technologies. *Nat. Med.* , 2014.doi:10.1038/nm.3545
95. Weinberger, F., I. Mannhardt, and T. Eschenhagen. Engineering Cardiac Muscle Tissue: A Maturating Field of Research. 2017.
96. Yang, H., L. P. Schmidt, Z. Wang, X. Yang, Y. Shao, T. K. Borg, R. Markwald, R. Runyan, and B. Z. Gao. Dynamic Myofibrillar Remodeling in Live Cardiomyocytes under Static Stretch. *Sci. Rep.* 6:1–12, 2016.
97. Yuan, H., B. Marzban, and K. K. Parker. Myofibrils in Cardiomyocytes Tend to Assemble Along the Maximal Principle Stress Directions. *J. Biomech. Eng.* 139:1–8, 2017.
98. Zhang, J., Z. Q. Hu, N. J. Turner, S. F. Teng, W. Y. Cheng, H. Y. Zhou, L. Zhang, H. W. Hu, Q. Wang, and S. F. Badylak. Perfusion-decellularized skeletal muscle as a three-dimensional scaffold with a vascular network template. *Biomaterials* 89:114–126, 2016.
99. Zimmermann, W. H., K. Schneiderbanger, P. Schubert, M. Didié, F. Münzel, J. F. Heubach, S. Kostin, W. L. Neuhuber, and T. Eschenhagen. Tissue engineering of a differentiated cardiac muscle construct. *Circ. Res.* , 2002.doi:10.1161/hh0202.103644

Chapter 3

Dynamic Loading of Engineered Heart Tissue Enhances Contractile Function

3.1. Introduction

Heart failure is a chronic condition most often caused by weakening of the heart muscle to the point that it is unable to maintain sufficient cardiac output and it affects nearly 5.7 million adults in the United States alone[49]. The most common cause of heart failure is progressive structural and functional remodeling following myocardial infarction[6,23], or death to the heart muscle wall after coronary artery occlusion. While medical and lifestyle changes can improve symptoms, it is common for heart failure to progress in severity requiring the need for a heart transplant and unfortunately, there are limited heart organs available for transplantation[14]. Thus, there is an urgent need for strategies that can repair damaged heart muscle in order to prevent heart failure progression.

Tissue engineered heart muscle has emerged as a potential therapeutic approach for creating contractile tissues to replace or repair damaged cardiac muscle[10,42,50]. A major challenge in achieving this objective is the generation of cardiomyocytes and cardiac tissues with adult level function that are capable of repairing the damaged heart[51]. Thus, cardiac tissue maturation strategies, including electrical stimulation and mechanical loading[35,44], as well as exposure to certain biochemical factors[9,20,33], have been the contemporary approach to improve the structure and function of current engineered cardiac tissues. Although significant improvements have been made with these strategies, current engineered heart muscle tissues (EHTs) still display reduced

function compared to the adult human heart, suggesting that alternative maturation platforms are necessary.

In particular, mechanical loading has been extensively explored as an EHT maturation strategy. Researchers have investigated casting cardiac tissues around static posts which can bend with EHT contraction and expose the tissue to a slight stretch during relaxation[5,35,41]. However, anchorage to static posts has important functional consequences on these tissues resulting in a nearly isometric contraction (i.e. minimal contractile shortening) and limited active preload, or force that stretches heart muscle between tissue contractions. This mechanical loading is in stark contrast to that observed *in vivo*, where heart muscle undergoes significant contractile shortening (>10%) and is exposed to preload during chamber filling. This finding suggests that a mechanical loading platform which more closely mimics heart muscle contractile function may improve the maturation of current EHTs.

Here, I report the development of a dynamic engineered heart tissue (dyn-EHT) platform designed to mimic preload and afterload observed in physiologic heart muscle. I do this by incorporating an elastic polydimethylsiloxane (PDMS) strip, which can be used to both mechanically load the tissues and measure tissue contractile force based on the degree of strip bending. The goal is to better recapitulate the effect of hemodynamic loading on heart muscle in order to understand how forces alter gene expression, cytoskeletal organization, cell-cell coupling, electrophysiology, and subsequent contractile force generation. Specifically, I sought to achieve (i) a dynamic preload and afterload that can drive adaptive changes in the EHT, (ii) physiologic contractile shortening of >10% (i.e., not isometrically constrained), and (iii) a straightforward optical readout of EHT contraction to facilitate experimental throughput. These results reveal that wild-type embryonic stem cell (ESC) derived EHTs demonstrate a load-dependent improvement

in tissue structure and function compared to traditional static (isometric) mechanical loading conditions.

3.2. Materials and Methods

3.2.1. Embryonic Stem Cell Culture, Cardiomyocyte Differentiation, and Metabolic Purification

Prior to differentiation, ESCs were maintained in Essential 8 (E8) medium (A1517001, ThermoFisher) on Geltrex (A1413202, ThermoFisher)-coated 6 well plates with daily medium changes and passaged at 80% confluence (approximately every 2-4 days). For passaging, cells were washed with 1X phosphate buffered saline (PBS) and incubated with TrypLE (12604021, ThermoFisher) for 5 minutes at 37ºC. Cells were then resuspended in DMEM/F12 (11320033, ThermoFisher), centrifuged at 200g for 5 minutes, and replated on Geltrex (A1413202, ThermoFisher)-coated plates in E8 with 2.5 μM ROCK inhibitor, thiazovivin (S1459, Selleck Chemicals). Cardiomyocyte differentiation of human HUES9 ESCs was accomplished by addition of factors that mimic mesoderm induction and cardiac specification during embryogenesis[7,26]. On day 0 of differentiation, cells were washed once with 1X PBS and incubated with RPMI/B27 media containing RPMI 1640 (21870076, ThermoFisher) supplemented with 1% v/v L glutamine (25030081, ThermoFisher) and B27 supplement (17504044, ThermoFisher) plus 6 μM CHIR99201 (C-6556, LC laboratories) for 48 hours. On day 2, ESCs were washed with 1X PBS and medium was replaced with RPMI/B27 containing 2 μM Wnt C-59 (S7037, Selleck Chemicals) for another 48 hours. On day 6, medium was replaced with RPMI/B27. On days 8 and 10, medium was changed to CDM3 media, consisting of RPMI 1640 supplemented with 1% v/v L glutamine, 213 μg/mL L-Ascorbic acid 2-phosphate sesquimagnesium salt hydrate >95% (A8960, Sigma),

and 500 μg/mL human albumin (A9731, Sigma). On day 12, spontaneously beating cells were passaged for lactate-based metabolic selection of cardiomyocytes[47]. To passage for purification, cells were incubated with TrypLE for 15 minutes at 37°C to enable single cell dissociation. Cells were then reseeded in CDM3L, consisting of RPMI 1640 without glucose (11879020, ThermoFisher) supplemented with 213 μg/mL L-Ascorbic acid 2-phosphate sesquimagnesium salt hydrate >95% (A8960, Sigma), 500 μg/mL human albumin (A9731, Sigma), and 7.1 mM sodium-lactate (L4263, Sigma). Cells were maintained in CDM3L for several days before replacing back to CDM3 medium.

3.2.2. Human Cardiac Ventricular Fibroblast Culture

Human ventricular cardiac fibroblasts (NHCF-Vs) were obtained from Lonza (CC-2904) and maintained via the manufacturer's instructions. Fibroblasts were used between passages 5-10 for all studies described in this chapter. Cells were maintained in FGM-3 Medium (CC-4526, Lonza) and passaged at 80% confluence.

3.2.3. Fabricating Engineered Heart Muscle Tissues Around PDMS Strips

To fabricate engineered heart muscle tissues (EHTs) around strips, first PDMS wells were created. To create the wells, molds were designed in Solidworks and printed using either Verowhite plus RGD835 using an Objet Connex350 (Stratasys) or Dental SG resin (RS-F2-DGOR-01, Formlabs) on a Form 2 SLA printer. Polydimethylsiloxane (PDMS) wells were created to cast the tissue around the strip using Sylgard 184 PDMS (Dow Corning) in a 10:1 base to curing agent ratio. Sylgard 184 was mixed prior to casting using a Thinky conditioning mixer (Phoenix Systems) for 2 minutes at 2000 RPM each for mixing and defoaming. Molds were degassed for 30 minutes under vacuum to remove bubbles, cured at 65 °C for 4 hours, and then the PDMS wells

were removed from the molds. Subsequently, PDMS-strips were laser-cut from PDMS sheets (Bioplexus, Inc), either ~130 μm (SH-20001-005) or ~260 μm (CUST-20001-010) thick, using a ProtoLaser U3 (LPK5) laser cutter. Because bending resistance of the strip is proportional to the thickness-cubed, a profilometer was used to determine the thickness of each strip (VHX-5000). Detailed information about dimensions of PDMS strips and molds is provided in Supplemental Figure 1.

Prior to cardiac tissue fabrication, wells were sterilized via sonication in 50% v/v ethanol for 30 minutes and PDMS strips were sterilized with UV-Ozone treatment for 15 minutes. Sterile PDMS wells were fixed to one well of a 6 well culture plate using a thin layer of vacuum grease. PDMS wells were then incubated with 1% w/v Pluronic F-127 (P2443, Sigma) for 10 minutes to reduce collagen attachment to the well and washed three times in 1X PBS. Sterile PDMS strips were then placed in the slits in the bottom of the well to secure the strip during cardiac tissue casting. Collagen I derived from rat tail (354249, Corning) and Matrigel (354263, Corning) were used to fabricate 3D cardiac tissues around the PDMS strips. The final concentrations were 1 mg/mL Collagen I, 1.7 mg/mL Matrigel, 10% 10X PBS, 2.3% 1N NaOH, 18.75×10^6 total cells/mL consisting of 90% cardiomyocytes and 10% cardiac fibroblasts. Ingredients were mixed and then 80 μL of the cell mixture was pipetted into each well around the PDMS strip. 6-well plates containing the molds and cell suspension were then placed at 37°C to allow for gelation. Following a 45-minute incubation period, cardiac tissues were maintained in heart muscle tissue media containing RPMI-1640 supplemented with 1% v/v KnockOut™ Serum Replacement (10828010, Thermofisher) and 1:1000 MycoZap Plus CL (Lonza, VZA 2012).

3.2.4. Cardiac Tissue Loading Regimes

To mechanically load the tissues, strips of two different thicknesses (either ~130 μm or ~260 μm) were incorporated into the cardiac tissues during tissue formation, where the thicker strip represented an approximate 8x increase in load being applied to the tissue. On day 14, tissues were randomized to either constrained or dynamic mechanical loading which was maintained up to day 28. In the constrained condition, the strip was held immobilized within the well throughout the entire culture period. In contrast, the dynamic condition allowed for the tissue to beat in an unconstrained manner against the PDMS strip. For dynamic loading, a PDMS block with a vertical cut was adhered to a new well with vacuum grease and one end of the strip was fixed into the vertical cut in the PDMS block. Tissues were maintained in heart muscle tissue media in either constrained or dynamic culture until day 28.

3.2.5. Tissue Contractility Assay and Measurements

During engineered heart muscle tissue contraction, the tissue decreases in length, resulting in PDMS strip bending. Based on known dimensions and elastic modulus of the PDMS strip, the degree of strip bending can be used to determine the force the tissue is exerting during contraction. Twitch stress measurements were found by dividing average twitch force (systolic force minus diastolic force) by average cross-sectional area of cardiomyocytes within the tissue. To image PDMS strip bending due to cardiac tissue contraction, a PDMS block with a vertical cut was adhered to a petri dish using vacuum grease and one end of the strip was fixed into the vertical cut in the PDMS block. During the contractility assay, tissues were maintained in Tyrode's (T2145, Sigma) solution on a custom-heated stage at 37°C +/- 1°C. The PDMS strip was imaged with a Nikon DSLR camera mounted on a Nikon SMZ1500 stereomicroscope. A custom-made

MATLAB program was created to automatically calculate the change in length of the tissue from contraction videos (Supplemental Figure 2). Look-up tables relating tissue length to force required to induce PDMS strip bending were created using a finite element modeling in ANSYS software (Supplemental Figure 3). Modeling was performed by applying known displacements to the PDMS strip and then obtaining the reaction force associated with these displacements. The PDMS strip was modeled as a 3D deformable, extruded solid with two different thicknesses. The strip was considered linearly elastic, isotropic, and incompressible with a Young's modulus of 1.59 MPa for ~130 μm strips and 1.89 MPa for ~260 μm strips, respectively. Elastic moduli were derived from tensile testing of laser cut dogbones derived from each respective material. Briefly, dogbones mounted on an Instron 5943 and stretched at a rate of 1 millimeter/minute. The average cross-sectional area of the dogbones was measured prior to testing using a profilometer and a stereomicroscope. Stress was calculated by dividing the force by the cross-sectional area of the dogbone. Stress was then plotted against the strain and slopes of the individual curves in the linear region of the stress-strain graph (0-10%) were averaged to obtain the elastic modulus of the PDMS.

3.2.6. Validation of Strip Bending Force Measurements

To validate forces obtained from the finite element model, strip bending forces were measured with a custom-mounted optical force transducer (World Precision Instruments, SI-KG20). Linear actuators moving the force transducer were used to bend the strip and measure the forces associated with strip bending. The linear actuators were moved to discrete tissue lengths and then compared to the model.

3.2.7. Reverse Transcription Polymerase Chain Reaction (RT-PCR)

Total RNA was isolated using TRIzol (Sigma). cDNA was synthesized by reverse transcription and real-time PCRs were performed using primers (Supplemental Table 1) to reveal expression of mRNA transcripts. Relative expression levels were calculated using the ddCt method.

3.2.8. Analysis of Twitch Kinetics

3D tissue twitch kinetics were analyzed using a custom MATLAB program. Tissue contractile videos were used to obtain waveforms of tissue change in length over time. These waveforms were post processed to find the time to 50% contraction (t50), time to 90% contraction (t90), and the time constant of cardiac muscle relaxation (tau). To find the contractile and relaxation velocity, tissue displacement during contraction or relaxation was divided by either the t90 or tau. Contractile work was found by multiplying the average twitch force by contractile shortening. Contractile Power was found by dividing the contractile work by the contractile time.

3.2.9. Calcium Imaging and Conduction Velocity Measurements

Tissue conduction velocity was determined by staining EHTs with 1 μM fluo-4 (F14201, Thermofisher), a calcium indicator dye. An excitation-contraction decoupler, 10 μM Blebbistatin (B0560, Sigma) was used to prevent spontaneous tissue contraction, which would make it difficult to perform analysis on the calcium wave front. Imaging of the calcium wavefront (50 frames per second) was performed using a Prime 95B Scientific CMOS camera (Photometrics) mounted on an epifluorescent stereomicroscope (Nikon SMZ1000) with a GFP filter and an X-cite Lamp (Excelitas). Conduction velocity (cm/s) was calculated by obtaining the average distance of the tissue in centimeters and dividing that by the average time (in seconds) it takes for the wave to

traverse the tissue. For activation maps, calcium transients from spontaneous contractions were then post-processed with a custom-made MATLAB program using calcium signal peak times and cross-correlation.

3.2.10. Sharp Electrode Measurements

Tissues were washed 5x times with Tyrode's solution. Glass microelectrodes with tip resistances of 8-20 MΩ were filled with 3 M KCl and used to impale the tissues. Measurements were performed using a MultiClamp 700B amplifier and analogue signals were low-pass filtered (10 kHz) and digitized at a sample rate of 20 kHz via a Digidata 1440A A/D digitizer (both Axon Instruments/Molecular Devices, Union City, CA). All recordings were performed at room temperature. Data was analyzed using pCLAMP 10.7 acquisition software (Axon Instrument), Excel (version 2010, Microsoft, Redmond, WA) and Prism 7.02 (GraphPad Software, La Jolla, CA). Both datasets were normalized (by dividing the number of events in each bin by the total number of events). Only measurements with stable resting membrane potentials were included in this study.

3.2.11. Immunofluorescent Staining

For whole mount staining, EHTs were fixed in 4% paraformaldehyde (15710, Electron Microscope Sciences) and permeabilized with 1:200 Triton-X 100 (9002-93-1, Sigma) for one hour at room temperature. Tissues were washed three times in 1X PBS for 30 minutes each on a rotary shaker and blocked overnight in 5% v/v Goat Serum (16210072, Thermofisher) in 1X PBS. Subsequently, tissues were then washed three times in 1X PBS for 30 minutes each on a rotary shaker and incubated with anti-sarcomeric alpha actinin (A7811, Sigma-Aldrich) primary antibody

(1:100) in 1X PBS overnight. The following day tissues were washed 3X in 1X PBS for 30 minutes each and then incubated overnight with 1:100 goat anti-mouse 555 secondary antibody, 3:200 Alexa-fluor 488 conjugated phalloidin (A12379, Invitrogen), and 1:100 4′,6-diamidino-2-phenylindole (DAPI) for cell nuclei. The next day tissues were washed with 1X PBS 3X for 30 minutes each and stored protected from light at 4°C prior to imaging.

3.2.12. Cardiac Tissue Imaging and Actin Alignment Analysis

Confocal images were acquired with a Zeiss LSM 700 Laser Scanning microscope with a 63x (NA 1.4) oil immersion objective to obtain high resolution images of actin filaments for alignment analysis. Maximum intensity projections of z-stacks (n=10 per tissue, about 20 μm depth) were used for actin alignment analysis (cardiomyocyte alignment). A custom MATLAB code was used to quantify the angular distribution of actin filaments[45]. Briefly, actin filaments were thresholded. The α-actinin channel was then used to create a binary mask for cardiomyocyte locations, which was used to determine cardiomyocyte alignment. Angular distribution of actin filaments was then used to calculate the orientational order parameter (OOP)—a measure of alignment, where OOP values close to 1 indicate completely coaligned actin filaments and values close to 0 indicate an isotropic distribution of actin filaments. An average OOP was obtained for each sample by considering angular distributions of actin filaments within all z-stacks (n=10 per tissue).

3.2.13. Sarcomere Length Analysis

Sarcomere length was found by measuring the distance between adjacent z-disks delineated by fluorescent alpha-actinin staining similar to previously described methods[35]. In ImageJ, a line was drawn perpendicular to the sarcomere bands and at least 3 adjacent and prominent sarcomeres were measured per cardiomyocyte and 5 separate measurements were made for each image. Quantification from 3 images per tissue were used to obtain an average sarcomere length.

3.2.14. Tissue Elastic Modulus Determination

To determine tissue elastic modulus, a custom mounted optical force transducer (World Precision Instruments, SI-KG20) and linear actuators were used to perform tensile testing of the EHTs. In short, tissues were removed from the PDMS strip and mounted onto the force transducer and static post. Linear actuators were used to stretch the tissue and obtain a plot of extension versus diastolic load on the tissue. Stress was calculated by dividing the diastolic load by the cross-sectional area of the tissue. Stress was then plotted against the strain and slopes of the individual curves were averaged to obtain the elastic modulus of the EHTs.

3.2.15. Tissue Electrical Stimulation and Analysis of Force Frequency Relationship

EHTs were field stimulated using paired platinum wires spaced 2-cm apart in Tyrode's solution (2 ms duration square wave at 16 V/cm). To measure the force frequency relationship, electrical stimulation frequency was increased from 1 to 3 Hz in 1 Hz increments. EHTs were stimulated for 30 seconds at each subsequent frequency.

3.2.16. Statistical Analysis

Data are represented as mean ± standard deviation (SD). Statistical analysis was performed using Prism software (GraphPad). Outliers were defined with ROUT (Q=1) testing. Statistical significance was considered a p-value<0.05. Appropriate statistical tests were chosen based on experimental conditions and data. If data did not meet assumptions of normality and homogeneity of variances, data were either transformed (in order to meet these assumptions) or an appropriate non-parametric test was utilized.

3.3. Results

3.3.1. Development of the dyn-EHT platform for modeling preload and afterload

To create the mechanical loading platform, EHTs were fabricated around a PDMS strip, which was used to both mechanically load the tissue and measure tissue contractile force based on strip deformation with tissue contraction. Briefly, human embryonic stem cells (hESC) or human induced pluripotent stem cells (hiPSCs) were differentiated into cardiomyocytes and primary adult cardiac fibroblasts were expanded (Figure 3.1Ai). At day 0 of the experimental timeline, cardiomyocytes and cardiac fibroblasts were mixed with collagen and Matrigel, and then cast around elastic polydimethylsiloxane (PDMS) strips immobilized within PDMS wells (Figure 3.1Aii). Fibroblasts within the mixture then compact the extracellular matrix hydrogel into a linear EHT anchored to the PDMS strip. All EHTs were maintained in the PDMS wells in a constrained state until day 14 (Figure 3.1Aiii). From day 14 to 28, EHTs were either continually cultured in the constrained state (EHTs) or were removed from the wells for dynamic culture (dyn-EHTs) (Figure 3.1Aiv). In the constrained state (EHTs), the PDMS strip is immobilized within the well during the entire culture period. This is similar to current EHT models, where the tissue is unable

to significantly shorten, and little active preload is provided to the tissue. In contrast, the dynamic state (dyn-EHTs) allows for the tissue to beat in an unconstrained manner against the PDMS strip, which provides preload between cardiac muscle contractions and allows for increased contractile shortening. At day 28, both EHTs and dyn-EHTs were removed from culture and functionally assessed based on the ability of the tissue to contract and bend the PDMS strip **(**Figure 3.1Av).

To measure EHT contractility, assays were performed in an organ bath where one end of the PDMS strip was mounted in a block and the other end was free to move during each contraction (Figure 3.1B). A custom MATLAB script was then used to analyze digital video to determine tissue length during contraction, and thus bending of the PDMS strip **(**Figure 3.1C). The force exerted by the tissue is based on the degree of strip bending as well as known dimensions and material properties of the PDMS strip. Strip thicknesses' of ~130 μm (1x) or ~260 μm (8x) were selected, where the thicker strip represented an approximate 8-fold increase in bending stiffness. Finite element modelling (FEM) was used to determine both the tensile force applied to the tissue during diastole (tissue relaxation) and the force required to bend the PDMS strip (Figure 3.1D). 1x and 8x strips were identified as applying appropriate tensile forces for these studies with forces ranging from 0.05 to 0.9 mN (Figure 3.1E). To validate the FEM, a force transducer was used to measure the force required to bend the PDMS strip (Supplemental Figure 4). Experimental strip bending forces displayed good agreement with the computational results (Figure 3.1E).

PDMS strip dimensions could also be altered to apply a wide range of additional forces to the EHTs (Supplemental Figure 5). For instance, strip thickness could be altered to create 1x, 4x, 8x, and 12x strips resulting in forces ranging from 0.05 to 5 mN. Finer control of applied tissue forces could also be achieved by changing the width of the strip or the length between tissue

attachment points on the strip with a linear relationship being observed between applied force and either strip width or length between attachment points (Supplemental Figure 5, A-D).

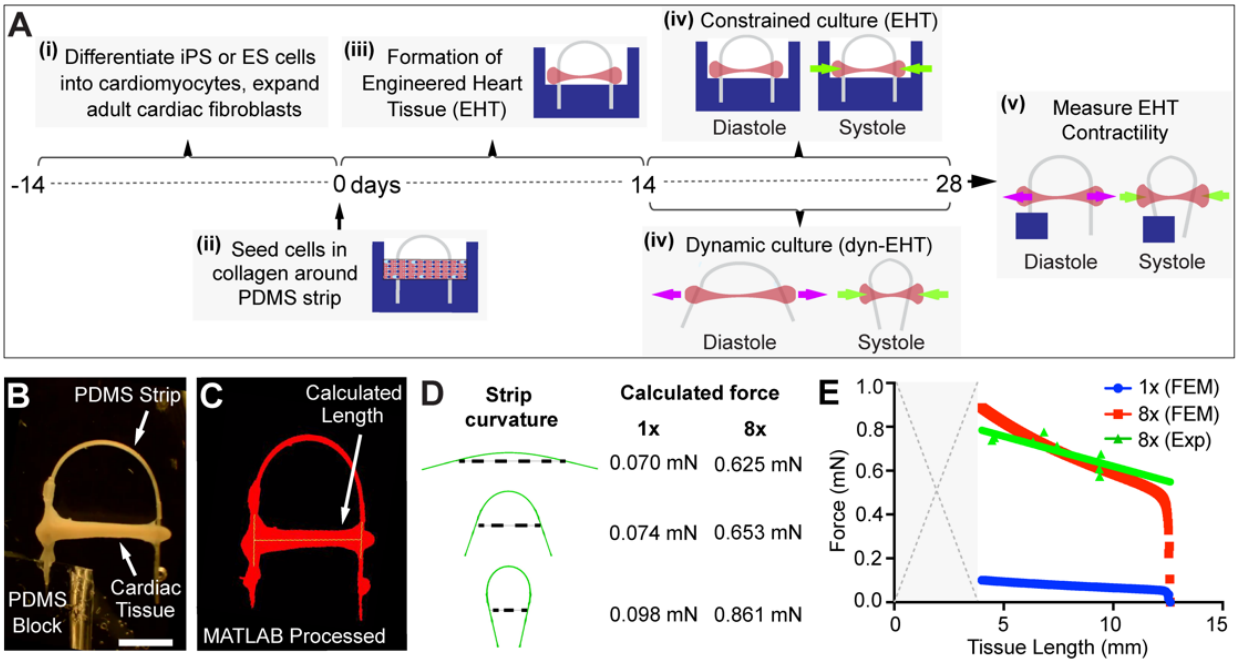

Fig. 3.1. EHTs can be fabricated around PDMS strips for loading and measuring tissue contractile force: (A) Schematic of EHTs cast around PDMS strips. (i) First, cardiomyocytes are differentiated from either ESCs or hiPSCs and cardiac fibroblasts are expanded. (ii) On day 0, cardiomyocytes and cardiac fibroblasts are cast within a Collagen/Matrigel mixture around PDMS strips that is able to apply two different loads, either 1x or 8x. (iii) From day 4-14, cardiac fibroblasts compact the gel into a linear cardiac tissue between the ends of the PDMS strip. (iv) On day 14 and until day 28, tissues are exposed to constrained (EHTs) or dynamic (dyn-EHTs) loading. Arrows represent the relative amount of preload (pink) and afterload (green) on this tissue within either the constrained or dynamic condition. (v) On day 28, all tissues are measured for contractile force based on the degree of PDMS strip bending. **(B)** Tissues were imaged from the side to observe PDMS strip bending with contraction. **(C)** To determine the contractile tissue forces or load that is being applied during diastole, a custom-made MATLAB program was used to track tissue length and change in length resulting in PDMS strip bending. **(D)** Finite element analysis was performed on both 1x and 8x strips to determine the tissue length (represented by the dotted line) needed to induce PDMS strip bending, which could subsequently be used to find the contractile tissue force, or the diastolic load being applied to the tissue. Representative tissue forces with 1x/8x PDMS strip curvature. Dotted line indicates length of the tissue. **(E)** Average force values obtained at each tissue length with either the 1x or 8x strips. Individual experimental data points are derived from force transducer measurements of strip bending at specific tissue lengths. Figure and data prepared by Jacqueline Bliley.

Since both collagen and fibroblasts are important load-bearing components in tissue, fibroblast and collagen concentration were also optimized to maximize our ability to observe the effects of applied tissue forces on cardiomyocytes within the tissues (Supplemental Figure 6). First, I found that fibroblasts were necessary to create a compact and contractile EHT where tissues

fabricated with 0% fibroblasts showed little to no contractility (Supplemental Figure 6A). This is similar to findings by others where EHTs fabricated with 0% fibroblasts demonstrate reduced contraction, and cardiomyocytes manifest a rounded and less elongated phenotype[28]. Tissues fabricated with higher fibroblast concentrations (20%) displayed irregular remodeling and oftentimes did not form a complete and linear muscle attached to the end of the PDMS strip (Supplemental Figure 6A). Eventually, I chose a 10% fibroblast concentration as these tissues consistently formed uniform, linear and highly contractile EHTs. Though a range of fibroblast concentrations have been reported in the literature, our value of 10% is also consistent with several other EHT papers[12,39]. However, this value is significantly lower than the fibroblast concentration observed in the human heart (~50%).

Similarly, collagen concentrations were also optimized by casting EHTs with a range of different concentrations (0.5 to 2.5 mg/mL). EHTs fabricated with reduced collagen concentrations had smaller tissue cross-sectional areas (Supplemental Figure 6B-C), greater contractile shortening (Supplemental Figure 6D), and increased tissue generated twitch stress (Supplemental Figure 6E).

3.3.2. 8x Loading Increases Tissue Contractility

At day 28, the contractile function of EHTs cultured under constrained or dynamic conditions and 1x or 8x loading were assessed. There were differences in tissue length and contractility across all four conditions, with a clear improvement in force generation in 8x dyn-EHTs (Figure 3.2A). The length of the EHT in the PDMS well during constrained culture was 6 mm, and all EHTs were analyzed out of the well. For the 1x loading, the constrained EHT maintained the same diastolic length as in the PDMS well indicating that the force generated by the 1x strip did not apply a sufficient load to stretch the EHT. Interestingly, for the 1x dyn-EHT

the diastolic tissue length actually decreased during culture from days 14 to 28, suggesting that the force generated by fibroblasts compacting the EHT was greater than the force exerted by the 1x strip. The 8x loading results were quite different, with the constrained EHT showing a small increase in diastolic length when removed from the well. However, the 8x dyn-EHT showed the greatest change, with an ~50% increase in diastolic length (Figure 3.2B). The tissue contractile shortening showed a similar trend to the diastolic length, with the 8x EHT and 8x dyn-EHT having contractile shortening of 13-15% compared to only 5-8% for both 1x loading conditions (Figure 3.2C).

In terms of contractility, the stresses generated by the EHTs were much greater for the 8x versus the 1x loading conditions with spontaneous contraction (Figure 3.2D). The 8x EHTs and 8x dyn-EHTs had elevated diastolic stresses (preload) compared to both 1x EHTs and 1x dyn-EHTs (Figure 3.2E). The elevated diastolic stresses in the 8x group were also associated with higher contractile stresses (afterload). A graph of normalized stress for each condition showing one full contractile cycle demonstrates the relative difference in magnitude in the 1x groups compared to both 8x groups (Figure 3.2F). Of note, is the twitch stress (equivalent to the peak systolic stress minus the diastolic stress) observed in the 8x dyn-EHT was more than an order-of-magnitude greater than both 1x conditions and nearly 4-times greater than the 8x constrained EHT (Figure 3.2G). Despite increases in contractility and twitch stress with 8x loading, peak twitch stresses appeared to be comparable to other EHT systems[37,42,48].

To determine if differences in tissue contractility were due to changes in tissue stiffness, tensile testing was performed on tissues from each loading condition at day 28 (Supplemental Figure 7). In general, average tissue elastic modulus measurements within each group were within the range reported for muscle tissue and other EHTs[52]. It was observed that 1x dyn-EHT had the

least contractile shortening, which together with the observation of reduced tissue length, suggested that tissue stiffness may have increased with 1x dyn-EHT culture. Surprisingly, there was no identifiable increase in tissue stiffness in 1x dyn-EHTs. There was, however, an increase in tissue elastic modulus in 8x dyn-EHTs (Supplemental Figure 7) suggesting that a more organized tissue ultrastructure may be responsible for this observation.

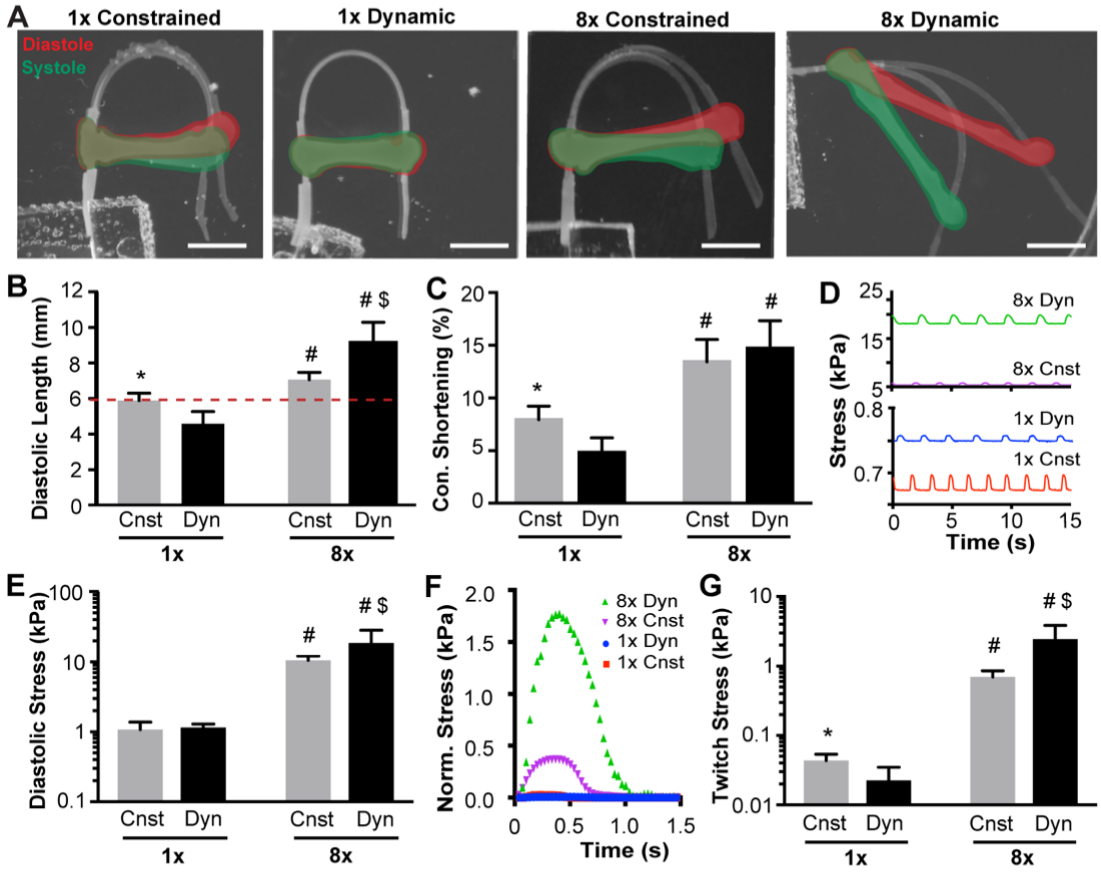

Fig 3.2: PDMS Strip Can be Used to Mechanically Load Engineered Heart Muscle Tissues. (A-D) Macroscopic tissue contractions overlaid with tissue in systole (green) and tissue in diastole (red). Scale bars are 2.5 mm. **(B)** Average diastolic tissue (resting) lengths under each loading condition. The red dotted line indicates the initial length of the tissue while it is immobilized within the PDMS well. **(C)** Contractile shortening under each loading condition. **(D)** Cardiomyocyte stress during contraction and relaxation at Day 28. **(E)** Cardiomyocyte diastolic stress at day 28. **(F)** Representative normalized twitch stresses for one single contraction under each loading condition. **(G)** Cardiomyocyte twitch stresses under each loading condition. All graphs show n=5/group for 8x EHT and 8x dyn-EHT, n=6/group for 1x EHT, n=4/group for 1x dyn-EHT. Statistics based on two-way ANOVA with post hoc Holm Sidak test. *p<0.05 vs. 1x dynamic; #p<0.05 vs. 1x dynamic and 1x constrained, $ p<0.05 vs. 8x constrained. One cardiomyocyte differentiation batch was used for all tissues in this figure. Cardiomyocyte cross-sectional area used for tissue stress measurements is located in supplemental figure 8. All data represented as mean ± SD. Figure and data prepared by Jacqueline Bliley.

Given the increase in EHT contractile shortening and stress with 8x loading, it was speculated that these EHTs also displayed other aspects of more mature heart muscle tissue, including a positive force frequency relationship or an increase in contractile force with an elevated stimulation frequency. At day 28, EHTs from each loading group were electrically field stimulated with a range of frequencies from 1-3 Hz. Twitch stress was comparable between spontaneous and tissues electrically stimulated at 1 Hz (Figure 3.3A). Further, similar differences were observed in tissue generated twitch stress (Figure 3.3B) and diastolic stresses (Figure 3.3C) among loading groups with electrical stimulation at 1Hz when compared to previous spontaneous measurements (Figure 3.2F).

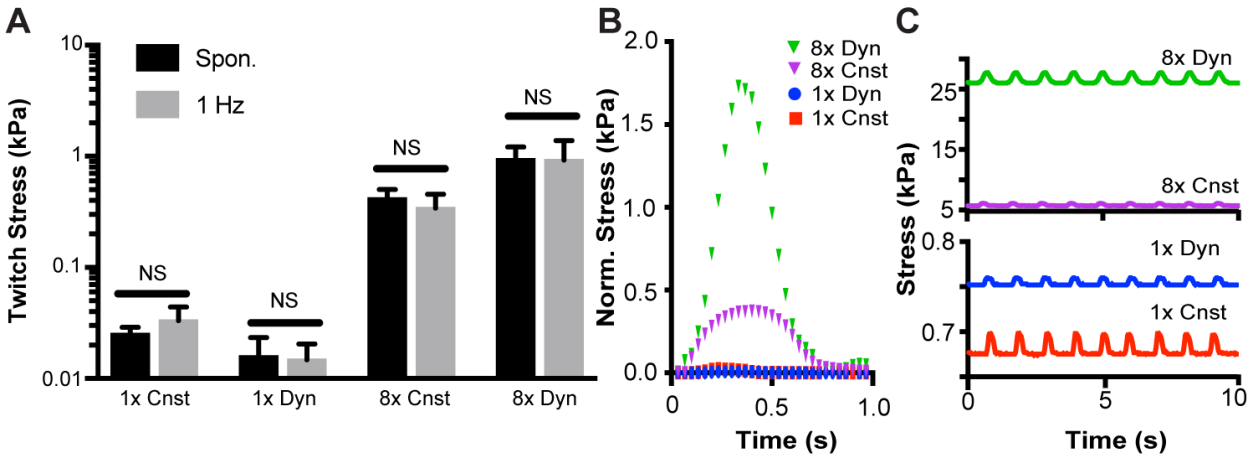

Fig 3.3: Contractile Stress Comparison Between Spontaneous and 1 Hz Paced Electrical Stimulation. **(A)** Comparison of twitch stress under paced electrical stimulation at 1 Hz compared to spontaneous beating. Graph shows n=5/group for 8x EHT and dyn-EHT, n=6/group for 1x dyn-EHT, n=4/group for 1x EHT. Student's t-test was used to compare average contractile stress values between spontaneous beating and 1 Hz stimulation within each loading condition. NS indicates not statistically significant. **(B)** Representative normalized tissue twitch stresses for one single contraction with 1 Hz stimulation. **(C)** Comparison of cardiomyocyte stress during contraction and relaxation at Day 28 when stimulated at 1 Hz. All data represented as mean ± SD. Figure and data prepared by Jacqueline Bliley.

With higher stimulation frequencies, EHTs did not display increased contractile shortening (Figure 3.4A) nor a positive force-frequency relationship (Figure 3.4B). Similarly, other researchers have also reported a lack of a positive force-frequency relationship in EHTs[30], despite

other signs of increased maturation (i.e. increased contractile shortening and twitch stress). Previous research has suggested that a positive force frequency relationship requires mature calcium handling[15] and it may be possible that our EHTs would benefit from additional maturation through either electrical stimulation[15,35] or treatment with IGF-1/neuregulin [38], which have both been shown to lead to the development of a positive force frequency relationship.

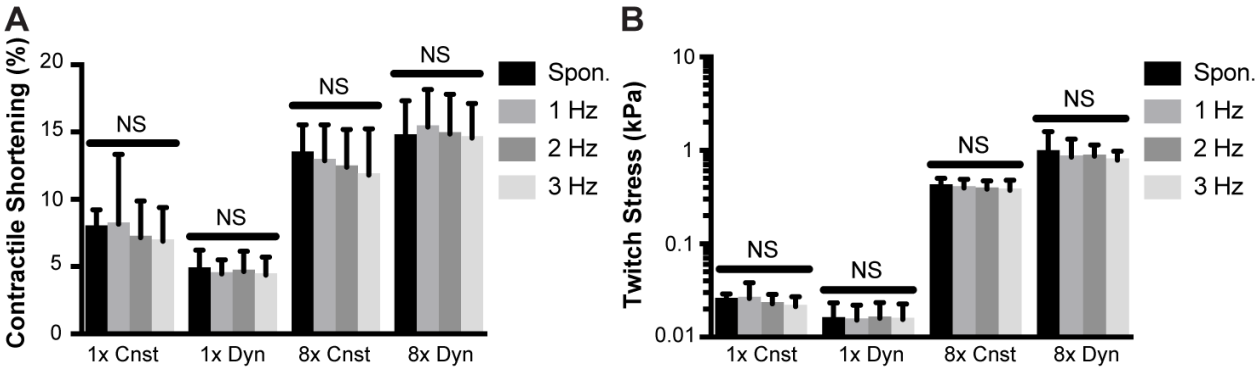

Fig 3.4. Positive Force Frequency Relationship Not Observed in EHTs Under Any Loading Amount or Condition. (A) Contractile shortening of the EHTs at different stimulation frequencies. **(B)** Contractile stress of EHTs at different stimulation frequencies. Graph shows n=5/group for 8x EHT and 8x dyn-EHT, n=6/group for 1x dyn-EHT, n=4/group for 1x EHT. One way ANOVA was used to compare average values with spontaneous beating and different stimulation frequencies within each loading condition. NS indicates not statistically significant. All data represented as mean ± SD. Figure and data prepared by Jacqueline Bliley.

Differences in tissue twitch kinetics were also observed between loading conditions. EHTs and dyn-EHTs displayed similar beat frequencies under all loading conditions, which is surprising considering the increased lengthening and diastolic stresses observed in 8x dyn-EHTs (Figure 3.5A). Despite similar beat frequencies, 8x dyn-EHTs showed decreased contraction times compared to 1x dyn-EHTs (Figure 3.8B-E), and this led to an increase in the contractile velocity in 8x dyn-EHTs compared to all other conditions (Figure 3.5F). Similarly, 8x-dyn EHTs had significantly increased relaxation velocities compared to all other loading conditions (Figure 3.5G). Contractile work and power increased in 8x EHTs and 8x dyn-EHTs compared to both 1x conditions (Figure 3.5H-I), showing a functional improvement in terms of producing greater force

over a longer distance in a shorter period of time.

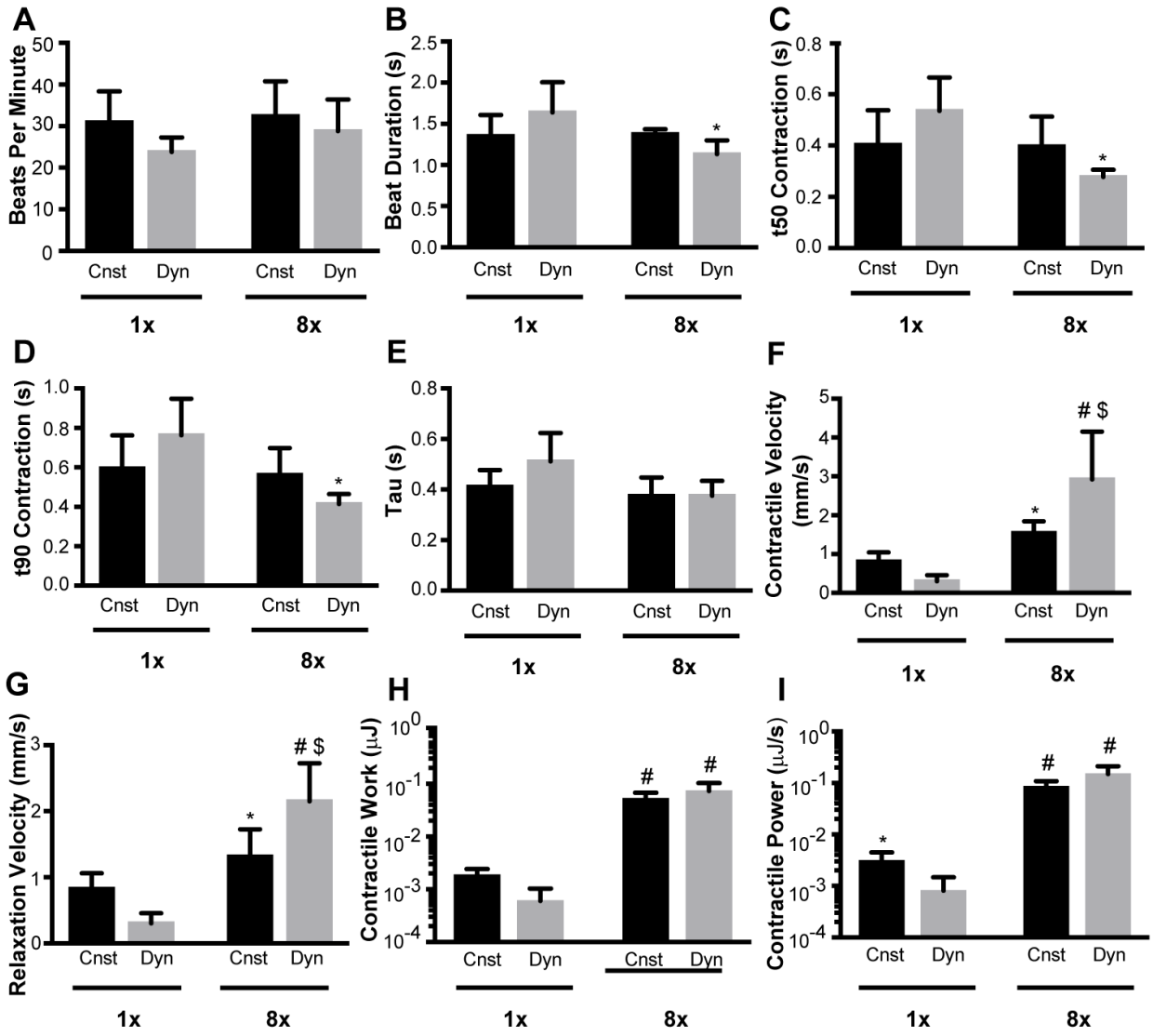

Figure 3.5: Wild-type ESC-Derived Engineered Heart Muscle Tissue Spontaneous Twitch Kinetics. **(A)** Beats per minute under each loading condition. **(B)** Total beat (twitch) duration (seconds) under each loading condition. **(C)** Time to 50% contraction (t50) within each loading condition. **(D)** Time to 90% contraction (t90) under each loading condition. **(E)** Time constant (seconds) of contractile transient decay (Tau) within each loading condition. **(F)** Contractile velocity (mm/s) under each loading condition. **(G)** Relaxation Velocity (mm/s) under each loading condition. (H) Contractile work, measured in microjoules, under each loading condition. **(I)** Contractile Power, measured in microjoules per second, within each loading condition. All graphs show n=5/group for 8x EHT and dyn-EHT, n=6/group for 1x EHT, n=4/group for 1x dyn-EHT. Statistics based on two-way ANOVA with post hoc Holm Sidak test. *p<0.05 vs. 1x dynamic; #p<0.05 vs. 1x dynamic and 1x constrained, $ p<0.05 vs. 8x constrained. All data represented as mean ± SD. Figure and data prepared by Jacqueline Bliley.

Similar results were also obtained under 1 Hz electrical stimulation (Figure 3.6), with 8x dyn-EHTs displaying increased contractile and relaxation velocities (Figure 3.6A-G), which was mainly attributed to the greater levels of contractile shortening as contraction times and relaxation times tended to be similar among the groups with electrical stimulation. 8x dyn-EHTs also displayed increased contractile work (Figure 3.6F) and power (Figure 3.6G) compared to all other conditions. This result highlights not only the unique impact that dynamic loading has on contractile stress for the 8x dyn-EHT, but also that the magnitude of the load applied to the EHT (1x versus 8x) is important in driving these functional differences.

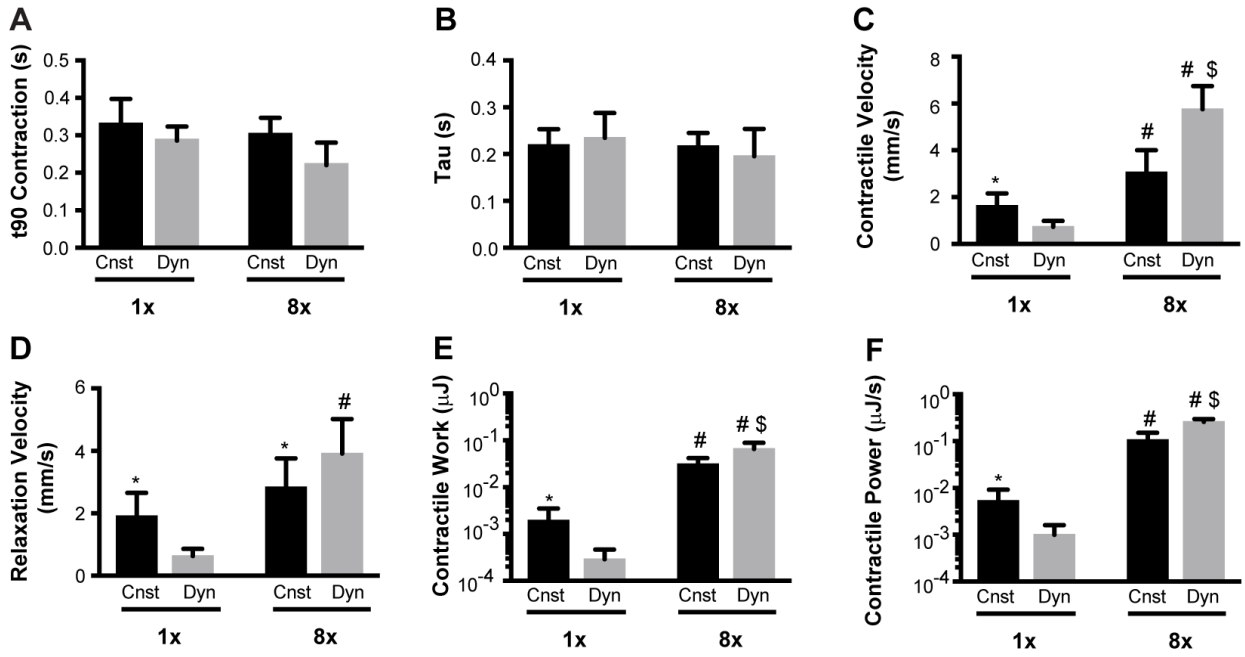

Figure 3.6: Wild-type ESC-Derived Engineered Heart Muscle Tissue Twitch Kinetics with 1 Hz Stimulation. (A) Time to 90% contraction (t90) under each loading condition. **(B)** Time constant (seconds) of contractile transient decay (Tau) within each loading condition. **(C)** Contractile velocity (mm/s) under each loading condition. **(D)** Relaxation Velocity (mm/s) under each loading condition. **(E)** Contractile work, measured in microjoules, under each loading condition. **(F)** Contractile Power, measured in microjoules per second, within each loading condition. All graphs show n=5/group for 8x EHT and dyn-EHT, n=6/group for 1x EHT, n=4/group for 1x dyn-EHT. Statistics based on two-way ANOVA with post hoc Holm Sidak test. *p<0.05 vs. 1x dynamic; #p<0.05 vs. 1x dynamic and 1x constrained, $ p<0.05 vs. 8x constrained. All data represented as mean ± SD. Figure and data prepared by Jacqueline Bliley.

3.3.3. 8x dyn-EHT significantly improves maturation state based on myofibrillar alignment, gene expression and electrophysiology

In terms of structure, the EHTs showed major differences in cytoskeletal organization as a function of the different loading conditions. This is important because the myocardium of the vertebrate heart already has highly aligned cardiomyocytes at early time points[21]. Similarly, a number of studies using 2D and 3D engineered cardiac tissue have shown that increases in cardiomyocyte alignment are associated with increases in contractile function[2,3,11,27]. Fixing and staining the EHTs for the myofibrils confirmed that all tissues had a dense network of well differentiated cardiomyocytes. However, it also revealed distinct differences in alignment between the 1x and 8x loading conditions (Figure 3.7AB). Actin is organized parallel to the direction of sarcomere contraction within cardiomyocytes and thus, actin alignment also serves as an indirect measure of sarcomere alignment. Quantification of the actin alignment confirmed that there were more myofibrils oriented in the direction of the applied load in the 8x condition, clearly demonstrating anisotropy. The orientational order parameter (OOP), a measure of alignment, where OOP values close to 1 indicate completely coaligned actin filaments and values close to 0 indicate an isotropic distribution of actin filaments, was then obtained. Comparison between the conditions using the OOP further demonstrated that alignment was significantly greater in the 8x versus 1x groups (Figure 3.7C). While not statistically significant, both qualitative and quantitative analysis of myofibril alignment suggested that the 8x dyn-EHT condition had the greatest degree of anisotropy (Figure 3.7A-B). Anisotropy is further supported by the elevated tensile elastic modulus observed in 8x dyn-EHTs (Supplemental Figure 7), which is likely due to increased alignment of the cardiomyocytes along the longitudinal axis of the tissue. In fact, elevated elastic moduli have been observed in tissues with increased cardiomyocyte alignment in other EHT

systems [52] and is also supported by finite element modelling[24].

Cardiac gene expression in the EHTs was also dependent on loading condition. Several genes typically associated with a more mature cardiomyocyte phenotype were upregulated in the 8x dyn-EHT (Figure 3.7D). This study revealed an upregulation of several sarcomere-related genes, including two different titin isoforms (TTN-N2B and TTN-N2A), as well as troponin I (TNNI3). There was also an upregulation of all desmosomal genes, including desmoplakin (*DSP*), plakoglobin, (*JUP*), plakophilin-2 (*PKP2*), desmoglein-2 (*DSG2*), desmocollin-2 (*DSC2*), and the intermediate filament gene desmin (*DES*), within the 8x dyn-EHT condition. This is in agreement with previous results, showing that mechanical loading leads to an upregulation of desmosomal genes[34]. Metabolic markers associated with fatty acid oxidation (the predominant form of metabolism in the adult heart), including *CPT1B* and *PDK4*, were also upregulated within the 8x dyn-EHT. Further, sodium channel *SCN5A* and gap junction Cx43 (*GJA1*) genes were also upregulated in the 8x dyn-EHT group. While not every gene examined showed an increase in the 8x dyn-EHT, it is evident that a number of genes associated with more mature heart muscle were upregulated.

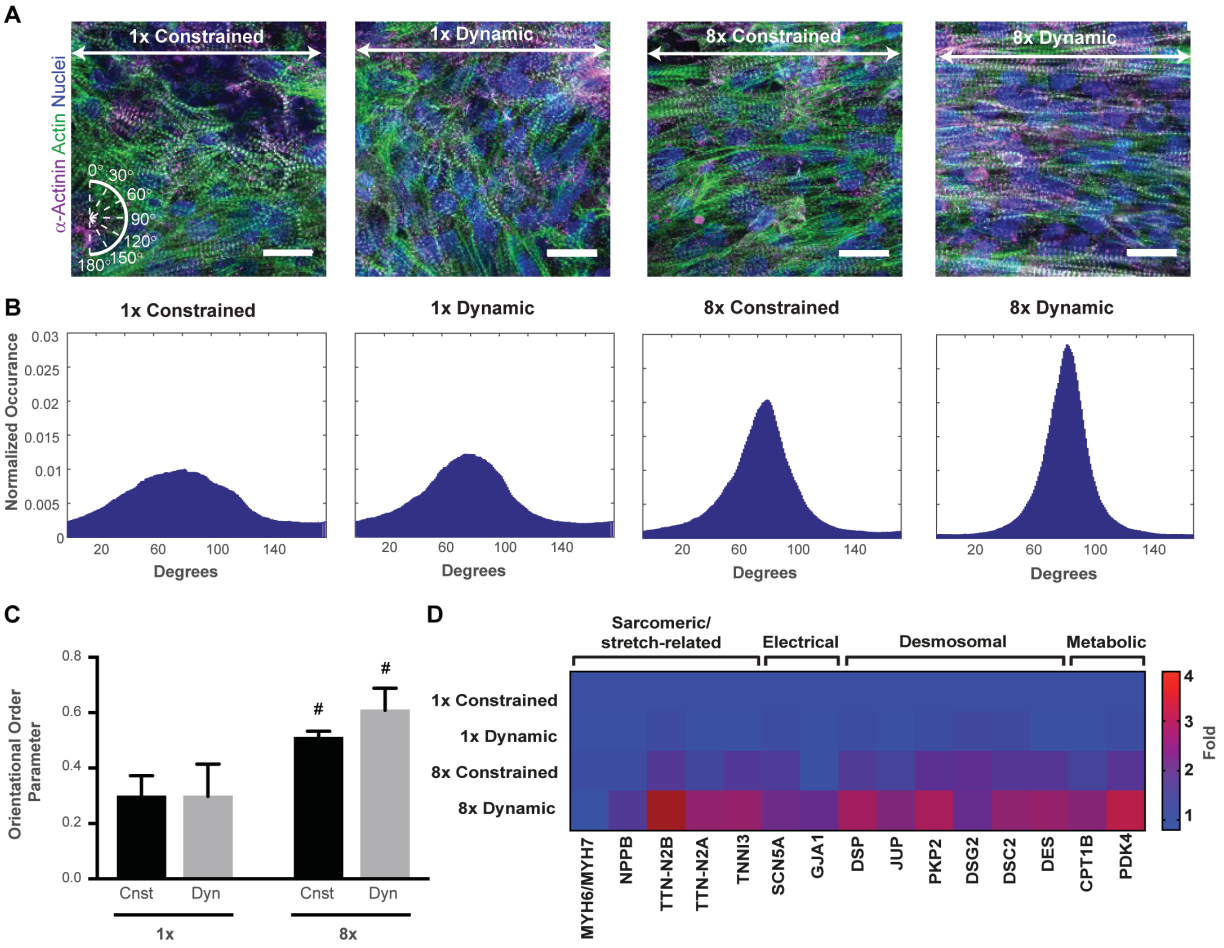

Figure 3.7: Impact of Loading on Cardiomyocyte Alignment and Cardiac Gene Expression. (A) Microscopic images of tissues under each loading condition. The white arrow represents the tissue's longitudinal axis. Orientation angles were based on white compass (bottom left) with a 90° orientation considered to be along the longitudinal axis of the tissue. Scale bars are 20 µm. **(B)** Histograms below each image display normalized actin angle occurrence of representative tissues from each loading condition. **(C)** Average cardiomyocyte alignment (OOP) within engineered heart muscle tissues exposed to different loading conditions. n=3/group. Statistics based on two-way ANOVA with post hoc Holm Sidak test. #p<0.05 vs. 1x dynamic and 1x constrained. One cardiomyocyte differentiation batch was used to prepare all tissues in panels A-C. **(D)** Heat map showing log scale geometrical mean of gene expression levels relative to the 1x constrained loading condition. n=3 tissues/group. One cardiomyocyte differentiation batch was used for gene expression analysis in panel D. All data represented as mean ± SD. Figure (A-C) and data (A-C) prepared by Jacqueline Bliley. Heat map (D) prepared by Mathilde Vermeer.

With a notable increase in tissue anisotropy induced by 8x loading, it was postulated that sarcomere spacing approached the commonly cited physiologic value of ~2 μm, where previous research has suggested that precise sarcomere spacing allows for maximum myofibril overlap and increased contractile force generation. The value of 2 μm sarcomere spacing is similar to values

observed in adult human ventricular myocytes and is also indicative of a more mature engineered heart muscle tissue[29]. To investigate this question, the distance between adjacent z-lines was measured, using alpha-actinin antibody immunostaining. This landmark was selected because the z lines represent the anatomic ends of a sarcomere. Similar to the previous findings with tissue cytoskeletal architectures, I observed more disorganized alpha actinin staining in both 1x conditions (Figure 3.8A-B) when compared to the 8x conditions (Figure 3.8C-D). Sarcomere spacing was also significantly increased in the 8x dyn-EHT condition compared to both 1x conditions (Figure 3.8D).

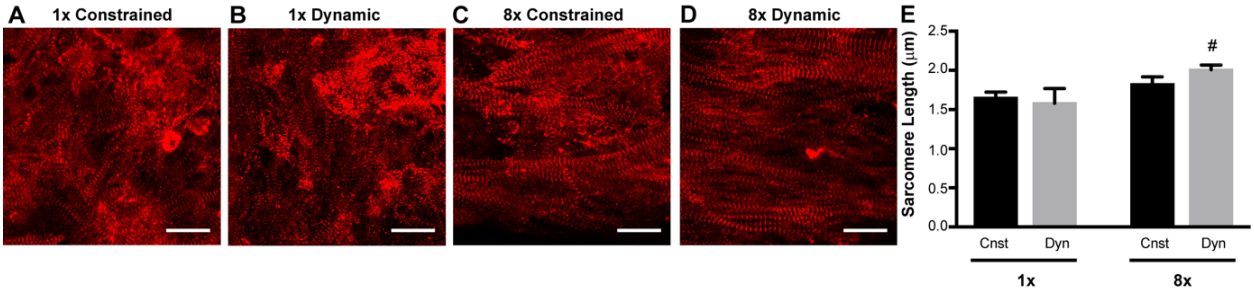

Figure 3.8: Sarcomere Length Increases in 8x dyn-EHT. (A-D) Representative α-actinin max intensity projections from each loading condition. Scale bars are 20 μm. **(E)** Average sarcomere length (μm) under all loading conditions (constrained versus dynamic) and loading amounts (1x or 8x). n=3/group. Statistics based on two-way ANOVA with post hoc Holm Sidak test. #$p<0.05$ vs. 1x dynamic and 1x constrained. All data represented as mean ± SD. Figure and data prepared by Jacqueline Bliley.

The electrophysiology of the 8x dyn-EHT condition also showed important differences at both the cellular and tissue scales. At the tissue level, calcium imaging revealed uniaxial conduction along the length of the EHTs from one end to the other (Figure 3.9A-D). Quantification of the longitudinal conduction velocity based on the calcium wave propagation showed a statistically significant increase in the conduction velocity of 8x dyn-EHTs compared to the 1x conditions from approximately 5 to 10 cm/s (Figure 3.9E). This is consistent with the changes in the alignment and

gene expression, as increases in both cardiomyocyte aspect ratio and Cx43 gap junction expression are known to increase conduction velocity[4,8,22,46]. At the cellular level, sharp electrode measurements of cardiomyocyte resting membrane potential (RMP) were performed on the 1x and 8x dyn-EHTs. The RMP for adult ventricular cardiomyocytes is reported to be in the range of -70 to -90 mV depending on species and measurement technique[17,19,40]. For hESC and hiPSC derived cardiomyocytes, the RMP is typically less negative and more fetal or embryonic-like[16], though a number of studies have reported the ability to use engineered cardiac tissue platforms to produce a more mature RMP[19,32,35]. For the 1x dyn-EHT, there were two distinct populations of cardiomyocytes, one with a less negative RMP (around -19 mV) and the other with a more negative RMP (around -62 mV) (Figure 3.9F). However, for the 8x dyn-EHTs the population of cardiomyocytes with a RMP around -20 mV were absent and there was an increase in the proportion of more negative RMP cells around -60 mV (Figure 3.9G). This suggests that the increase in applied load between the 1x and 8x strips is able to drive immature cardiomyocytes towards a more mature phenotype in terms of RMP.

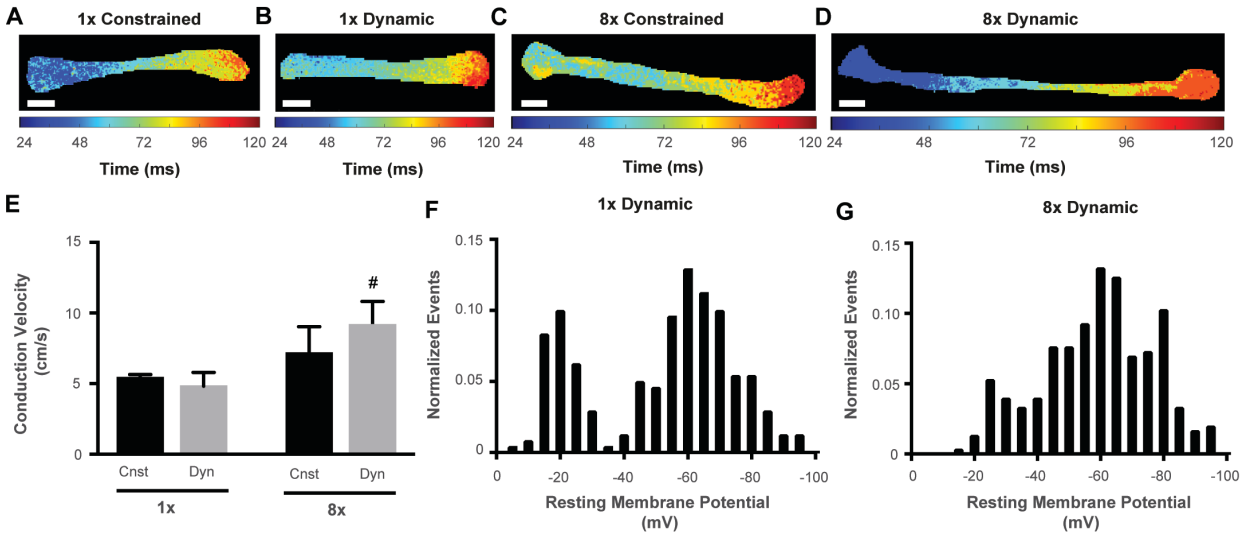

Figure 3.9: 8x Loading Increases Tissue Conduction Velocity and Electrical Excitability. (A-D) Calcium wave propagation across engineered heart muscle tissues under each loading condition. Color map shows time delay of calcium wave as it travels across the tissue. **(E)** Bar graph of average conduction velocity obtained from calcium transients. Conduction velocity based on n=4 for 8x constrained, 8x dynamic and 1x dynamic groups, and n=3 for 1x constrained group. Statistics based on two-way ANOVA with post hoc Holm Sidak test, where # indicates $p<0.05$ compared to both 1x dynamic and 1x constrained loading conditions. One cardiomyocyte differentiation batch was used for conduction velocity measurements in panels A-E. **(F-G)** Empirical probability distribution of cells resting membrane potential obtained via sharp electrode measurements from multiple spatial locations (n=3 tissues/group, n=80 cells measured throughout each tissue) within 1x dyn-EHT and 8x dyn-EHT. One cardiomyocyte batch was used for sharp electrode measurements in panels F and G. All data represented as mean ± SD. Figure (A-E) and data (A-E) prepared by Jacqueline Bliley. Figure (F-G) and data (F-G) prepared by Daniel Pijnappel's group.

3.4. Discussion

In this chapter, a novel dyn-EHT platform was developed that builds off of previous work from our laboratory and other investigators that have used primary, hESC and hiPSC derived cardiomyocytes to engineer functional cardiac tissues *in vitro*. Indeed, it is critical to acknowledge the important contributions to the field made by researchers implementing more physiologic-like electromechanical conditioning to drive maturation[1,5,25,31,35–37,42,54]. However, these other 2D and 3D EHTs are generally isometrically constrained, meaning they undergo low levels of contractile shortening ranging from 1-5%[18,25,35] and are exposed to minimal stretch with preload. For instance, current 3D EHTs are cast around PDMS/plastic posts or frames that can bend during contraction

but do not allow the tissue to significantly change its length. This is in stark contrast to the heart muscle shortening observed *in vivo* where fractional shortening from the mid ventricle was has been reported to be from 10-40% depending on the location within the ventricle wall (endocardial versus mid-wall- versus epicardial) [55]. If we assume a mid-wall estimate of longitudinal fractional shortening, the average contractile strain ranges from 10-20%.

To test whether isometrically constraining the tissue (similar to current EHT systems) leads to reduced function, I compared EHT function following constrained and dynamic culture using two different loads, either 1x or 8x. These results demonstrate that using the dyn-EHT platform with a sufficient load (8x) increased a number of important cardiac functional markers, including twitch stress, twitch kinetics (contractile velocities, work and power under 1 Hz stimulation), and cardiac gene expression. In contrast, essentially the opposite effect was observed with 1x culture where the 1x dyn-EHT displayed reduced function compared to the 1x constrained EHTs. 1x dyn-EHTs tended to shorten over time in culture and displayed reduced contractile shortening and twitch stress as well as reduced contractile velocity, work, and power under 1 Hz stimulation. The reduced contractility together with the observation of reduced tissue length in the 1x dyn-EHT suggested that tissue stiffness may have increased with 1x dyn-EHT culture. However, an increase in tissue tensile elastic modulus in the 1x dyn-EHTs was not identified. Thus, the reduced contractile shortening observed in the 1x dyn-EHT is likely due to a combination of disorganized sarcomeres and reduced sarcomere length, or other factors that were not directly investigated here.

Despite dramatic differences observed with constrained and dynamic culture, it is important to note that during constrained culture, EHTs were still able to contract against and bend the PDMS strip. This type of constrained control was utilized as it most closely relates to current EHT models with PDMS posts. In the future, it would be interesting to compare to a completely

constrained control that would not permit tissue contractile shortening by using a substrate with increased stiffness as a post and then directly comparing results against the dynamic model.

While 8x dyn-EHT culture improved function and maturation, it is worthy to note that extensive research has been performed on other cardiomyocyte maturation techniques, including exposure to growth factors, and hormones such as triiodothyronine[53], neuregulin[20,38], and glucocorticoids[33]. Supplementation of media with fatty acids to promote a metabolic switch in cardiomyocytes from glycolysis to fatty acid oxidation has also resulted in dramatic increases in contractility and improved electrophysiology[13,43]. Further, in recent work, Ronaldson-Bouchard et al. combined constrained mechanical loading with field electrical stimulation to produce EHTs with highly organized ultrastructure, improved contractility and calcium handling[35]. In comparison, while 8x dyn-EHTs displayed markers of improved maturation, the tissue ultrastructure did not appear as highly organized. By combining our mechanical loading platform with such other approaches, it may be possible to further enhance the function of our 8x dyn-EHTs. Future studies using this 8x dyn-EHT will explore this hypothesis.

As with any experimental system, there are important considerations to understand in regard to the dyn-EHT platform. First, the dimensions of the PDMS strip determine the bending stiffness and the load applied to a tissue. While it is straightforward to change the PDMS strip thickness, length, and width to tune the bending stiffness and applied load (Supplemental Figure 2), this cannot be changed once integrated into the EHT. A more realistic approach might be to achieve a dynamic change in strip stiffness to change the mechanical load in the same dyn-EHT, similar to what is experienced by the heart during certain disease states. Development of a PDMS strip with a photoactivatable crosslinker that upon illumination would substantially increase the stiffness, is one possible approach. Second, although cardiomyocytes were derived from hESCs,

the cardiac fibroblasts were commercially available and derived from a healthy donor. This was done to minimize variability that can occur between hESC differentiations. Additionally, other cardiac cell types including endothelial cells and smooth muscle cells could be incorporated into our 3D model but were not explored here.

3.5. Conclusions

In conclusion, I developed a model of mechanical loading of EHTs (dyn-EHTs) by incorporating a PDMS strip whose deformation can be used to determine tissue contractile forces but can also be used to mechanically load tissues. By simply changing dimensions of the PDMS strip, modulation of loading on the EHT is enabled. Further, because the PDMS strip and EHT can be cultured dynamically, this system allows the tissue to undergo significant contractile shortening, and enables the modulation of the preload the cardiac tissue experiences. By incorporating a strip with sufficient load in a dynamic condition (8x dyn-EHTs), the function of wild-type EHTs was improved.

3.6. Acknowledgements

Financial support was provided from Human Frontier Science Program [grant number RGY 0071/2014 to P.v.d.M. and A.W.F.], the National Institutes of Health [grant number DP2HL117750 to A.W.F.], the Office of Naval Research [grant number N00014-17-1-2566 to A.W.F.], and the Dowd Fellowship and Presidential Fellowship, Carnegie Mellon University [to J.M.B.]. and in part by the European Research Council [grant number: ERC-2016-StG – 715732 to P.v.d.M]. We would also like to thank Professor Carmel Majidi, Eric Markvicka, and Tong Lu for their providing and assisting with the UV laser cutter for the PDMS strips. We would also like

to thank Wei Chen and Professor Burak Ozdoganlar for providing and assisting with the profilometer for measuring strip thickness, as well as Aishwarya Paward and Professor Jessica Zhang for assistant with setting up and validating the strip bending finite element model.

3.7. References

1. A. W. Feinberg, A. Feigel, S. S. Shevkoplyas, S. Sheehy, G. M. Whitesides, and K. K. Parker. Muscular thin films for building actuators and powering devices. *Science (80-.).* , 2007.
2. Bian, W., C. P. Jackman, and N. Bursac. Controlling the structural and functional anisotropy of engineered cardiac tissues. *Biofabrication* , 2014.doi:10.1088/1758-5082/6/2/024109
3. Black, L. D., J. D. Meyers, J. S. Weinbaum, Y. A. Shvelidze, and R. T. Tranquillo. Cell-Induced Alignment Augments Twitch Force in Fibrin Gel-Based Engineered Myocardium via Gap Junction Modification. *Tissue Eng. - Part A* , 2009.doi:10.1089/ten.tea.2008.0502
4. Blazeski, A., G. M. Kostecki, and L. Tung. Engineered heart slices for electrophysiological and contractile studies. *Biomaterials* , 2015.doi:10.1016/j.biomaterials.2015.03.026
5. Boudou, T., W. R. Legant, A. Mu, M. A. Borochin, N. Thavandiran, M. Radisic, P. W. Zandstra, J. A. Epstein, K. B. Margulies, and C. S. Chen. A microfabricated platform to measure and manipulate the mechanics of engineered cardiac microtissues. *Tissue Eng. - Part A* , 2012.doi:10.1089/ten.tea.2011.0341
6. BS, M. Heart failure after myocardial infarction in the era of primary percutaneous coronary intervention: Mechanisms, incidence and identification of patients at risk. *World J. Psychiatry* 19:57–58, 2019.
7. Burridge, P. W., E. Matsa, P. Shukla, Z. C. Lin, J. M. Churko, A. D. Ebert, F. Lan, S. Diecke, B. Huber, N. M. Mordwinkin, J. R. Plews, O. J. Abilez, B. Cui, J. D. Gold, and J. C. Wu. Chemically defned generation of human cardiomyocytes. *Nat. Methods* , 2014.doi:10.1038/nMeth.2999
8. Bursac, N., K. K. Parker, S. Iravanian, and L. Tung. Cardiomyocyte cultures with controlled macroscopic anisotropy: a model for functional electrophysiological studies of cardiac muscle. *Circ. Res.* , 2002.doi:10.1161/01.RES.0000047530.88338.EB
9. Chattergoon, N. N., G. D. Giraud, S. Louey, P. Stork, A. L. Fowden, and K. L. Thornburg. Thyroid hormone drives fetal cardiomyocyte maturation. *FASEB J.* 26:397–408, 2012.
10. Cui, H., C. Liu, T. Esworthy, Y. Huang, Z. X. Yu, X. Zhou, H. San, S. J. Lee, S. Y. Hann, M. Boehm, M. Mohiuddin, J. P. Fisher, and L. G. Zhang. 4D physiologically adaptable cardiac patch: A 4-month in vivo study for the treatment of myocardial infarction. *Sci. Adv.* , 2020.doi:10.1126/sciadv.abb5067
11. Feinberg, A. W., P. W. Alford, H. Jin, C. M. Ripplinger, A. A. Werdich, S. P. Sheehy, A. Grosberg, and K. K. Parker. Controlling the contractile strength of engineered cardiac muscle by hierarchal tissue architecture. *Biomaterials* , 2012.doi:10.1016/j.biomaterials.2012.04.043
12. Feric, N. T., I. Pallotta, R. Singh, D. R. Bogdanowicz, M. M. Gustilo, K. W. Chaudhary, R. N. Willette, T. P. Chendrimada, X. Xu, M. P. Graziano, and R. Aschar-Sobbi. Engineered Cardiac Tissues Generated in the Biowire II: A Platform for Human-Based Drug Discovery. *Toxicol. Sci.* , 2019.doi:10.1093/toxsci/kfz168
13. Feyen, D. A. M., W. L. McKeithan, A. A. N. Bruyneel, S. Spiering, L. Hörmann, B. Ulmer, H. Zhang, F. Briganti, M. Schweizer, B. Hegyi, Z. Liao, R. P. Pölönen, K. S. Ginsburg, C. K. Lam, R. Serrano, C. Wahlquist, A. Kreymerman, M. Vu, P. L. Amatya, C. S. Behrens, S. Ranjbarvaziri, R. G. C. Maas, M. Greenhaw, D. Bernstein, J. C. Wu, D. M. Bers, T. Eschenhagen, C. M. Metallo, and M. Mercola. Metabolic Maturation Media Improve Physiological Function of Human iPSC-Derived Cardiomyocytes. *Cell Rep.* , 2020.doi:10.1016/j.celrep.2020.107925
14. Girlanda, R. Deceased organ donation for transplantation: Challenges and opportunities. *World J. Transplant.* 6:451, 2016.
15. Godier-Furnémont, A. F. G., M. Tiburcy, E. Wagner, M. Dewenter, S. Lämmle, A. El-Armouche, S. E. Lehnart, G. Vunjak-Novakovic, and W. H. Zimmermann. Physiologic force-frequency response in engineered heart muscle by electromechanical stimulation. *Biomaterials* , 2015.doi:10.1016/j.biomaterials.2015.03.055
16. Goversen, B., M. A. G. van der Heyden, T. A. B. van Veen, and T. P. de Boer. The immature

electrophysiological phenotype of iPSC-CMs still hampers in vitro drug screening: Special focus on IK1. , 2018.
17. Halbach, M., F. Pillekamp, K. Brockmeier, J. Hescheler, J. Müller-Ehmsen, and M. Reppel. Ventricular slices of adult mouse hearts - A new multicellular in vitro model for electrophysiological studies. *Cell. Physiol. Biochem.* , 2006.doi:10.1159/000095132
18. Hansen, K. J., M. A. Laflamme, and G. R. Gaudette. Development of a Contractile Cardiac Fiber From Pluripotent Stem Cell Derived Cardiomyocytes. *Front. Cardiovasc. Med.* 5:1–11, 2018.
19. Horváth, A., M. D. Lemoine, A. Löser, I. Mannhardt, F. Flenner, A. U. Uzun, C. Neuber, K. Breckwoldt, A. Hansen, E. Girdauskas, H. Reichenspurner, S. Willems, N. Jost, E. Wettwer, T. Eschenhagen, and T. Christ. Low Resting Membrane Potential and Low Inward Rectifier Potassium Currents Are Not Inherent Features of hiPSC-Derived Cardiomyocytes. *Stem Cell Reports* , 2018.doi:10.1016/j.stemcr.2018.01.012
20. Iglesias-García, O., S. Baumgartner, L. Macrí-Pellizzeri, J. R. Rodriguez-Madoz, G. Abizanda, E. Guruceaga, E. Albiasu, D. Corbacho, C. Benavides-Vallve, M. Soriano-Navarro, S. González-Granero, J. J. Gavira, B. Krausgrill, M. Rodriguez-Mañero, J. M. García-Verdugo, C. Ortiz-De-Solorzano, M. Halbach, J. Hescheler, B. Pelacho, and F. Prósper. Neuregulin-1β induces mature ventricular cardiac differentiation from induced pluripotent stem cells contributing to cardiac tissue repair. *Stem Cells Dev.* , 2015.doi:10.1089/scd.2014.0211
21. Jallerat, Q., and A. W. Feinberg. Extracellular Matrix Structure and Composition in the Early Four-Chambered Embryonic Heart. *Cells* , 2020.doi:10.3390/cells9020285
22. Kim, D. H., E. A. Lipke, P. Kim, R. Cheong, S. Thompson, M. Delannoy, K. Y. Suh, L. Tung, and A. Levchenko. Nanoscale cues regulate the structure and function of macroscopic cardiac tissue constructs. *Proc. Natl. Acad. Sci. U. S. A.* , 2010.doi:10.1073/pnas.0906504107
23. Konstam, M. A., D. G. Kramer, A. R. Patel, M. S. Maron, and J. E. Udelson. Left ventricular remodeling in heart failure: Current concepts in clinical significance and assessment. , 2011.doi:10.1016/j.jcmg.2010.10.008
24. Kuthe, C. D., and R. V. Uddanwadiker. Investigation of effect of fiber orientation on mechanical behavior of skeletal muscle. *J. Appl. Biomater. Funct. Mater.* , 2016.doi:10.5301/jabfm.5000275
25. Leonard, A., A. Bertero, J. D. Powers, K. M. Beussman, S. Bhandari, M. Regnier, C. E. Murry, and N. J. Sniadecki. Afterload promotes maturation of human induced pluripotent stem cell derived cardiomyocytes in engineered heart tissues. *J. Mol. Cell. Cardiol.* , 2018.doi:10.1016/j.yjmcc.2018.03.016
26. Lian, X., J. Zhang, S. M. Azarin, K. Zhu, L. B. Hazeltine, X. Bao, C. Hsiao, T. J. Kamp, and S. P. Palecek. Directed cardiomyocyte differentiation from human pluripotent stem cells by modulating Wnt/??-catenin signaling under fully defined conditions. *Nat. Protoc.* 8:162–175, 2013.
27. Liau, B., N. Christoforou, K. W. Leong, and N. Bursac. Pluripotent stem cell-derived cardiac tissue patch with advanced structure and function. *Biomaterials* , 2011.doi:10.1016/j.biomaterials.2011.08.050
28. Liau, B., C. P. Jackman, Y. Li, and N. Bursac. Developmental stage-dependent effects of cardiac fibroblasts on function of stem cell-derived engineered cardiac tissues. *Sci. Rep.* 7:1–11, 2017.
29. Lundy, S. D., W. Z. Zhu, M. Regnier, and M. A. Laflamme. Structural and functional maturation of cardiomyocytes derived from human pluripotent stem cells. *Stem Cells Dev.* , 2013.doi:10.1089/scd.2012.0490
30. Mannhardt, I., K. Breckwoldt, D. Letuffe-Brenière, S. Schaaf, H. Schulz, C. Neuber, A. Benzin, T. Werner, A. Eder, T. Schulze, B. Klampe, T. Christ, M. N. Hirt, N. Huebner, A. Moretti, T. Eschenhagen, and A. Hansen. Human Engineered Heart Tissue: Analysis of Contractile Force. *Stem Cell Reports* 7:29–42, 2016.
31. Morgan, K. Y., and L. D. Black. Mimicking isovolumic contraction with combined electromechanical stimulation improves the development of engineered cardiac constructs. *Tissue Eng. - Part A* , 2014.doi:10.1089/ten.tea.2013.0355
32. Nunes, S. S., J. W. Miklas, J. Liu, R. Aschar-Sobbi, Y. Xiao, B. Zhang, J. Jiang, S. Massé, M. Gagliardi, A. Hsieh, N. Thavandiran, M. A. Laflamme, K. Nanthakumar, G. J. Gross, P. H. Backx, G. Keller, and M. Radisic. Biowire: A platform for maturation of human pluripotent stem cell-derived cardiomyocytes. *Nat. Methods* , 2013.doi:10.1038/nmeth.2524
33. Parikh, S. S., D. J. Blackwell, N. Gomez-Hurtado, M. Frisk, L. Wang, K. Kim, C. P. Dahl, A. Fiane, T. Tønnessen, D. O. Kryshtal, W. E. Louch, and B. C. Knollmann. Thyroid and Glucocorticoid Hormones Promote Functional T-Tubule Development in Human-Induced Pluripotent Stem Cell-Derived Cardiomyocytes. *Circ. Res.* 121:1323–1330, 2017.
34. Price, A. J., A. L. Cost, H. Ungewiß, J. Waschke, A. R. Dunn, and C. Grashoff. Mechanical loading of desmosomes depends on the magnitude and orientation of external stress. *Nat. Commun.* 9:, 2018.

35. Ronaldson-Bouchard, K., S. P. Ma, K. Yeager, T. Chen, L. J. Song, D. Sirabella, K. Morikawa, D. Teles, M. Yazawa, and G. Vunjak-Novakovic. Advanced maturation of human cardiac tissue grown from pluripotent stem cells. *Nature* 556:239–243, 2018.
36. Ronaldson-Bouchard, K., K. Yeager, D. Teles, T. Chen, S. Ma, L. J. Song, K. Morikawa, H. M. Wobma, A. Vasciaveo, E. C. Ruiz, M. Yazawa, and G. Vunjak-Novakovic. Engineering of human cardiac muscle electromechanically matured to an adult-like phenotype. *Nat. Protoc.* , 2019.doi:10.1038/s41596-019-0189-8
37. Ruan, J. L., N. L. Tulloch, M. V. Razumova, M. Saiget, V. Muskheli, L. Pabon, H. Reinecke, M. Regnier, and C. E. Murry. Mechanical Stress Conditioning and Electrical Stimulation Promote Contractility and Force Maturation of Induced Pluripotent Stem Cell-Derived Human Cardiac Tissue. *Circulation* , 2016.doi:10.1161/CIRCULATIONAHA.114.014998
38. Rupert, C. E., and K. L. K. Coulombe. IGF1 and NRG1 Enhance Proliferation, Metabolic Maturity, and the Force-Frequency Response in hESC-Derived Engineered Cardiac Tissues. *Stem Cells Int.* , 2017.doi:10.1155/2017/7648409
39. Rupert, C. E., T. Y. Kim, B. R. Choi, and K. L. K. Coulombe. Human Cardiac Fibroblast Number and Activation State Modulate Electromechanical Function of hiPSC-Cardiomyocytes in Engineered Myocardium. *Stem Cells Int.* 2020:, 2020.
40. Santana, L. F., E. P. Cheng, and W. J. Lederer. How does the shape of the cardiac action potential control calcium signaling and contraction in the heart? , 2010.doi:10.1016/j.yjmcc.2010.09.005
41. Schaaf, S., A. Shibamiya, M. Mewe, A. Eder, A. Stöhr, M. N. Hirt, T. Rau, W. H. Zimmermann, L. Conradi, T. Eschenhagen, and A. Hansen. Human engineered heart tissue as a versatile tool in basic research and preclinical toxicology. , 2011.
42. Shadrin, I. Y., B. W. Allen, Y. Qian, C. P. Jackman, A. L. Carlson, M. E. Juhas, and N. Bursac. Cardiopatch platform enables maturation and scale-up of human pluripotent stem cell-derived engineered heart tissues. *Nat. Commun.* , 2017.doi:10.1038/s41467-017-01946-x
43. Soyombo, A. A., Y. Wu, L. Kolski, J. J. Rios, D. Rakheja, A. Chen, J. Kehler, H. Hampel, A. Coughran, and T. S. Ross. Fatty Acids Enhance the Maturation of Cardiomyocytes Derived from Human Pluripotent Stem Cells. *Stem Cell Reports* 1:336–349, 2013.
44. Stoppel, W. L., D. L. Kaplan, and L. D. Black. Electrical and mechanical stimulation of cardiac cells and tissue constructs. Elsevier B.V., 2016.
45. Sun, Y., Q. Jallerat, J. M. Szymanski, and A. W. Feinberg. Conformal nanopatterning of extracellular matrix proteins onto topographically complex surfaces. *Nat. Methods* 12:134–136, 2015.
46. Thomas, S. P., L. Bircher-Lehmann, S. A. Thomas, J. Zhuang, J. E. Saffitz, and A. G. Kléber. Synthetic strands of neonatal mouse cardiac myocytes: Structural and electrophysiological properties. *Circ. Res.* , 2000.doi:10.1161/01.RES.87.6.467
47. Tohyama, S., F. Hattori, M. Sano, T. Hishiki, Y. Nagahata, T. Matsuura, H. Hashimoto, T. Suzuki, H. Yamashita, Y. Satoh, T. Egashira, T. Seki, N. Muraoka, H. Yamakawa, Y. Ohgino, T. Tanaka, M. Yoichi, S. Yuasa, M. Murata, M. Suematsu, and K. Fukuda. Distinct metabolic flow enables large-scale purification of mouse and human pluripotent stem cell-derived cardiomyocytes. *Cell Stem Cell* 12:127–137, 2013.
48. Turnbull, I. C., I. Karakikes, G. W. Serrao, P. Backeris, J. J. Lee, C. Xie, G. Senyei, R. E. Gordon, R. A. Li, F. G. Akar, R. J. Hajjar, J. S. Hulot, and K. D. Costa. Advancing functional engineered cardiac tissues toward a preclinical model of human myocardium. *FASEB J.* , 2014.doi:10.1096/fj.13-228007
49. Virani, S. S. *et al.* Heart disease and stroke statistics—2020 update: A report from the American Heart Association. , 2020.doi:10.1161/CIR.0000000000000757
50. Weinberger, F., K. Breckwoldt, S. Pecha, A. Kelly, B. Geertz, J. Starbatty, T. Yorgan, K. H. Cheng, K. Lessmann, T. Stolen, S. C. Marielle, G. Smith, H. Reichenspurner, A. Hansen, and T. Eschenhagen. Cardiac repair in Guinea pigs with human engineered heart tissue from induced pluripotent stem cells. *Sci. Transl. Med.* , 2016.doi:10.1126/scitranslmed.aaf8781
51. Weinberger, F., I. Mannhardt, and T. Eschenhagen. Engineering Cardiac Muscle Tissue: A Maturating Field of Research. 2017.
52. Xiao, Y., B. Zhang, H. Liu, J. W. Miklas, M. Gagliardi, A. Pahnke, N. Thavandiran, Y. Sun, C. Simmons, G. Keller, and M. Radisic. Microfabricated perfusable cardiac biowire: A platform that mimics native cardiac bundle. *Lab Chip* , 2014.doi:10.1039/c3lc51123e
53. Yang, X., M. Rodriguez, L. Pabon, K. A. Fischer, H. Reinecke, M. Regnier, N. J. Sniadecki, H. Ruohola-Baker, and C. E. Murry. Tri-iodo-l-thyronine promotes the maturation of human cardiomyocytes-derived from induced pluripotent stem cells. *J. Mol. Cell. Cardiol.* , 2014.doi:10.1016/j.yjmcc.2014.04.005

54. Zimmermann, W. H., K. Schneiderbanger, P. Schubert, M. Didié, F. Münzel, J. F. Heubach, S. Kostin, W. L. Neuhuber, and T. Eschenhagen. Tissue engineering of a differentiated cardiac muscle construct. *Circ. Res.* , 2002.doi:10.1161/hh0202.103644
55. Zoccali, C., F. A. Benedetto, F. Mallamaci, G. Tripepi, G. Giacone, A. Cataliotti, G. Seminara, B. Stancanelli, and L. S. Malatino. Prognostic Value of Echocardiographic Indicators of Left Ventricular Systolic Function in Asymptomatic Dialysis Patients. *J. Am. Soc. Nephrol.* 15:1029–1037, 2004.

3.8. Supplemental Information

Supplemental Table 1: RT PCR Primers			
Gene		**Forward '5 - '3**	**Reverse '3 - '5**
DSP (NG_008803.1)		CAGTGGTGTCAGCGATGATGT	TGACGCTGGATATGGTGGAA
	DSP_ex1-4	GGACGGCTACTG**TCAAACC**	GACTCGAGGGACACTGATG
	DSP_ex2-5	**CT**GTCAAACCGGCACGATGTC	TCCAGCTGCCAGCGATAGTC
	DSP_ex2-int2	AGGCACCAGAACCAGAACAC	CCCAACCCAGGAACAGAAAC
	DSP_ex1-int2A	GGACGGCTACTG**TCAAACC**	CCCAACCCAGGAACAGAAAC
JUP		AGTAGCCACGATGGAGGTGA	AGGTGTATGTCTGCTGCCAC
PKP2		GCAAATGGTTTGCTCGATTT	GGCTGGTAATCTGCAATGGT
DSG2		TCCACTATGCCACCAACCAC	GCTGGAGCATACACCCTCTC
DSC2		CGGAGATTGTTGCGGTTGA	GGAAAGACGTGCTGCTGTATCA
DES		CTGAGCAAAGGGGTTCTGAG	ACTTCATGCTGCTGCTGTGT
GJA1		GGAATGCAAGAGAGGTTGAAAG	GGCATTTGGAGAAACTGGTAGA
PPIA		ACTTCACACGCCATAATG	ACCCGTATGCTTTAGGAT
MYH6		GATAGAGAGACTCCTGCGGC	TCGGTCATCTTGGTGCTTCC
MYH7		CGAAGGGCTTGAATGAGGAGT	TCCTCCCAAGGAGCTGTTAC
TTN	N2B	CACTAACTGTGACAGTGCC	CTTCTTCCTTTGGTTCAGGT
TTN	N2A	ATGGAAATGAAAGCTGCCC	GGTGAATTTGGCTAGGTGG
TNNI3		CCAACTACCGCGCTTATGC	CTCGCTCCAGCTCTTGCTTT
SCN5A		CACCAACTGCGTGTTCATGG	CAGAAGCCTCGAGCCAGAAT
CPT1B		CTCCTTTCCTTGCTGAGGTG	TCTCGCCTGCAATCATGTAG
PDK4		CCTTTGGCTGGTTTTGGTTA	CCTGCTTGGGATACACCAGT

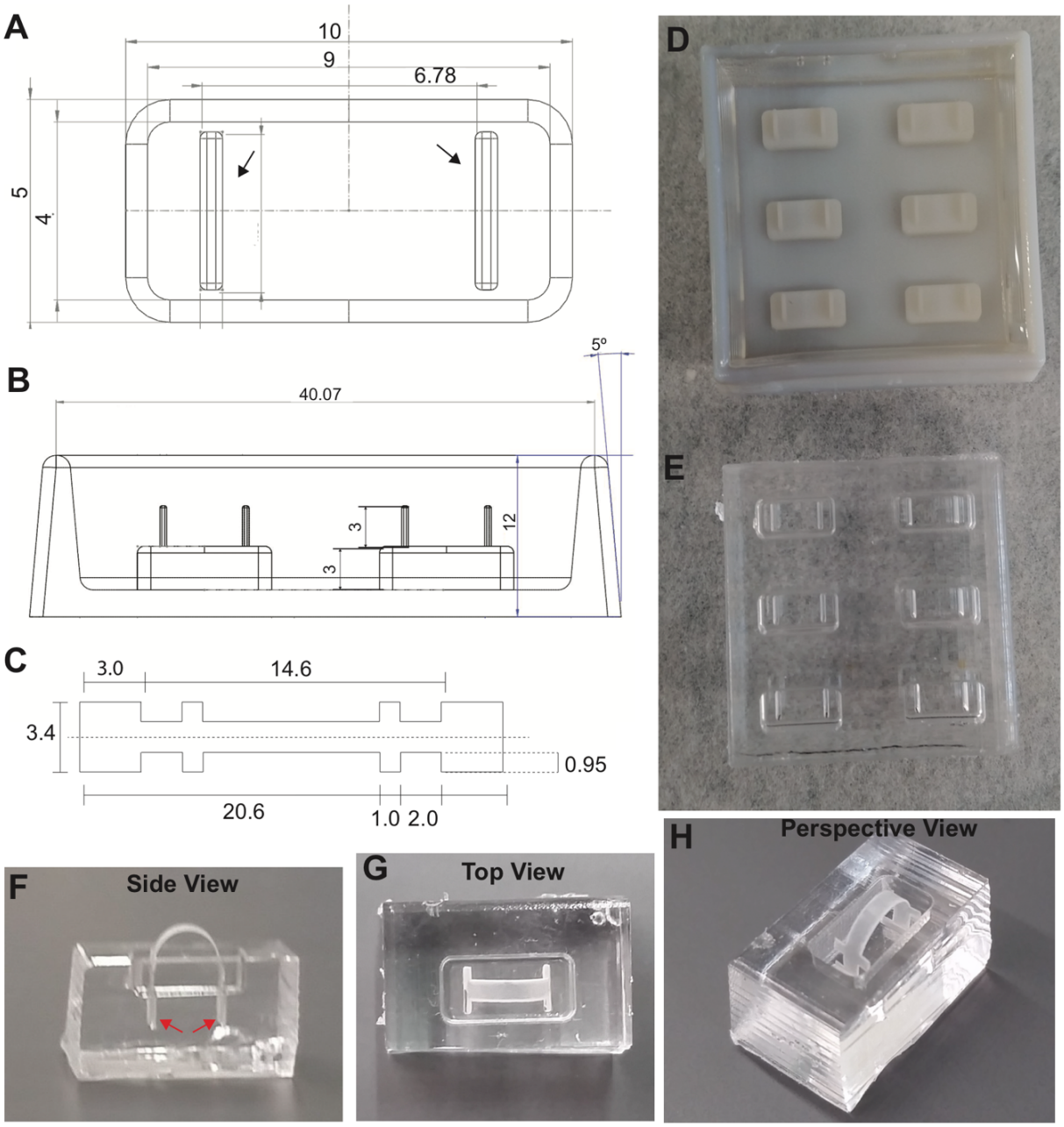

Supplemental Figure 1. Mold and Strip Design and Fabrication. (A) Aerial view of plastic mold dimensions used to create individual PDMS wells for tissue casting. Raised portions of the plastic molds (indicated by the arrows) served as slots in the casted well where the PDMS Strip would eventually sit. **(B)** Side view of dimensions for plastic mold used to create individual PDMS wells. **(C)** PDMS strip dimensions demonstrating a 1 mm wide necking region for tissue attachment and a small 3.4 mm wide overhang to prevent tissue from sliding up the PDMS strip during culture and contraction studies. (D) Aerial image of plastic mold used for casting to create PDMS wells. **(E)** PDMS was cast into wells to create multiple PDMS wells which could be cut out to form individual PDMS wells for tissue fabrication. **(F-G)** Side, Top and Perspective Views of the PDMS strip placed in the PDMS well design. The PDMS strip sits within the slits in the bottom of the PDMS well (red arrows). All dimensions are in mm. Figure from Rebecca Duffy's dissertation.

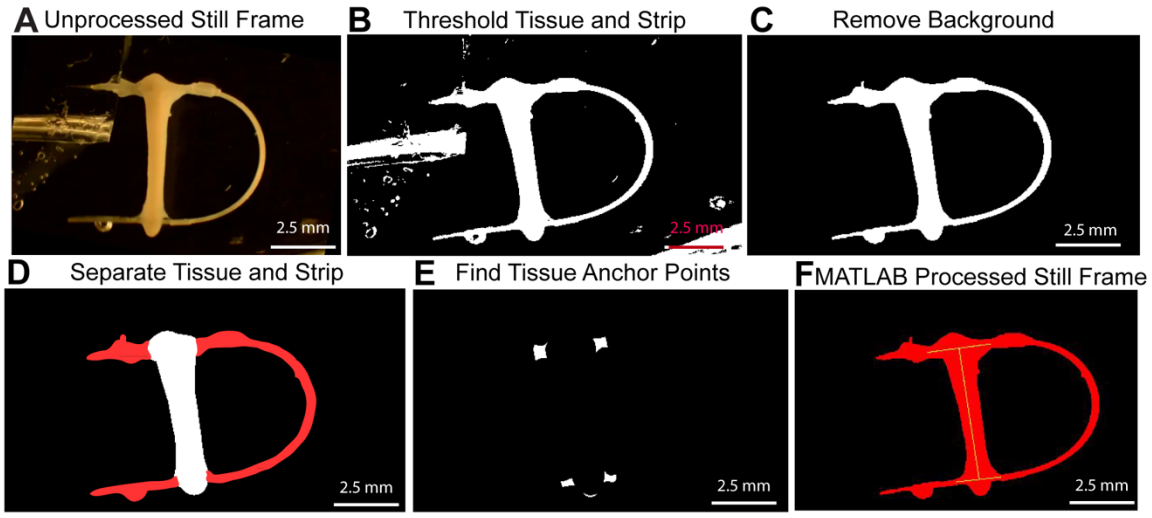

Supplemental Figure 2. MATLAB Processing of Tissue Contractility Videos. (A) Tissue contraction videos are taken on a stereomicroscope equipped with a Nikon DSLR camera. A representative still frame of the tissue is shown. **(B)** Tissue videos are uploaded into a MATLAB program where a user thresholds the tissue and the strip. The thresholded region is shown in white. **(C)** Thresholded area that is neither the tissue nor the strip, also known as background, is removed. **(D)** The program then separates the tissue from its associated strip. **(E)** Tissue anchor points, or where the tissue attaches to the strip, is then detected. This is used to calculate the length between tissue attachment points on the strip. **(F)** Tissue length can then be determined based on the change in distance between tissue attachment points over time. Scale bars are 2.5 mm. Figure and data prepared by Jacqueline Bliley.

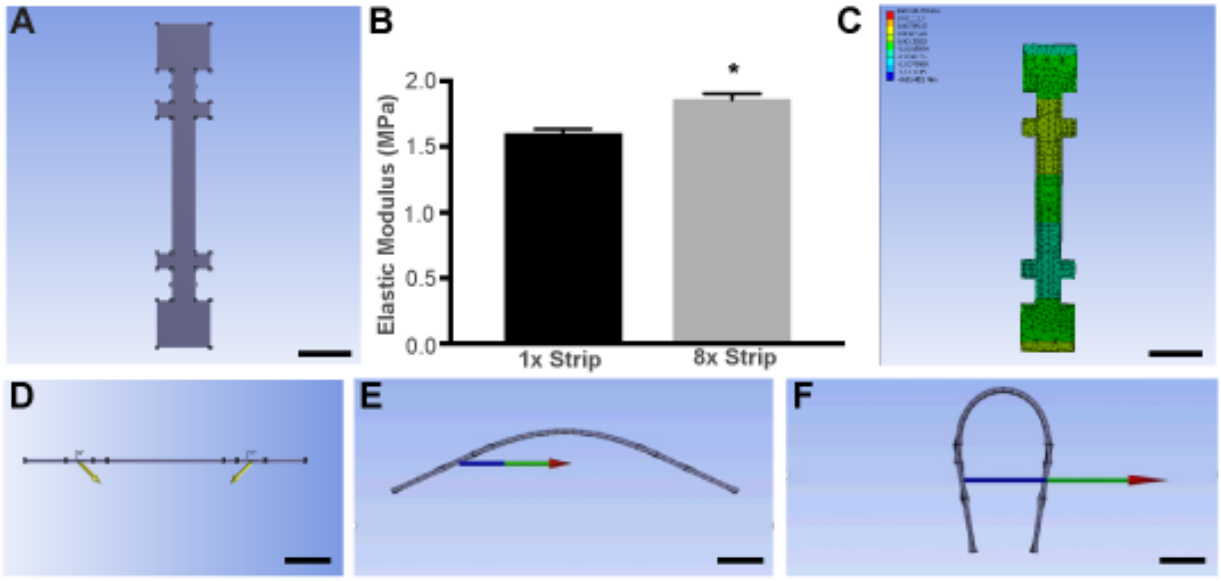

Supplemental Figure 3: Finite Element Modeling (FEM) of Force Required to Bend PDMS Strip. (A) A 3D model of strip was created using ANSYS SpaceClaim software. **(B)** Material properties (elastic modulus and Poisson's ratio) and assumptions were entered in order to model material deformation. Bar graph showing average elastic modulus of each strip used in these studies. * p=0.0043 (Mann-Whitney U test on ranks). **(C)** Program generated mesh used for modeling. **(D)** The PDMS strip was modeled as initially flat and displacements (indicated by the yellow arrows) were applied to the tissue attachments points. Reaction forces (i.e. force required to deform the strip under such a displacement) were obtained and examples of relative reaction forces (colored arrows) are shown comparing minimal strip bending **(E)** and large strip bending **(F).** Relative increase in length of arrow indicates the increase in force required to bend the strip at larger deformations. All data represented as mean ± SD. Figure and data prepared by Jacqueline Bliley.

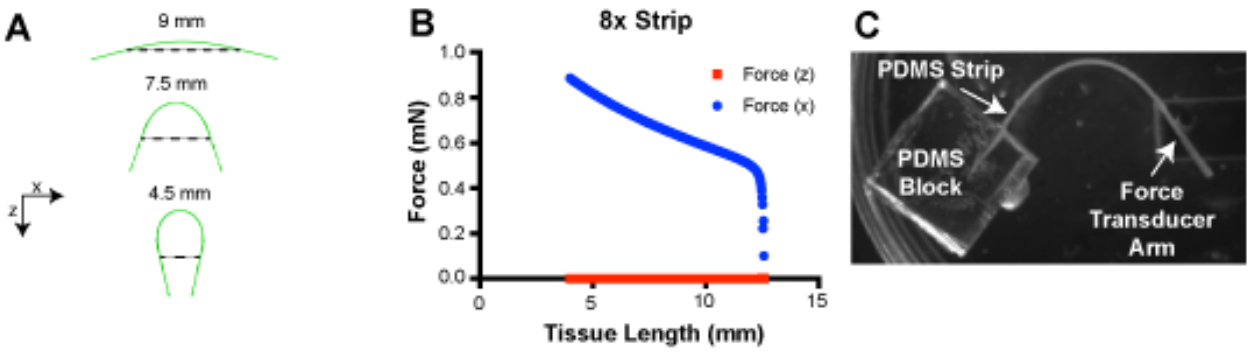

Supplemental Figure 4: Force Transducer Validation of Strip Bending Forces. (A) Strip deformation associated with different tissue lengths (indicated by dotted lines). X and z displacements were applied to the strip at tissue attachment points. **(B)** Respective contributions of x and z bending reaction forces with strip deformation during modeling observed in 8x strips. Both x and z deformation forces were obtained with strip modeling; however, the z component of bending was orders of magnitude lower than the x component of bending in both 1x and 8x strips . Thus, only the x component of bending was used to validate the strip bending forces. **(C)** Force Transducer set-up used to validate force measurements obtained from strips. All measurements were obtained via x bending of 8x strip. Figure and data prepared by Jacqueline Bliley.

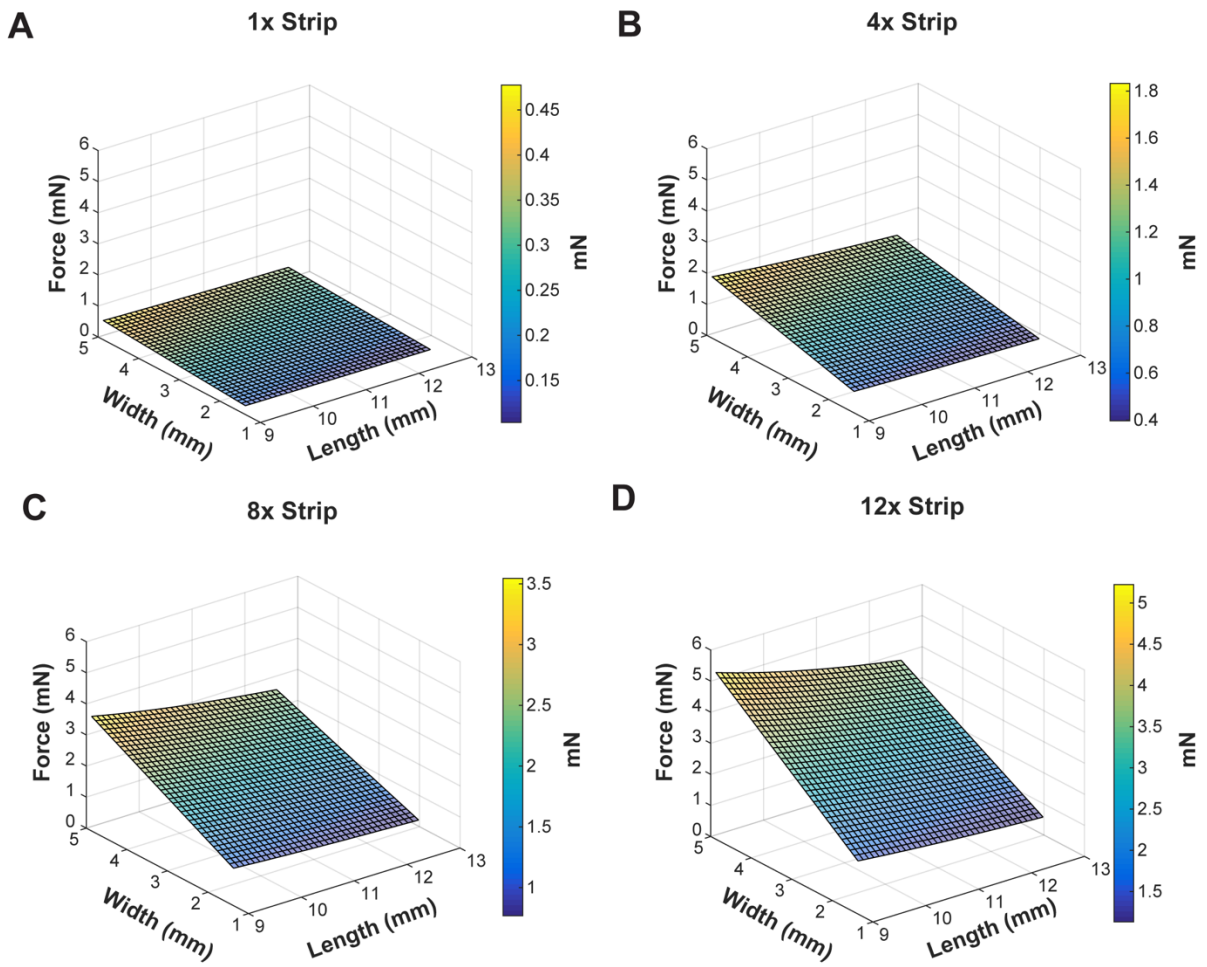

Supplemental Figure 5: Altering Strip Dimensions for a Specified Force Output. Surface plot of forces associated with different strip widths and length of the strip between tissue attachment points. Tissue length was kept constant (6 mm). Graphs are shown for **(A)** 1x strips **(B)** 4x strips **(C)** 8x Strips and **(D)** 12x strips. Figure and data prepared by Jacqueline Bliley.

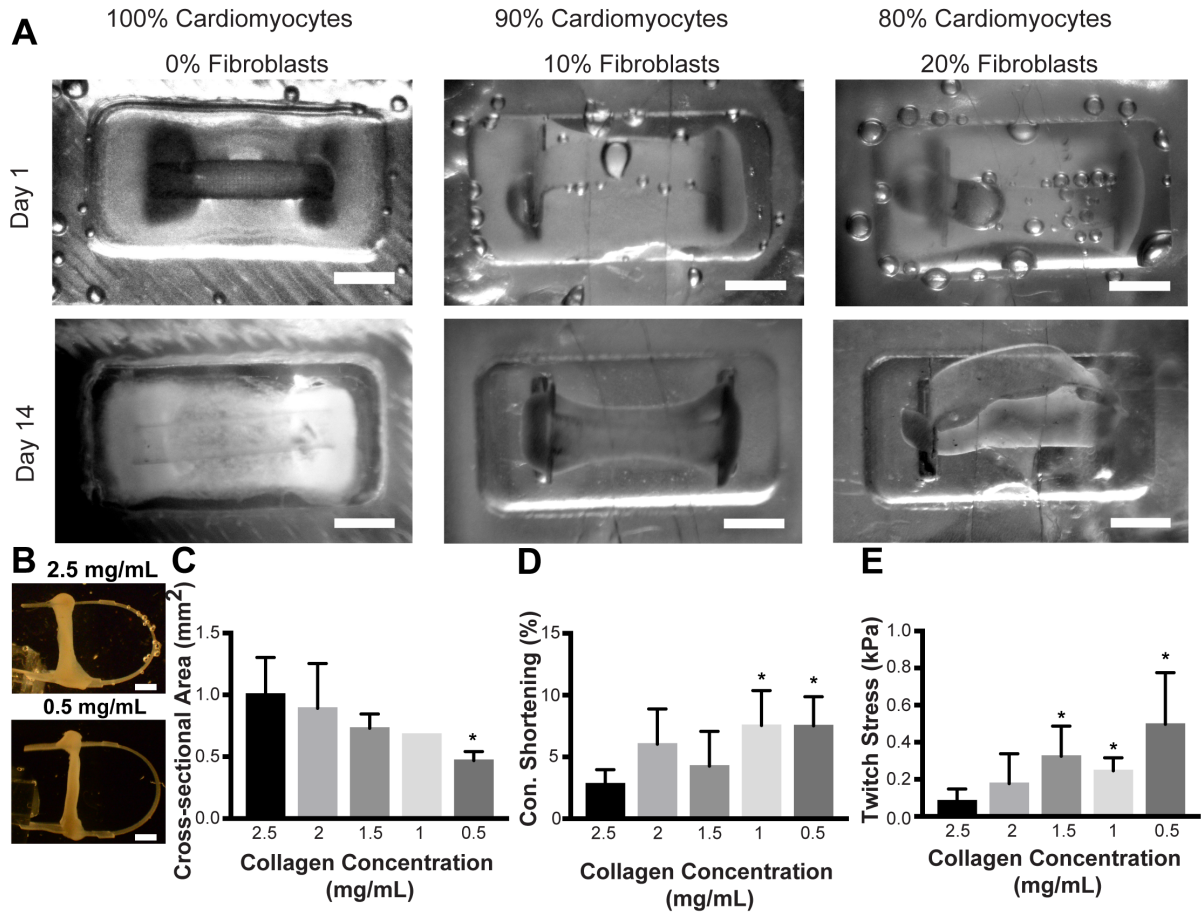

Supplemental Figure 6: Impact of Collagen and Fibroblast Concentration on Tissue Morphology and Function. (A) Macroscopic images during tissue compaction with different ratios of cardiomyocytes to cardiac fibroblasts. **(B)** Tissue macroscopic images from the side showing differences in tissue cross-sectional area when different casting collagen concentrations are used. Tissues were made with 10% fibroblasts. Scale bars are 2 mm. **(C)** Tissue cross-sectional area with collagen concentrations ranging from 2.5 mg/mL to 0.5 mg/mL. **(D)** Tissue contractile shortening in EHTs fabricated with 2.5 mg/mL to 0.5 mg/mL collagen. **(E)** Cardiomyocyte generated twitch stress in tissues fabricated with different collagen concentrations (0.5 mg/mL to 2.5 mg/mL). Results are based on one-way ANOVA with post hoc Holm Sidak test. * indicates $p<0.05$ compared to 2.5 mg/mL collagen. Figure and data prepared by Jacqueline Bliley.

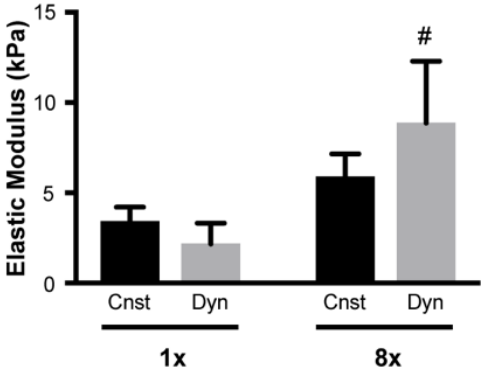

Supplemental Figure 7: Tissue Elastic Modulus Under Different Loading Conditions. Elastic modulus determined from tensile testing of tissues under different loading conditions. Two-way ANOVA with a post hoc Holm Sidak test was performed within each loading condition (either 1x or 8x). # indicates $p<0.05$ vs. 1x dynamic and 1x constrained. Graph shows n=4/group for 8x EHT, n=3 for 8x dyn-EHT, n=3/group for 1x EHT, n=4/ group 1x dyn-EHT. All data represented as mean ± SD. Figure and data prepared by Jacqueline Bliley.

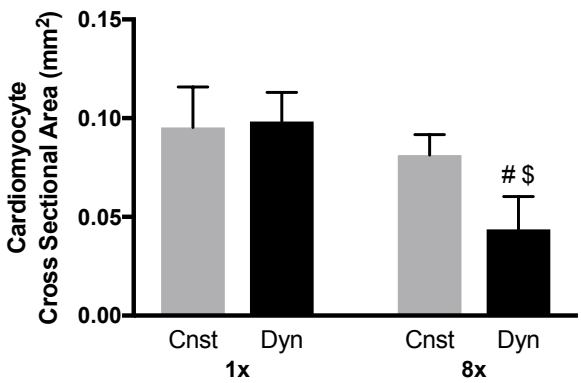

Supplemental Figure 8: Cardiomyocyte cross-sectional area of ESC-derived EHTs. Average cardiomyocyte cross-sectional area used for tissue stress measurements. Results are based on two-way ANOVA with post hoc Holm Sidak test. # indicates $P<0.05$ versus 1x dyn-EHT and 1x EHT. $ indicates $P<0.05$ versus 8x EHT. All data represented as mean ± SD. Figure and data prepared by Jacqueline Bliley.

Chapter 4

Dynamic Loading of Engineered Heart Muscle Tissue Drives a Desmosome-Linked Disease Phenotype

4.1. Introduction

Arrhythmogenic cardiomyopathy (ACM) is a condition characterized by dilation and fibrofatty replacement of either one or both of the ventricles, which results in reduced cardiac output and the production of arrhythmias. Patients with ACM also suffer from a higher risk of sudden cardiac death and are advised to avoid activities that increase mechanical loading on heart muscle, such as exercise[1,31]. Despite the established link between ACM and exercise, there is still a poor understanding about the extent and duration of mechanical loading on heart muscle and how that contributes to disease progression and poor prognosis in ACM.

Animal models have helped explain how genetic mutations associated with ACM in combination with increased mechanical loading on heart muscle contribute to adverse disease progression. In fact, greater than 50% of reported cases of ACM are due to mutations in desmosomes[16], which are important intercellular junctions between adjacent cardiomyocytes. Though animal models have increased our understanding of ACM progression, there are inherent differences in animal versus human pathology of ACM progression (and many other cardiovascular diseases[12]) that limit the ability to draw direct comparisons to human models. For instance, many animal models do not display the fibrofatty accumulation nor the complex electrophysiological signatures that are hallmarks of ACM progression in human patients[13]. Thus, development of a patient-specific, tissue engineered model of ACM disease progression would be tremendously valuable.

Human engineered heart muscle tissue (EHT) platforms have the potential to provide insight into mechanical loading induced disease progression, but current platforms are unable to capture the tissue remodeling, such as changes in tissue length and ventricular dilation, that occur with ACM, as well as many other cardiac diseases[3,15,19,24]. This is because most current EHTs are cast around static posts which results in them being isometrically constrained (unable to change significantly in length). Further, most current EHTs are exposed to limited active preload, or force that stretches the heart muscle during ventricular filling, which is thought to be one of the predominant drivers of increased tissue stress and subsequent tissue remodeling. For instance, current models, like muscular thin films (MTFs), consist of cardiomyocytes attached to a PDMS film, where cardiomyocytes can contract to bend the PDMS sheet but are otherwise constrained to the PDMS surface. Further, many linear EHTs are cast around static PDMS posts, which can similarly bend with contraction but do not allow for significant changes in tissue length that may be critical in capturing a cardiac disease phenotype. These findings suggest that current EHT systems can be improved by allowing for dynamic changes in tissue length and by providing an active preload.

Building upon the dyn-EHT platform presented in Chapter 3, I demonstrate that dyn-EHT conditioning leads to maladaptive structural and functional changes in patient-derived human induced pluripotent stem cells (hiPSCs) with a desmosomal mutation (DSPmut) that led to clinical ACM. Importantly, DSPmut 8x dyn-EHTs show maladaptive remodeling under the same loading range that contributed to increases in function observed in both control hESC and hiPSC-derived 8x dyn-EHTs. Further, deficits in DSPmut 8x dyn-EHTs were limited to dynamic conditions and were unable to be observed in either 2D or 3D constrained culture suggesting that this mechanical

loading platform is an important development in further understanding the physiologic evolution of an ACM disease phenotype.

4.2. Materials and Methods

4.2.1. Patient Heart Tissue Analysis

This study conforms to the Declaration of Helsinki. Approval of human participants was granted by the medical ethical committee of the University of Groningen (METC 2015.213). Written informed consent was received prior to inclusion of patients. Skin biopsies were gathered for fibroblast culture and heart tissues were obtained for immunofluorescent staining.

4.2.2. Human Induced Pluripotent Stem Cell (hiPSC) Culture, Cardiomyocyte differentiation and Metabolic Purification

Fibroblasts were cultured and reprogrammed to hiPSCs using nucleofection with three plasmids, pCXLE-hSK, pCXLE-hMLN and pCXLE-hOCT3/4 that were a gift from Shinya Yamanaka (Addgene plasmid # 27078, 27079 and 27076), according to previously reported papers[39,53]. Pluripotent colonies were hand-picked and dissociated to single cells using Accutase (07920, Stem Cell Technologies) and TrypLE Express Enzyme (12604021, Thermofisher). hiPSCs were seeded, using Y27632 ROCK inhibitor (SM02-10, Bio-connect) on Geltrex (A1413202, ThermoFisher)-coated plates, and maintained in E8 medium (A1517001, ThermoFisher). Cardiomyocyte differentiation was based on slight modifications of previously established protocols[27]. Cells were incubated with RPMI-1640 (21870076, ThermoFisher) supplemented with 1% v/v L glutamine (25030081, ThermoFisher), 5% Knockout™ serum replacement (10828028, ThermoFisher) containing factors CHIR99201 (C-6556, LC laboratories)

and Activin A (120-14E, Peprotech) to initiate differentiation (Day 0). On day 2 of differentiation, cells were incubated with medium containing factors Wnt-C59 (S7037, Selleck Chemicals) and BMP4 (SRP3016, Sigma) for an additional 48 hours. Cells were then maintained in previously reported CDM3 medium[4] until day 17. On day 17, cardiomyocytes were lifted to obtain a single cell suspension using both Dispase (07923, Stem Cell Technologies) and TrypLE Express Enzyme. Cells were then reseeded for metabolic purification in CDM3L consisting of RPMI 1640 without glucose (11879020, ThermoFisher) supplemented with 213 μg/mL L-Ascorbic acid 2-phosphate sesquimagnesium salt hydrate >95% (A8960, Sigma), 500 μg/mL human albumin (A9731, Sigma), and 7.1 mM sodium-lactate (L4263, Sigma), and 2% Knockout Serum Replacement on Matrigel (47743-722, VWR)-coated 6 well plates. Cells were maintained in CDM3L for several days before replacing back to CDM3 medium. Cardiomyocytes were then used for either 2D or 3D experiments.

4.2.3. Sanger Sequencing

To investigate the effect of the splice site variant c.273+5G>A in DSP on RNA levels, equal amount of RNA was synthesized to first-strand cDNA using the RevertAid H Minus First Strand cDNA synthesis kit (Thermo Fisher Scientific, Rockford, IL). Total RNA was isolated from samples of cardiomyocytes and fibroblasts of the DSPmut patient and a control. Reverse transcription qPCR was performed using gene-specific primers designed to amplify the exon expected to be affected by the mutation and flanking sequence. The resulting PCR products were examined by 2% agarose gel electrophoresis and subsequently subjected to Sanger sequencing. For sequencing, amplified PCR products were purified using EXOSAP IT (GE Healthcare) and sequenced using BigDye V3.1 Terminator chemistry (Applied Biosystems, UK). Reaction

products were run on the ABI3730XL Genetic Analyzer (Applied Biosystems, UK). Sequences were evaluated using Mutation Surveyor (SoftGenetics LCC).

4.2.4. Effect of DSP mutation c.6687delA on Protein Expression

To investigate the effect of *DSP* mutation c.6687delA on protein expression, nonsense mediated decay inhibition was performed on cardiomyocytes using 50 μM NMDi14 for 6 hours based on previously described methods[33].

4.2.5. Analysis of Membrane Potential in 2D culture

The membrane potential of cardiac monolayers were analyzed using FluoVolt™ (Invitrogen, F10488) according to the manufacturer's instructions. Monolayers were incubated and measured in RPMI medium (w/o phenol red) containing HEPES at 37°C. Monolayers were paced at 1Hz and videos were obtained with a DeltaVision Elite Olympus IX-71 microscope. Videos were processed with Fiji using the "time series analyzer V3" plugin. Signals were post processed to find the average maximum upstroke velocity (Vmax) and the duration of the action potential at 50% amplitude (APD50) and 90% amplitude (APD90).

4.2.6. Cyclic Stretch of 2D Monolayers

Cardiomyocytes were re-plated as monolayers on Bioflex® plates. Monolayers were subjected to cyclic stretch for 3 days using a FlexCell® system FX-4000™. Cardiomyocytes were then stretched in 2D for 22 hours with 15% strain at 1 Hz to mimic heart muscle strain during normal activities and then for 2 hours with 15% strain at 3 Hz to mimic heart muscle strain during exercise.

4.2.7. Gel Electrophoresis and Western Blotting

Proteins from cells or tissues were extracted using a buffer containing 62 mM Tris-HCl, 2.5% SDS and 1 mM EDTA. Before extraction, protease inhibitor (Roche 11873580001), phosphatase inhibitor cocktail 3 (p2850; Sigma) and Sodium orthovanadate were added. After protein quantification (Pierce), sample buffer was added (final solution contains 10% glycerol, 5% β-Mercaptoethanol and bromophenol blue). Samples were heated to 99°C before loading. Proteins were separated using SDS-PAGE gels and transferred to PVDF membranes using semi-dry or tank blotting. Membranes were blocked using 5% milk and incubated on a shaker overnight at 4°C with primary antibody (Supplemental Table 1) and for 1 hour on a shaker at room temperature with secondary HRP-labeled antibodies. GAPDH or vinculin was used as a loading control depending on the protein's molecular weight. For detection, electrochemiluminescence was used. ImageJ gel analyzer was used to assess protein quantification.

4.2.8. Fabrication Cardiac Tissues Around PDMS Strips

To fabricate engineered heart muscle tissues around strips, first PDMS wells were created. Molds were designed in Solidworks and printed using either Verowhite plus RGD835 using an Objet Connex350 (Stratasys) or Dental SG resin (RS-F2-DGOR-01, Formlabs) on a Form 2 SLA printer. Polydimethylsiloxane (PDMS) wells were created to cast the tissue around the strip using Sylgard 184 PDMS (Dow Corning) in a 10:1 base to curing agent ratio. Sylgard 184 was mixed prior to casting using a Thinky conditioning mixer (Phoenix Systems) for 2 minutes at 2000 RPM each for mixing and defoaming. Molds were degassed for 30 minutes under vacuum to remove bubbles, cured at 65 ℃ for 4 hours, and then the PDMS wells were removed from the molds.

Subsequently, PDMS-strips were laser-cut from PDMS sheets (Bioplexus, Inc), either ~130 μm (SH-20001-005) or ~260 μm (CUST-20001-010) thick, using a ProtoLaser U3 (LPK5) laser cutter. Because the bending resistance of the strip is proportional to the thickness-cubed, a profilometer was used to measure the thickness of each strip (VHX-5000).

Prior to cardiac tissue fabrication, wells were sterilized via sonication in 50% v/v ethanol for 30 minutes and PDMS strips were sterilized with UV-Ozone treatment for 15 minutes. Sterile PDMS wells were fixed to one well of a 6 well culture plate using a thin layer of vacuum grease. PDMS wells were then incubated with 1% w/v Pluronic F-127 (P2443, Sigma) for 10 minutes to reduce collagen attachment to the well and washed three times in 1X PBS. Sterile PDMS strips were then placed in the slits in the bottom of the well to secure the strip during cardiac tissue casting. Collagen I derived from rat tail (354249, Corning) and Matrigel (354263, Corning) were used to fabricate 3D cardiac tissues around the PDMS strips. The final concentrations were 1 mg/mL Collagen I, 1.7 mg/mL Matrigel, 10% 10X PBS, 2.3% 1N NaOH, 18.75×10^6 total cells/mL consisting of 90% cardiomyocytes and 10% cardiac fibroblasts. Ingredients were mixed with a pipette and then 80 μL of the cell mixture was pipetted into each well around the PDMS strip. 6-well plates containing the molds and cell suspension were then placed at 37℃ to allow for gelation. Following a 45-minute incubation period, cardiac tissues were incubated and maintained in heart muscle tissue media containing RPMI-1640 supplemented with 1% v/v KnockOut™ Serum Replacement (10828010, Thermofisher) and 1:1000 MycoZap Plus CL (Lonza, VZA 2012).

4.2.9. Human Cardiac Ventricular Fibroblast Culture

Human Ventricular cardiac fibroblasts (NHCF-Vs) were obtained from Lonza and maintained in FGM-3 Medium as per manufacturer's instructions. Fibroblasts were used between

passages 5-10 for all studies described in this chapter.

4.2.10. Cardiac Tissue Loading

To mechanically load the tissues, strips of two different thicknesses (either ~130 μm or ~260 μm) were incorporated into the cardiac tissues during tissue formation, where the thicker strip represented an approximate 8x increase in load being applied to the tissue. On day 14, tissues were randomized to either constrained or dynamic mechanical loading from day 14 to day 28. In the constrained condition, the strip was held immobilized within the well throughout the entire culture period. In contrast, the dynamic condition allowed for the tissue to beat in an unconstrained manner against the PDMS strip. For dynamic loading, a PDMS block with a vertical cut was adhered to a new well with vacuum grease and one end of the strip was fixed into the vertical cut in the PDMS block. Tissues were maintained in heart muscle tissue media in either constrained or dynamic culture until day 28.

4.2.11. Tissue Contractility Assay and Measurements

During engineered heart muscle tissue contraction, the tissue decreases in length, resulting in PDMS strip bending. Based on known dimensions and elastic modulus of the PDMS strip, the degree of strip bending can be used to determine the force the tissue is exerting during contraction. Twitch stress measurements were found by dividing average twitch force by average cross-sectional area of cardiomyocytes within the tissue. To image PDMS strip bending due to cardiac tissue contraction, a PDMS block with a vertical cut was adhered to a petri dish using vacuum grease and one end of the strip was fixed into the vertical cut in the PDMS block. During the contractility assay, tissues were maintained in Tyrode's (T2145, Sigma) solution on a custom-heated stage at 37°C +/- 1°C. The PDMS strip was imaged with a Nikon DSLR camera mounted

on a Nikon SMZ1500 stereomicroscope to visualize strip bending. A custom-made MATLAB program was created to automatically calculate the change in length of the tissue from contraction videos. Look-up tables relating tissue length to force required to induce PDMS strip bending were created using a finite element modeling. Look-up tables were derived from finite element modeling of strip bending performed in ANSYS software. Modeling was performed by applying known displacements to the PDMS strip and then obtaining the reaction force associated with these displacements. The PDMS strip was modeled as a 3D deformable, extruded solid with two different thicknesses. The strip was considered linearly elastic, isotropic, and incompressible with a Young's modulus of 1.59 MPa for ~130 μm strips and 1.89 MPa for ~260 μm strips, respectively. Elastic moduli were derived from tensile testing of laser-cut, dogbones derived from each respective material. Briefly, dogbones mounted on an Instron 5943 and stretched at a rate of 1 millimeter/minute. The average cross-sectional area of the inserts was manually determined prior to testing and dogbone thickness was determined with profilometer (VHX-1000) measurements. Stress was calculated by dividing the force by the cross-sectional area of the dogbone. Stress was then plotted against the strain and slopes of the individual curves in the linear region of the stress-strain graph (0-10%) and were averaged to obtain the elastic modulus of the PDMS.

4.2.12. Analysis of Twitch Kinetics

Twitch kinetics of 3D EHTs were analyzed using a custom MATLAB program. Tissue contractile videos were used to obtain waveforms of tissue change in length over time. These waveforms were post processed to find the average twitch duration, time to 50% contraction (t50), time to 90% contraction (t90), and tau (the time constant of cardiac muscle relaxation). To find the contractile and relaxation velocity, tissue displacement during contraction or relaxation was

divided by either the contraction or relaxation time. Contractile Work was found by multiplying the average force by contractile shortening. Contractile Power was found by dividing the contractile work by the contractile time.

4.2.13. Immunofluorescent Staining

For whole mount imaging, cardiac tissues were fixed in 4% paraformaldehyde (15710, Electron Microscope Sciences) and permeabilized with 1:200 Triton-X 100 (9002-93-1, Sigma) for one hour at room temperature. Tissues were washed three times in 1X PBS for 30 minutes each on a rotary shaker and blocked overnight in 5% v/v Goat Serum (16210072, Thermofisher) in 1X PBS. Subsequently, tissues were then washed three times in 1X PBS for 30 minutes each on a rotary shaker and incubated with anti-sarcomeric alpha actinin (A7811, Sigma-Aldrich) primary antibody (1:100) in 1X PBS overnight. The following day tissues were washed 3X in 1X PBS for 30 minutes each and then incubated overnight with 1:100 goat anti-mouse 555 secondary antibody, 3:200 Alexa-fluor 488 conjugated phalloidin (A12379, Invitrogen), and 1:100 4′,6-diamidino-2-phenylindole (DAPI) for cell nuclei. The next day tissues were washed with 1X PBS 3X for 30 minutes each and stored protected from light at 4°C prior to imaging.

2D cultured cells were fixed and permeabilized with ice cold methanol:acetone for 10 min. Sectioned tissues were cut with a cryostat and air dried before staining. Tissues/cells were incubated with bovine serum albumin (BSA) and PBS blocking buffer. Tissues/cells were then incubated with primary antibodies in blocking buffer accordingly. Following primary antibody incubation, tissues were washed with 1X PBS. Alexa-fluor labeled 488 or 555 antibodies were used as secondary antibodies in blocking buffer, and tissues/cells were incubated accordingly with either Hoechst or DAPI for nuclei labeling. Tissues were then washed 1X PBS and mounted.

4.2.14. Electron Microscopy

Cells/tissues were fixed with 2% glutaraldehyde and 2% formaldehyde mixture in 0.1M sodium cacodylate at 4°C. Cells/tissues were then post-fixed in 1% osmium tetroxide and 1.5% potassium ferrocyanide (2 hours at 4°C) and then were dehydrated using ethanol and embedded in EPON epoxy resin. 60 nm sections were cut transverse in cell direction and contrasted using 5% uranyl acetate in water for 20min followed by Reynolds lead citrate for 2min. Whole nanotomy scans were made of tissues [51].

4.2.15. RT-PCR

Total RNA was isolated using TRIzol (Sigma). Complementary DNA (cDNA) was synthesized by reverse transcription and real-time PCRs were performed using primers (Supplemental Table 2) to reveal expression of mRNA transcripts. Relative expression levels were calculated using the ddCt method.

4.2.16. Inter-desmosomal Space Estimation

Images of desmosomes in 2D cultured cells and cell-cell borders were taken with a CM100 TEM microscope at a 46.000x magnification. ImageJ was used to make intensity plots of up to 50 desmosomes per condition. To determine the inter-desmosomal space, the length between the two highest intensity peaks (located approximately within both membranes/outer dense plaques) was measured.

4.2.17. Statistical Analysis

Data are represented as mean ± standard deviation. Statistical analysis was performed in GraphPad Prism. Outliers were defined using the ROUT method (Q=1). Statistical significance was considered a p-value less than 0.05.

4.3. Results

4.3.1. Reduced Desmosomal Protein Staining Observed in Heart Tissue of ACM Patient

A key advantage of engineered heart tissue is the potential to study human disease states in an in vitro system using patient-specific hiPSC-derived cardiomyocytes. As proof-of-concept, we chose to study ACM in a patient diagnosed with end-stage heart failure, that underwent a heart transplantation at the age of 45. The right ventricle of the explanted heart showed fat deposition and fibrosis, while the dilated left ventricle (LV) showed endocardial fibrosis (Figure 4.1A). Next generation sequencing with a targeted gene panel revealed two segregating mutations in *DSP* (Figure 4.1B), where mutation c.273+5G>A was located on one *DSP* allele and a c.6687delA on the other *DSP* allele.

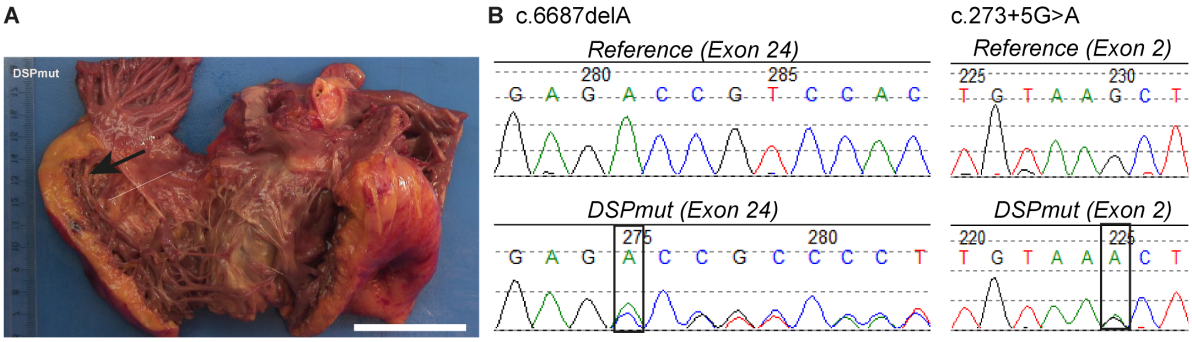

Fig. 4.1: Desmosomal Staining of DSPmut Patient Heart Tissue. (A) Explanted heart of the DSPmut patient, where the arrow points to fat deposition. Scale bar is 5 cm. **(B)** Sanger sequencing of both *DSP* alleles in DSPmut patient showing c.273+5G>A and c.6687delA mutations. Data obtained by M. Vermeer.

Immunofluorescent staining of the explanted patient heart also showed a severe reduction in desmoplakin and other components of the desmosome, including plakoglobin, desmocollin 2, and desmoglein 2 (Figure 4.2). Subjectively, plakophilin-2 and connexin 43 appeared to be more disorganized compared to control heart muscle tissue.

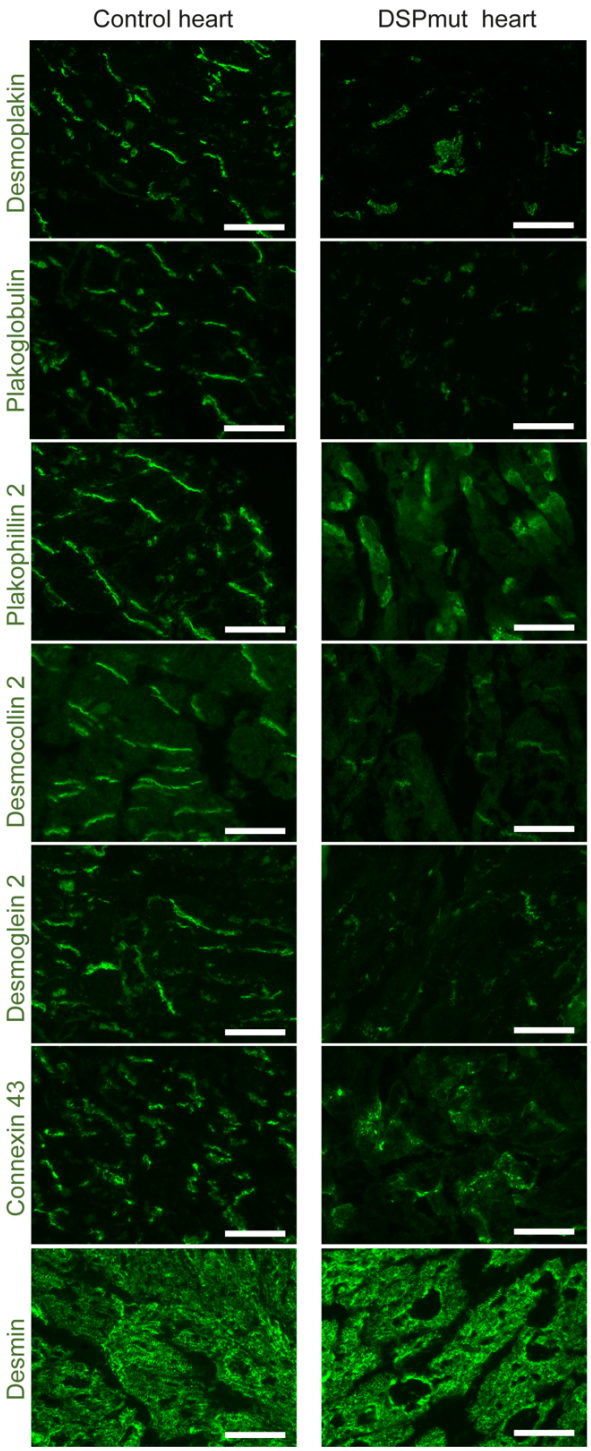

Fig. 4.2: Immunofluorescent staining of desmosomal proteins (desmoplakin, plakoglobin, plakophilin 2, desmoglein 2, and desmocollin 2), Cx 43, and desmin in heart of DSPmut patient in comparison to a control heart. Scale bars are 50 µm. Data obtained by M. Vermeer.

4.3.2. Control and DSPmut hiPSCs Express Pluripotency Markers and Differentiate Into Cardiomyocytes

To evaluate the functional effects of the described desmoplakin mutations on heart muscle, hiPSCs were created from control and DSPmut patients based on previously described protocols [39,53]. Karyotype analysis revealed normal chromosomal structure in control and DSPmut hiPSCs (Figure 4.3A). Further, hiPSCs expressed known pluripotency markers, including octamer binding transcription factor 3/4 (Oct3/4) and

stage-specific embryonic antigen 4 (SSEA-4) suggesting successful reprogramming to a pluripotent state (Figure 4.3B). Control and DSPmut hiPSCs could also be successfully differentiated into cardiomyocytes based on the expression of Cardiac Troponin T (Figure 4.3C).

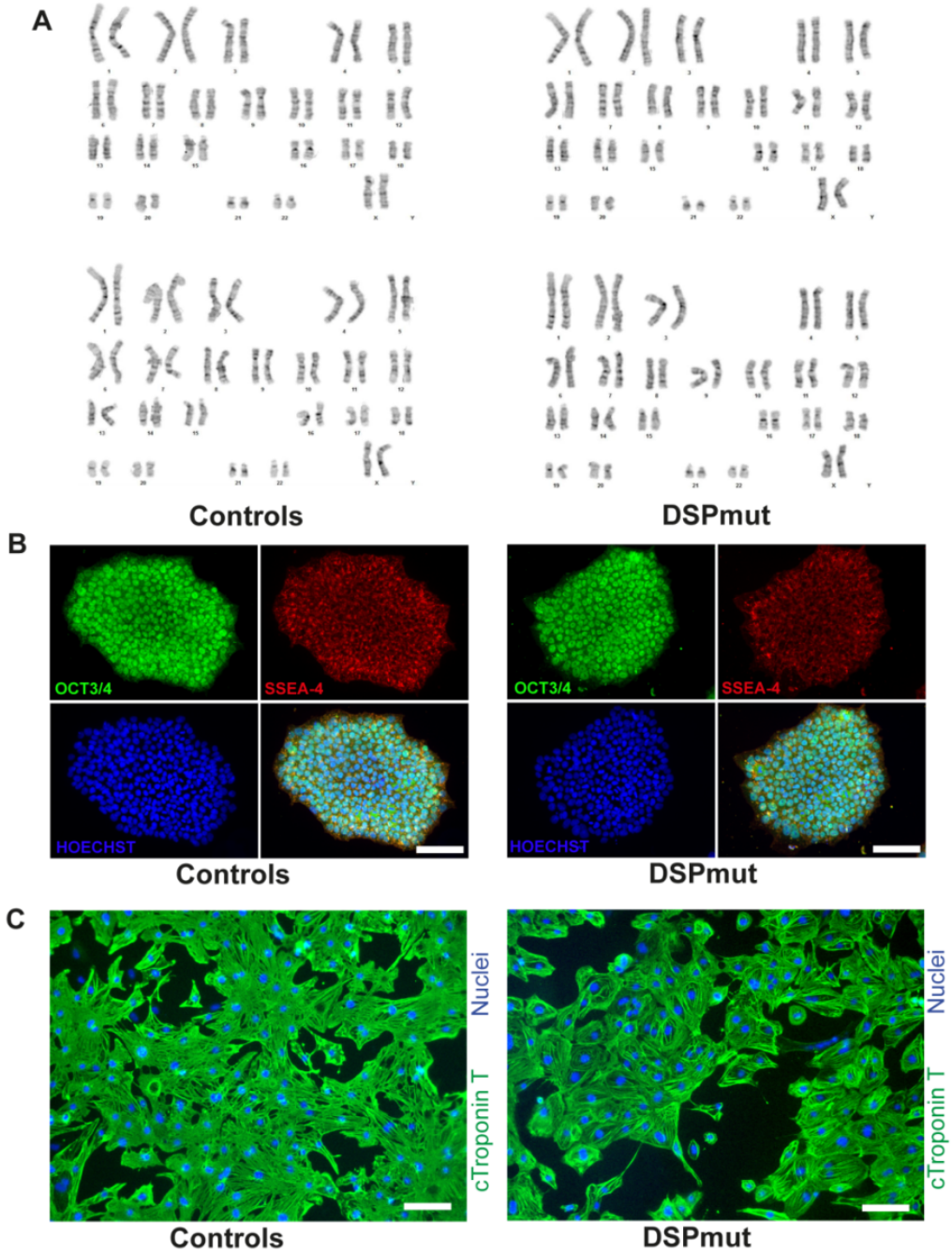

Fig. 4.3: Validation of hiPSC lines. (A) Karyotypes of Control and DSPmut hiPSCs. **(B)** Immunofluorescent staining for pluripotency markers OCT3/4 and SSEA-4 of hiPSC colonies after passage 10. Scale bars are 100 µm. **(C)** Immunofluorescent staining of Cardiac Troponin T on hiPSC differentiated cardiomyocytes. Scale bars are 50 µm. Data obtained by M. Vermeer.

4.3.3. Reduced Desmoplakin and Desmocollin in DSPmut Cardiomyocytes in 2D culture

After deriving hiPSCs and inducing the differentiation of cardiomyocytes from the DSPmut patient, the expression of the mutated DSP protein transcripts in cultured cardiomyocytes was quantified. The *DSP*:c.273+5G>A splice site mutation did not result in alternative mRNA splicing leading to a protein similarly sized as wild type DSP. Nonetheless, protein transcripts from this allele were barely visible on western blot. Mutation *DSP*:c.6687delA, located on the last exon, predicted a frame-shift resulting in a premature stop-codon p.(Arg2229Serfs*32). However, the truncated protein originating from this *DSP* allele was only detected after inhibition of nonsense mediated mRNA decay p.(Arg2229Serfs*32). This indicates that the truncated protein is not normally expressed, and that nonsense mediated decay is responsible for the breakdown of the desmoplakin product p.(Arg2229Serfs*32) originating from the DSP allele with the c.6687delA mutation (Figure 4.4A). DSPmut hiPSC-derived cardiomyocytes displayed reduced desmoplakin immunofluorescent signal compared to control (Figure 4.3B). Total desmoplakin protein and gene levels were 3-fold reduced in DSPmut cardiomyocytes compared to control (Figure 4.4C-D). Among other desmosomal components, levels of desmocollin 2 (DSC2), one of the transmembrane components of the desmosome, were 2-fold reduced (Figure 4.4C). The severe reduction in desmoplakin hence represents the pathology of a predominant group of patients with loss-of-function mutations in *DSP*, leading to DSP deficiency[34].

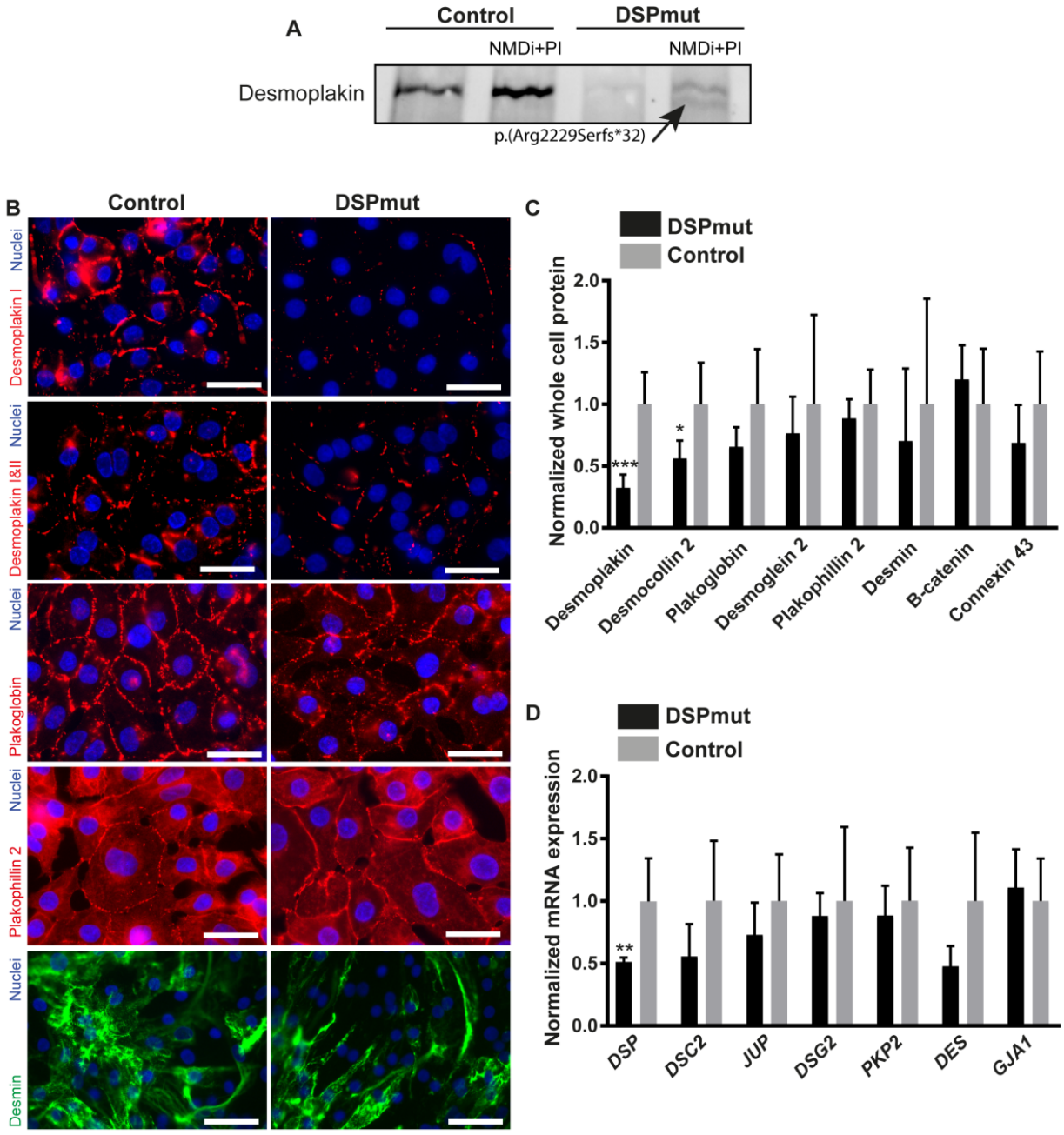

Fig. 4.4: Desmosomal protein and gene expression in 2D culture. (A) Western blot of desmoplakin expression in control and DSPmut cells under nonsense mediated decay inhibitor (NMDi) and proteasome inhibitor (PI, bortezomib). **(B)** Immunofluorescent staining of desmosomal proteins and desmin in control and DSPmut cardiomyocytes cultured in 2D. Scale bars are 50 µm. **(C)** Expression of desmosomal proteins, beta-catenin and Cx43 measured in control and DSPmut cardiomyocytes determined by western blot. n=6 vs. 4 differentiations (patient vs. control); * $p<0.05$ (unpaired two-sided t-test compared to control);*** $p<0.05$ (unpaired two-sided t-test compared to control). **(D)** mRNA expression levels of desmosomal genes. n=5 differentiations; ** $p<0.05$ (unpaired two-sided t-test compared to control). All data represented as mean ± SD. Data obtained by M. Vermeer.

4.3.4. Few differences Observed in DSPmut Cardiomyocytes with 2D Stretch

To understand the functional impact of the desmoplakin mutations, the electrophysiology of static 2D cultured DSPmut and control cardiomyocytes were investigated. DSPmut monolayers showed comparable maximum upstroke velocities (dV/dT) compared to control monolayers (Figure 4.5A). DSPmut monolayers also showed slightly elevated action potential durations (APD50 or 90) compared to controls but this was not statistically significant (Figure 4.5B-C). Together these findings suggest comparable membrane potential kinetics between DSPmut and control monolayers in the 2D settings, which is surprising given the dramatic 3-fold reduction in desmoplakin protein levels (Figure 4.5C).

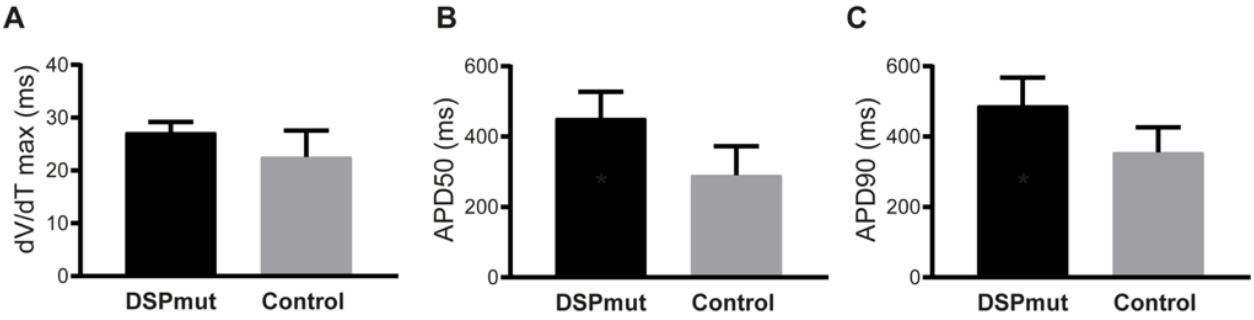

Fig. 4.5: Membrane potential of DSPmut and Control Cardiomyocyte Monolayers with 1 Hz stimulation. (A) Maximum upstroke velocity in DSPmut compared to control cardiomyocytes monolayers. **(B)** Action potential duration (APD) at 50%. **(C)** APD at 90%. Measurements of individual ROIs (cellular patches) within each monolayer. All graphs show n=4 differentiations for both DSPmut and control, each derived from the 2 different hiPSC clonal lines included in this study. *p<0.05 (Mann-Whitney U-test). All data represented as mean ± SD. Data obtained by M. Vermeer.

Given the limited electrophysiological differences observed in static 2D culture of DSPmut cardiomyocytes combined with the clinical observation that ACM can be exacerbated with increased mechanical loading on heart muscle, the possibility that mechanical stretch during 2D culture might provoke a disease phenotype was investigated. To do this, DSPmut and control

monolayers were mechanically stretched using 2D FLEXCELL monolayer culture for 3 days.

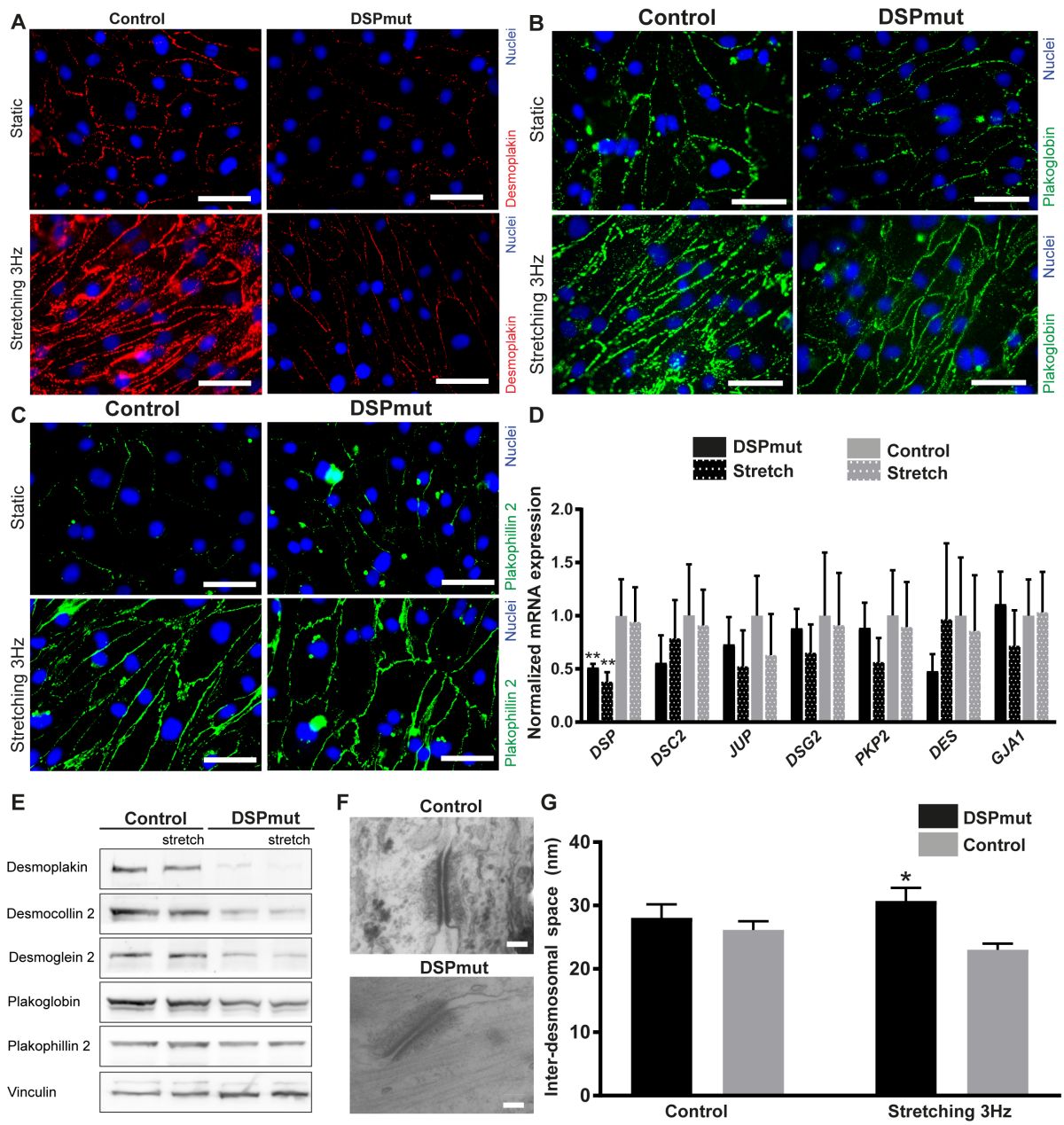

Fig. 4.6: Desmosomal Expression with 2D Stretch. (A-C) Immunofluorescent staining of desmoplakin, plakoglobin and plakophillin-2 in cardiomyocytes at baseline and after 3Hz stretch. Scale bars are 50 µm. **(D)** mRNA expression levels of desmosomal genes at baseline and after 3Hz stretch. ** $p<0.05$ (two-way ANOVA, post hoc Bonferroni's multiple comparisons test). **(E)** Protein expression levels of desmosomal genes at baseline and after 3Hz stretch. **(F)** Representative TEM images of desmosomes in control and DSPmut cardiomyocytes. Scale bars are 50 nm. **(G)** Inter-desmosomal space was measured based on 50 desmosomes in each group at baseline and after 3Hz stretch. * $p<0.05$ (two-way ANOVA, post hoc Bonferroni's multiple comparisons test). n=5 differentiations were used for both control and DSPmut in stretching experiments. All data represented as mean ± SD. Data obtained by M. Vermeer.

To mimic normal activity cardiomyocytes were exposed to 15% strain at 1 Hz for 22 hours. To mimic daily exercise cardiomyocytes were exposed to 15% strain at 3 Hz for 2 hours. The total duration of stretching was 3 days. Upon application of mechanical stretch, controls demonstrated a significant increase in localization of desmosomal components to the cell periphery, including desmoplakin, plakoglobin and plakophillin-2 (Figure 4.6 A-C). In contrast, DSPmut cardiomyocytes did not appear to significantly increase their desmoplakin localization to cell borders upon application of 2D stretch (Figure 4.6A). However, this lack of a response to stretch appeared to be specific to desmoplakin since other desmosomal components (plakoglobin and plakophillin-2) localized to the cell borders following application of 2D stretch in DSPmut cardiomyocytes (Figure 4.6B-C).

Despite these significant differences in desmosomal protein localization observed between DSPmut and control monolayers, whole cell protein levels and mRNA levels were not increased by mechanical stretch applied in a 2D setting (Figure 4.6D-E). This is in stark contrast to the findings observed in Chapter 3, where we found that there was an upregulation of desmosomal genes with 8x dyn-EHT culture (Figure 3.10D). This finding suggests that the desmosomes may contribute less to handling mechanical stretch in a 2D setting and that other junctions, including adherens junctions or even integrins attached to the 2D surface, may also be contributing to the distribution of mechanical load throughout the cell. However, further research would be required to support this observation.

Previous animal research has shown a reduction in desmosome counts following endurance exercise in animals with desmosomal genetic defects[32]. Therefore, desmosomal ultrastructure was examined following 2D stretch. Although a minor increase in the inter-desmosomal space was found (Figure 4.6F-G), no changes in the number and protein density of desmosomes were

observed after 2D stretch. Combined with previous gene and protein expression findings, this further suggests that desmosomes may contribute less to the handling of mechanical stress in a 2D setting.

4.3.5. 8x dyn-EHT reveals a disease phenotype based on a patient-derived model of arrhythmogenic cardiomyopathy

Following investigation of DSPmut and control cells with 2D culture, the next experiments were designed to investigate possible differences in how DSPmut and control EHTs respond to mechanical loading in 3D culture using the dyn-EHT system described in Chapter 3. Control iPS derived EHTs demonstrated similar responses to the loading conditions observed in control ESC-derived EHTs with 8x dyn-EHTs lengthening significantly (Figure 4.7A). Despite the significant increase in tissue length being observed in control 8x dyn-EHTs, measurements over time in culture indicate that tissue length stabilized in control 8x dyn-EHTs one week after removal from the PDMS well (Supplemental Figure 1). This suggests that control tissues remodel in response to the elevated diastolic stress imposed by the 8x strip, and also that their length stabilizes during dynamic culture. DSPmut tissues also displayed similar responses to the varied loading regimes with respect to tissue length, including a decrease in tissue length with 1x dynamic loading and a similar increase in length in 8x constrained EHTs after removal from the PDMS well. In contrast, DSPmut 8x dyn-EHTs demonstrated excessive remodeling with tissues lengthening significantly more than controls (Figure 4.7A).

Immunofluorescence of DSPmut EHTs showed an expected reduction in desmoplakin protein compared to control EHTs (Figure 4.7B-C). Transmission electron microscopy (TEM) indicated less protein dense desmosomes **(**Figure 4.7D-E**)** and reduced number of desmosomes in

DSPmut 8x dyn-EHTs compared to control 8x dyn-EHTs (Supplemental Figure 2).

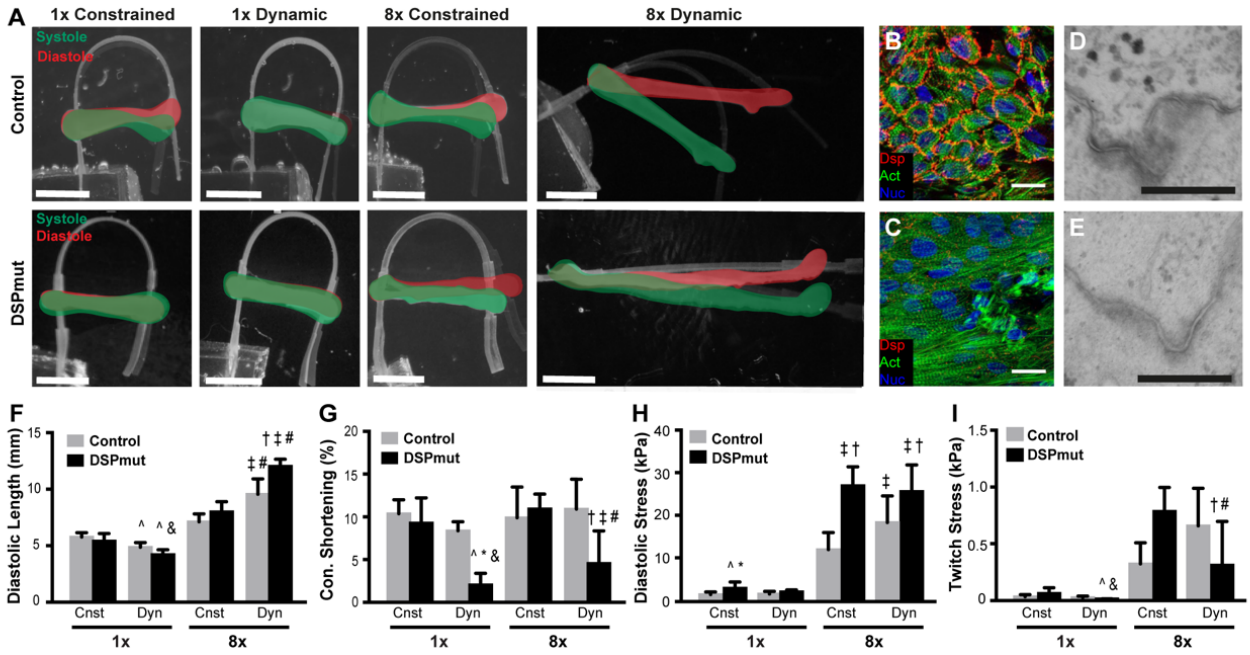

Fig 4.7: The 8x dyn-EHT model progresses DSPmut Tissues into Disease. (A) Macroscopic tissue contraction of control and *DSP*mut tissues exposed to each loading amount (1x and 8x) and condition taken at day 28. Pictures are an overlay of tissues in systole (green) and diastole (red). Scale bars are 2.5 mm. **(B-C)** Desmoplakin staining of control **(B)** and **(C)** DSPmut 8x dyn-EHTs. Scale bars are 20 µm. **(D-E)** TEM images of desmosomes of **(D)** control and **(E)** DSPmut 8x dyn-EHTs. Scale bars are 300 nm. **(F)** Diastolic tissue length in control and DSPmut tissues under each loading condition. **(G)** Contractile shortening in control and DSPmut tissues under all loading conditions. **(H)** Diastolic stress in control and DSPmut tissues under all loading conditions. **(I)** Cardiomyocyte tissue twitch stresses (kPa) in control and DSPmut tissues under all loading conditions. Two-way ANOVA with a post hoc Holm Sidak test was performed within each loading amount (either 1x or 8x). ‡ indicates $p<0.05$ compared to control 8x constrained. † indicates $p<0.05$ compared to control 8x dynamic. # indicates $p<0.05$ compared to DSPmut 8x constrained. ^ indicates $p<0.05$ compared to control 1x constrained. & indicates $p<0.05$ compared to DSPmut 1x constrained. * indicates $p<0.05$ control 1x dynamic. All graphs show n=8 (DSPmut 1x constrained), n=6 (DSPmut 1x dynamic), n=6 (DSPmut 8x constrained), n=16 (DSPmut 8x dynamic), n=8 (control 1x constrained), n=7 (control 1x dynamic), n=11 (control 8x constrained), n=12 (control 8x dynamic). 10 CM differentiation batches were used for DSPmut tissues and 4 batches were used for the control tissues. A larger number of DSPmut batches were included due to the high rate of breakage observed in 8x dyn-EHT DSPmut tissues. Cardiomyocyte cross-sectional area used for tissue stress measurements are displayed in Supplemental Figure 4. All data represented as mean ± SD. Figure and data prepared by Jacqueline Bliley and Mathilde Vermeer.

These results establish a clear impairment in the desmosomal ultrastructure between control and DSPmut cardiomyocytes. This is likely the reason why ~50% of the DSPmut 8x dyn-EHTs broke within 48 hours of removal from the PDMS well. The remaining intact DSPmut 8x dyn-EHTs

lengthened significantly more than Control 8x dyn-EHTs (Figure 4.7F). Contractile shortening was also significantly impacted by loading conditions, where the DSPmut 1x and 8x dyn-EHTs showed a significant decrease from ~10% to <5% (Figure 4.7G). Diastolic stresses also tended to be significantly higher in DSPmut 8x EHTs and 8x dyn-EHTs compared to controls suggesting that this may be the force causing the tissue lengthening and remodeling as observed (Figure 4.7H).

However, there was a major difference in the twitch stress in DSPmut 8x EHTs and DSPmut 8x dyn-EHTs (Figure 4.7I). DSPmut 8x EHTs showed a large increase in twitch stress compared to the control EHTs, suggesting that the increased diastolic stress may initially lead to elevated contractile stresses (afterload). In contrast, DSPmut 8x dyn-EHTs demonstrated a significant decrease in contractile force (Supplemental Figure S3) and twitch stress (Figure 4.7I) compared to control EHTs, as the contractile shortening was also evidentially impaired.

Differences in contraction kinetics, work and power, were also observed between control and DSPmut tissues with respect to loading condition under both spontaneous (Figure 4.8) and electrically stimulated conditions (Figure 4.9). Similar to the previous results in ESC-derived EHTs, iPSC derived control EHTs displayed similar beat frequencies under all loading conditions (Figure 4.8A). However, the DSPmut 8x EHTs and 8x dyn-EHTs had faster spontaneous beat rates (Figure 4.8A), suggesting that the increased diastolic stress from the 8x PDMS strips combined with the genetic mutation may be the cause. The DSPmut 8x dyn-EHTs also had shorter contraction and relaxation times (Figure 4.8, C-E) compared to controls, though this was due to reduced contractile shortening as contraction and relaxation velocities were similar to controls (Figure 4.8, F-G). Interestingly, DSPmut 1x dyn-EHTs displayed highly variable and increased contraction and relaxation times resulting in markedly decreased contraction and relaxation velocities compared to controls (Figure 4.8, F-G). It is possible that the disorganized sarcomere

structure observed in 1x dyn-EHTs (Chapter 3) combined with the genetic mutations in desmoplakin yields tissues with impaired contractile behavior, which then becomes magnified in the context of a more disorganized tissue.

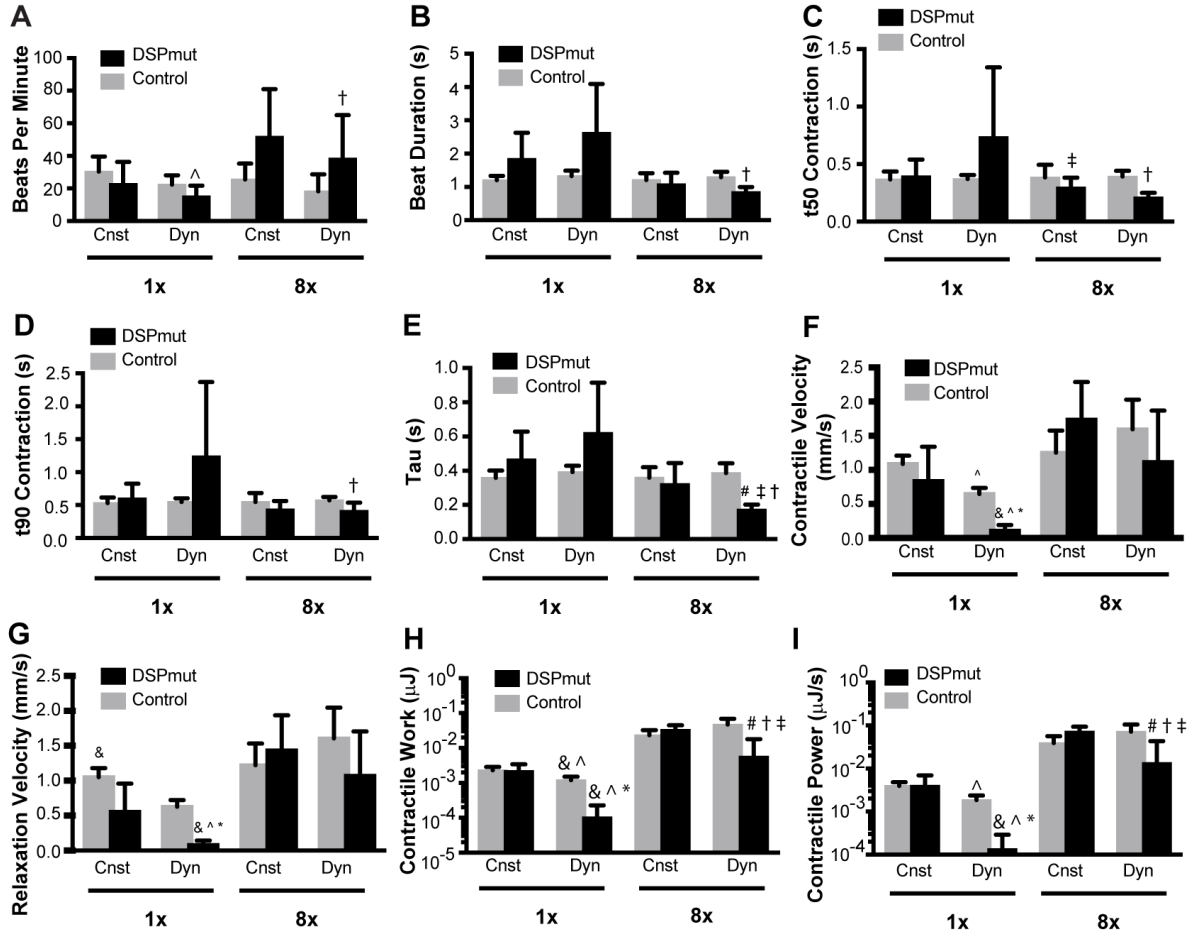

Fig 4.8: Spontaneous Twitch Kinetic Comparison DSPmut and Control. (A) Beats per minute under each loading condition. **(B)** Total beat (twitch) duration (seconds) under each loading condition. **(C)** Time to 50% contraction (t50) within each loading condition. **(D)** Time to 90% contraction (t90) under each loading condition. **(E)** Time constant (seconds) of contractile transient decay (Tau) within each loading condition. **(F)** Contractile velocity (mm/s) under each loading condition. **(G)** Relaxation Velocity (mm/s) under each loading condition. **(H)** Contractile work, measured in microjoules, under each loading condition. **(I)** Contractile Power, measured in microjoules per second, within each loading condition. Two-way ANOVA with a post hoc Holm Sidak test was performed within each loading condition (either 1x or 8x). All graphs show n=7 (DSPmut 1x constrained), n=7 (DSPmut 1x dynamic), n=6 (DSPmut 8x constrained), n=10 (DSPmut 8x dynamic), n=7 (control 1x constrained), n=6 (control 1x dynamic), n=6 (control 8x constrained), n=5 (control 8x dynamic). ‡ indicates $p<0.05$ compared to control 8x constrained. † indicates $p<0.05$ compared to control 8x dynamic. # indicates $p<0.05$ compared to DSPmut 8x constrained. ^ indicates $p<0.05$ compared to control 1x constrained. & indicates $p<0.05$ compared to DSPmut 1x constrained. * indicates $p<0.05$ control 1x dynamic. All data represented as mean ± SD. Figure and data prepared by Jacqueline Bliley.

However, future work is required to confirm this observation. Importantly, both DSPmut 8x and 1x dyn-EHTs displayed a decrease in contractile work and power generation compared to constrained and control tissues (Figure 4.8H-I), which further supports the role of dynamic culture in revealing a disease phenotype. Results were similar with 1 Hz electrical stimulation, but in this case DSPmut tissues had faster contraction and relaxation times (Figure 4.9A-B) than controls, which led to elevated contractile and relaxation velocities (Figure 4.9C-D), though not statistically different.

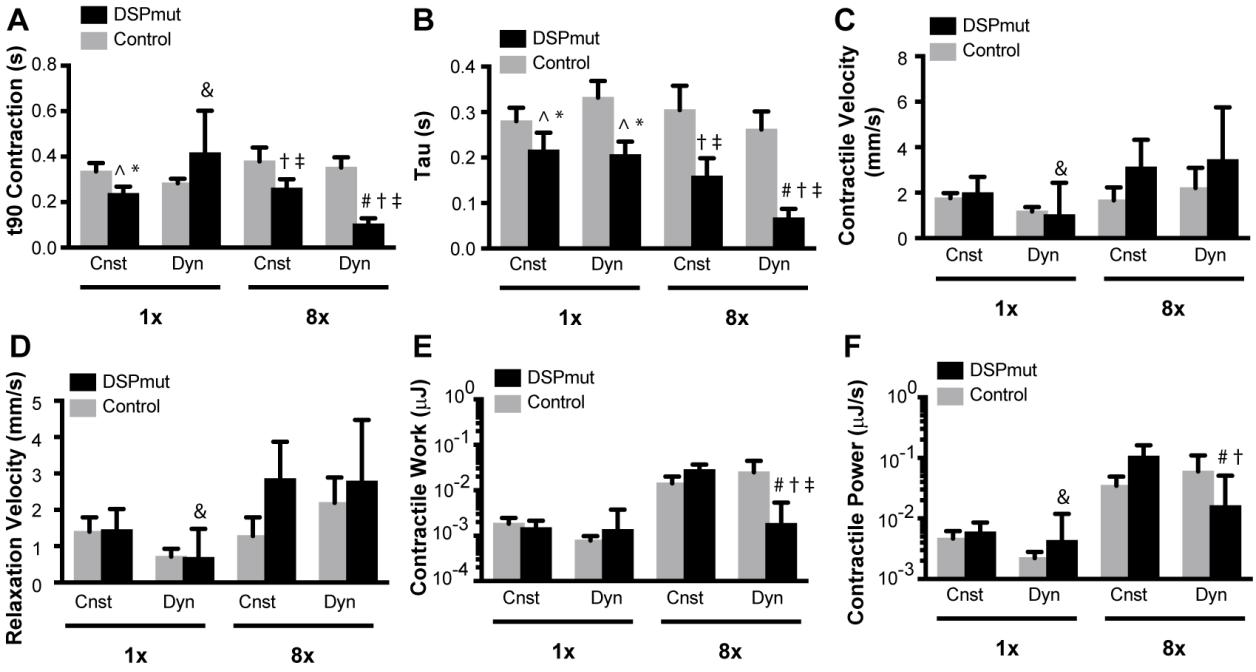

Fig 4.9: Twitch Kinetics in DSPmut and Control Tissues with 1 Hz Stimulation. (A) Time to 90% contraction (t90) under each loading condition. **(B)** Time constant (seconds) of contractile transient decay (Tau) within each loading condition. **(C)** Contractile velocity (mm/s) under each loading condition. (D) Relaxation Velocity (mm/s) under each loading condition. **(E)** Contractile work, measured in microjoules, under each loading condition. **(F)** Contractile Power, measured in microjoules per second, within each loading condition. Two-way ANOVA with a post hoc Holm Sidak test was performed within each loading condition (either 1x or 8x). All graphs show n=7 (DSPmut 1x constrained), n=7 (DSPmut 1x dynamic), n=6 (DSPmut 8x constrained), n=10 (DSPmut 8x dynamic), n=7 (control 1x constrained), n=6 (control 1x dynamic), n=6 (control 8x constrained), n=5 (control 8x dynamic). ‡ indicates $p<0.05$ compared to control 8x constrained. † indicates $p<0.05$ compared to control 8x dynamic. # indicates $p<0.05$ compared to DSPmut 8x constrained. ^ indicates $p<0.05$ compared to control 1x constrained. & indicates $p<0.05$ compared to DSPmut 1x constrained. * indicates $p<0.05$ control 1x dynamic. All data represented as mean ± SD. Figure and data prepared by Jacqueline Bliley.

As with spontaneous and paced studies, DSPmut 8x dyn-EHTs had lower contractile work and power compared to controls (Figure 4.9E-F). These findings further highlight the impaired function of DSPmut 8x dyn-EHTs and that the dynamic loading uniquely drives this disease-like phenotype strongly suggesting that simulating both preload and afterload are required to model certain primary endpoints of cardiac disease in ACM.

4.4. Discussion

In this chapter, the dyn-EHT platform explored how varying the amount of load and constraining the tissue influences disease progression in an *in vitro* model of ACM. These results demonstrate that the dyn-EHT system is important for revealing an ACM disease phenotype in patient-derived EHTs with mutations in desmoplakin. In 2D culture, DSPmut cardiomyocytes displayed similar desmosome ultrastructure and protein density compared to controls (Figure 4.6) despite a 65% reduction in desmoplakin and a 50% reduction in desmocollin-2 (Figure 4.4C). Investigating the consequence of these differences in a 2D model of stretch (2D FLEXCELL monolayer culture), there was only a minor increase in the inter-desmosomal space in the DSPmut setting (Figure 4.6F-G). This suggests that cardiomyocyte monolayers may inadequately represent ACM progression due to being constrained to a 2D surface, which may then contribute to increased stability to the desmosomes through support by other junctions, such as adherens junctions, or even integrins attached to the 2D surface. These 2D findings starkly contrast with previous animal studies demonstrating that the desmosomal mutations result in loss of desmosomal contacts between adjacent cardiomyocytes following endurance exercise [32]. With 3D 8x constrained EHT culture, DSPmut tissues displayed elevated contractile stress values and similar levels of

contractile shortening to control 8x constrained EHTs following removal from their constrained condition. However, with extended 8x dyn-EHT culture deterioration of DSPmut function with tissue elongation and reduction in contractile stress was observed. This finding mimics the hallmarks of disease in human patients, such as ventricular dilation and reduced ejection fraction. These data are supported by the deterioration of the desmosomes, as ultrastructural findings showed a reduction in the amount and protein density of desmosomes. This resulted in loss of cell-cell contact, which directly resulted in tissue elongation (dilation) and the amount of contractile force that can be generated by the tissue. Altogether, this data suggests that current constrained cultures are limited in their ability to model diseases like ACM and researchers should consider the suitability of their model in being able to assess primary endpoints of disease. This new model has direct implications for future ACM patient health where patient-specific dyn-EHTs could be used to evaluate response to loads that would provoke a disease phenotype. However, future research would be required to confirm this postulate. Further, in order to reach full understanding of specific disease mechanisms of ACM, more patients with different genetic backgrounds should be investigated using this platform.

Despite the standardized use of current ACM guidelines, the precise mechanism by which mechanical loading on heart muscle influences disease progression in ACM patients remains poorly understood. The patient investigated in this study suffered from end-stage heart failure, ultimately requiring transplantation. In this patient, the frame-shift mutation actually resulted in full loss of protein product, whereas the splice mutation caused partial loss of protein product. Together, this represented a 65% reduction of total desmoplakin protein and consequentially caused 50% reduction in desmocollin-2. This likely contributed to the reduced stability of the desmosomal ultrastructure observed in DSPmut 8x dyn-EHTs. Although observed in a single

ACM patient, the altered genetic background resulted in severe desmoplakin deficiency and may apply to a much larger group of patients with loss-of-function-causing *DSP* variants [5,57]. Such patients may demonstrate a severely dysmorphic cardiac phenotype, often manifesting in combination with skin abnormalities [34,38,45,55,59–61]. To gather a broader understanding of ACM pathophysiology, future studies using the dyn-EHT system will require addressing *DSP* mutations that cause functionally altered desmoplakin protein products, in addition to mutations in *PKP2, JUP, DSG2, DSC2* and other ACM causative genes.

While the linear structure and uniaxial stresses in the dyn-EHT are a simplification of the lamellar architecture and biaxial stresses in the ventricular wall of the heart, it appears that this platform is able to capture aspects of stress-induced remodeling that have been challenging to observe in other EHT models. In the case of the DSPmut EHT, the dynamic 8x loading resulted in thinning and lengthening of the tissue with increased diastolic stress and decreased twitch stress (Figure 4.7). This suggests a possible corollary between our work and previous in vivo findings where tissue remodeling (including chamber thinning and eccentric dilation) is accelerated with elevated ventricular wall stresses [3,56]. In fact, elevated ventricular wall stresses have been proposed to drive the infarct expansion seen post-myocardial infarction [37,47], as well as increase ventricular dilation in dilated cardiomyopathy patients [17,48]. Further, strategies aimed at reducing the ventricular wall stress by integrating a temporary patch over the myocardial infarct [10] or injecting materials to thicken the ventricle wall [35] have proved successful to combat the pathological remodeling observed following myocardial infarction. However, further studies are required to validate that the tissue remodeling observed in the 8x dyn-EHT is similar to post-infarct expansion and ventricular dilation observed in vivo. While there have been recent advances in engineering ventricle-like chambers using scaffolds and 3D bioprinting [22,25,26,29], compared to the dyn-EHT,

these chambers are much more difficult to fabricate, require a relatively large number of cells to form, and must be connected to a complicated flow system with valves and pressure transducers in order to generate preload.

Interestingly, the dyn-EHT model can also be used to investigate temporal changes in contractility, which is important in order to understand the rate of disease progression. For example, studies have reported an increase in heart muscle contractility with initial exposure to pathological wall stresses [8,46,49], which is likely due to hypertrophy or hypercontractility of heart muscle cells responding to an increase in stretch. Interestingly, a similar finding was observed with DSPmut 8x EHTs showing an increase in tissue twitch stress immediately after being removed from the PDMS well (Figure 4.7). Only with prolonged 8x dyn-EHT culture of 14 days was there an observable deterioration in DSPmut tissues, resulting in decreased contractile shortening, contractile force, and tissue twitch stress (Figure 4.7). While we did not study different time spans of dynamic culture, these pathologic functional changes are likely a direct consequence of the reduced cardiomyocyte coupling (number and density of desmosomes) observed via TEM imaging (Supplemental Figure S2). This also parallels heart failure, where remodeling of the ventricle occurs prior to decrements in function being observed [3,19].

The ability to mimic disease states using EHTs demonstrates the value of this technology for better understanding the link between genetics and function. Indeed, many studies have already investigated heart diseases based on patient-specific mutations, using either genome-edited or patient-derived hiPSCs. For example, Hinson and colleagues showed sarcomere abnormalities and impaired contractility in EHTs with titin truncating mutations (TTNtv), especially in response to an increased afterload, which was modulated by changing the stiffness of incorporated PDMS posts [18]. Wang et al showed reduced contractility in MTFs derived from patients with a genetic

defect in Tafazzin, the major phospholipid in the mitochondrial inner membrane [58]. Healy and colleagues used variable stiffness microfibers to modulate the afterload on genome edited tissues lacking cardiac myosin binding protein C and found impaired contraction only when tissues were cultured on stiffer fibers [28]. The dyn-EHT provides expanded capability by adding preload, which is of particular interest for modeling heart diseases that have a cardiomyocyte junctional or cytoskeletal component, which in fact accounts for a large number of inherited genetic cardiomyopathies [11,36,40,50]. This is further supported by the data within this paper showing that the distribution of mechanical load throughout the cell is different in a dynamic 3D environment when compared either 2D or 3D constrained models (Figure 4.6 and Figure 4.7). Importantly, 8x dyn-EHTs formed using control hESC derived cardiomyocytes resulted in upregulation of desmosomal genes, suggesting a significant contribution of desmosomes in the adaptive response to mechanical load (Chapter 3). In contrast, 8x dyn-EHTs formed using DSPmut cardiomyocytes resulted in tissue lengthening and reduced contractile stress generation. Furthermore, in DSPmut tissues we found reduced amount and expression of desmosomes compared to control, which has also been observed in patients and small animal studies with desmosomal defects [32]. Taken together, these findings suggest that 3D dynamic mechanical loading of EHTs may be better suited to investigate heart diseases with a cardiomyocyte junctional or cytoskeletal component.

As with any experimental system, there are important considerations to understand in regard to the dyn-EHT platform. In this study, a constant ratio of 10% cardiac fibroblasts was used to compare between DSPmut and control tissues. Though different fibroblast percentages were not directly tested in the dyn-EHT model, it is possible that using different concentrations of cardiac fibroblasts may impact the remodeling observed in the dyn-EHT system. It would be interesting to study if other factors known to influence diseased heart muscle function could be incorporated

into our dyn-EHT model. One such factor, fibrosis, which is an important secondary outcome due to injury and remodeling, can reduce compliance of the ventricle and decrease heart muscle contractile shortening [54] and should be considered as a target for future studies. Further, it would be interesting to see if the dyn-EHT could be used to model hypertrophic cardiomyopathies, where increased myocardial thickness and lower wall stress would be observed [62].

One major limitation of the DSPmut 8x dyn-EHT model is that no arrhythmia phenotype was observed, which commonly occurs during the course of ACM disease progression. Several potential explanations may be considered. First, the linear architecture of our tissues with highly aligned cells has essentially 1D conduction and thus limits our ability to detect arrhythmias. Findings both in vivo [41,43] and in vitro [7,21,44] support the concept that the absence of complex tissue architecture may make it difficult to detect arrhythmias. In fact, engineered tissues with more complex 3D architecture have been shown to reproduce arrhythmias [29], including previous work FRESH 3D bioprinting ventricle-like tissue constructs [26]. Second, arrhythmia in ACM occurs in the presence of abnormal collagen deposition and lipid droplets which form during disease progression and which have been suggested to impact tissue electrical conduction. Neither were observed in our DSPmut tissues, nor were there signs of excessive collagen deposits within the nanotomy scans. This is not surprising, given that these changes take years to decades to manifest in patients and our tissues were cultured for only 1 month. Further, only the cardiomyocytes contained the *DSP* mutation while the cardiac fibroblasts did not, potentially impacting both collagen deposition and lipid accumulation. Indeed, there is disagreement in the literature as to whether lipid accumulation is due to cardiomyocytes alone or in combination with other cell types that drives arrhythmia [6,23,42,52]. The fibro-fatty infiltrates in ACM patient hearts often contain inflammatory infiltrates (T lymphocytes) in association with cardiomyocyte apoptosis, suggesting

that the pathologic process may be immunologically mediated [9]. As with nearly all in vitro systems, there is no immune modulation applied in this outlined laboratory system. Many studies indicate that fibrosis, cardiomyocyte death and fibro-fatty infiltration are the substrate for triggering arrhythmia due to loss of electrical connectivity [2,30]. However, there is also evidence that arrhythmias in ACM can precede structural abnormalities [14,20]. In total, the results of these studies provide insight into the lack of identifiable arrhythmia in DSPmut 8x dyn-EHTs, suggesting that more complex 3D tissue architecture, fibro-fatty infiltration, and additional cell types may be contributing factors.

4.5. Conclusion

In conclusion, I developed a novel model of mechanical loading of EHTs (dyn-EHTs) and demonstrate that dynamic loading is important for studying ACM, which is known to be exacerbated by increased mechanical loading. This 3D platform revealed a disease phenotype (tissue lengthening, impaired contractility, fewer and reduced protein density of the desmosomes), which is similar to the pathological course of disease, including ventricular dilation and reduced cardiac output. Looking forward, this model may have implications for the pharmaceutical industry where patient-derived dyn-EHTs could be used to model heart failure progression in individualized patients with genetic predispositions. This information could be used to test efficacy of drugs that reduce ventricular wall stress, or screen for off-target effects of non-cardiac drugs on heart function.

4.6. Acknowledgements

Financial support was provided from Human Frontier Science Program [grant number RGY 0071/2014 to P.v.d.M. and A.W.F.], the National Institutes of Health [grant number

DP2HL117750 to A.W.F.], the Office of Naval Research [grant number N00014-17-1-2566 to A.W.F.], and the Dowd Fellowship and Presidential Fellowship, Carnegie Mellon University [to J.M.B.]. and in part by the European Research Council [grant number: ERC-2016-StG – 715732 to P.v.d.M]. We would also like to thank Professor Carmel Majidi, Eric Markvicka, and Tong Lu for their providing and assisting with the UV laser cutter for the PDMS strips. We would also like to thank Wei Chen and Professor Burak Ozdoganlar for providing and assisting with the profilometer for measuring strip thickness, as well as Aishwarya Paward and Professor Jessica Zhang for assistant with setting up and validating the strip bending finite element model.

4.7. References

1. Al-Khatib, S. M., W. G. Stevenson, M. J. Ackerman, W. J. Bryant, D. J. Callans, A. B. Curtis, B. J. Deal, T. Dickfeld, M. E. Field, G. C. Fonarow, A. M. Gillis, M. A. Hlatky, C. B. Granger, S. C. Hammill, J. A. Joglar, G. N. Kay, D. D. Matlock, R. J. Myerburg, and R. L. Page. 2017 AHA/ACC/HRS Guideline for Management of Patients With Ventricular Arrhythmias and the Prevention of Sudden Cardiac Death: A Report of the American College of Cardiology/American Heart Association Task Force on Clinical Practice Guidelines and the Hea. 2017, CIR.0000000000000549 pp.doi:10.1161/CIR.0000000000000549
2. Asimaki, A., A. G. Kleber, and J. E. Saffitz. Pathogenesis of Arrhythmogenic Cardiomyopathy. , 2015.doi:10.1016/j.cjca.2015.04.012
3. Burchfield, J. S., M. Xie, and J. A. Hill. Pathological ventricular remodeling: Mechanisms: Part 1 of 2. *Circulation* , 2013.doi:10.1161/CIRCULATIONAHA.113.001878
4. Burridge, P. W., A. Holmström, and J. C. Wu. Chemically Defined Culture and Cardiomyocyte Differentiation of Human Pluripotent Stem Cells. *Curr. Protoc. Hum. Genet.* , 2015.doi:10.1002/0471142905.hg2103s87
5. Carruth, E. D., W. Young, D. Beer, C. A. James, H. Calkins, L. Jing, S. Raghunath, D. N. Hartzel, J. B. Leader, H. L. Kirchner, D. T. Smelser, D. J. Carey, M. A. Kelly, A. C. Sturm, A. Alsaid, B. K. Fornwalt, and C. M. Haggerty. Prevalence and Electronic Health Record-Based Phenotype of Loss-of-Function Genetic Variants in Arrhythmogenic Right Ventricular Cardiomyopathy-Associated Genes. *Circ. Genomic Precis. Med.* 12:, 2019.
6. Caspi, O., I. Huber, A. Gepstein, G. Arbel, L. Maizels, M. Boulos, and L. Gepstein. Modeling of arrhythmogenic right ventricular cardiomyopathy with human induced pluripotent stem cells. *Circ. Cardiovasc. Genet.* 6:557–568, 2013.
7. Chung, C. Y., H. Bien, and E. Entcheva. The role of cardiac tissue alignment in modulating electrical function. *J. Cardiovasc. Electrophysiol.* , 2007.doi:10.1111/j.1540-8167.2007.00959.x
8. Cokkinos, D. V., and C. Belogianneas. Left ventricular remodelling: A problem in search of solutions. *Eur. Cardiol. Rev.* , 2016.doi:10.15420/ecr.2015:9:3
9. Corrado, D., M. S. Link, and H. Calkins. Arrhythmogenic Right Ventricular Cardiomyopathy. *N. Engl. J. Med.* 376:61–72, 2017.
10. D'Amore, A., T. Yoshizumi, S. K. Luketich, M. T. Wolf, X. Gu, M. Cammarata, R. Hoff, S. F. Badylak, and W. R. Wagner. Bi-layered polyurethane – Extracellular matrix cardiac patch improves ischemic ventricular wall remodeling in a rat model. *Biomaterials* , 2016.doi:10.1016/j.biomaterials.2016.07.039
11. Dellefave, L., and E. M. McNally. The genetics of dilated cardiomyopathy. ,

2010.doi:10.1097/HCO.0b013e328337ba52
12. Egido, J., C. Zaragoza, C. Gomez-Guerrero, J. L. Martin-Ventura, L. Blanco-Colio, B. Lavin, B. Mallavia, C. Tarin, S. Mas, and A. Ortiz. Animal models of cardiovascular diseases. *J. Biomed. Biotechnol.* 2011:, 2011.
13. Gerull, B., and A. Brodehl. Genetic Animal Models for Arrhythmogenic Cardiomyopathy. *Front. Physiol.* 11:1–20, 2020.
14. Gomes, J., M. Finlay, A. K. Ahmed, E. J. Ciaccio, A. Asimaki, J. E. Saffitz, G. Quarta, M. Nobles, P. Syrris, S. Chaubey, W. J. McKenna, A. Tinker, and P. D. Lambiase. Electrophysiological abnormalities precede overt structural changes in arrhythmogenic right ventricular cardiomyopathy due to mutations in desmoplakin-A combined murine and human study. *Eur. Heart J.* 33:1942–1953, 2012.
15. Grossman, W., and W. J. Paulus. Myocardial stress and hypertrophy: A complex interface between biophysics and cardiac remodeling. *J. Clin. Invest.* , 2013.doi:10.1172/JCI69830
16. Den Haan, A. D., B. Y. Tan, M. N. Zikusoka, L. I. Lladó, R. Jain, A. Daly, C. Tichnell, C. James, N. Amat-Alarcon, T. Abraham, S. D. Russell, D. A. Bluemke, H. Calkins, D. Dalal, and D. P. Judge. Comprehensive desmosome mutation analysis in North Americans with arrhythmogenic right ventricular dysplasia/cardiomyopathy. *Circ. Cardiovasc. Genet.* , 2009.doi:10.1161/CIRCGENETICS.109.858217
17. Hayashida, W., T. Kumada, R. Nohara, H. Tanio, M. Kambayashi, N. Ishikawa, Y. Nakamura, Y. Himura, and C. Kawai. Left ventricular regional wall stress in dilated cardiomyopathy. *Circulation* , 1990.doi:10.1161/01.CIR.82.6.2075
18. Hinson, J. T., A. Chopra, N. Nafissi, W. J. Polacheck, C. C. Benson, S. Swist, J. Gorham, L. Yang, S. Schafer, C. C. Sheng, A. Haghighi, J. Homsy, N. Hubner, G. Church, S. A. Cook, W. A. Linke, C. S. Chen, J. G. Seidman, and C. E. Seidman. Titin mutations in iPS cells define sarcomere insufficiency as a cause of dilated cardiomyopathy. *Science (80-.).* , 2015.doi:10.1126/science.aaa5458
19. St. John Sutton, M. G., and N. Sharpe. Left ventricular remodeling after myocardial infarction: Pathophysiology and therapy. *Circulation* , 2000.doi:10.1161/01.cir.101.25.2981
20. Karmouch, J., Q. Q. Zhou, C. Y. Miyake, R. Lombardi, K. Kretzschmar, M. Bannier-Hélaouët, H. Clevers, X. H. T. Wehrens, J. T. Willerson, and A. J. Marian. Distinct Cellular Basis for Early Cardiac Arrhythmias, the Cardinal Manifestation of Arrhythmogenic Cardiomyopathy, and the Skin Phenotype of Cardiocutaneous Syndromes. *Circ. Res.* 121:1346–1359, 2017.
21. Kawatou, M., H. Masumoto, H. Fukushima, G. Morinaga, R. Sakata, T. Ashihara, and J. K. Yamashita. Modelling Torsade de Pointes arrhythmias in vitro in 3D human iPS cell-engineered heart tissue. *Nat. Commun.* , 2017.doi:10.1038/s41467-017-01125-y
22. Keung, W., P. K. W. Chan, P. C. Backeris, E. K. Lee, N. Wong, A. O. T. Wong, G. K. Y. Wong, C. W. Y. Chan, B. Fermini, K. D. Costa, and R. A. Li. Human Cardiac Ventricular-Like Organoid Chambers and Tissue Strips From Pluripotent Stem Cells as a Two-Tiered Assay for Inotropic Responses. *Clin. Pharmacol. Ther.* , 2019.doi:10.1002/cpt.1385
23. Kim, C., J. Wong, J. Wen, S. Wang, C. Wang, S. Spiering, N. G. Kan, S. Forcales, P. L. Puri, T. C. Leone, J. E. Marine, H. Calkins, D. P. Kelly, D. P. Judge, and H.-S. V. Chen. Studying arrhythmogenic right ventricular dysplasia with patient-specific iPSCs. *Nature* 494:105–10, 2013.
24. Konstam, M. A., D. G. Kramer, A. R. Patel, M. S. Maron, and J. E. Udelson. Left ventricular remodeling in heart failure: Current concepts in clinical significance and assessment. , 2011.doi:10.1016/j.jcmg.2010.10.008
25. Kupfer, M. E., W.-H. Lin, V. Ravikumar, K. Qiu, L. Wang, L. Gao, D. Bhuiyan, M. Lenz, J. Ai, R. R. Mahutga, D. Townsend, J. Zhang, M. C. McAlpine, E. G. Tolkacheva, and B. M. Ogle. In Situ Expansion, Differentiation and Electromechanical Coupling of Human Cardiac Muscle in a 3D Bioprinted, Chambered Organoid . *Circ. Res.* , 2020.doi:10.1161/circresaha.119.316155
26. Lee, A., A. R. Hudson, D. J. Shiwarski, J. W. Tashman, T. J. Hinton, S. Yerneni, J. M. Bliley, P. G. Campbell, and A. W. Feinberg. 3D bioprinting of collagen to rebuild components of the human heart. *Science (80-.).* , 2019.doi:10.1126/science.aav9051
27. Lian, X., J. Zhang, S. M. Azarin, K. Zhu, L. B. Hazeltine, X. Bao, C. Hsiao, T. J. Kamp, and S. P. Palecek. Directed cardiomyocyte differentiation from human pluripotent stem cells by modulating Wnt/??-catenin signaling under fully defined conditions. *Nat. Protoc.* 8:162–175, 2013.
28. Ma, Z., N. Huebsch, S. Koo, M. A. Mandegar, B. Siemons, S. Boggess, B. R. Conklin, C. P. Grigoropoulos, and K. E. Healy. Contractile deficits in engineered cardiac microtissues as a result of MYBPC3 deficiency and mechanical overload. *Nat. Biomed. Eng.* , 2018.doi:10.1038/s41551-018-0280-4
29. Macqueen, L. A., S. P. Sheehy, C. O. Chantre, J. F. Zimmerman, F. S. Pasqualini, X. Liu, J. A. Goss, P. H.

Campbell, G. M. Gonzalez, S. J. Park, A. K. Capulli, J. P. Ferrier, T. Fettah Kosar, L. Mahadevan, W. T. Pu, and K. K. Parker. A tissue-engineered scale model of the heart ventricle. *Nat. Biomed. Eng.* , 2018.doi:10.1038/s41551-018-0271-5

30. Maione, A. S., C. A. Pilato, M. Casella, A. Gasperetti, I. Stadiotti, G. Pompilio, and E. Sommariva. Fibrosis in Arrhythmogenic Cardiomyopathy: The Phantom Thread in the Fibro-Adipose Tissue. , 2020.doi:10.3389/fphys.2020.00279
31. Mairesse, G. H. Guidelines for the management of patients with ventricular arrhythmias (VA) and the prevention of sudden cardiac death (SCD). , 2016.
32. Martherus, R., R. Jain, K. Takagi, U. Mendsaikhan, S. Turdi, H. Osinska, J. F. James, K. Kramer, E. Purevjav, and J. A. Towbin. Accelerated cardiac remodeling in desmoplakin transgenic mice in response to endurance exercise is associated with perturbed Wnt/β-catenin signaling. *Am. J. Physiol. - Hear. Circ. Physiol.* 38103:ajpheart.00295.2015, 2015.
33. Martin, L., A. Grigoryan, D. Wang, J. Wang, L. Breda, S. Rivella, T. Cardozo, and L. B. Gardner. Identification and characterization of small molecules that inhibit nonsense-mediated rna decay and suppress nonsense p53 mutations. *Cancer Res.* 74:3104–3113, 2014.
34. Maruthappu, T., A. Posafalvi, S. Castelletti, P. J. Delaney, P. Syrris, E. A. O'Toole, K. J. Green, P. M. Elliott, P. D. Lambiase, A. Tinker, W. J. McKenna, and D. P. Kelsell. Loss-of-function desmoplakin I and II mutations underlie dominant arrhythmogenic cardiomyopathy with a hair and skin phenotype. *Br. J. Dermatol.* , 2019.doi:10.1111/bjd.17388
35. Matsumura, Y., Y. Zhu, H. Jiang, A. D'Amore, S. K. Luketich, V. Charwat, T. Yoshizumi, H. Sato, B. Yang, T. Uchibori, K. E. Healy, and W. R. Wagner. Intramyocardial injection of a fully synthetic hydrogel attenuates left ventricular remodeling post myocardial infarction. *Biomaterials* , 2019.doi:10.1016/j.biomaterials.2019.119289
36. McNally, E., M. Allikian, M. T. Wheeler, J. M. Mislow, and A. Heydemann. Cytoskeletal defects in cardiomyopathy. , 2003.doi:10.1016/S0022-2828(03)00018-X
37. Moustakidis, P., H. S. Maniar, B. P. Cupps, T. Absi, J. Zheng, J. M. Guccione, T. M. Sundt, and M. K. Pasque. Altered left ventricular geometry changes the border zone temporal distribution of stress in an experimental model of left ventricular aneurysm: A finite element model study. *Circulation* , 2002.doi:10.1161/01.cir.0000032898.55215.0d
38. Ng, R., H. Manring, N. Papoutsidakis, T. Albertelli, N. Tsai, C. J. See, X. Li, J. Park, T. L. Stevens, P. J. Bobbili, M. Riaz, Y. Ren, C. E. Stoddard, P. M. L. Janssen, T. J. Bunch, S. P. Hall, Y.-C. Lo, D. L. Jacoby, Y. Qyang, N. Wright, M. A. Ackermann, and S. G. Campbell. Patient mutations linked to arrhythmogenic cardiomyopathy enhance calpain-mediated desmoplakin degradation. *JCI Insight* 4:, 2019.
39. Okita, K., Y. Matsumura, Y. Sato, A. Okada, A. Morizane, S. Okamoto, H. Hong, M. Nakagawa, K. Tanabe, K. I. Tezuka, T. Shibata, T. Kunisada, M. Takahashi, J. Takahashi, H. Saji, and S. Yamanaka. A more efficient method to generate integration-free human iPS cells. *Nat. Methods* 8:409–412, 2011.
40. Parvari, R., and A. Levitas. The mutations associated with dilated cardiomyopathy. , 2012.doi:10.1155/2012/639250
41. Pashakhanloo, F., D. A. Herzka, H. Halperin, E. R. McVeigh, and N. A. Trayanova. Role of 3-Dimensional Architecture of Scar and Surviving Tissue in Ventricular Tachycardia. *Circ. Arrhythmia Electrophysiol.* , 2018.doi:10.1161/circep.117.006131
42. Paylor, B., J. Fernandes, B. McManus, and F. Rossi. Tissue-resident Sca1+ PDGFRα+ mesenchymal progenitors are the cellular source of fibrofatty infiltration in arrhythmogenic cardiomyopathy. *F1000Research* 2:141, 2013.
43. Peters, N. S., and A. L. Wit. Myocardial architecture and ventricular arrhythmogenesis. , 1998.doi:10.1161/01.CIR.97.17.1746
44. Pong, T., W. J. Adams, M. A. Bray, A. W. Feinberg, S. P. Sheehy, A. A. Werdich, and K. K. Parker. Hierarchical architecture influences calcium dynamics in engineered cardiac muscle. *Exp. Biol. Med.* , 2011.doi:10.1258/ebm.2010.010239
45. Rasmussen, T., J. Hansen, P. Nissen, J. Palmfeldt, S. Dalager, U. Jensen, W. Kim, L. Heickendorff, H. Mølgaard, H. Jensen, K. Sørensen, U. Baandrup, P. Bross, and J. Mogensen. Protein expression studies of desmoplakin mutations in cardiomyopathy patients reveal different molecular disease mechanisms. *Clin. Genet.* 84:20–30, 2013.
46. Sabbah, H. N. Silent disease progression in clinically stable heart failure. , 2017.doi:10.1002/ejhf.705
47. Sáez, P., and E. Kuhl. Computational modeling of acute myocardial infarction. *Comput. Methods Biomech. Biomed. Engin.* , 2016.doi:10.1080/10255842.2015.1105965

48. Scardulla, F., A. Rinaudo, S. Pasta, and C. Scardulla. Evaluation of ventricular wall stress and cardiac function in patients with dilated cardiomyopathy. *Proc. Inst. Mech. Eng. Part H J. Eng. Med.* , 2016.doi:10.1177/0954411915617984
49. Seidman, J. G., and C. Seidman. The Genetic Basis for Cardiomyopathy. *Cell* , 2001.doi:10.1016/s0092-8674(01)00242-2
50. Sheikh, F., R. S. Ross, and J. Chen. Cell-Cell Connection to Cardiac Disease. , 2009.doi:10.1016/j.tcm.2009.12.001
51. Sokol, E., D. Kramer, G. F. H. Diercks, J. Kuipers, M. F. Jonkman, H. H. Pas, and B. N. G. Giepmans. Large-scale electron microscopy maps of patient skin and mucosa provide insight into pathogenesis of blistering diseases. *J. Invest. Dermatol.* , 2015.doi:10.1038/jid.2015.109
52. Sommariva, E., S. Brambilla, C. Carbucicchio, E. Gambini, V. Meraviglia, A. Dello Russo, F. M. Farina, M. Casella, V. Catto, G. Pontone, M. Chiesa, I. Stadiotti, E. Cogliati, A. Paolin, N. Ouali Alami, C. Preziuso, G. D'Amati, G. I. Colombo, A. Rossini, M. C. Capogrossi, C. Tondo, and G. Pompilio. Cardiac mesenchymal stromal cells are a source of adipocytes in arrhythmogenic cardiomyopathy. *Eur. Heart J.* 57:1835–1846, 2016.
53. Takahashi, K., K. Tanabe, M. Ohnuki, M. Narita, T. Ichisaka, K. Tomoda, and S. Yamanaka. Induction of Pluripotent Stem Cells from Adult Human Fibroblasts by Defined Factors. *Cell* 131:861–872, 2007.
54. Travers, J. G., F. A. Kamal, J. Robbins, K. E. Yutzey, and B. C. Blaxall. Cardiac fibrosis: The fibroblast awakens. , 2016.doi:10.1161/CIRCRESAHA.115.306565
55. Uzumcu, a, E. E. Norgett, a Dindar, O. Uyguner, K. Nisli, H. Kayserili, S. E. Sahin, E. Dupont, N. J. Severs, I. M. Leigh, M. Yuksel-Apak, D. P. Kelsell, and B. Wollnik. Loss of desmoplakin isoform I causes early onset cardiomyopathy and heart failure in a Naxos-like syndrome. *J. Med. Genet.* 43:e5, 2006.
56. Voorhees, A. P., and H. C. Han. Biomechanics of cardiac function. *Compr. Physiol.* , 2015.doi:10.1002/cphy.c140070
57. Walsh, R., K. L. Thomson, J. S. Ware, B. H. Funke, J. Woodley, K. J. McGuire, F. Mazzarotto, E. Blair, A. Seller, J. C. Taylor, E. V. Minikel, D. G. MacArthur, M. Farrall, S. A. Cook, and H. Watkins. Reassessment of Mendelian gene pathogenicity using 7,855 cardiomyopathy cases and 60,706 reference samples. *Genet. Med.* 19:192–203, 2017.
58. Wang, G., M. L. McCain, L. Yang, A. He, F. S. Pasqualini, A. Agarwal, H. Yuan, D. Jiang, D. Zhang, L. Zangi, J. Geva, A. E. Roberts, Q. Ma, J. Ding, J. Chen, D. Z. Wang, K. Li, J. Wang, R. J. A. Wanders, W. Kulik, F. M. Vaz, M. A. Laflamme, C. E. Murry, K. R. Chien, R. I. Kelley, G. M. Church, K. K. Parker, and W. T. Pu. Modeling the mitochondrial cardiomyopathy of Barth syndrome with induced pluripotent stem cell and heart-on-chip technologies. *Nat. Med.* , 2014.doi:10.1038/nm.3545
59. Whittock, N. V., G. H. S. Ashton, P. J. C. Dopping-Hepenstal, M. J. Gratian, F. M. Keane, R. A. J. Eady, and J. A. McGrath. Striate Palmoplantar Keratoderma Resulting from Desmoplakin Haploinsufficiency. *J. Invest. Dermatol.* 113:940–946, 1999.
60. Williams, T., W. Machann, L. Kühler, H. Hamm, J. Müller-Höcker, M. Zimmer, G. Ertl, O. Ritter, M. Beer, and J. Schönberger. Novel desmoplakin mutation: juvenile biventricular cardiomyopathy with left ventricular non-compaction and acantholytic palmoplantar keratoderma. *Clin. Res. Cardiol.* 100:1087–1093, 2011.
61. Yang, Z., N. E. Bowles, S. E. Scherer, M. D. Taylor, D. L. Kearney, S. Ge, V. V. Nadvoretskiy, G. DeFreitas, B. Carabello, L. I. Brandon, L. M. Godsel, K. J. Green, J. E. Saffitz, H. Li, G. A. Danieli, H. Calkins, F. Marcus, and J. A. Towbin. Desmosomal Dysfunction due to Mutations in Desmoplakin Causes Arrhythmogenic Right Ventricular Dysplasia/Cardiomyopathy. *Circ. Res.* 99:646–655, 2006.
62. Zhao, X., R. S. Tan, H. C. Tang, S. K. Teo, Y. Su, M. Wan, S. Leng, J. M. Zhang, J. Allen, G. S. Kassab, and L. Zhong. Left ventricular wall stress is sensitive marker of hypertrophic cardiomyopathy with preserved ejection fraction. *Front. Physiol.* , 2018.doi:10.3389/fphys.2018.00250

Supplemental Table 1:Immunolabeling			
Protein	**Clone/ Cat no.**	**Clonality**	**Usage**
Desmoplakin-I (ROD)	DP2.17	moAb	WB, IHC-Fr, IF
Desmoplakin-I&II (C-ter)	2A5	moAb	WB, IHC-Fr, IF
Plakoglobin	15F11	moAb	WB, IHC-Fr, IF
Plakophilin 2	PP2/62;8/86;2/150	moAb	WB, IHC-Fr, IF
Desmoglein 2	10G11	moAb	WB, IHC-Fr
Desmocollin 2	610120 (Progen)	poAb	WB, IHC-Fr
Desmin	Y-20 (Santa Cruz)	poAb	WB, IF
Desmin	DE-R-11	moAb	ICH-Fr
Connexin 43	H-150 (Santa Cruz)	poAb	IHC-Fr
cardiac Troponin T	ab45932 (Abcam)	poAb	IF
α-actinin	A7811, Sigma-Aldrich	moAb	Whole mount IF
GAPDH	10R-G109a	moAb	WB
Vinculin	SPM227	moAb	WB
SSEA-4	MC813	moAb	IF
OCT3/4	H-134	moAb	IF
Alexa Fluor™ 488 Phalloidin	A12379 (Invitrogen)	NA	Whole Mount IF

Supplemental Table 2: RT-PCR Primers			
Gene		**Forward '5 - '3**	**Reverse '3 - '5**
DSP (NG_008803.1)		CAGTGGTGTCAGCGATGATGT	TGACGCTGGATATGGTGGAA
	DSP_ex1-4	GGACGGCTACTG**TCAAACC**	GACTCGAGGGACACTGATG
	DSP_ex2-5	**CT**GTCAAACCGGCACGATGTC	TCCAGCTGCCAGCGATAGTC
	DSP_ex2-int2	AGGCACCAGAACCAGAACAC	CCCAACCCAGGAACAGAAAC
	DSP_ex1-int2A	GGACGGCTACTG**TCAAACC**	CCCAACCCAGGAACAGAAAC
JUP		AGTAGCCACGATGGAGGTGA	AGGTGTATGTCTGCTGCCAC
PKP2		GCAAATGGTTTGCTCGATTT	GGCTGGTAATCTGCAATGGT
DSG2		TCCACTATGCCACCAACCAC	GCTGGAGCATACACCCTCTC
DSC2		CGGAGATTGTTGCGGTTGA	GGAAAGACGTGCTGCTGTATCA
DES		CTGAGCAAAGGGGTTCTGAG	ACTTCATGCTGCTGCTGTGT
GJA1		GGAATGCAAGAGAGGTTGAAAG	GGCATTTGGAGAAACTGGTAGA
PPIA		ACTTCACACGCCATAATG	ACCCGTATGCTTTAGGAT
MYH6		GATAGAGAGACTCCTGCGGC	TCGGTCATCTTGGTGCTTCC
MYH7		CGAAGGGCTTGAATGAGGAGT	TCCTCCCAAGGAGCTGTTAC
TTN	N2B	CACTAACTGTGACAGTGCC	CTTCTTCCTTTGGTTCAGGT
TTN	N2A	ATGGAAATGAAAGCTGCCC	GGTGAATTTGGCTAGGTGG
TNNI3		CCAACTACCGCGCTTATGC	CTCGCTCCAGCTCTTGCTTT
SCN5A		CACCAACTGCGTGTTCATGG	CAGAAGCCTCGAGCCAGAAT
CPT1B		CTCCTTTCCTTGCTGAGGTG	TCTCGCCTGCAATCATGTAG
PDK4		CCTTTGGCTGGTTTTGGTTA	CCTGCTTGGGATACACCAGT

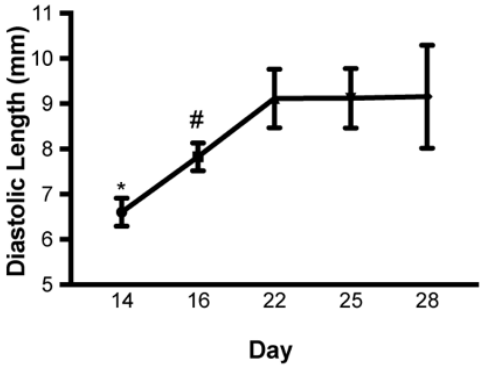

Supplemental Figure 1: Tissue Diastolic Length Over Time in Control ESC-Derived 8x dyn-EHTs. Graph showing average tissue diastolic length in control 8x dyn-EHTs at day 14, 16, 22, 25, and 28. * indicates $p<0.05$ statistical significance from day 16, 22, 25, and 28. # indicates $p<0.05$ statistical significance from day 22, 25, 28. Statistics based on one way ANOVA with post hoc Holm Sidak test. All graphs show n=5/group for 8x dyn-EHT. All data represented as mean ± SD. Figure and data prepared by Jacqueline Bliley.

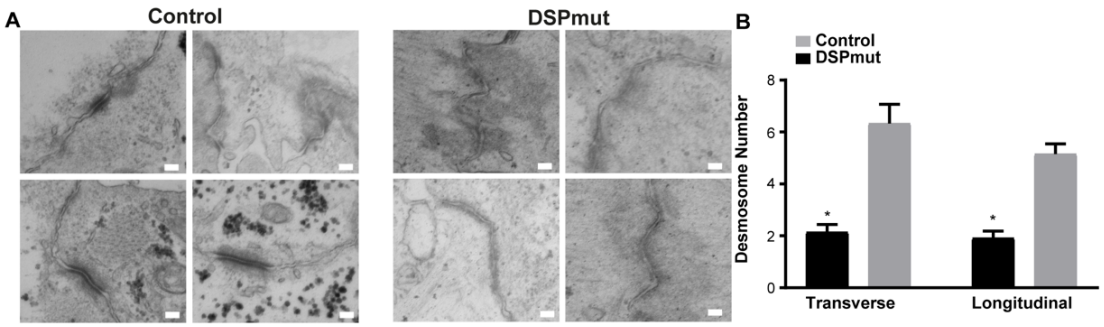

Supplemental Figure 2: Electron microscopy of Control and DSPmut Tissues. (A) Panels depict representative overview pictures of intercalated disc found throughout patient and control 3D tissues. Scale bars are 150 nm. **(B)** Desmosomal number per TEM high powered field in control and DSPmut 8x dyn-EHTs. *$p<0.05$ unpaired t-test compared to control. All data represented as mean ± SD. Data obtained by M. Vermeer.

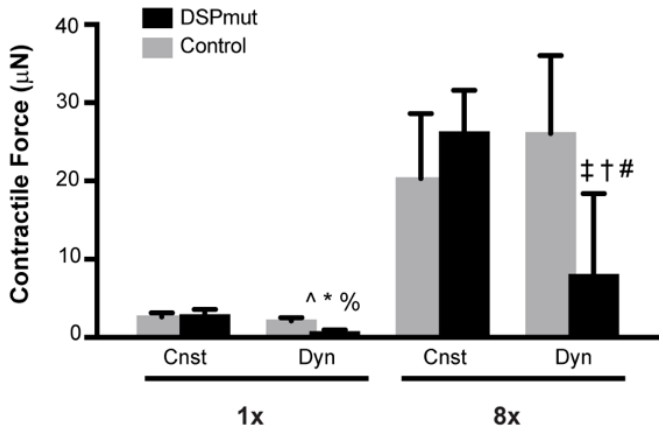

Supplemental Figure 3: Contractile Force in Control and DSPmut Tissues. Results are based on two-way ANOVA with post hoc Holm Sidak test. ^ $p<0.05$ versus Control 1x constrained. * $p<0.05$ versus Control 1x dynamic. % $p<0.05$ versus DSPmut 1x constrained. ‡ $p<0.05$ control 8x constrained. † $p<0.05$ from control 8x dynamic. # $p<0.05$ from DSPmut 8x constrained. All data represented as mean ± SD. Figure and data prepared by Jacqueline Bliley.

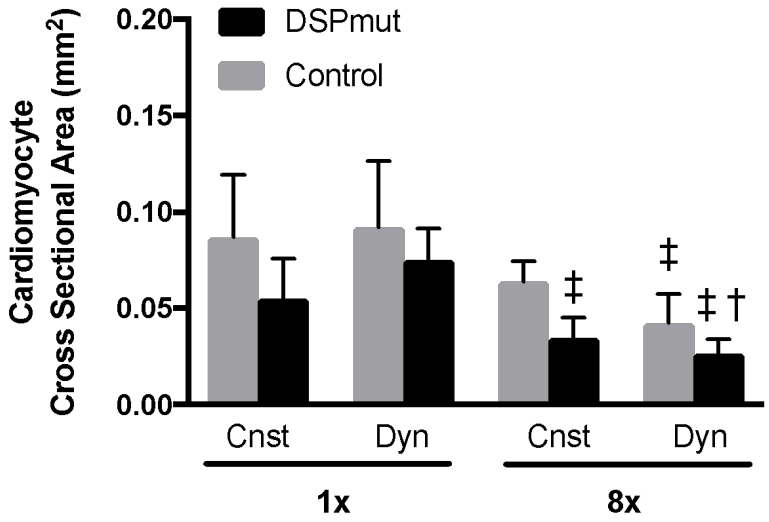

Supplemental Figure 4: Cardiomyocyte Cross-Sectional Area of DSPmut and Control Tissues. Cardiomyocyte cross-sectional area used for tissue stress measurements. Results are based on two-way ANOVA with post hoc Holm Sidak test within each loading amount (either 1x or 8x). ‡ indicates $p<0.05$ compared to control 8x constrained. † indicates $p<0.05$ compared to control 8x dynamic. All data represented as mean ± SD. Figure and data prepared by Jacqueline Bliley.

Chapter 5

FRESH 3D Bioprinting a Contractile Heart Tube Using Human Stem Cell-Derived Cardiomyocytes

5.1 Introduction

Heart failure affects more than 26 million patients worldwide and more than half of those patients will die within 5 years of their diagnosis[29,34]. A key challenge is that the adult human heart has minimal regenerative capacity and cannot repair the damage due to myocardial infarction (MI) and other diseases[33]. Current pharmaceutical treatments and medical devices such as ventricular assist devices, can only slow disease progression. Thus, the only long term treatment for severe heart failure is a heart transplant but, unfortunately, available donor organs are severely limited with only ~3000 heart transplants being performed per year in the United States[9].

With the advent of stem cell-based approaches to generate potentially unlimited amounts of cardiomyocytes[1], heart muscle tissue engineering has emerged as a promising field to generate new cardiac muscle with the long term goal of repairing or replacing the human heart. Indeed, recent work injecting self-organized embryoid body stem cell-derived cardiomyocytes into the mammalian heart post-MI has shown the ability to achieve remuscularization[7,16]. Further, significant progress has been made using self-organization or casting-based approaches to generate cardiac sheets or tissues which can be used to repair heart muscle damage[8,14,30,35,37,39]. While these approaches have demonstrated success in being able to integrate and repair damaged heart muscle, these techniques have primarily been used to fabricate simple structures such as sheets and linear tissues, and are unable to generate complex structures capable of replacing the entire heart.

In contrast, several methods have been developed to generate structures reminiscent of the adult human heart. For instance, tissue decellularization can be used to generate unmatched heart organ structure, but there remain limitations in being able to fully integrate cardiomyocytes and other heart muscle cells within decellularized scaffolds[25]. Alternatively, several advanced biofabrication approaches, such as electrospinning and 3D printing, have been used to produce ventricles[17,22] and even simplified versions of the entire organ[15,24]. However, a challenge that still exists is our ability to capture the structural and functional complexity observed in the whole human heart.

Here, I sought to engineer a contractile model of the human heart as early proof-of-concept of organ-scale biofabrication using stem cell-derived cardiomyocytes. Since the adult 4-chambered heart is highly complex, as a foundational approach I focused on building a simpler heart structure, much like that observed during embryonic development. Specifically, during early cardiogenesis the heart exists as a linear tube that then bends, loops, and septates to form the mature 4-chambered structure[23]. The linear heart tube, while structurally much simpler, still displays hall-marks of cardiac function including action potential propagation, synchronized contraction, and the ability to pump fluid. To build the linear heart tube I used Freeform Reversible Embedding of Suspended Hydrogels (FRESH) 3D bioprinting[12], which allows for the printing of soft materials including biopolymers, like collagen, into cellularized cardiac tissue[17]. The objective was to create a bioinspired model of the embryonic heart tube and assess its structure and functional outputs, including electrophysiology and contractility.

5.2 Materials and Methods

5.2.1. Cardiomyocyte Differentiation and Purification

Cardiomyocytes were differentiated from HES3 (ES03, Wicell) embryonic stem cells (ESCs) using mesoderm induction and cardiac specification according to previously described methods[4,21]. The HES3 ESCs were maintained in Essential 8 (E8) medium (A1517001, Life Technologies) on Geltrex (A1413301, Life Technologies)-coated (12 μg/cm^2) 6 well plates and passaged every 4 days (~80% confluence). To prepare for differentiation, HES3 ESCs were seeded at 8,000 cells/cm^2 in Geltrex-coated T75 flasks with daily E8 media changes for 3 days. At 80% confluence (Day 0 of differentiation), cells were washed with 1x PBS and media was switched to RPMI-1640 (21870076, Thermofisher) supplemented with 1% v/v L-glutamine (25030081, Thermofisher), B27 supplement (17504044, Thermofisher), and 6 μM CHIR99201 (C-6556, LC laboratories). On day 2 of differentiation, cells were washed with 1X PBS and media was changed to RPMI-1640 (21870076, Thermofisher) supplemented with 1% v/v L-glutamine (25030081, Thermofisher), B27 supplement (17504044, Thermofisher), and 2 μM Wnt C-59 (S7037, Selleck Chemicals). On days 4 and 6, cells were switched to RPMI 1640 media (21870076, Thermofisher) containing 1% v/v L-glutamine (25030081, Thermofisher) and B27 supplement (17504044, Thermofisher). On days 8 and 10, medium was changed to CDM3 media, consisting of RPMI-1640 supplemented with 1% v/v L glutamine, 213 μg/mL L-Ascorbic acid 2-phosphate sesquimagnesium salt hydrate >95% (A8960, Sigma), and 500 μg/mL human albumin (A9731, Sigma). On day 12, spontaneously beating cells were passaged for lactate-based metabolic selection of cardiomyocytes[32].

To passage for cardiomyocyte purification, cells were incubated with TrypLE for 15 mins at 37°C to enable single cell dissociation. Cells were then reseeded in CDM3L, consisting of

RPMI-1640 without glucose (11879020, Thermofisher) supplemented with 7.1 mM sodium-lactate (L4263, Sigma), 213 μg/mL L-Ascorbic acid 2-phosphate sesquimagnesium salt hydrate >95% (A8960, Sigma), and 500 μg/mL human albumin (A9731, Sigma). Cells were maintained in CDM3L for several days before replacing back to CDM3 medium.

5.2.2. Human ventricular fibroblast culture

Normal human primary ventricular cardiac fibroblasts (CC-2904, Lonza) were obtained and cultured via manufacturer's instructions. Fibroblasts were cultured at an initial density of 5,000 cells per cm^2 in FGM-3 media (CC-4526, Lonza) and passaged prior to reaching 80% confluence. Fibroblasts were used between passage 5 and passage 8 for these studies.

5.2.3. Bioprinter Setup

A custom high-precision bioprinter was assembled using a precision ballscrew z stage (MX80S, Parker-Hannefin) and a microscope stage (H117, Prior Scientific) mounted in a cartesian setup using extruded aluminum profiles. Mounted to the Z stage was a Replistruder 4 high-precision open-source syringe pump[31], used with a 2.5 mL gastight syringe (1000 series, Hamilton). The stages and syringe pump were controlled using a Duet 3 6HC (Duet3D) motion control board with a raspberry pi microcontroller running a dedicated user interface with mouse, keyboard, and display.

5.2.4. FRESH Slurry Support Bath Generation

FRESH v2.0 gelatin support bath was prepared using previously described methods[18]. Briefly, 2% w/v Gelatin B (G7, Fisher Chemicals), 0.25% w/v Pluronic® F-127 (P2443, Sigma

Aldrich), and 0.5% w/v Gum Arabic (G9752, Sigma-Aldrich) were dissolved in 50% v/v ethanol solution at 45°C in a 1 liter beaker. The pH was then adjusted to 5.8 by dropwise addition of 2N hydrochloric acid. The beaker was then placed under an overhead stirrer at ~600 RPM (IKA, Model RW20), sealed with parafilm, and allowed to cool to room temperature while stirring overnight. The resulting slurry was evenly distributed in 50 mL conical tubes and centrifuged at 300g for 3 minutes. The slurry was then washed three times in distilled water followed by three times in in 50 mM HEPES (61-034-RO, Corning) with centrifuging at 2000g for 3 mins. The washed slurry was stored at 4°C prior to printing.

5.2.5. FRESH Printing of Heart Tubes

Digital models of the heart tube were created using Fusion 360 (Autodesk) computer aided design (CAD) software and then exported as an STL file format. To generate G-code instructions for the printer, STL files were sliced in Slic3r (version 1.3.0, https://slic3r.org/). In general, slicer settings were a print speed of 10 mm/s, 2 perimeters, 30% infill, 35 µm layer height, 0.2 mm retraction length, and a 2 mm z-hop. Collagen type I bioink (LifeInk 200, Advanced Biomatrix) was prepared by addition of 0.24 M acetic acid in a 2:1 ratio with the 35 mg/mL collagen stock concentration to create a 24 mg/mL acidic collagen solution. This bioink was then centrifuged at 3000g for 5 mins to remove air bubbles and transferred to a gas-tight, 2.5 mL syringe with an 80 µm needle (JG34-0.25HPX, Jensen Global). To compact the support bath for printing, tubes were degassed for 30 minutes to remove air bubbles and then centrifuged at 1800g for 3 minutes. The supernatant was removed, and compacted slurry was transferred to a Petri dish and secured onto the print bed. Upon print completion, the Petri dish was removed from the print bed and placed in a 37°C incubator for 45 mins to melt the support bath. Prints were then transferred to 50 mM

HEPES solution and placed in a rotating 37°C incubator for an l hour to remove excess gelatin. Finally, printed heart tubes were sterilized with UV for 15 min and stored in 50 mM HEPES supplemented with 1% v/v penicillin streptomycin prior to cardiomyocyte casting.

5.2.6. Optical Imaging of Printed Heart Tubes

Printed heart tubes were imaged under brightfield with a stereomicroscope (SMZ1000, Nikon) using both a digital SLR camera (Model 70D, Canon) and a Prime 95B Scientific CMOS camera (Photometrics). In addition, 3D imaging was performed using a 1300 nm optical coherence tomography (OCT) system (VEG210C1, ThorLabs). ImageJ and Imaris 9.1 (Bitplane) were used for visualization and 3D renderings. For OCT imaging, both 2D linescan and 3D volumetric imaging modes were used.

5.2.7. Heart Muscle Tissue Casting and Culture

To hold the printed heart tubes in place during the tissue casting process, polydimethylsiloxane (PDMS) wells were first created. To do this, negative molds were 3D printed with polylactic acid filament (MK3S+, Prusa) and then PDMS was cast around them in 6 well plates and cured overnight at 65°C. The Sylgard 184 PDMS (Dow Corning) was mixed at a 10:1 weight ratio of base to curing agent in a Thinky conditioning mixer (Phoenix Equipment Inc.) using a 2 min 2000 RPM mixing cycle followed by a 2 min 2000 RPM defoaming cycle. The PDMS wells in the 6 well plate were then sterilized with UV-Ozone for 45 mins. PDMS wells were treated with 1% w/v Pluronic® F-127 to limit casted tissue attachment to the PDMS well. Sterile heart tubes were then placed in the PDMS wells and submerged in sterile 50 mM HEPES with 1% v/v penicillin- streptomycin until tissue casting.

To cast cardiac tissue around the printed tubes, cardiomyocytes and fibroblasts were combined in a 9:1 ratio within a mixture of collagen type I derived from rat tail (354249, Corning) and Matrigel (354263, Corning) at a final concentration of 30 million cells/mL. The final concentrations were 1 mg/mL collagen type I, 1.7 mg/mL Matrigel, 10% v/v 10X PBS, and 2.3% v/v 1N NaOH. Next, the HEPES solution was removed from the PDMS wells and each printed tube was covered with 375 μL of cell and ECM solution. Constructs were then incubated at 37°C for 1 hour to gel collagen and Matrigel and then covered in media consisting of RPMI-1640 supplemented with 1% v/v KnockOut™ Serum Replacement (10828028, Thermofisher) and 1:1000 MycoZap Plus CL (VZA-2012, Lonza). Heart tubes were maintained in media for 14 days, which was changed every 2 days.

5.2.8. Contractility Analysis

To determine if heart tubes were capable of pumping fluid, fluorescent beads (556286, BD Biosciences) were slowly injected into the tube lumen and were allowed to settle for 5 minutes following injection. This was done to ensure that movement of the beads was not due to fluid movement associated with the injection process. Tubes were imaged on a custom heated stage using a fluorescent stereomicroscope (SMZ1000, Nikon) equipped with DAPI, GFP, and TRITC filters, an X-Cite lamp (Excelitas), and a Prime 95B Scientific CMOS camera. Videos of the bead displacement at the tube lumen following spontaneous and electrically stimulated cyclical contractions of the heart tube were recorded up to 100 frames per second. To track the beads, the IMARIS 9.1 spot tracking algorithm was used. Peak and average bead velocity were calculated. Peak bead velocity was defined as the maximum displacement of the bead during contraction divided by the time it took for this displacement to occur whereas average bead velocity was

defined as the average displacement over 3 contractions divided by the time.

5.2.9. Electrical Stimulation and Calcium Imaging

Calcium imaging was performed on heart tubes during spontaneous and paced contractions after 14 days in culture. Briefly, heart tubes were stained with Cal520 (21130, AAT Bioquest) based on previously described methods[18]. An excitation-contraction decoupler, 10 μM Blebbistatin (B0560, Sigma), was used to prevent spontaneous contractions of the heart tubes that would preclude automated analysis. Heart tubes were field stimulated using paired parallel platinum electrodes immersed in the Tyrodes solution and point stimulated with a concentric bipolar microelectrode (30202, FHC Inc.) composed of an inner platinum-iridium pole and outer stainless-steel pole. Tubes were imaged on a custom heated stage maintaining the temperature at 37°C ±1°C using the fluorescent stereomicroscope. Calcium transients were analyzed using custom MATLAB code (R2019, MathWorks) using signal peak times and cross correlation to create activations maps and calculate conduction velocities, as previously published[18].

5.2.10. Immunofluorescent Imaging and Analysis

Heart tubes were stained and imaged whole mount to assess their structure. Tubes were fixed in 4% paraformaldehyde (Electron Microscope Sciences) in 1X PBS supplemented with 1:200 Triton-X 100 (9002-93-1, Sigma) for 1 hour. Next, tubes were washed 3 times for 30 mins each in 1X PBS on a rotary shaker. Samples were then blocked in 5% goat serum in 1X PBS overnight on a shaker followed by washing 3 times for 30 min in 1X PBS. Mouse anti-sarcomeric α-actinin antibody (A7811, Sigma-Aldrich) was diluted to 1:100 in 1X PBS and incubated with the tissues overnight on a shaker. Tubes were then washed 3 times for 30 mins each in 1X PBS

before incubating with 1:200 DAPI (D1306, Molecular Probes), 3:200 phalloidin conjugated with Alexa-Fluor 488 (A12379, Life Technologies), and 1:100 goat anti-mouse antibody conjugated with Alexa-Fluor 555 (A21422, Life Technologies) in 1X PBS overnight on a shaker. After the final incubation step, samples were rinsed 3 times for 30 mins each in 1X PBS.

5.2.11. Statistical Methods

All graphs were created and statistical analyses performed using GraphPad Prism 7. Data are presented as mean ± standard deviation and assessed for normality using Shapiro-Wilk normality test and homogeneity of variances with Brown-Forsythe test. T-tests were used to compare data with two groups. Welch's correction was used on data that had unequal standard deviations. To compare multiple groups, Kruskal-Wallis test was performed. If statistical significance was found, Dunn's multiple comparison test was used to evaluate differences between each group.

5.3 Results

5.3.1. Heart Tube Printing

To create the collagen heart tube, I used CAD to design a linear tube with supports on either end (Figure 5.1A). The tube had a 1.4 mm inner diameter, 2.0 mm outer diameter, and 300 μm wall thickness. While these dimensions are larger than the embryonic heart tube which has an inner diameter of ~300 μm[23], the goal was to test basic feasibility at a length scale our bioprinter could reliably fabricate. The model of the tube was processed into g-code for 3D printing, and the collagen extrusions for the tube wall were oriented along the longitudinal axis (Figure 5.1B). Heart tubes were FRESH 3D bioprinted using acidified type I collagen bioink (24 mg/mL) using

established methods (Figure 5.1C), where the printed collagen rapidly gels due to pH-driven neutralization by the buffered gelatin support bath[17]. Following printing, melting of the support bath at 37°C further gels the collagen and then releases the printed structure. To verify print fidelity, I used a combination of brightfield imaging and optical coherence tomography (OCT). Results demonstrate that the tubes were printed with high fidelity and with no visible defects (Figure 5.1D-E). It is notable that there was no stringing (unwanted extrusion of printed material out of the needle as it travels to a different place) or crowning (over-extrusion of material). Further, OCT of the printed tube confirmed that tube lumens were patent and displayed consistent wall thickness of ~300 µm, demonstrating that we were able to print the tube design with high fidelity (Figure 5.1F-G).

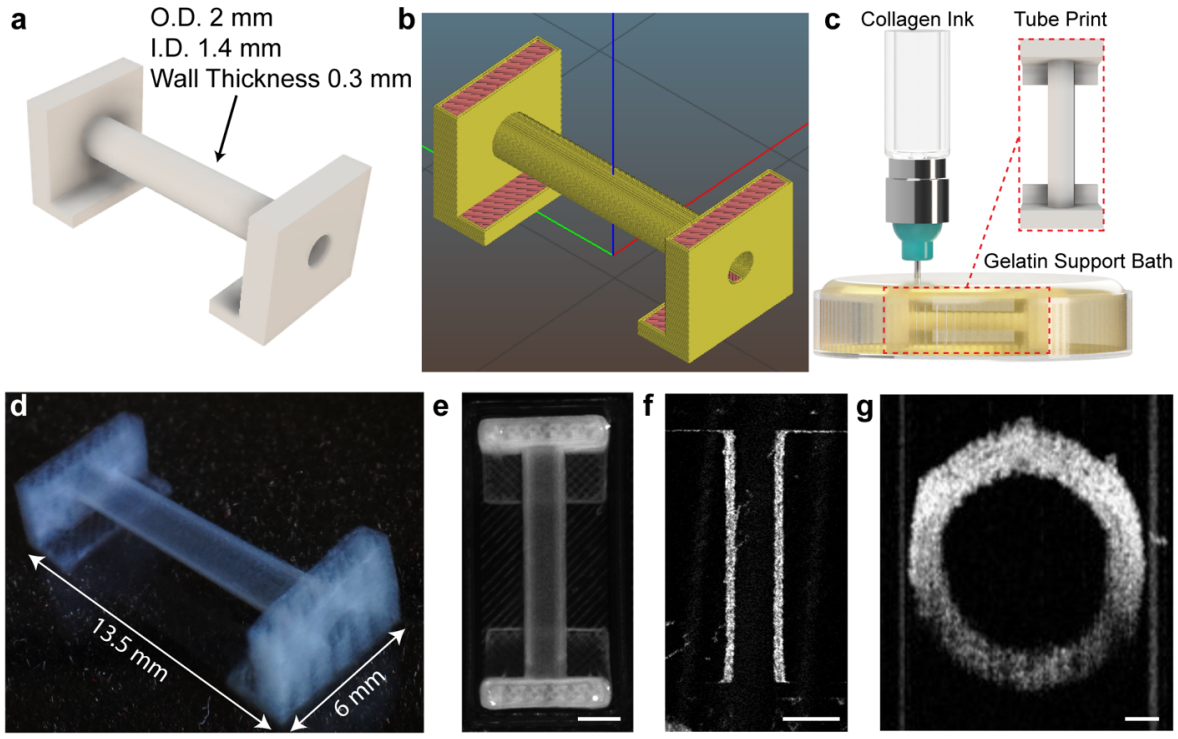

Fig 5.1: Heart Tube Printing. (A) A simplified 3D CAD model was first made to represent the linear heart tube. **(B)** A sliced model was then created to allow layer by layer 3D printing. **(C)** The collagen tube was printed using Freeform Reversible Embedding of Suspended Hydrogels (FRESH). Macroscopic images of tube structure in **(D)** isometric and **(E)** top down views. **(F)** A horizontal slice of the 3D OCT image showing the longitudinal axis of the tube and consistent wall thickness. **(G)** A vertical slice of the 3D OCT image showing the cross-section of the tube and consistent wall thickness. For panels **(E)** and **(F)** scale bars are 2 mm, and for panel **(G)** scale bar is 300 µm. Figure and data prepared by Jacqueline Bliley.

5.3.2. Formation of Cellularized Heart Tubes

To create the cellularized heart tubes, collagen tubes were placed in custom-fabricated PDMS wells (Figure 5.2A) designed to create a chamber around the tube for cell seeding. Rather than 3D printing the cardiac cells directly, I used a casting approach in order to rapidly cellularize many scaffolds and minimize cell handling time. For seeding, ESC-derived cardiomyocytes and primary cardiac fibroblasts at a 9:1 ratio were combined with a mixture of collagen type I and Matrigel and then cast around the 3D printed collagen tube (Figure 5.2B). Comparable to cast cardiac tissues in the literature[2,36], the cells rapidly compacted the gel around the collagen tubes to form a dense tissue layer (Figure 5.2C). Heart tubes displayed spontaneous and synchronous contractions 3-4 days after casting. Confocal images of the heart tube surface revealed dense layers of interconnected cardiomyocytes expressing sarcomeric α-actinin, a marker of z-lines within the myofibrils (Figure 5.2D). Higher magnification images confirmed that the cardiomyocytes were differentiated and expressed a dense network of striated myofibrils that were connected between adjacent cells (Figure 5.2E). It should be noted that cardiomyocytes did not appear to be aligned.

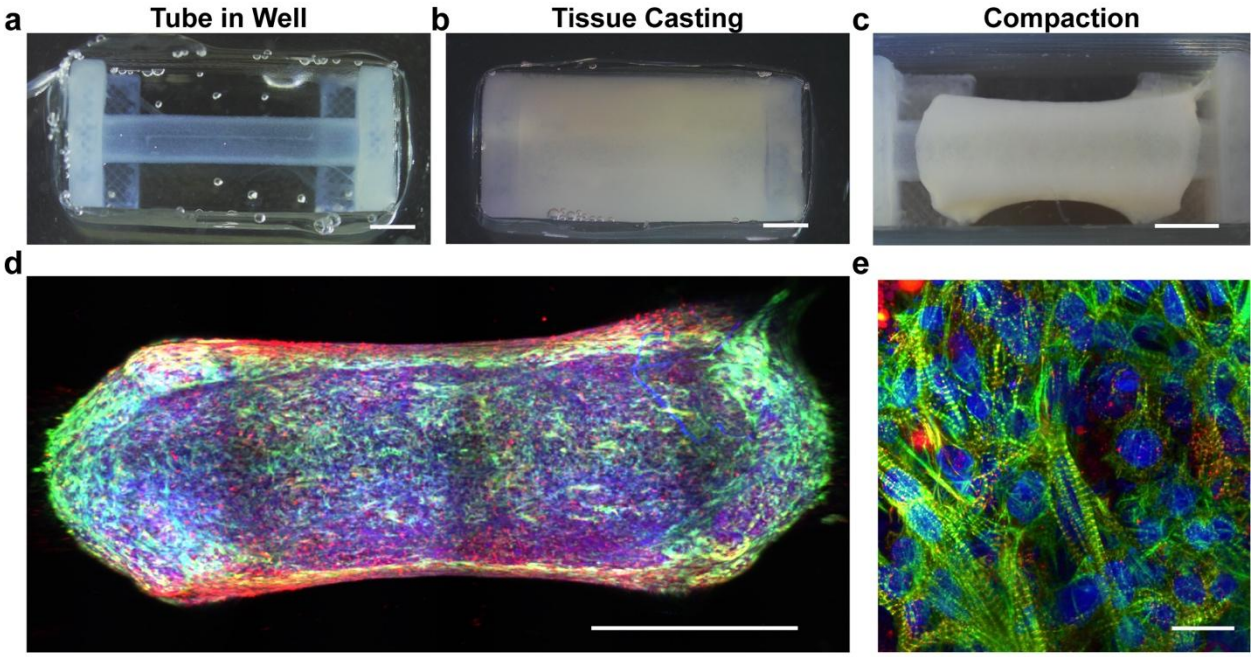

Fig 5.2. Heart Tube Formation. (A) The FRESH 3D bioprinted collagen heart tube scaffold is placed inside of a PDMS well to create a chamber of cell seeding. **(B)** Casting of cardiomyocytes and fibroblasts in a collagen gel around the collagen tube. **(C)** Cardiac fibroblasts compact the casted collagen gel with cardiomyocytes around the printed collagen tube forming the contractile heart tube. Scale bar is 2 mm. **(D)** Max intensity projection of heart tube surface showing cardiomyocytes positive for sarcomeric α-actinin (red), actin (green), and DAPI (blue). Scale bar is 2.5 mm. **(E)** High magnification images of heart tube surface showing densely interconnected and striated cardiomyocytes. Scale bar is 20 μm. Figure and data prepared by Jacqueline Bliley.

5.3.3. Calcium Activity and Action Potential Propagation

Electrophysiology of the contractile heart tubes was assessed using calcium imaging during spontaneous and paced contractions. Optical mapping of the engineered heart tube revealed anisotropic conduction along the longitudinal axis, with wavefronts consistently originating at one end and travelling to the other (Figure 5.3A). During spontaneous contractions, heart tubes had conduction velocities of 5.44 ± 1.04 cm/s, which is similar to that observed within the inner curvature of the early embryonic heart tube[11]. Fluorescent intensity analysis performed at different regions of interest (ROIs) of the heart tube showed similar waveform morphology and expected latency across the tissue (Figure 5.3B). Point stimulation at 1 Hz at one end of the heart tubes using a bipolar electrode was used to control the location of initial depolarization and achieve more

consistent propagation. In this case I observed a conduction velocity of 4.95 ± 1.49 cm/s (Figure 5.3C), which was not statistically different from the observed spontaneous conduction velocity. Comparing ROIs across the tissue demonstrated consistent waveform morphology and expected latency across the tissue under point stimulation (Figure 5.3D). Heart tubes field stimulated at 1 Hz showed synchronized contraction across the tissue and no calcium wave propagation, as expected (Figure 5.3E). Heart tubes were able to be consistently field stimulated at 1 and 2 Hz, however, at 3 Hz stimulation most tissues could not be consistently captured and displayed irregular calcium waveforms (Figure 5.3F).

5.3.4. Heart Tube Contractility

In order to investigate the ability of the engineered heart tubes to pump fluid, 10 μm fluorescent beads were injected into the tube lumen and their displacement during contraction was viewed just outside the tube lumen (Figure 5.4A). When the tissue was not actively contracting (diastole), beads were identified just outside the tube lumen (Figure 5.4B). They were then tracked frame-by-frame during contraction (systole) as the pressure inside the tube lumen increased and beads were displaced (Figure 5.4C). When bead displacement was tracked over multiple contractions, unidirectional pumping of the beads away from the tube lumen was observed with the tracks showing individual displacement of single beads (Figure 5.4D).

Because there are no valves present in the heart tubes, the net displacement was limited as the beads moved back and forth during the contractile cycle. This observation suggests that unidirectional calcium wave propagation across the tissue may result in a peristaltic-like wave that displaces beads away from the tube lumen over time; however, further research would be required to confirm this observation.

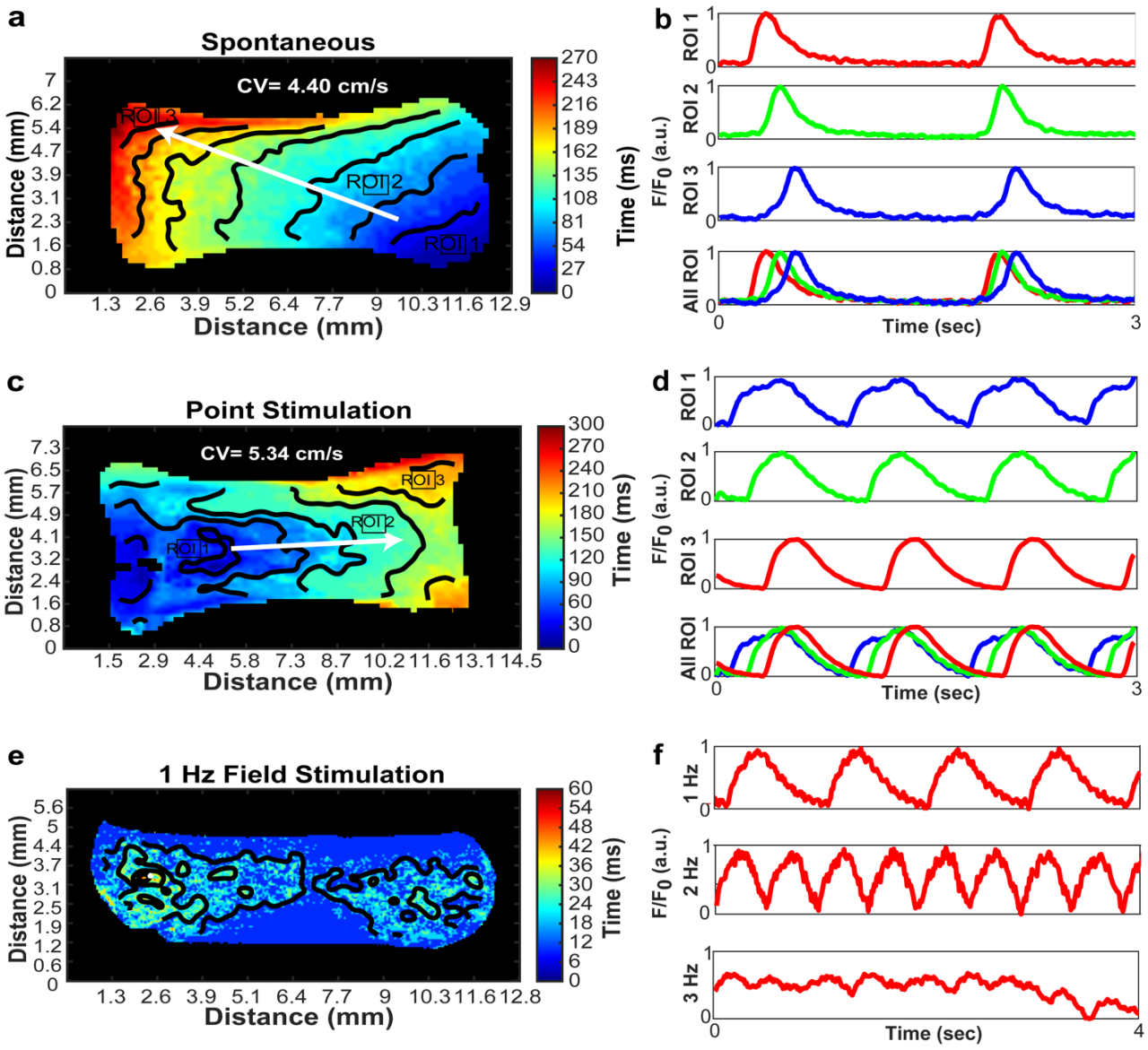

Fig 5.3: Heart Tubes Display Unidirectional Calcium Wave Propagation. (A) Calcium optical mapping during spontaneous beating. Image shows activation map of peak calcium intensity as it travels across the tissue. **(B)** Plots of relative calcium fluorescent intensity from different ROIs across the spontaneously beating heart tube. **(C)** Calcium activation map during 1 Hz point stimulation using a bipolar stimulating electrode. **(D)** Plots of relative calcium fluorescent intensity from different ROIs across the tissue. (E) Calcium activation map during field stimulation at 1 Hz. **(F)** Plots of relative calcium fluorescent intensity from an ROI at the center of the tissue showing calcium intensity at 1, 2 and 3 Hz field stimulation. Figure and data prepared by Jacqueline Bliley.

Peak bead velocity was ~1.5 mm/s, which increased to ~2 mm/s following field stimulation at 2 Hz (Figure 5.4E). Mean bead velocity was lower at ~0.35 mm/s due to the cyclical bead

displacement during each contraction, and only a small net displacement was observed. These results clearly show that the heart tube can displace fluid during each contraction, however, valves or other structural features to achieve directional flow are required to achieve higher net displacement.

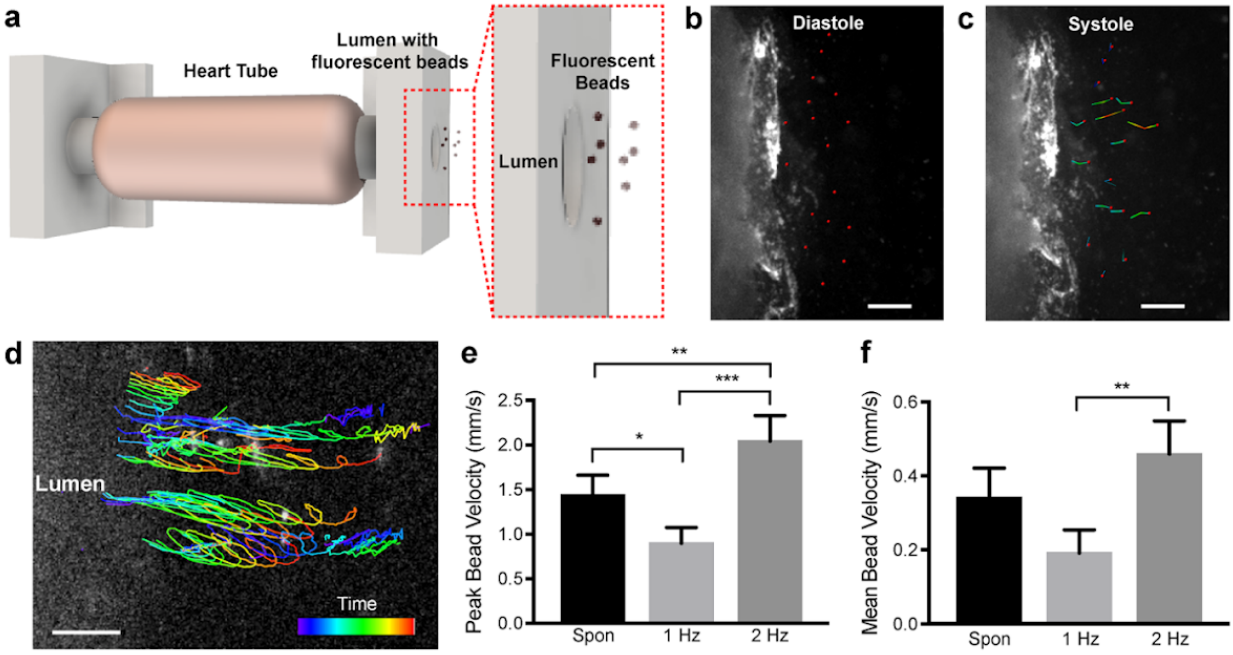

Fig 5.4: Heart Tubes Are able to Pump Fluid Based on Bead Displacement. (A) Schematic showing where fluorescent beads were tracked just outside of the tube lumen. **(B)** Bead tracking at diastole showing beads chosen for tracking. Scale bar is 300 µm. **(C)** Bead tracking at systole showing that beads are displaced after tissue contraction, which generates pressure in tube lumen. Scale bar is 300 µm. **(D)** Tracks of bead displacement over time showing that beads are unidirectionally displaced away from the tube lumen. Scale bar is 300 µm. **(E)** Graph of peak bead velocity under spontaneous, 1 Hz, and 2 Hz electrical stimulation. **(F)** Graph of mean bead velocity under spontaneous, 1 Hz, and 2 Hz electrical field stimulation. Data shown as mean ± SD. Statistics based on Kruskal-Wallis test with Dunn's multiple comparisons test (*p<0.01, ** p<0.01, ***p<0.0001). Figure and data prepared by Jacqueline Bliley.

5.4 Discussion

The goal of this study was to engineer a linear heart tube using human ESC-derived cardiomyocytes and assess basic structure, calcium wave propagation and pumping via displacement of fluorescent beads. This tube design was inspired by embryonic development, and the fabrication enabled with the FRESH 3D bioprinting approach[18]. Here, I demonstrated that

FRESH can be used to generate linear collagen tubes with high fidelity and that we can use a hydrogel casting approach to create contractile engineered heart tubes. The casting approach was purposely chosen because it enabled very rapid fabrication of the engineered tissue and minimized the amount of time the ESC-derived human cardiomyocytes were outside of the cell culture incubator.

Heart tubes had dense layers of interconnected cardiomyocytes and the spontaneous calcium wave propagation showed anisotropic conduction along the longitudinal axis of the heart tube. However, the cardiomyocytes themselves generally had an isotropic orientation within the tissue, suggesting that the tube shape itself is important for the conduction anisotropy. While the conduction velocity of ~5-6 cm/s is typically for many other cardiac tissues engineered from ESC-derived cardiomyocytes, it is possible that better cell alignment could produce and increase conduction velocity. Previous research has suggested that mechanical loading[3,13,19,38] and electrical stimulation[27,28] can guide alignment of cardiomyocytes, and a similar strategy could be used here to increase cardiomyocyte alignment, which could potentially aid in improving the calcium handling and pumping capability of our engineered heart tubes. Along with mechanical and electrical stimulation, several design features of the printed tube could also be altered to increase the ability of the tube to pump fluid, including decreasing the wall thickness and thus, increasing its ability to be deformed with cardiomyocyte contraction. Similarly, decreasing the tube diameter to physiologically relevant dimensions might also allow for the directional, peristaltic-like contractions seen in the engineered heart tube to further displace fluid out of the tube lumen. Incorporation of features that would ensure unidirectional pumping, such as valves, could also significantly aid in the unidirectional pumping of these engineered heart tubes. Previous work has

demonstrated the 3D bioprinting of functional valves[10,18] and incorporating these will be the focus of future work.

In comparison to embryonic development, the maximum pumping velocity I observed in our engineered heart tube is much lower than that observed in the embryonic linear heart tube, which ranges from 5-25 cm/s based on the developmental stage of the chick embryonic heart tube[5]. However, increased flow rates were observed when comparing this work to other engineered skeletal and heart muscle engineered tissue pumps, or so called "pump bots". For instance, Park et al. developed a hybrid micropump consisting of a dome-shaped membrane with attached cardiomyocytes to generate unidirectional displacement of beads at 3.78 μm/s, which is less than the average pumping velocity observed in our engineered heart tube[26]. Similarly, Li et al. created an impedance pump bot consisting of a engineered skeletal muscle ring wrapped around PDMS tubing and was able to achieve a maximum average flow rate of 39.9 μm/s, which is approximately an order of magnitude less than the average flow achieved with this engineered heart tube[20]. This could be due to the relative increase in size of our engineered heart muscle tissue compared to their much smaller skeletal muscle tissue ring; however, future work would need to be performed to validate this observation.

Finally, this design is a simplification of the embryonic linear heart tube shape and size. As noted, this engineered heart tube is larger than the embryonic heart tube (~1.4 mm diameter versus ~300 μm diameter). However, I wanted to test our design concept at this larger scale before printing the much smaller embryonic heart tube. It is possible to FRESH 3D print smaller heart tubes but will need to improve our print resolution using smaller collagen filaments to decrease the wall thickness. In terms of shape, Cetnar et al. 3D printed heart tubes based on patient-specific geometries to understand flow deviations in the developing heart[6]. These heart tubes were

fabricated with photocurable resins and could be endothelialized. However, cardiomyocytes were not included and thus they could not assess heart tube contractile function, calcium wave propagation and pumping capability. Future work will focus on combining more realistic heart tube shape and size with our collagen and cell printing capability in order to replicate more complex embryonic heart tube structure and function.

5.5 Conclusions

In conclusion, I have engineered a contractile human heart tube inspired by early embryonic development. I demonstrated that the heart tubes have dense layers of cardiomyocytes on their surface, display unidirectional calcium wave propagation, and are able to be electrically paced up to 2 Hz. Heart tubes were also able to displace fluorescent beads via generation of increased pressure within the tube lumen with each contraction.

5.6 Acknowledgements

Financial support was provided from Additional Ventures Single Ventricle Research Fund [to A.W.F.], National Institutes of Health [grant number DP2HL117750 to A.W.F.], the Office of Naval Research [grant number N00014-17-1-2566 to A.W.F.], and the Dowd Fellowship and Presidential Fellowship, Carnegie Mellon University [to J.M.B.].

5.7 References

1. Batalov, I., and A. W. Feinberg. Differentiation of cardiomyocytes from human pluripotent stem cells using monolayer culture. *Biomark. Insights* 10:71–76, 2015.
2. Bliley, J. M., M. Vermeer, R. Duffy, I. Batalov, D. Kramer, J. W. Tashman, D. J. Shiwarski, A. Lee, A. Teplenin, L. Volkers, B. Coffin, M. Hoes, A. Kalmykov, R. N. Palchesko, Y. Sun, J. D. H. Jongbloed, N. Bomer, R. A. de Boer, A. J. H. Suurmeijer, D. Pijnappels, M. C. Bolling, P. Van Der Meer, and A. W. Feinberg. Dynamic loading of human engineered heart tissue enhances contractile function and drives desmosome-linked disease phenotype. *bioRxiv* , 2020.

3. Boudou, T., W. R. Legant, A. Mu, M. A. Borochin, N. Thavandiran, M. Radisic, P. W. Zandstra, J. A. Epstein, K. B. Margulies, and C. S. Chen. A microfabricated platform to measure and manipulate the mechanics of engineered cardiac microtissues. *Tissue Eng. - Part A* , 2012.doi:10.1089/ten.tea.2011.0341
4. Burridge, P. W., E. Matsa, P. Shukla, Z. C. Lin, J. M. Churko, A. D. Ebert, F. Lan, S. Diecke, B. Huber, N. M. Mordwinkin, J. R. Plews, O. J. Abilez, B. Cui, J. D. Gold, and J. C. Wu. Chemically defned generation of human cardiomyocytes. *Nat. Methods* , 2014.doi:10.1038/nMeth.2999
5. Butcher, J. T., T. C. McQuinn, D. Sedmera, D. Turner, and R. R. Markwald. Transitions in early embryonic atrioventricular valvular function correspond with changes in cushion biomechanics that are predictable by tissue composition. *Circ. Res.* 100:1503–1511, 2007.
6. Cetnar, A. D., M. L. Tomov, L. Ning, B. Jing, A. S. Theus, A. Kumar, A. N. Wijntjes, S. R. Bhamidipati, K. P. Do, A. Mantalaris, J. N. Oshinski, R. Avazmohammadi, B. D. Lindsey, H. D. Bauser-Heaton, and V. Serpooshan. Patient-Specific 3D Bioprinted Models of Developing Human Heart. *Adv. Healthc. Mater.* 2001169:1–15, 2020.
7. Chong, J. J. H., X. Yang, C. W. Don, E. Minami, Y. W. Liu, J. J. Weyers, W. M. Mahoney, B. Van Biber, S. M. Cook, N. J. Palpant, J. A. Gantz, J. A. Fugate, V. Muskheli, G. M. Gough, K. W. Vogel, C. A. Astley, C. E. Hotchkiss, A. Baldessari, L. Pabon, H. Reinecke, E. A. Gill, V. Nelson, H. P. Kiem, M. A. Laflamme, and C. E. Murry. Human embryonic-stem-cell-derived cardiomyocytes regenerate non-human primate hearts. *Nature* 510:273–277, 2014.
8. Cui, H., C. Liu, T. Esworthy, Y. Huang, Z. X. Yu, X. Zhou, H. San, S. J. Lee, S. Y. Hann, M. Boehm, M. Mohiuddin, J. P. Fisher, and L. G. Zhang. 4D physiologically adaptable cardiac patch: A 4-month in vivo study for the treatment of myocardial infarction. *Sci. Adv.* , 2020.doi:10.1126/sciadv.abb5067
9. Deng, M. Cardiac Transplantation. *Heart* 87:177–184, 2002.
10. Grigoryan, B., S. J. Paulsen, D. C. Corbett, D. W. Sazer, C. L. Fortin, A. J. Zaita, P. T. Greenfield, N. J. Calafat, J. P. Gounley, A. H. Ta, F. Johansson, A. Randles, J. E. Rosenkrantz, J. D. Louis-Rosenberg, P. A. Galie, K. R. Stevens, and J. S. Miller. Multivascular networks and functional intravascular topologies within biocompatible hydrogels. *Science (80-.).* 364:458–464, 2019.
11. Gu, S., Y. T. Wang, P. Ma, A. A. Werdich, A. M. Rollins, and M. W. Jenkins. Mapping conduction velocity of early embryonic hearts with a robust fitting algorithm. *Biomed. Opt. Express* , 2015.doi:10.1364/boe.6.002138
12. Hinton, T. J., Q. Jallerat, R. N. Palchesko, J. H. Park, M. S. Grodzicki, H. J. Shue, M. H. Ramadan, A. R. Hudson, and A. W. Feinberg. Three-dimensional printing of complex biological structures by freeform reversible embedding of suspended hydrogels. *Sci. Adv.* 1:, 2015.
13. Hirt, M. N., N. A. Sörensen, L. M. Bartholdt, J. Boeddinghaus, S. Schaaf, A. Eder, I. Vollert, A. Stöhr, T. Schulze, A. Witten, M. Stoll, A. Hansen, and T. Eschenhagen. Increased afterload induces pathological cardiac hypertrophy: A new in vitro model. *Basic Res. Cardiol.* , 2012.doi:10.1007/s00395-012-0307-z
14. Jackman, C. P., A. M. Ganapathi, H. Asfour, Y. Qian, B. W. Allen, Y. Li, and N. Bursac. Engineered cardiac tissue patch maintains structural and electrical properties after epicardial implantation. *Biomaterials* , 2018.doi:10.1016/j.biomaterials.2018.01.002
15. Kupfer, M. E., W. H. Lin, V. Ravikumar, K. Qiu, L. Wang, L. Gao, D. B. Bhuiyan, M. Lenz, J. Ai, R. R. Mahutga, D. W. Townsend, J. Zhang, M. C. McAlpine, E. G. Tolkacheva, and B. M. Ogle. In Situ Expansion, Differentiation, and Electromechanical Coupling of Human Cardiac Muscle in a 3D Bioprinted, Chambered Organoid. *Circ. Res.* , 2020.doi:10.1161/CIRCRESAHA.119.316155
16. Laflamme, M. A., K. Y. Chen, A. V. Naumova, V. Muskheli, J. A. Fugate, S. K. Dupras, H. Reinecke, C. Xu, M. Hassanipour, S. Police, C. O'Sullivan, L. Collins, Y. Chen, E. Minami, E. A. Gill, S. Ueno, C. Yuan, J. Gold, and C. E. Murry. Cardiomyocytes derived from human embryonic stem cells in pro-survival factors enhance function of infarcted rat hearts. *Nat. Biotechnol.* 25:1015–1024, 2007.
17. Lee, A., A. R. Hudson, D. J. Shiwarski, J. W. Tashman, T. J. Hinton, S. Yerneni, J. M. Bliley, P. G. Campbell, and A. W. Feinberg. 3D bioprinting of collagen to rebuild components of the human heart. *Science (80-.).* , 2019.doi:10.1126/science.aav9051
18. Lee, A., A. R. Hudson, D. J. Shiwarski, J. W. Tashman, T. J. Hinton, S. Yerneni, J. M. Bliley, P. G. Campbell, and A. W. Feinberg. 3D bioprinting of collagen to rebuild components of the human heart. *Science (80-.).* , 2019.doi:10.1126/science.aav9051
19. Leonard, A., A. Bertero, J. D. Powers, K. M. Beussman, S. Bhandari, M. Regnier, C. E. Murry, and N. J. Sniadecki. Afterload promotes maturation of human induced pluripotent stem cell derived cardiomyocytes in engineered heart tissues. *J. Mol. Cell. Cardiol.* , 2018.doi:10.1016/j.yjmcc.2018.03.016
20. Li, Z., Y. Seo, O. Aydin, M. Elhebeary, R. D. Kamm, H. Kong, and M. A. Taher Saif. Biohybrid valveless

pump-bot powered by engineered skeletal muscle. *Proc. Natl. Acad. Sci. U. S. A.* 116:1543–1548, 2019.
21. Lian, X., J. Zhang, S. M. Azarin, K. Zhu, L. B. Hazeltine, X. Bao, C. Hsiao, T. J. Kamp, and S. P. Palecek. Directed cardiomyocyte differentiation from human pluripotent stem cells by modulating Wnt/??-catenin signaling under fully defined conditions. *Nat. Protoc.* 8:162–175, 2013.
22. Macqueen, L. A., S. P. Sheehy, C. O. Chantre, J. F. Zimmerman, F. S. Pasqualini, X. Liu, J. A. Goss, P. H. Campbell, G. M. Gonzalez, S. J. Park, A. K. Capulli, J. P. Ferrier, T. Fettah Kosar, L. Mahadevan, W. T. Pu, and K. K. Parker. A tissue-engineered scale model of the heart ventricle. *Nat. Biomed. Eng.* , 2018.doi:10.1038/s41551-018-0271-5
23. Mandrycky, C. J., N. P. Williams, I. Batalov, D. El-Nachef, B. S. de Bakker, J. Davis, D. H. Kim, C. A. DeForest, Y. Zheng, K. R. Stevens, and N. J. Sniadecki. Engineering Heart Morphogenesis. , 2020.doi:10.1016/j.tibtech.2020.01.006
24. Noor, N., A. Shapira, R. Edri, I. Gal, L. Wertheim, and T. Dvir. 3D Printing of Personalized Thick and Perfusable Cardiac Patches and Hearts. *Adv. Sci.* , 2019.doi:10.1002/advs.201900344
25. Ott, H. C., T. S. Matthiesen, S. K. Goh, L. D. Black, S. M. Kren, T. I. Netoff, and D. A. Taylor. Perfusion-decellularized matrix: Using nature's platform to engineer a bioartificial heart. *Nat. Med.* 14:213–221, 2008.
26. Park, J., I. C. Kim, J. Baek, M. Cha, J. Kim, S. Park, J. Lee, and B. Kim. Micro pumping with cardiomyocyte-polymer hybrid. *Lab Chip* 7:1367–1370, 2007.
27. Radisic, M., H. Park, H. Shing, T. Consi, F. J. Schoen, R. Langer, L. E. Freed, and G. Vunjak-Novakovic. Functional assembly of engineered myocardium by electrical stimulation of cardiac myocytes cultured on scaffolds. *Proc. Natl. Acad. Sci. U. S. A.* , 2004.doi:10.1073/pnas.0407817101
28. Ronaldson-Bouchard, K., S. P. Ma, K. Yeager, T. Chen, L. J. Song, D. Sirabella, K. Morikawa, D. Teles, M. Yazawa, and G. Vunjak-Novakovic. Advanced maturation of human cardiac tissue grown from pluripotent stem cells. *Nature* 556:239–243, 2018.
29. Savarese, G., and L. H. Lund. Global Public Health Burden of Heart Failure. *Card. Fail. Rev.* , 2017.doi:10.15420/cfr.2016:25:2
30. Stevens, K. R., L. Pabon, V. Muskheli, and C. E. Murry. Scaffold-free human cardiac tissue patch created from embryonic stem cells. *Tissue Eng. - Part A* , 2009.doi:10.1089/ten.tea.2008.0151
31. Tashman, J. W., D. J. Shiwarski, and A. W. Feinberg. A high performance open-source syringe extruder optimized for extrusion and retraction during FRESH 3D bioprinting. *HardwareX* 9:1–18, 2021.
32. Tohyama, S., F. Hattori, M. Sano, T. Hishiki, Y. Nagahata, T. Matsuura, H. Hashimoto, T. Suzuki, H. Yamashita, Y. Satoh, T. Egashira, T. Seki, N. Muraoka, H. Yamakawa, Y. Ohgino, T. Tanaka, M. Yoichi, S. Yuasa, M. Murata, M. Suematsu, and K. Fukuda. Distinct metabolic flow enables large-scale purification of mouse and human pluripotent stem cell-derived cardiomyocytes. *Cell Stem Cell* 12:127–137, 2013.
33. Tzahor, E., and K. D. Poss. Cardiac regeneration strategies: Staying young at heart. *Science (80-.).* 356:1035–1039, 2017.
34. Virani, S. S. *et al.* Heart disease and stroke statistics—2020 update: A report from the American Heart Association. , 2020.doi:10.1161/CIR.0000000000000757
35. Weinberger, F., K. Breckwoldt, S. Pecha, A. Kelly, B. Geertz, J. Starbatty, T. Yorgan, K. H. Cheng, K. Lessmann, T. Stolen, S. C. Marielle, G. Smith, H. Reichenspurner, A. Hansen, and T. Eschenhagen. Cardiac repair in Guinea pigs with human engineered heart tissue from induced pluripotent stem cells. *Sci. Transl. Med.* , 2016.doi:10.1126/scitranslmed.aaf8781
36. Zhao, Y., N. Rafatian, N. T. Feric, B. J. Cox, R. Aschar-Sobbi, E. Y. Wang, P. Aggarwal, B. Zhang, G. Conant, K. Ronaldson-Bouchard, A. Pahnke, S. Protze, J. H. Lee, L. Davenport Huyer, D. Jekic, A. Wickeler, H. E. Naguib, G. M. Keller, G. Vunjak-Novakovic, U. Broeckel, P. H. Backx, and M. Radisic. A Platform for Generation of Chamber-Specific Cardiac Tissues and Disease Modeling. *Cell* , 2019.doi:10.1016/j.cell.2018.11.042
37. Zimmermann, W. H., M. Didié, G. H. Wasmeier, U. Nixdorff, A. Hess, I. Melnychenko, O. Boy, W. L. Neuhuber, M. Weyand, and T. Eschenhagen. Cardiac grafting of engineered heart tissue in syngenic rats. *Circulation* , 2002.doi:10.1161/01.cir.0000032876.55215.10
38. Zimmermann, W. H., I. Melnychenko, and T. Eschenhagen. Engineered heart tissue for regeneration of diseased hearts. *Biomaterials* , 2004.doi:10.1016/S0142-9612(03)00521-0
39. Zimmermann, W. H., I. Melnychenko, G. Wasmeier, M. Didié, H. Naito, U. Nixdorff, A. Hess, L. Budinsky, K. Brune, B. Michaelis, S. Dhein, A. Schwoerer, H. Ehmke, and T. Eschenhagen. Engineered heart tissue grafts improve systolic and diastolic function in infarcted rat hearts. *Nat. Med.* , 2006.doi:10.1038/nm1394

Chapter 6

Programmed Tube Bending Morphogenesis of a 3D Bioprinted Heart Tube

6.1 Introduction

The adult heart has little capacity to repair itself following significant damage, such as that due to toxicity or following coronary artery obstruction (myocardial infarction)[29]. In fact, following significant damage, it is common for the heart to undergo progressive structural and functional remodeling culminating in heart failure, a condition where heart is unable to pump enough blood to meet the body's demands. Under these circumstances, a heart transplant is the gold standard of care, but unfortunately, there is limited donor heart organ supply[5]. Thus, strategies to increase whole heart organ availability are needed.

The field of cardiac tissue engineering was developed with the hope of generating heart tissues and organs that are capable of repairing or replacing the damaged human heart. To date, many of our current engineering strategies have focused on using the adult heart macroscopic organ as a template, but we are currently unable to achieve adult heart function. For instance, heart tissue decellularization methods have been able to achieve unparalleled heart organ extracellular matrix structure but there are significant challenges with recellularization, directing cells to their appropriate spatial locations within the tissue, and achieving heart organ structures with adult-level functional output[14,18,21]. For instance, Ott et al. showed recellularized rat hearts had 2% of the contractile function of adult rat hearts, which could be due to the low cell infiltration observed in these studies (~33% 1-2 mm from injection site)[18]. Alternatively, several advanced biofabrication strategies, such as 3D printing, have created ventricles[12,15], or even simplified versions of whole

hearts[11,17], but still are only able to accomplish a fraction of the function observed in the adult human heart. For example, Kupfer et al. creating a simplified version of a whole heart by printing human pluripotent stem cells and subsequently differentiating them into cardiomyocytes in 3D[10]. This construct only achieved ~1.1% of the ejection fraction observed in the adult human heart. Thus, it is evident that there are still major challenges that exist in being able to replicate adult heart organ structure and function in engineered heart tissues and organs.

A limitation of these previously described techniques is that they assume that adult heart macroscopic structure will yield adult heart function. However, much of what we know from embryogenesis suggests that morphogenesis, or changes in the structure and shape of a developing tissues and organs, imparts specific mechanical stresses and strains that are critical to later organ structure and function. This is particularly evident in the case of heart morphogenesis, where the heart tube undergoes bending, looping, and septation to form its mature three-dimensional structure. Further, it has been observed that deviations in this process can contribute to the formation of congenital heart defects. This finding is also further supported by the fact that the heart morphogenesis process is evolutionarily conserved[4], with many animals undergoing a similar sequence or portion of heart morphogenesis. Further, there is also a case for convergent evolution of heart structure, where similar morphogenesis pathways and heart structures have evolved independently in distinct species[19]. This suggests that the template for heart morphogenesis may be the best way to make a heart.

Thus, an alternative approach to using the adult heart as a structural template to generate heart organs, would be to use embryonic heart morphogenesis as a guiding principle to develop whole heart organs. During morphogenesis, the heart first starts as a linear tube that then bends, loops, and septates to form its mature 4-chambered structure. This complex change in shape is

accompanied by changes in tissue loads, which can contribute to later heart structure and function. In this chapter, I sought to replicate the tissue bending observed in morphogenesis process by inserting structural and mechanical asymmetries with 3D printing to drive heart tube bending following application of cardiac fibroblast compaction forces. I found that the heart tube bending process resulted in region specific changes in heart tube structure and function. This work suggests that the heart morphogenesis process and its impact on the structure and function should be considered in the fabrication of whole heart organs.

6.2 Materials and Methods

6.2.1. Cardiomyocyte Differentiation and Purification

Cardiomyocytes were differentiated from HES3 (ES03, Wicell) human embryonic stem cells (ESCs) based on previously described methods[2,13]. Prior to differentiation, ESCs were maintained on Geltrex (A1413301, Life Technologies)-coated (12 μg/cm^2) 6 well plates in Essential 8 medium[3] and passaged every 4 days (~80% confluence). For differentiation, HES 3 ESCs were seeded on Geltrex-coated T75 flasks with daily E8 media changes for 3 days. At 80% confluence (Day 0 of differentiation), cells were washed with 1x PBS and media was switched to RPMI-1640 (21870076, Thermofisher) supplemented with 1% v/v L-glutamine (25030081, Thermofisher), B27 supplement (17504044, Thermofisher), and 6 μM CHIR99201 (C-6556, LC laboratories). On day 2 of differentiation, cells were washed with 1X PBS and media was changed to RPMI-1640 (21870076, Thermofisher) supplemented with 1% v/v L-glutamine (25030081, Thermofisher), B27 supplement (17504044, Thermofisher), and 2 μM Wnt C-59 (S7037, Selleck Chemicals). On days 4 and 6, cells were switched to RPMI 1640 media (21870076, Thermofisher) containing 1% v/v L-glutamine (25030081, Thermofisher) and B27 supplement (17504044,

Thermofisher). On days 8 and 10, medium was changed to CDM3 media, consisting of RPMI-1640 supplemented with 1% v/v L glutamine, 213 μg/mL L-Ascorbic acid 2-phosphate sesquimagnesium salt hydrate >95% (A8960, Sigma), and 500 μg/mL human albumin (A9731, Sigma). On day 12, spontaneously beating cells were passaged for lactate-based metabolic selection of cardiomyocytes[28].

To passage for cardiomyocyte purification, cells were incubated with TrypLE for 15 mins at 37°C to enable single cell dissociation. Cells were then reseeded in CDM3L, consisting of RPMI-1640 without glucose (11879020, Thermofisher) supplemented with 7.1 mM sodium-lactate (L4263, Sigma), 213 μg/mL L-Ascorbic acid 2-phosphate sesquimagnesium salt hydrate >95% (A8960, Sigma), and 500 μg/mL human albumin (A9731, Sigma). Cells were maintained in CDM3L for several days before replacing back to CDM3 medium.

6.2.2. Cardiac Ventricular Fibroblast Culture

Normal human primary ventricular cardiac fibroblasts (CC-2904, Lonza) were obtained and cultured via manufacturer's instructions. Fibroblasts were cultured at an initial density of 5,000 cells per cm^2 in FGM-3 media (CC-4526, Lonza) and passaged prior to reaching 80% confluence. Fibroblasts were used between passage 5 and passage 8 for these studies.

6.2.3. Bioprinter Setup

Two bioprinters were used to print the collagen tubes. First, a MakerGear 3D printer, which was modified to allow for bioprinting. Second, a custom high-precision bioprinter was assembled using a precision ballscrew z stage (MX80S, Parker-Hannefin) and a microscope stage (H117, Prior Scientific) mounted in a cartesian setup using extruded aluminum profiles. Mounted to the Z

stage was a Replistruder 4 high-precision open-source syringe pump[27], used with a 2.5 mL gastight syringe (1000 series, Hamilton). The stages and syringe pump were controlled using a Duet 3 6HC (Duet3D) motion control board with a raspberry pi microcontroller running a dedicated user interface with mouse, keyboard, and display.

6.2.4. FRESH Slurry Support Bath Generation

FRESH v2.0 gelatin support bath was prepared using previously described methods[12]. Briefly, 2% w/v Gelatin B (G7, Fisher Chemicals), 0.25% w/v Pluronic® F-127 (P2443, Sigma Aldrich), and 0.5% w/v Gum Arabic (G9752, Sigma-Aldrich) were dissolved in 50% v/v ethanol solution at 45°C in a 1 liter beaker. The pH was then adjusted to 5.8 by dropwise addition of 2N hydrochloric acid. The beaker was then placed under an overhead stirrer at ~600 RPM (IKA, Model RW20), sealed with parafilm, and allowed to cool to room temperature while stirring overnight. The resulting slurry was evenly distributed in 50 mL conical tubes and centrifuged at 300g for 3 minutes. The slurry was then washed three times in distilled water followed by three times in in 50 mM HEPES (61-034-RO, Corning) with centrifuging at 2000g for 3 mins. The washed slurry was stored at 4°C prior to printing.

6.2.5. Finite Element Modelling (FEM)

FEM of tube deformation following fibroblast compaction was performed in ANSYS software (ANSYS, inc). Briefly, computer aided design (CAD) models were created in ANSYS SpaceClaim Software. Material properties and elastic moduli were derived from compression stress-strain curves of 3D printed collagen discs[12]. The 3D printed collagen was assumed to be incompressible. Modelling was performed by applying a pressure to the outside of the tube and by

observing displacements of the tube ends. Mesh size was initially computer generated but then was validated using a convergence plot with a <10% change in displacement being considered acceptable.

6.2.6. FRESH Printing of Tubes

Digital models of the heart tube were created using Fusion 360 (Autodesk) CAD software and then exported as an STL file format. To generate G-code instructions for the printer, STL files were sliced in Slic3r (version 1.3.0, https://slic3r.org/). In general, slicer settings were a print speed of 10 mm/s, 2 perimeters, 30% infill, 35 µm layer height, 0.2 mm retraction length, and a 2 mm z-hop. Collagen type I bioink (LifeInk 200, Advanced Biomatrix) was prepared by addition of 0.24 M acetic acid in a 2:1 ratio with the 35 mg/mL collagen stock concentration to create a 24 mg/mL acidic collagen solution. This bioink was then centrifuged at 3000g for 5 mins to remove air bubbles and transferred to a gas-tight, 2.5 mL syringe with an 80 µm needle (JG34-0.25HPX, Jensen Global). To compact the support bath for printing, tubes were degassed for 30 minutes to remove air bubbles and then centrifuged at 1800g for 3 minutes. The supernatant was removed, and compacted slurry was transferred to a Petri dish and secured onto the print bed. Upon print completion, the Petri dish was removed from the print bed and placed in a 37°C incubator for 45 mins to melt the support bath. Prints were then transferred to 50 mM HEPES solution and placed in a rotating 37°C incubator for an 1 hour to remove excess gelatin. Finally, printed heart tubes were sterilized with UV for 15 min and stored in 50 mM HEPES supplemented with 1% v/v penicillin streptomycin prior to cardiomyocyte casting.

6.2.7. Optical Imaging of Printed Tubes

Printed heart tubes were imaged under brightfield with a stereomicroscope (SMZ1000, Nikon) using both a digital SLR camera (Model 70D, Canon) and a Prime 95B Scientific CMOS camera (Photometrics). In addition, 3D imaging was performed using a 1300 nm optical coherence tomography (OCT) system (VEG210C1, ThorLabs). ImageJ and Imaris 9.1 (Bitplane) were used for visualization and 3D renderings. For OCT imaging, both 2D linescan and 3D volumetric imaging modes were used.

6.2.8. Fibroblast and Heart Muscle Tissue Casting and Culture

To hold the printed tubes in place during the tissue casting process, polydimethylsiloxane (PDMS) wells were first created. To do this, negative molds were 3D printed with polylactic acid filament (MK3S+, Prusa) and then PDMS was cast around them in 6 well plates and cured overnight at 65°C. The Sylgard 184 PDMS (Dow Corning) was mixed at a 10:1 weight ratio of base to curing agent in a Thinky conditioning mixer (Phoenix Equipment Inc.) using a 2 min 2000 RPM mixing cycle followed by a 2 min 2000 RPM defoaming cycle. The PDMS wells in the 6 well plate were then sterilized with UV-Ozone for 15 mins. PDMS wells were treated with 1% w/v Pluronic® F-127 to limit casted tissue attachment to the PDMS well. Sterile heart tubes were then placed in the PDMS wells and submerged in sterile 50 mM HEPES with 1% v/v penicillin-streptomycin until tissue casting.

To cast tissues around the printed tubes, either fibroblasts alone (3 million/mL) or cardiomyocytes and fibroblasts (18.75 million cells/mL) were combined in a 9:1 ratio within a mixture of collagen type I derived from rat tail (354249, Corning) and Matrigel (354263, Corning). The final concentrations were 1 mg/mL collagen type I, 1.7 mg/mL Matrigel, 10% v/v 10X PBS,

and 2.3% v/v 1N NaOH. Next, the HEPES solution was removed from the PDMS wells and each printed tube was covered with 375 μL of cell and ECM solution. Constructs were then incubated at 37°C for 1 hour to gel collagen and Matrigel and then covered in media consisting of RPMI-1640 supplemented with 1% v/v KnockOut™ Serum Replacement (10828028, Thermofisher) and 1:1000 MycoZap Plus CL (VZA-2012, Lonza). Heart tubes were maintained in media for 14 days, which was changed every 2 days.

6.2.9. Calcium Imaging

Calcium imaging was performed on heart tubes during spontaneous and paced contractions after 14 days in culture. Briefly, heart tubes were stained with Cal520 (21130, AAT Bioquest) based on previously described methods[12]. An excitation-contraction decoupler, 10 μM Blebbistatin (B0560, Sigma), was used to prevent spontaneous contractions of the heart tubes that would preclude automated analysis. Heart tubes were field stimulated using paired parallel platinum electrodes immersed in the Tyrodes solution and point stimulated with a concentric bipolar microelectrode (30202, FHC Inc.) composed of an inner platinum-iridium pole and outer stainless-steel pole. Tubes were imaged on a custom heated stage maintaining the temperature at 37°C ±1°C using the fluorescent stereomicroscope. Calcium transients were analyzed using custom MATLAB code (R2019, MathWorks) using signal peak times and cross correlation to create activations maps and calculate conduction velocities, as previously published[12].

6.2.10. Immunofluorescent Staining, Tissue Clearing, and Imaging

Heart tubes were stained and imaged whole mount to assess their structure. Tubes were fixed in 4% paraformaldehyde (Electron Microscope Sciences) in 1X PBS supplemented with

1:200 Triton-X 100 (9002-93-1, Sigma) for 1 hour. Next, tubes were washed 3 times for 30 mins each in 1X PBS on a rotary shaker. Samples were then blocked in 5% goat serum in 1X PBS overnight on a shaker followed by washing 3 times for 30 min in 1X PBS. Mouse anti-sarcomeric α-actinin antibody (A7811, Sigma-Aldrich) was diluted to 1:100 in 1X PBS and incubated with the tissues overnight on a shaker. Tubes were then washed 3 times for 30 mins each in 1X PBS before incubating with 1:200 DAPI (D1306, Molecular Probes), 3:200 phalloidin conjugated with Alexa-Fluor 488 (A12379, Life Technologies), and 1:100 goat anti-mouse antibody conjugated with Alexa-Fluor 555 (A21422, Life Technologies) in 1X PBS overnight on a shaker. After the final incubation step, samples were rinsed 3 times for 30 mins each in 1X PBS. To image the entire tube structure, a tissue clearing technique was employed[8,9]. Briefly, tissues were dehydrated in successive series of solutions containing increasing isopropanol (25%, 50%, 75% and 100% v/v in 1x PBS). After the final dehydration step, the isopropanol solution was replaced with a 1:2 solution of benzyl alcohol to benzyl benzoate (BABB) for one hour at room temperature, which yielded a clear tissue that was difficult to see with the naked eye. The fluorescently stained heart tubes were imaged with a Nikon A1R microscope in either confocal or multiphoton mode.

6.2.11. Actin Alignment Analysis

Maximum intensity projections of z-stacks were used for actin alignment analysis (cardiomyocyte alignment). A custom MATLAB code was used to quantify the angular distribution of actin filaments[25]. Briefly, actin filaments were thresholded. The α-actinin channel was then used to create a binary mask for cardiomyocyte locations, which was used to determine cardiomyocyte alignment. Angular distribution of actin filaments was then used to calculate the orientational order parameter (OOP)—a measure of alignment, where OOP values close to 1

indicate completely coaligned actin filaments and values close to 0 indicate an isotropic distribution of actin filaments. An average OOP was obtained for each sample by considering angular distributions of actin filaments within all z-stacks.

6.2.12. Statistics

All graphs were created and statistical analyses performed using GraphPad Prism 7. Appropriate statistical tests were chosen based on experimental conditions and data. Statistical significance was considered a p-value less than 0.05.

6.3 Results

6.3.1. Asymmetric Tubes Bend with Applied Fibroblast Tube Compaction Forces

Previous research has utilized fibroblast compaction to drive tissue bending and folding[7]. Similar to this work, I plan to use material mechanics and compaction of fibroblasts to drive changes in tissue shape. However, instead of altering fibroblast patterning to induce tissue folding, I hypothesized that we could create tube models that would deform in a specific direction by first inserting planned structural asymmetries in the tube wall using 3D printing (Figure 6.1). Then, I planned to use fibroblast compaction to apply a force to these tubes causing them to deform in a certain direction. To do this, I created computer aided design (CAD) tube models with a thinner wall on one side (150 μm) and a thicker wall (450 μm) on the other side, which were denoted asymmetric tubes (Figure 6.1B). As a control, I created tubes with constant wall thickness along their cross-section (300 μm), which were called symmetric tubes (Figure 6.1A). Finite element modeling (FEM) was used to observe model deformation following application of fibroblast compaction forces. Following application of a uniform pressure to the outside of the tube models,

I observed two distinct deformations in symmetric and asymmetric tubes. Symmetric tubes tended to compress along their length, whereas asymmetric tubes tended to bend with the thinner wall compressing more than the thicker wall (Supplemental Figure 1). However, because I was also interested in evaluating the assumption that the force applied during compaction was uniform in every direction, I made two different asymmetric tube models, where the thinner wall was either located on the side of the cross-section (Asymmetric Side) or the bottom of the cross-section (Asymmetric Bottom). Following creation of CAD designs (Figure 6.2A-D), tube models were printed out of type I collagen using FRESH 3D bioprinting based on previously reported methods[12]. Optical coherence tomography of the tube cross-section revealed that 3D printed tubes accurately depicted the dimensions of the CAD model. Printed symmetric tubes had a constant wall thickness of ~300 µm along the cross-section, whereas asymmetric tubes had a thinner wall on one side of the cross-section (~150 µm) and a thicker wall on the other (~450 µm) (Figure 6.2C-D). OCT imaging of tube cross-sections validated that I could print

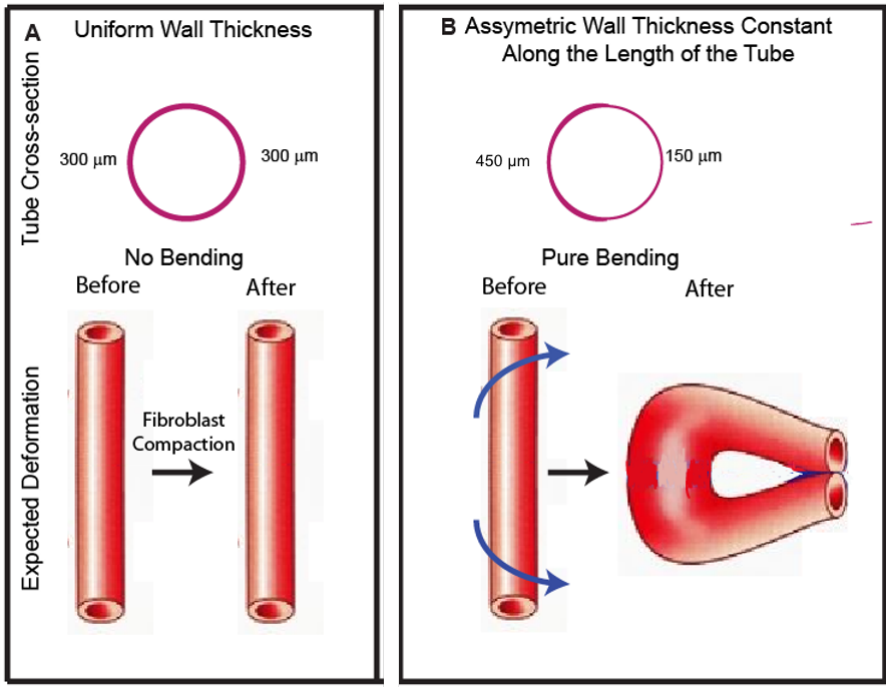

Figure 6.1 Proposed Tube Model and Expected Deformations. (A) Symmetric tubes have a uniform wall thickness (~300 µm) along their length and I would expect them to stay linear following fibroblast compaction. **(B)** Asymmetric tubes have a thinner wall (150 µm) on one side of the cross-section and a thicker wall (450 µm) on the other. I hypothesized they would undergo pure bending following fibroblast compaction. Figure prepared by Jacqueline Bliley.

symmetric and asymmetric tubes as intended (Figure 6.2E-G). Fibroblast tissues were then cast around the different tube designs (Figure 6.2H). Following fibroblast compaction, symmetric tubes stayed straight and did not bend. In contrast, asymmetric tubes bent with fibroblast compaction. The direction of bending was determined by location of the thinner wall where the side with thinner wall tended to form the inner curvature of the bent tube. This implies that asymmetric tube bending observed was specific to the type of design, either asymmetric bottom or asymmetric side. Interestingly, the time scale of deformation appeared to be different between asymmetric side and asymmetric bottom models with asymmetric bottom models achieving maximum deformation within 1-2 days of casting. In contrast, maximum deformation of asymmetric side tubes occurred approximately one week after casting. Although asymmetric side and bottom tube designs appeared to achieve similar amounts of bending, it appears initial compaction forces were greatest along the longitudinal axis of the tube length based on the expedited deformation of asymmetric bottom tubes. Because heart tube bending is a relatively rapid process (occurs over a period of couple days), the asymmetric bottom model was used for all subsequent studies[23].

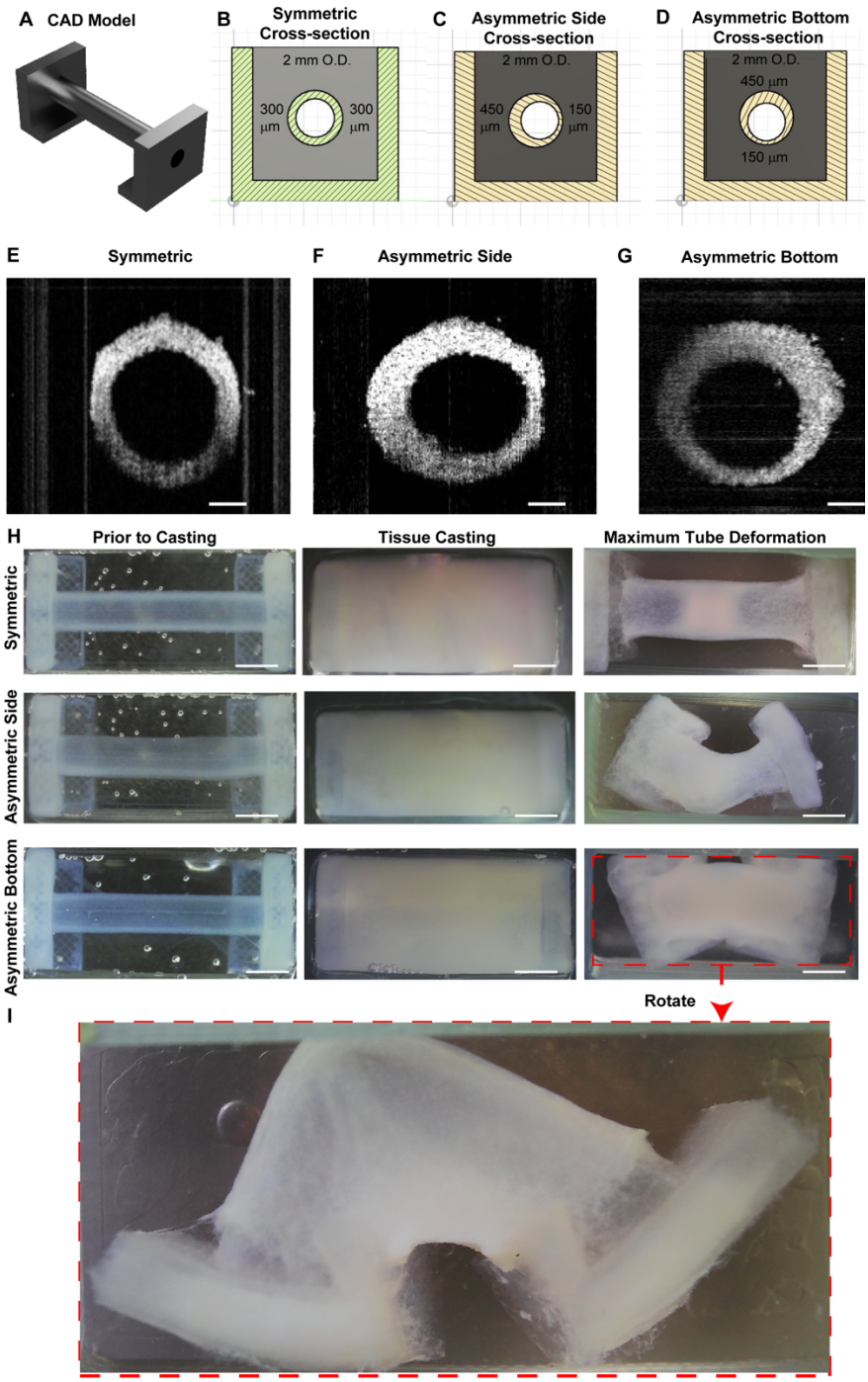

Figure 6.2. Tube Bending with Fibroblast Compaction Forces. (A) Computer aided design (CAD) model of tube model used for fibroblast compaction studies. **(B)** Cross-section of symmetric tube CAD model. **(C)** Cross-section of asymmetric side tube CAD model. **(D)** Cross-section of asymmetric bottom tube CAD model. OCT imaging of tube cross-sections of symmetric tube **(E)** asymmetric side tube, and asymmetric bottom tube **(F). (H)** Fibroblast compaction studies around different tube models where far right panel shows maximum tube deformation initially observed in the well. **(I)** Asymmetric bottom tube rotated within well to show maximum tube deformation. Figure and data prepared by Jacqueline Bliley.

6.3.2. Engineered Heart Tissues Cast Around Asymmetric Tubes Bend And Demonstrate A Trend Towards Increased Cardiomyocyte Alignment

To determine if heart muscle tissues cast around asymmetric tubes would similarly bend, I cast cardiomyocytes and cardiac fibroblasts within a collagen/Matrigel mixture around symmetric and asymmetric bottom tubes. Similar to our fibroblast only compaction studies, symmetric heart tubes stayed linear following fibroblast compaction, whereas asymmetric tubes bent with the thinner wall forming the location of the inner curvature of the tube wall (Figure 6.3A-B).

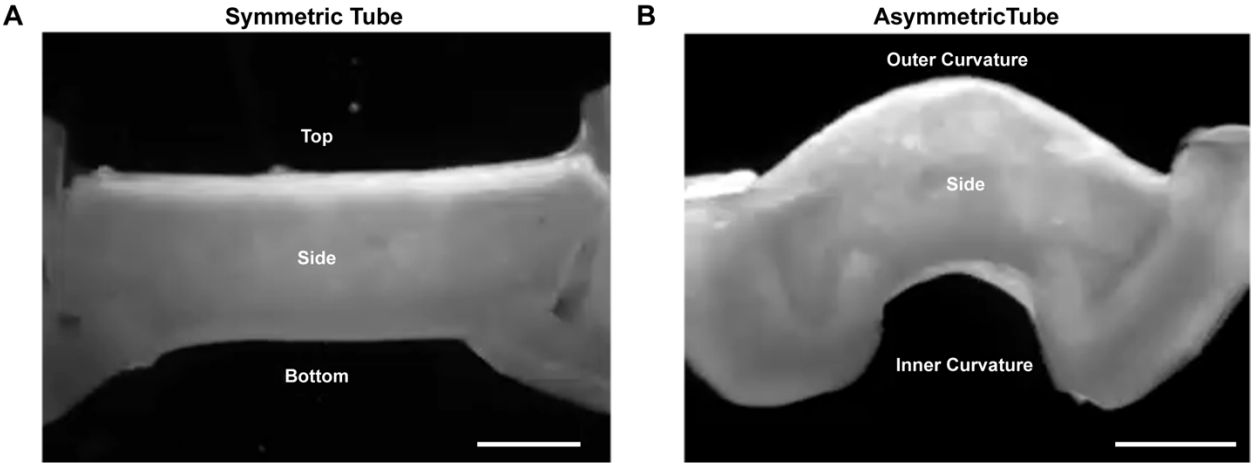

Figure 6.3. Heart Tube Bending and Cardiomyocyte Alignment. (A-B) Brightfield images of symmetric and asymmetric heart tubes. Symmetric tubes stay linear following fibroblast compaction and asymmetric tubes bend. Scale bar is 2 mm. Figure and data prepared by Jacqueline Bliley.

Asymmetric heart tubes tended to bend less than those with fibroblast only compaction. This could be due to differences in culture time (28 versus 14 days) or differences in compaction force observed with casting higher density tissues. Indeed, previous work suggests that overall compaction amount is lower as density of the casted tissue increases (see Appendix B). This indicates that the force applied to the tube could also be less. However, future studies would be required to confirm this observation.

Previous research suggests that cardiomyocyte alignment is highest on the outer curvature of the bent heart tube[1] and I was interested in investigating this in our model of simulated heart morphogenesis. Thus, symmetric (linear) and asymmetric (bent) heart tubes were stained and imaged to observe cardiomyocyte alignment in different regions of the tube. Similar to the previous findings in Chapter 5, symmetric tubes had a general isotropic organization of cardiomyocytes on their surface. Cardiomyocyte alignment was similar among different regions of the symmetric tube (Figure 6.4 A) In contrast, asymmetric tubes tended to display increased alignment in each region compared to symmetric tubes (Figure 6.3 B). A trend toward increased alignment ($p=0.0547$) was observed in the outer curvature of the bent heart tube when compared to the top region of the symmetric tube (Figure 6.3C). However, given the small sample size ($n=3$), these results should be confirmed with further studies. Previous research has suggested that the alignment of outer curvature of bent heart tubes tends to be perpendicular to the direction of blood flow[1] (or perpendicular to the long axis of the tube). In contrast, we found higher levels of alignment on the outer convex curvature of the bent heart tube to be in the direction of the long axis of the tube. This suggests that other forces, like preload, may be responsible for driving this directional alignment and will be an important focus for future studies.

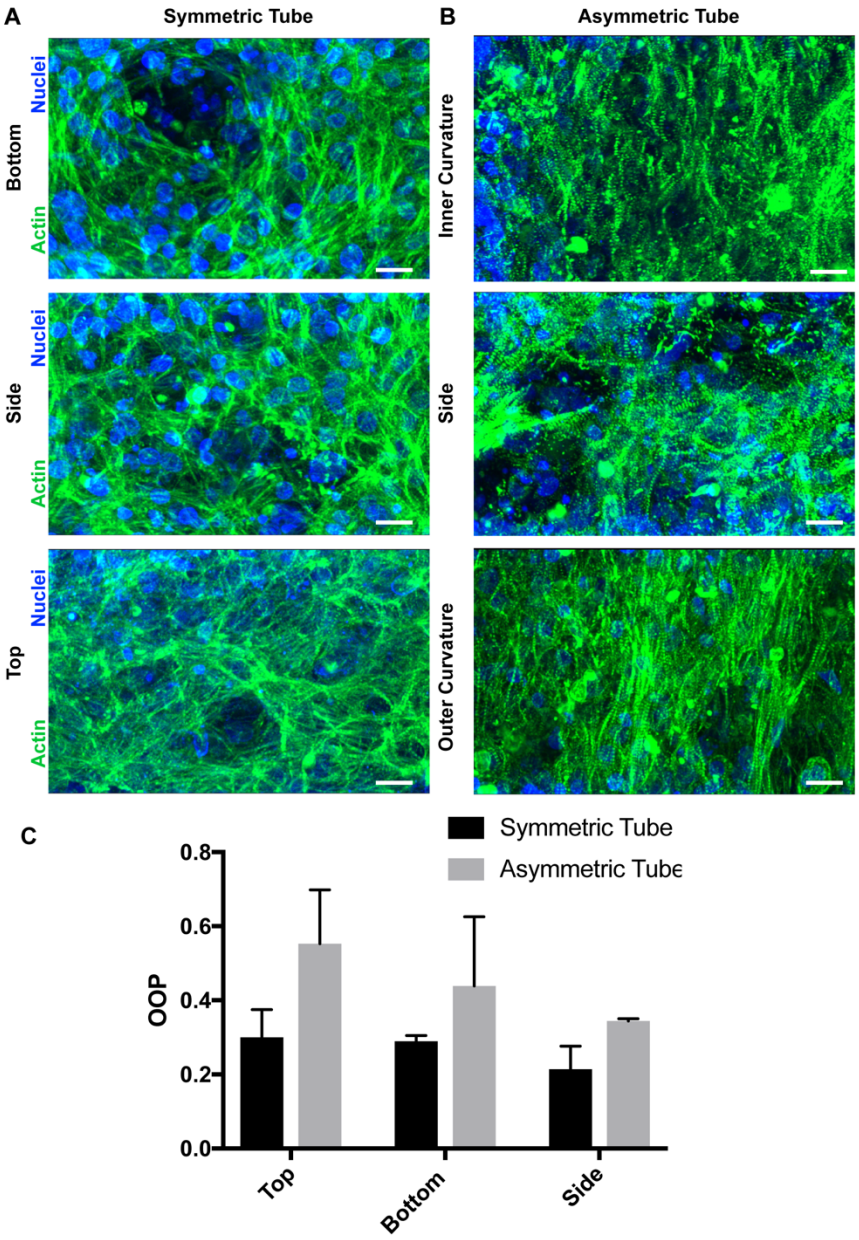

Figure 6.4 Cardiomyocyte Alignment in Symmetric and Asymmetric Heart Tubes. (A) Confocal maximum intensity projections of tube surface in different regions (Bottom, Side or Top) of the symmetric tube (defined in panel A). Scale bars are 20 μm. **(B)** Confocal maximum intensity projections of the tube surface (Inner Curvature, Side, Outer Curvature) in different regions of the asymmetric tube (defined in panel A). Scale bars are 20 μm. **(C)** Orientational Order Parameter (OOP) of actin filaments within symmetric and asymmetric tubes, where an OOP of 1 indicates completely aligned actin filaments. Results based on n=3 tubes per condition. A minimum of 5 z stacks from each region was used to determine an average OOP value for each region of the tube. One way ANOVA (symmetric tubes) or Kruskal-Wallis (asymmetric tubes) was used to assess statistical significance in OOP between different regions of either asymmetric or symmetric tubes. $p<0.05$ was considered statistically significant. Students t-test (top, bottom) or Mann-Whitney (side) was used to compare OOP between top/outer curvature, side/side, and bottom/inner curvature in symmetric in asymmetric tubes. Figure and data prepared by Jacqueline Bliley.

6.3.4. Conduction Velocity in Bent and Straight Heart Tubes

Previous heart development research suggests that heart tubes also develop increased conduction velocity on the outer curvature of the bent heart tube[21]. To see if this was observed in our simulated tube bending morphogenesis model, I cast heart muscle tissues around symmetric and asymmetric bottom tubes and compared their conduction velocities in different regions of the tube at 28 days of culture. Similar to the previous 14 day study, linear heart tubes stayed straight and did not bend. In contrast, asymmetric tubes bent significantly more leading to a cleft formation on the inner curvature where presumably the thin wall invaginated into the tube (Figure 6.5B). Linear tubes in general also displayed similar conduction compared to previous studies with conduction beginning on one end of the tube and travelling to the other. In contrast, asymmetric tubes appeared to change their conduction pattern (Figure 6.5A). Half of the tubes studied (3 out of 6) initiated calcium wave propagation at the outer curvature, which then travelled toward the bottom of the tube (Figure 6.5C). This is interesting because during heart morphogenesis the heart tube changes its conduction patterns. In the linear heart tube, conduction is spread from the one end of the tube to the other[21]. Just after trabeculation and the appearance of the interventricular septum, the heart shifts its conduction through the ventricles to start at the apex (located near the initial outer curvature of the heart) and travel towards the base[22]. This is also associated with the development of the His-purkinje conduction system. While we believe it is highly unlikely that that there is spontaneously development of a *de novo* cardiac conduction system, future research is required to thoroughly understand the shift in observed conduction. The other half of the asymmetric tubes (3 out of 6) did not switch their conduction path and showed somewhat slowed, disorganized calcium conduction around at the inner curvature or where the cleft tended to form on the heart tube (Figure 6.5D). Conduction velocity among symmetric tubes (n=8) was similar in

all regions (top, bottom, and side) with no significant difference being observed (Figure 6.5E). Formation of the cleft at the inner curvature of asymmetric tubes complicated conduction velocity measurements in this region so multiple higher magnification calcium conduction videos were obtained to get an average conduction velocity in this region. Conduction on the sides of the tube also tended to display differences based on relative location to the inner versus outer curvature so conduction velocities were obtained from approximately halfway between the inner and outer curvature. Interestingly, the outer curvature of asymmetric tubes (n=6 tubes) had a significantly higher conduction velocity than the inner curvature (Figure 6.5F). However, the conduction velocity of the outer curvature of the asymmetric tube (bent tube) was similar to that observed in all regions of the symmetric tube (linear tube) suggesting that, rather than seeing an increase in conduction at the outer curvature, conduction is slowed at the inner curvature. This could possibly be due to the cleft formation observed at the inner curvature. A limitation of these studies is that symmetric (3 different batches) and asymmetric tubes (2 different batches) were not prepared from the same batches of cardiomyocytes. Future studies will require larger numbers of asymmetric and symmetric tubes prepared from the same batch of cardiomyocytes to further confirm these findings. Similar to previous studies, cardiomyocyte alignment in different regions of these tubes should also be thoroughly assessed since day 28 tubes tended to bend more than day 14 tubes.

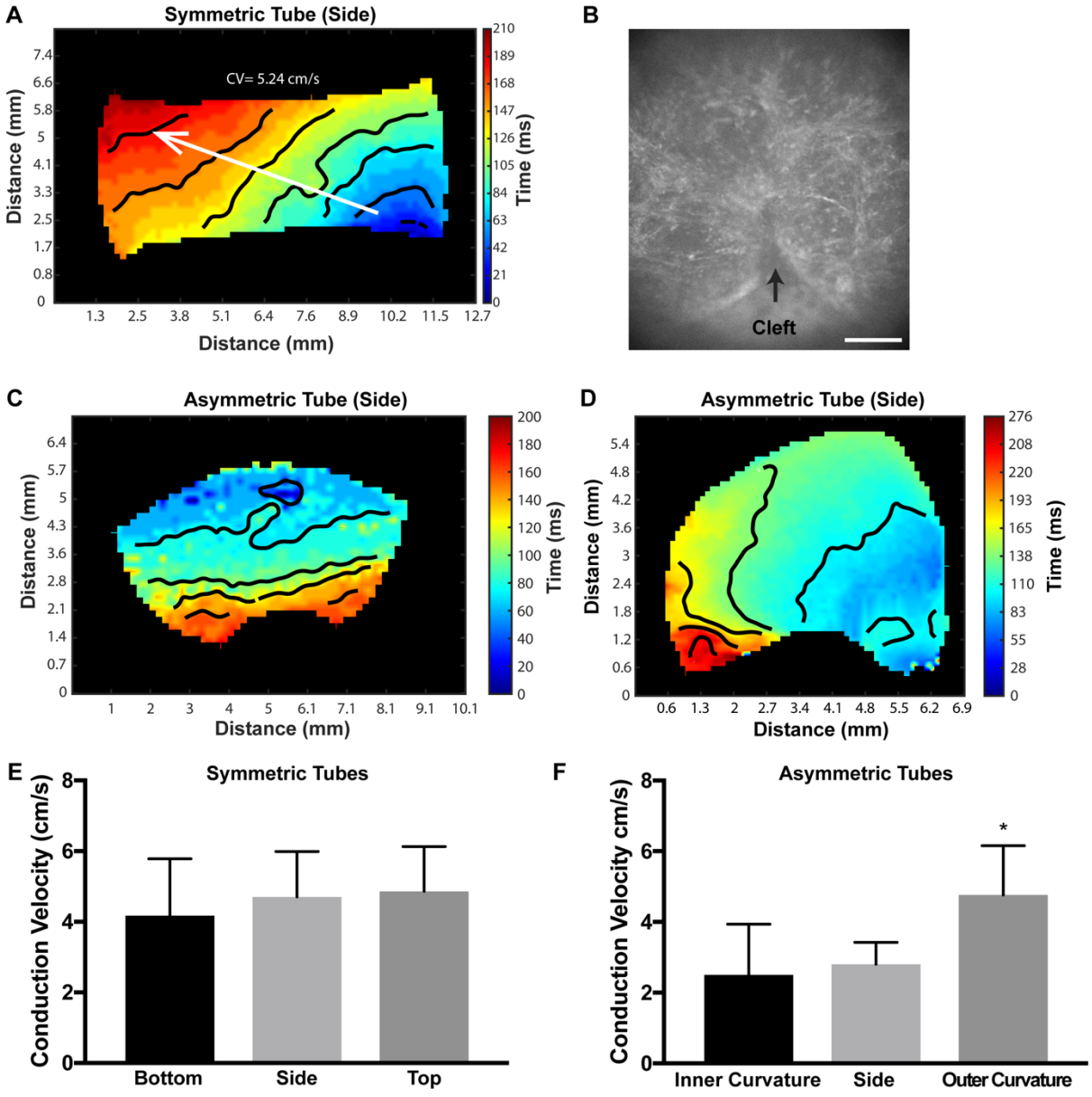

Figure 6.5. Conduction in Symmetric and Asymmetric Tubes. (A) Conduction map of linear tube shown from side. **(B)** Side view of cleft formed at bottom of bent heart tubes. Scale bar is 500 µm. **(C)** Conduction map of asymmetric tube showing calcium wave starting at the outer curvature. **(D)** Conduction map of asymmetric tube wave traveling from one end to the other. **(E)** Conduction velocity in different regions (top, bottom, and side) of symmetric tubes. Statistics based on one way ANOVA. $P<0.05$ was considered statistically significant. **(F)** Conduction velocity in different regions of asymmetric tubes. Statistics based on Kruskal-Wallis with post hoc Dunn's test. * indicates statistical significance from the inner curvature ($p<0.05$). Figure and data prepared by Jacqueline Bliley.

6.3.5. Collapse of Thinner Wall Drives Tube Bending in Asymmetric Tubes

To better understand the mechanism by which asymmetric heart tubes bend, I performed whole mount staining and tissue clearing techniques to view the internal structures of the day 14 heart tubes. Symmetric tubes displayed a linear configuration that was maintained after heart muscle tissue was cast around it (Figure 6.6A). In contrast, asymmetric tubes displayed a bent configuration following heart muscle tissue casting with the inner curvature being the location of the thin wall of the tube (Figure 6.6B). If I examined longitudinal cross-sections of each of the tubes, I saw that the symmetric tubes maintained a straight tube geometry even after heart muscle tissue formation around the tube (Figure 6.6C). In contrast, the longitudinal cross-section of asymmetric tubes appear to display a collapse of the thinner wall, which seems to close off the tube lumen (Figure 6.6D). This could possibly be driven by buckling of the thinner wall, though I cannot exclude that this process is potentiated by cellular migration and invasion into the thin wall without additional studies.

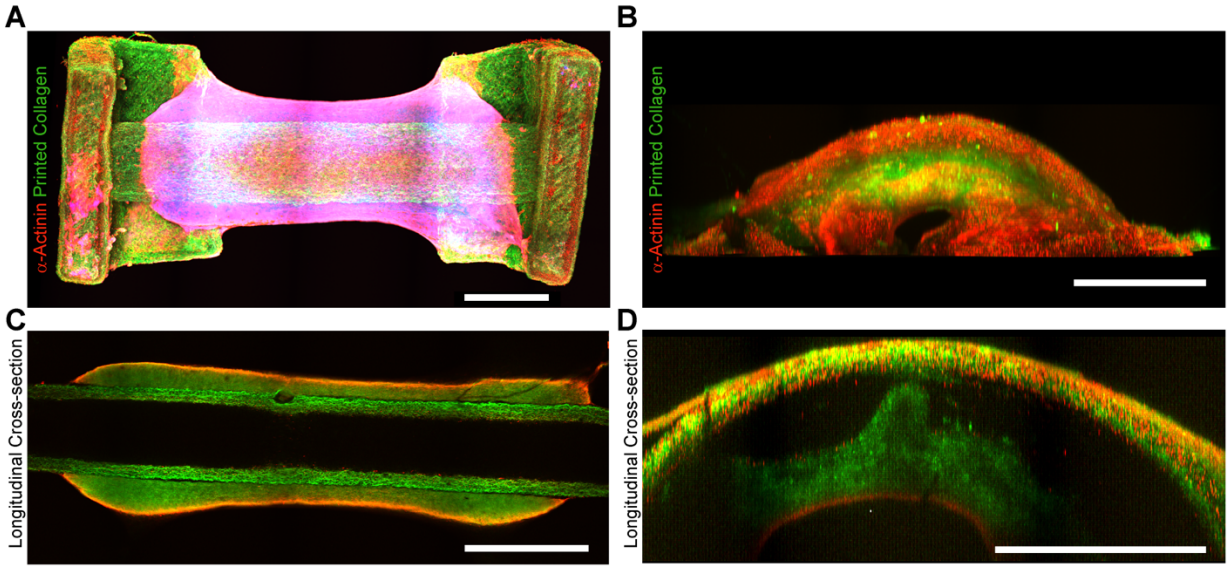

Figure 6.6. Thinner Wall of Asymmetric Tube Collapses with Fibroblast Compaction. (A) Confocal image of symmetric tube with heart muscle tissue cast around it. Scale bar is 2 mm. **(B)** Confocal image of asymmetric tube with heart muscle tissue cast around it. Scale bar is 2 mm. **(C)** Longitudinal cross-section of symmetric bottom tube. Scale bar is 2 mm. **(D)** Longitudinal cross-section of asymmetric bottom tube. Scale bar is 2 mm. Figure and data prepared by Jacqueline Bliley.

6.4 Discussion

Though previous developmental research highly suggests that tissue forces observed during morphogenesis are critical to later tissue heart function[6,26,30], most tissue engineering investigations has focused on building the final adult structure of the heart[11,12,17,18]. Thus, in this chapter, I sought to better understand if the heart bending observed during morphogenesis contributes to later heart tissue structure and function using a bioprinting approach. This research was inspired from previous work by Hughes et al. where the researchers patterned fibroblast clusters into collagen gels[7]. Here, the authors showed that fibroblast clusters generated tension between their closest neighbors that could drive specific changes in the gel shape, including cups, ridges, coils, rolled tubes, and even the Miura origami fold. There was also evidence that by altering tissue shape the authors could preferentially influence cell migration and localization within the gels. In fact, endothelial cells (HUVECs) tended to migrate along emerging folds and

later form lumenized vessels and Caco2 cells (a colon carcinoma cell line) preferentially formed clusters at the bases of the valley folds. In contrast to this previous approach, I sought to use a bioprinting approach, which allows for the precise printing of materials, to change the mechanics of the printed structure. Further, rather than using a fibroblast patterning technique as previously described, I chose to use "isotropic" compaction of fibroblasts around the tube structure to apply a force resulting in preferentially deformation of the tube based on the structural mechanics of the printed tube structure.

In this study, I showed that fibroblasts bent asymmetric tube designs in different directions based on the location of the thinner wall. In Gartner and colleagues previous work, they found that tension is highest between pairs of adjacent fibroblast clusters[7] and it is tempting to suggest that tension would be highest on the outer curvature of the bent heart tube, which has previously been observed during heart tube bending morphogenesis using both finite element modeling[24] and heart tube explants[24,31,32]. I also observed higher levels of cardiomyocyte alignment on the outer curvature of our bent heart tube (though this was not statistically significant), which also suggests that the tension may be elevated in this area. However, it is necessary to confirm that tension is higher on the outer curvature of our bent heart tube compared to the inner curvature. Future work will assess tissue tension in different regions of our bent heart tube by damaging the tissue in precise locations via either laser ablation[7] or cutting[23] and measuring tissue rebound. Indeed, it is also clear from previous research that tension and compression can drive large changes in gene and protein expression[16] and this is an exciting avenue for future investigations.

While we were able to predict that asymmetric tubes bent with an applied force, the current finite element model was unable to accurately depict the complete tube deformation upon application of a fibroblast compaction force. There are several reasons why this might be. First, it

is likely a poor assumption that fibroblast gel compaction in our model is isotropic. Indeed, there appears to be directionality and different time scales of the applied force based on our fibroblast compaction experiments. All in all, these experiments suggest there is a larger contribution of force applied initially along the longitudinal axis of the tube. A more thorough analysis of compaction around the tubes using fluorescent beads and time-lapse microscopy could help gain insight into the forces applied during the compaction process throughout the gel. This will be an important goal for future work. Second, in the finite element model, buckling, or a sudden change in shape of the thin wall under loading, was not taken into account. In fact, whole tissue imaging of the bent heart tubes does suggest that the thin wall may be buckling. However, we cannot exclude that cell migration and invasion may also impacted the final observed structure of the bent tube. Further analysis will attempt to better understand the contribution of thin wall buckling with both finite element modeling and time-lapse microscopy.

One interesting finding is that the deformation of the thin wall appeared to collapse and close off the tube lumen. This created a cleft near the central region of the inner curvature of the tube and what appears to be an invagination into the tube lumen that was extending towards the outer curvature of the bent heart tube. This was also accompanied by changes in conduction direction on the heart tube surface. Symmetric heart tubes always displayed linear conduction starting from one end of the heart tube and travelling to the other. In contrast, bent heart tubes seemed to develop two different conduction pathways. In half of the bent tubes, the conduction started at the outer curvature and travelled towards each tube end. In the other half, the calcium wave traveled from one end to the other but appeared to slow down around the inner curvature of the tube. The slowing down of conduction could possibly be due the formation of this cleft on the bottom of the tube. This is interesting because previous work in heart development suggests that

the linear heart tube does initially have linear conduction, but during the bending, looping, and septating process, the direction of conduction changes. Specifically, septation drives a transition in conduction from apex of the ventricle to the base[22]. This is also associated with the appearance of the His-purkinje fiber system. Future work will investigate to what degree this change in conduction represents what is observed in heart morphogenesis by further investigating potential cell invagination into the tube lumen and what is causing this change in conduction. While *de novo* creation of conduction pathways would be highly unlikely in our model, this still requires further investigation.

As with any *in vitro* system, there are several limitations of our model with respect to modeling heart development. Though several theories have been proposed for heart tube bending and looping, the current predominant and well-favored theory is that differential growth drives heart tube bending[23]. In our model, I did not use differential growth to drive heart tube bending, but instead surmised, if I could mimic the mechanics of tube bending, I could drive similar alterations in heart tube structure and function. Further, in this work, I am also not accurately depicting all of the forces observed during heart tube morphogenesis. While cardiomyocytes around this tube would be exposed to an afterload via contraction to generate pressure within the tube lumen, they are likely exposed to very minimal preload compared to that observed *in vivo*. Previous work in chapter 3 suggests that preload, or active stretch on cardiomyocytes during relaxation, can drive dramatic changes in heart muscle myofibrillar structure, contractile function, electrical conduction, and gene expression. This is also in line with previous heart development research, where Yelon and colleagues very elegantly dissected the contribution of altered tissue stresses during heart tube bending/looping and preload/afterload on the ultimate structure and function of fetal zebrafish hearts[1]. Here, the authors used combinations of wea and haf mutant

zebrafish, which have a deficiencies in atrial sarcomeres (wea) and ventricular myosin heavy chain (haf), leading to impaired atrial and ventricular contraction, respectively. Interestingly, both mutants can still undergo the heart morphogenesis process. Because of the absence of atrial sarcomeres, there is reduced preload placed on the ventricle during heart morphogenesis in wea mutants, which bears some similarities to the simulated morphogenesis model. Interestingly, wea mutants still display elongated and aligned cardiomyocytes on the outer curvature of the heart tube, but this alignment was less when compared to wild-type controls. In this context, this suggests that heart tube bending establishes differential stresses on the heart tube, which are further potentiated by the preload the cardiomyocytes experience as development proceeds. Thus, incorporating a mechanism that can actively imitate the preload in our heart tube will be an important to investigate in future studies.

6.5 Conclusions

In this chapter, I found that 3D printing could be used to alter the mechanics of a tube structure and that fibroblast compaction around the structure resulted in preferential tube bending based on the location of the thin wall. Similarly, heart muscle tissues cast around these structures could achieve a bent configuration. These concepts can also potentially be applied to create models that can undergo more complicated morphogenetic events, including heart tube looping. Interestingly, cardiomyocyte alignment and conduction appeared to be affected by bending. Future work will further investigate these changes and determine why they are occurring in our model. However, it is clear from the abundance of previous heart morphogenesis research as well as this study, that the morphogenetic movements the heart undergoes during development are critical to its later structure and function and that researchers should aim to incorporate these when attempting to build tissues and organs as future therapeutic replacements.

6.6 Acknowledgements

Financial support was provided from Additional Ventures Single Ventricle Research Fund [grant number to A.W.F.], National Institutes of Health [grant number DP2HL117750 to A.W.F.], the Office of Naval Research [grant number N00014-17-1-2566 to A.W.F.], and the Dowd Fellowship and Presidential Fellowship, Carnegie Mellon University [to J.M.B.].

6.7 References

1. Auman, H. J., H. Coleman, H. E. Riley, F. Olale, H. J. Tsai, and D. Yelon. Functional modulation of cardiac form through regionally confined cell shape changes. *PLoS Biol.* 5:0604–0615, 2007.
2. Burridge, P. W., E. Matsa, P. Shukla, Z. C. Lin, J. M. Churko, A. D. Ebert, F. Lan, S. Diecke, B. Huber, N. M. Mordwinkin, J. R. Plews, O. J. Abilez, B. Cui, J. D. Gold, and J. C. Wu. Chemically defned generation of human cardiomyocytes. *Nat. Methods* 11:855–860, 2014.
3. Chen, G., D. R. Gulbranson, Z. Hou, J. M. Bolin, M. D. Probasco, K. Smuga-otto, S. E. Howden, R. Nicole, N. E. Propson, R. Wagner, G. O. Lee, J. M. C. Teng, and J. A. Thomson. Chemically defined conditions for human iPS cell derivation and culture. 8:424–429, 2011.
4. Cripps, R. M., and E. N. Olson. Control of cardiac development by an evolutionarily conserved transcriptional network. *Dev. Biol.* 246:14–28, 2002.
5. Deng, M. Cardiac Transplantation. *Heart* 87:177–184, 2002.
6. Goenezen et al. Biomechanics of Early Cardiac Development. *Biomech Model Mechan* 23:1–7, 2008.
7. Hughes, A. J., H. Miyazaki, M. C. Coyle, J. Zhang, M. T. Laurie, D. Chu, Z. Vavrušová, R. A. Schneider, O. D. Klein, and Z. J. Gartner. Engineered Tissue Folding by Mechanical Compaction of the Mesenchyme. *Dev. Cell* 44:165-178.e6, 2018.
8. Jallerat, Q., and A. W. Feinberg. Extracellular Matrix Structure and Composition in the Early Four-Chambered Embryonic Heart. *Cells* , 2020.doi:10.3390/cells9020285
9. Kim, H. Y., and L. A. Davidson. Punctuated actin contractions during convergent extension and their permissive regulation by the non-canonical Wnt-signaling pathway. *J. Cell Sci.* 124:635–646, 2011.
10. Kupfer, M. E., W.-H. Lin, V. Ravikumar, K. Qiu, L. Wang, L. Gao, D. Bhuiyan, M. Lenz, J. Ai, R. R. Mahutga, D. Townsend, J. Zhang, M. C. McAlpine, E. G. Tolkacheva, and B. M. Ogle. In Situ Expansion, Differentiation and Electromechanical Coupling of Human Cardiac Muscle in a 3D Bioprinted, Chambered Organoid . *Circ. Res.* , 2020.doi:10.1161/circresaha.119.316155
11. Kupfer, M. E., W. H. Lin, V. Ravikumar, K. Qiu, L. Wang, L. Gao, D. B. Bhuiyan, M. Lenz, J. Ai, R. R. Mahutga, D. W. Townsend, J. Zhang, M. C. McAlpine, E. G. Tolkacheva, and B. M. Ogle. In Situ Expansion, Differentiation, and Electromechanical Coupling of Human Cardiac Muscle in a 3D Bioprinted, Chambered Organoid. *Circ. Res.* , 2020.doi:10.1161/CIRCRESAHA.119.316155
12. Lee, A., A. R. Hudson, D. J. Shiwarski, J. W. Tashman, T. J. Hinton, S. Yerneni, J. M. Bliley, P. G. Campbell, and A. W. Feinberg. 3D bioprinting of collagen to rebuild components of the human heart. *Science (80-.).* , 2019.doi:10.1126/science.aav9051
13. Lian, X., J. Zhang, S. M. Azarin, K. Zhu, L. B. Hazeltine, X. Bao, C. Hsiao, T. J. Kamp, and S. P. Palecek. Directed cardiomyocyte differentiation from human pluripotent stem cells by modulating Wnt/??-catenin signaling under fully defined conditions. *Nat. Protoc.* 8:162–175, 2013.
14. Lu, T. Y., B. Lin, J. Kim, M. Sullivan, K. Tobita, G. Salama, and L. Yang. Repopulation of decellularized mouse heart with human induced pluripotent stem cell-derived cardiovascular progenitor cells. *Nat. Commun.* , 2013.doi:10.1038/ncomms3307
15. Macqueen, L. A., S. P. Sheehy, C. O. Chantre, J. F. Zimmerman, F. S. Pasqualini, X. Liu, J. A. Goss, P. H. Campbell, G. M. Gonzalez, S. J. Park, A. K. Capulli, J. P. Ferrier, T. Fettah Kosar, L. Mahadevan, W. T. Pu,

and K. K. Parker. A tissue-engineered scale model of the heart ventricle. *Nat. Biomed. Eng.* , 2018.doi:10.1038/s41551-018-0271-5
16. Muncie, J. M., N. M. E. Ayad, J. N. Lakins, X. Xue, J. Fu, and V. M. Weaver. Mechanical Tension Promotes Formation of Gastrulation-like Nodes and Patterns Mesoderm Specification in Human Embryonic Stem Cells. *Dev. Cell* 55:679-694.e11, 2020.
17. Noor, N., A. Shapira, R. Edri, I. Gal, L. Wertheim, and T. Dvir. 3D Printing of Personalized Thick and Perfusable Cardiac Patches and Hearts. *Adv. Sci.* , 2019.doi:10.1002/advs.201900344
18. Ott, H. C., T. S. Matthiesen, S. K. Goh, L. D. Black, S. M. Kren, T. I. Netoff, and D. A. Taylor. Perfusion-decellularized matrix: Using nature's platform to engineer a bioartificial heart. *Nat. Med.* 14:213–221, 2008.
19. Poelmann, R. E., and A. C. Gittenberger-de Groot. Development and evolution of the metazoan heart. *Dev. Dyn.* 248:634–656, 2019.
20. Sánchez, P. L., M. E. Fernández-Santos, S. Costanza, A. M. Climent, I. Moscoso, M. A. Gonzalez-Nicolas, R. Sanz-Ruiz, H. Rodríguez, S. M. Kren, G. Garrido, J. L. Escalante, J. Bermejo, J. Elizaga, J. Menarguez, R. Yotti, C. Pérez del Villar, M. A. Espinosa, M. S. Guillem, J. T. Willerson, A. Bernad, R. Matesanz, D. A. Taylor, and F. Fernández-Avilés. Acellular human heart matrix: A critical step toward whole heart grafts. *Biomaterials* 61:279–289, 2015.
21. Sedmera, D., M. Reckova, M. R. Bigelow, A. Dealmeida, C. P. Stanley, T. Mikawa, R. G. Gourdie, and R. P. Thompson. Developmental transitions in electrical activation patterns in chick embryonic heart. *Anat. Rec. - Part A Discov. Mol. Cell. Evol. Biol.* 280:1001–1009, 2004.
22. Sedmera, D., M. Reckova, C. Rosengarten, M. I. Torres, R. G. Gourdie, and R. P. Thompson. Optical Mapping of Electrical Activation in the Developing Heart. *Can. J. Cardiol.* 209–215, 2005.
23. Shi, Y., J. Yao, G. Xu, and L. A. Taber. Bending of the looping heart: Differential growth revisited. *J. Biomech. Eng.* 136:1–15, 2014.
24. Shi, Y., J. Yao, J. M. Young, J. A. Fee, R. Perucchio, and L. A. Taber. Bending and twisting the embryonic heart: A computational model for c-looping based on realistic geometry. *Front. Physiol.* 5 AUG:1–14, 2014.
25. Sun, Y., Q. Jallerat, J. M. Szymanski, and A. W. Feinberg. Conformal nanopatterning of extracellular matrix proteins onto topographically complex surfaces. *Nat. Methods* , 2015.doi:10.1038/nmeth.3210
26. Taber, L. A. Biomechanics of Early Cardiovascular Development. 1–25, 2001.
27. Tashman, J. W., D. J. Shiwarski, and A. W. Feinberg. A high performance open-source syringe extruder optimized for extrusion and retraction during FRESH 3D bioprinting. *HardwareX* 9:1–18, 2021.
28. Tohyama, S., F. Hattori, M. Sano, T. Hishiki, Y. Nagahata, T. Matsuura, H. Hashimoto, T. Suzuki, H. Yamashita, Y. Satoh, T. Egashira, T. Seki, N. Muraoka, H. Yamakawa, Y. Ohgino, T. Tanaka, M. Yoichi, S. Yuasa, M. Murata, M. Suematsu, and K. Fukuda. Distinct metabolic flow enables large-scale purification of mouse and human pluripotent stem cell-derived cardiomyocytes. *Cell Stem Cell* 12:127–137, 2013.
29. Tzahor, E., and K. D. Poss. Cardiac regeneration strategies: Staying young at heart. *Science (80-.).* 356:1035–1039, 2017.
30. Voorhees, A. P., and H. C. Han. Biomechanics of cardiac function. *Compr. Physiol.* , 2015.doi:10.1002/cphy.c140070
31. Voronov, D. A., P. W. Alford, G. Xu, and L. A. Taber. The role of mechanical forces in dextral rotation during cardiac looping in the chick embryo. *Dev. Biol.* 272:339–350, 2004.
32. Zamir, E. A., and L. A. Taber. Material properties and residual stress in the stage 12 chick heart during cardiac looping. *J. Biomech. Eng.* 126:823–830, 2004.

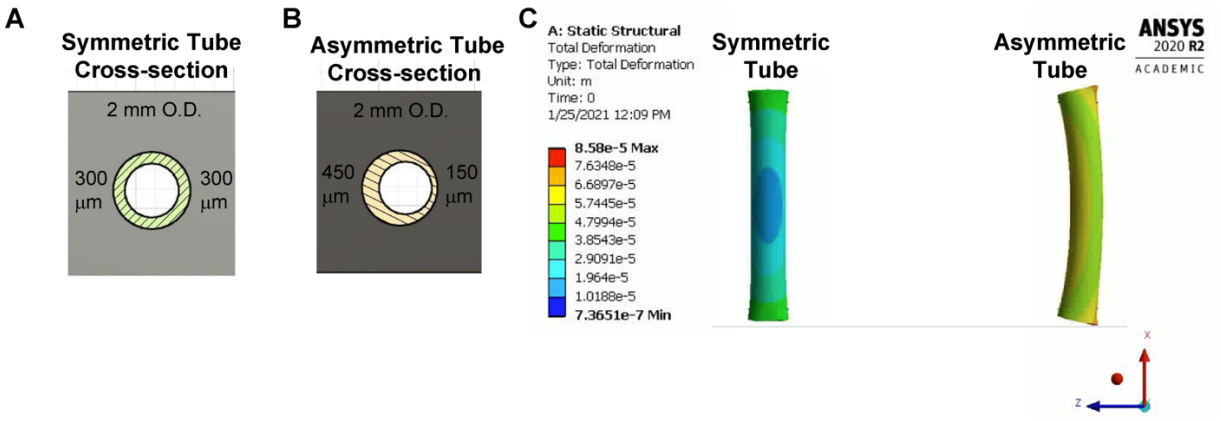

Supplemental Figure 1. Finite Element Modeling of Symmetric and Asymmetric Tube Bending. (A) Cross-sections of CAD models of symmetric **(A)** and asymmetric **(B)** tube designs used for modeling. **(C)** Finite element modeling of displacement of tube ends upon application of a uniform pressure to the outside of the tube surface. Figure and data prepared by Jacqueline Bliley.

Chapter 7
Conclusions and Future Directions

7.1 Summary

In this dissertation, I first discussed the importance of heart muscle structure and its relation to mechanical loading using two key examples, embryonic heart development and heart disease. I then discussed the current fabrication techniques for both 2D and 3D engineered cardiac tissues and mechanical loading strategies that have been used to create more mature engineered cardiac tissues for heart repair and *in vitro* disease modeling. Building off these previous models, I created a novel *in vitro* model of mechanical loading (dyn-EHT) that mimics physiologic preload and afterload through the incorporation of an elastic PDMS strip. I then demonstrated that dynamic loading with a sufficient load (8x) increases EHT function, including contractility, myofibrillar architecture, cardiac specific gene expression and electrophysiological properties.

Dynamic conditioning with the 8x dyn-EHT was also important in revealing a disease phenotype in patient derived cells with mutations in desmoplakin (DSPmut) resulting in arrhythmogenic cardiomyopathy (ACM). Here, I was able to show that control iPS derived 8x dyn-EHTs demonstrated similar increases in function to that observed in control ESC derived 8x dyn-EHTs. Under this same regime, I saw decrements in function observed in DSPmut 8x dyn-EHTs that were not observed in constrained DSPmut 8x EHTs nor in constrained 2D models of stretch suggesting that this 3D dynamic loading regime is important for modeling certain decreases in function that are observed with disease. I also observed decreased amount of desmosomes in DSPmut 8x dyn-EHTs compared to controls, which is similar to previous findings observed in animal studies with desmosomal genetic defects and human patient histology findings. These

discoveries have important implications for disease modeling with EHTs and suggest that incorporation of physiologic preload and afterload is necessary to observe certain morphological and functional aspects of disease progression.

Taking these findings observed in our simplified dyn-EHT model, I wondered if we could also apply certain aspects of mechanical loading to more advanced 3D engineered heart muscle structures, but first, I needed to create an appropriate 3D model. Here, I chose to fabricate a bioinspired design of the early embryonic linear heart tube using a 3D printing technique, Freeform Reversible Embedding of Suspended Hydrogels (FRESH). I was able to show that collagen tubes could be reliably printed and that engineered heart muscle tissues could be cast around them to create contractile heart tubes. Heart tubes displayed dense layers of interconnected cardiomyocytes that did not appear to be aligned in any certain direction. Further, heart tubes were able to be electrically paced and displayed similar conduction velocities to that observed in the in the inner curvature of the bent heart tube. Interestingly, heart tubes were also able to increase pressure within their lumens and displace fluorescent beads with contraction. Preliminary evidence also suggests that heart tubes were able to displace these beads away from the tube lumen in a unidirectional manner; however, this finding will need to be confirmed with future studies.

Finally, I chose to see if we could use mechanical loading to drive cardiomyocyte alignment in our bioinspired heart tube model. For this, I chose to create a model of heart tube bending reminiscent of the early embryonic heart morphogenesis, where previous research has suggested that bending creates increased tensile stresses on the outer curvature of the heart tube[6,7] leading to enhanced cardiomyocyte elongation and alignment[1]. To do this, I leveraged our FRESH 3D printing technique to create tube models that would bend in a certain direction when a force was applied. Cardiac fibroblast compaction forces were sufficient to drive heart tube bending and

the direction of bending could be changed by altering the printed model. Symmetric, linear tubes displayed low levels of cardiomyocyte alignment with similar levels of conduction in each region of the tube. In contrast, tube bending resulted in distinct morphological changes within specific spatial regions of the tube where there was a trend towards increased cardiomyocyte alignment on the outer curvature of the bent heart tube. Conduction velocity also appeared to be impacted with cardiomyocytes displaying an increase in conduction velocity compared to the inner curvature. However, this work was complicated by the fact that asymmetric, bent heart tubes developed a cleft on the inner curvature of the tube, where it appeared that the tube had invaginated into the lumen. This led to slowing and disorganization of the calcium conduction around this cleft and thus, different imaging methods and a higher magnification objective were required. It will be important to repeat these studies and evaluate these findings in heart tubes derived from the same batch of cardiomyocytes. Interestingly, I observed a change in the conduction pattern of asymmetric, bent heart tubes with 50% of the tubes initiating conduction from the outer curvature. This was in stark contrast to linear tubes, which consistently had linear conduction travelling from one end to the other. It is unknown what is causing this change in conduction and future work will need to be performed to better understand this phenomenon. However, these findings in combination with previous heart morphogenesis studies largely suggest that the specific stresses and strains observed during heart tube bending and looping are important in developing heart. Further, if the goal is to build more advanced organs and tissues, rather than building the final adult stage of an organ, we should consider the impact morphogenesis has on ultimate organ function and incorporate these ideas into our organ fabrication strategies.

7.2 Future Directions

There were several exciting findings in this dissertation and future directions should be focused on further evaluating and investigating these. For instance, I found that the 8x dyn-EHT conditioning increased cardiac specific gene expression and function in control tissues. While these findings are interesting, I only considered a small panel of genes and proteins. It will be important to perform a more thorough analysis of genes and proteins expressed within these 8x dyn-EHTs and compare these to both embryonic and adult heart muscle tissues. Further, future work should focus on combining this dynamic mechanical loading platform with other aspects known to increase EHT function, such as electrical stimulation[5], where we may be able to create engineered heart muscle tissues with adult-like function. Ultimately, it will be important to see if these maturation strategies will create engineered heart muscle tissues that are better able to repair heart muscle following damage and this will be an important avenue for future studies.

With regard to the 8x dyn-EHT as a disease modeling platform, future investigations could improve this model. First, while I did not observe spontaneous electrical arrythmias in our DSPmut 8x dyn-EHTs, a more thorough investigation of the electrophysiology in these tissues is needed. Previous research investigating arrhythmias in animal models suggests that heart muscle tissues often have to be challenged, either through high frequency electrical pacing or drugs[4], to observe the propensity of heart muscle to develop arrhythmias. Future studies should evaluate the presence of arrhythmias in our DSPmut 8x dyn-EHTs with similar protocols. Further, the structural changes (fibrofatty infiltration and fibrosis) associated with ACM are also important in disease pathogenesis. While I did not observe these changes in our DSPmut 8x dyn-EHTs, several protocols have been developed to increase lipid accumulation in cardiomyocytes with genetic predispositions to ACM. Specifically, cardiomyocytes derived from patients with genetic

mutations in plakophilin have been shown to spontaneously increase lipid accumulation in culture[3] and that this can be potentiated with proadipogenic culture medium[2]. It will be interesting to investigate whether these structural changes contribute to arrhythmia production in the 8x dyn-EHT model.

I am also are very interested in applying our findings on mechanical loading to more complex three-dimensional structures, like the bioinspired model of the heart tube created in Chapter 5. For instance, while I was able to create a contractile heart tube, functional properties, like the ability to displace fluorescent beads, were limited. It will also be important to validate that unidirectional displacement of beads is occurring in our model with more comprehensive electrical stimulation studies showing that the direction of displacement can be changed with stimulation. However, because cardiomyocytes displayed a largely isotropic orientation and alignment on the tube surface, it may be more suitable to evaluate this in tubes that have more aligned cardiomyocytes. Several strategies could be employed to increase alignment, such as incorporating struts into the 3D print that can guide cardiomyocyte alignment during the compaction process, or even incorporating hemodynamic loading, like preload, by pressurizing the heart tube.

Finally, future work should focus on using this bioinspired heart tube to build a structure reminiscent of the human heart. While fibroblast compaction was used as the force to bend the heart tube structure, it would be interesting to see if other materials could be incorporated that could apply a similar force to bend the tube, such as materials that swell or dissolve/melt with temperature, pH or other stimuli, as it is possible to incorporate these as well into our 3D prints. Further, while some efforts were made to create a finite element model that would allow us to predict tube deformations when forces are applied, this could be substantially improved. Future work will focus on time-lapse microscopy of fibroblast compaction around the tube to better

understand the forces applied to the tube during this process in order to improve our finite element model. It also may be interesting to see if I can print structures that can undergo different types of morphogenetic changes, such as the looping observed during heart morphogenesis or the bending of a flat sheet observed in neural tube closure. This will not only provide us with a better understanding of how these processes contribute to ultimate organ function, but can also provide us with a template on how to design and build organs and tissues.

7.3 References

1. Auman, H. J., H. Coleman, H. E. Riley, F. Olale, H. J. Tsai, and D. Yelon. Functional modulation of cardiac form through regionally confined cell shape changes. *PLoS Biol.* 5:0604–0615, 2007.
2. Caspi, O., I. Huber, A. Gepstein, G. Arbel, L. Maizels, M. Boulos, and L. Gepstein. Modeling of arrhythmogenic right ventricular cardiomyopathy with human induced pluripotent stem cells. *Circ. Cardiovasc. Genet.* 6:557–568, 2013.
3. Ma, D., H. Wei, J. Lu, S. Ho, G. Zhang, X. Sun, Y. Oh, S. H. Tan, M. L. Ng, W. Shim, P. Wong, and R. Liew. Generation of patient-specific induced pluripotent stem cell-derived cardiomyocytes as a cellular model of arrhythmogenic right ventricular cardiomyopathy. *Eur. Heart J.* 34:1122–1133, 2013.
4. Piktel, J. S., and L. D. Wilson. Translational Models of Arrhythmia Mechanisms and Susceptibility: Success and Challenges of Modeling Human Disease. *Front. Cardiovasc. Med.* 6:1–18, 2019.
5. Ronaldson-Bouchard, K., S. P. Ma, K. Yeager, T. Chen, L. J. Song, D. Sirabella, K. Morikawa, D. Teles, M. Yazawa, and G. Vunjak-Novakovic. Advanced maturation of human cardiac tissue grown from pluripotent stem cells. *Nature* 556:239–243, 2018.
6. Shi, Y., J. Yao, G. Xu, and L. A. Taber. Bending of the looping heart: Differential growth revisited. *J. Biomech. Eng.* 136:1–15, 2014.
7. Shi, Y., J. Yao, J. M. Young, J. A. Fee, R. Perucchio, and L. A. Taber. Bending and twisting the embryonic heart: A computational model for c-looping based on realistic geometry. *Front. Physiol.* 5 AUG:1–14, 2014.

Appendix A:

Shrink-Wrapped Cardiomyocytes for Damaged Heart Muscle Repair

8.1 Introduction

Myocardial infarction (MI) is heart muscle death following coronary artery occlusion. This is an important concern because following such an injury, cardiomyocytes have little ability to divide and repair the damaged heart muscle[6]. When large areas of heart muscle are damaged, this can lead to irreversible structural and functional changes resulting in eventual heart failure[3]. Currently, the only long term solution for intractable heart failure is a heart transplant, but unfortunately, there are simply not enough donor organs available for those who need them[2]. Thus, strategies aimed at repairing damaged heart muscle should be evaluated in order to prevent the permanent decrements in heart function that occur with heart failure.

In this regard, researchers have investigated several strategies to heal damaged heart muscle, including injection of cellular suspensions of stem-cell derived cardiomyocytes[1,4]. While this is an exciting avenue for future investigations, there remains several critical challenges in delivery and integration of these cells into damaged heart muscle. In fact, current cardiomyocyte injection strategies lead to only moderate functional improvements, which is likely due to cell washout (lack of integration) or cell anoikis during injection due to lack of cell-cell or cell-ECM attachments.

An alternative strategy to single cell injections is to deliver cardiomyocytes as functional units to preserve their cell-cell junctions such as gap junctions, cadherins, and desmosomal

junctions, that are important to heart muscle tissue electromechanical function. Here, I encapsulate, or "shrink-wrap", functional units of cardiomyocytes within an extracellular matrix shell to enhance cell survival and integration into damaged heart muscle. Previous work in our laboratory has evaluated this technique as a delivery method for corneal endothelial cells and has demonstrated improved retention and integration compared to isolated single cell injections[7]. Here, I demonstrate that muscle cells (C2C12 myoblasts and cardiomyocytes) can adhere to fibronectin ECM squares that have been patterned on a sacrificial poly n-isopropyl acrylamide (PIPAAm) substrate. Upon dissolution of the PIPAAm, cells are shrink-wrapped in fibronectin. Clusters can then be injected and integrate into engineered muscle tissues in the hope of creating an eventually therapeutic strategy to heal damaged heart muscle tissues.

8.2 Materials and Methods

8.2.1. C2C12 Culture

C2C12 myoblasts were initially used as a model for shrink-wrapping. C2C12 were cultured in DMEM with 1% Penicillin-Streptomycin, 1% v/v L-Glutamine (200mM), and 10% v/v Heat-inactivated Fetal Bovine Serum. Media was changed every two days and cells were passaged prior to reaching 80% confluence.

8.2.2. Cardiomyocyte Differentiation, Purification, and Fibronectin Conditioning

HES3 Human embryonic stem cells were maintained in Essential 8 medium (A1517001, Life Technologies) on 6 well plates coated with 12 μg/cm^2 Geltrex (A1413301, Life Technologies). Media was changed daily and ESCs were passaged every four days in E8 supplemented with 2 μM ROCK inhibitor, Thiazovivin (S1459, Selleck Chemicals).

For differentiation, HES3 ESCs were detached from the plate with TrypLE express (12604013, Thermo Fisher Scientific) and seeded at 16,000 cells/cm^2 in Geltrex-coated dishes with E8 with 2 μM thiazovivin. ESCs were then allowed to proliferate until ~50% confluence was achieved. Cardiomyocyte differentiation was then carried out using a combination of previously described protocols. On day 0, the media was changed to RPMI/B27 with 6 μM CHIR99021 (C-6556, LC laboratories). On day 2, the media was changed to RPMI/B27 with 2 μM Wnt-C59 (S7037, Selleck Chemicals). On day 4 and 6, media was changed to RPMI/B27. On day 8 and 10, media was changed to CDM3. On day 12, spontaneously beating CMs were passaged for metabolic purification using a lactate-supplemented media (CDM3L). Specifically, beating CMs were washed with 1X PBS and detached from the surface with TrypLE express for 15 min at 37℃. Detached cells were pipetted into DMEM/F12 media and centrifuged at 200 X g for 7 min to pellet the cells. CMs were seeded on 12 μg/cm^2 Matrigel (356231, Corning)-coated plates with CDM3L and purified for 5 days.

Following purification, cardiomyocytes were conditioned on an isotropic coating of fibronectin (Corning, catalog no. 356008) to select for those cells with the ability to bind fibronectin. To create substrates for fibronectin conditioning, six well plates were coated with 1 mL of 50 μg/mL fibronectin per well in sterile distilled water for 1 h at room temperature. Excess fibronectin was then washed with 1X PBS and plates were either used immediately or stored at 4 °C in 1X PBS for less than 2 weeks prior to use. To passage for fibronectin conditioning, cardiomyocytes were washed with 1X PBS and then lifted with TrypLE for 15 min at 37 °C. Detached cells were pipetted into DMEM/F12 (ThermoFisher, catalog no. 11320033) and centrifuged at 200 *g* for 7 min to pellet the cells. CMs were then resuspended in CDM3 supplemented with 10% fetal bovine serum (FBS) and 2 μM Thiazovivin and seeded onto

fibronectin-coated six well plates at a ratio of 1:1. Cardiomyocytes were maintained on fibronectin-coated plates for 5 days prior to use.

8.2.3. Engineered Skeletal and Heart Muscle Tissues

Engineered skeletal muscle tissues were used initially as a preliminary model to assess shrink-wrapping and integration. These results were also later repeated in engineered heart muscle tissues. Engineered skeletal muscle tissues were created by encapsulating C2C12 myoblasts in a collagen/Matrigel mixture. The tissue components consisted of 15,000,000 C2C12 per mL in 2.5 mg/mL collagen derived from rat tail and 20% v/v Matrigel. 50 µL tissues were cast around sterile PDMS posts within a small well. Following tissue compaction, C2C12 differentiation medium was added onto the tissues to induce C2C12 myoblast fusion into skeletal muscle myofibers. C2C12 differentiation media consisted of 500 mL of DMEM-high glucose, 5 mL of 10,000 unit-10 mg/mL Penicillin-Streptomycin, 5 mL of 200 mM L-Glutamine (200mM), and 10 mL of Heat-inactivated Horse Serum.

Engineered heart muscle tissues were fabricated around PDMS strips as previously described in chapters 2 and 3. Briefly, sterile PDMS wells were fixed to one well of a 6 well culture plate using a thin layer of vacuum grease. PDMS wells were then incubated with 1% w/v Pluronic F-127 (P2443, Sigma) for 10 minutes to reduce collagen attachment to the well and washed three times in 1X PBS. Sterile PDMS strips were then placed in the slits in the bottom of the well to secure the strip during cardiac tissue casting. Collagen I derived from rat tail (354249, Corning) and Matrigel (354263, Corning) were used to fabricate 3D cardiac tissues around the PDMS strips. The final concentrations were 1 mg/mL Collagen I, 1.7 mg/mL Matrigel, 10% 10X PBS, 2.3% 1N NaOH, 18.75×10^6 total cells/mL consisting of 90% cardiomyocytes and 10% cardiac fibroblasts.

Ingredients were mixed and then 80 μL of the cell mixture was pipetted into each well around the PDMS strip. 6-well plates containing the molds and cell suspension were then placed at 37℃ to allow for gelation. Following a 45-minute incubation period, cardiac tissues were maintained in heart muscle tissue media containing RPMI-1640 supplemented with 1% v/v KnockOut™ Serum Replacement (10828010, Thermofisher) and 1:1000 MycoZap Plus CL (Lonza, VZA 2012).

8.2.4. Shrink-Wrapping of C2C12 or Cardiomyocytes

Polydimethylsiloxane (PDMS) stamps were first prepared using established soft lithography techniques[5]. PDMS stamps were utilized to pattern 200 μm by 200 μm squares of fibronectin onto PIPAAm coated glass cover slips. PDMS stamps were sterilized via sonication in 50% ethanol solution for 30 minutes and subsequently dried using a nitrogen air gun. The stamps were then incubated in 50 μg/mL fibronectin doped with a 10% Alexa-633 labelled fibronectin solution for 60 minutes. Fibronectin squares were then microcontact printed by placing the stamps onto PIPAAm substrates for 30 minutes. The fidelity of the transferred patterns were assessed with a Nikon AZ100 laser scanning confocal microscope.

To seed cells onto the fibronectin squares, patterned coverslips were first adhered to a 35-mm dishes and placed on a hot plate at 40°C to prevent dissolution of the PIPAAm during cell seeding. C2C12 were lifted and suspended at a concentration of 200,000 cells per cover slip while cardiomyocytes were suspended in growth media 3,000,000 cells per cover slip. Cell solutions were placed at 42°C. When a temperature of ~39°C was reached, 2 mL of the cell solution was pipetted onto warmed coverslip. Immediately after seeding, coverslips were transferred into a 37°C incubator. Cells were incubated for 24 hours to allow their attachment to the fibronectin squares.

To “shrink-wrap” the cells, coverslips were washed with warmed media (~39°C) to remove

any unattached cells. Temperature in the dish was then gradually lowered allowed for the temperature to drop below the critical solution temperature of the PIPAAm (~32°C). Once the PIPAAm dissolved, the fibronectin was released from the surface and cells were effectively shrink-wrapped.

8.2.5. Cell Tracker Labelling

To track cellular integration, C2C12 and cardiomyocytes were labelled with CellTracker Green. Prior to the shink-wrapping process, adherent cells were labelled with 10 μM CellTracker Green in DMEM for 30 minutes at 37°C. Cells were then washed with serum-containing growth medium to remove any unbound dye.

8.2.6. Injecting or Seeding Shrink-Wrapped Cells in/on Tissues

A solution of shrink-wrapped cells was made by combining all shrink-wrapped cells into 15 mL centrifuge tubes. This solution was centrifuged at 200 rpm for 7 minutes and the pellet was suspended in a ~30 μL of cell culture medium. Shrink-wrapped C2C12 myoblasts were injected into or seeded on engineered skeletal muscle tissue while shrink-wrapped cardiomyocytes were injected into or seeded on engineered cardiac tissue.

To inject the cells, the solution was injected into the center of a tissue (2 μL per single tissue) using a 10 μL beveled Nanofil syringe using a standard stereomicroscope and a micromanipulator. To seed shrink-wrapped cells on top of the tissues, ~10 μL of the cell solution was pipetted on top of the tissue. Tissues were then allowed to sit in the incubator for 30 minutes at 37°C to ensure that the shrink-wrapped cells attached to the tissue. Tissues were then rinsed 3x to ensure that only the cells attached to the tissue within the 30 minutes would be there and then

cell culture media was added for an additional 72 hours prior to imaging.

8.2.7. Assessing Shrink-wrapped Cell Integration

To assess cellular integration, tissues were fixed in 4% formaldehyde and stained with phalloidin and DAPI based on previously described protocols. Tissues were imaged with a Zeiss LSM Laser Scanning confocal or a Nikon A1R multiphoton microscope.

8.2.8. Tissue Damage

To damage a localized region of tissues, we submerged a paperclip in liquid nitrogen for 1 minute and then immediately pressed it on the center of the tissue for either 10, 20 or 30 seconds. Tissue damage was verified using the commercially available LIVE/DEAD assay (L3224, Life Technologies). Tissues were stained with 2.5 μM Calcein and 4 μM Ethidium Homodimer in Tyrodes solution for 15 minutes at room temperature. The staining solution was then aspirated and replaced with Tyrodes solution. Tissues were imaged with a Nikon AZ100 Laser Scanning Confocal Microscope to assess tissue damage.

8.3 Results

8.3.1 Cellular Shrink-Wrapping Procedure

Cells (either C2C12 or cardiomyocytes) can be shrink-wrapped via the procedure described in Figure 1. Briefly, PDMS stamps with raised features consisting of arrays of 200 x 200 μm squares are incubated in a fibronectin solution (Figure 8.1A). The pattern is then transferred by bringing the stamp into conformal contact with a PIPAAm coated coverslip (Figure 8.1B).

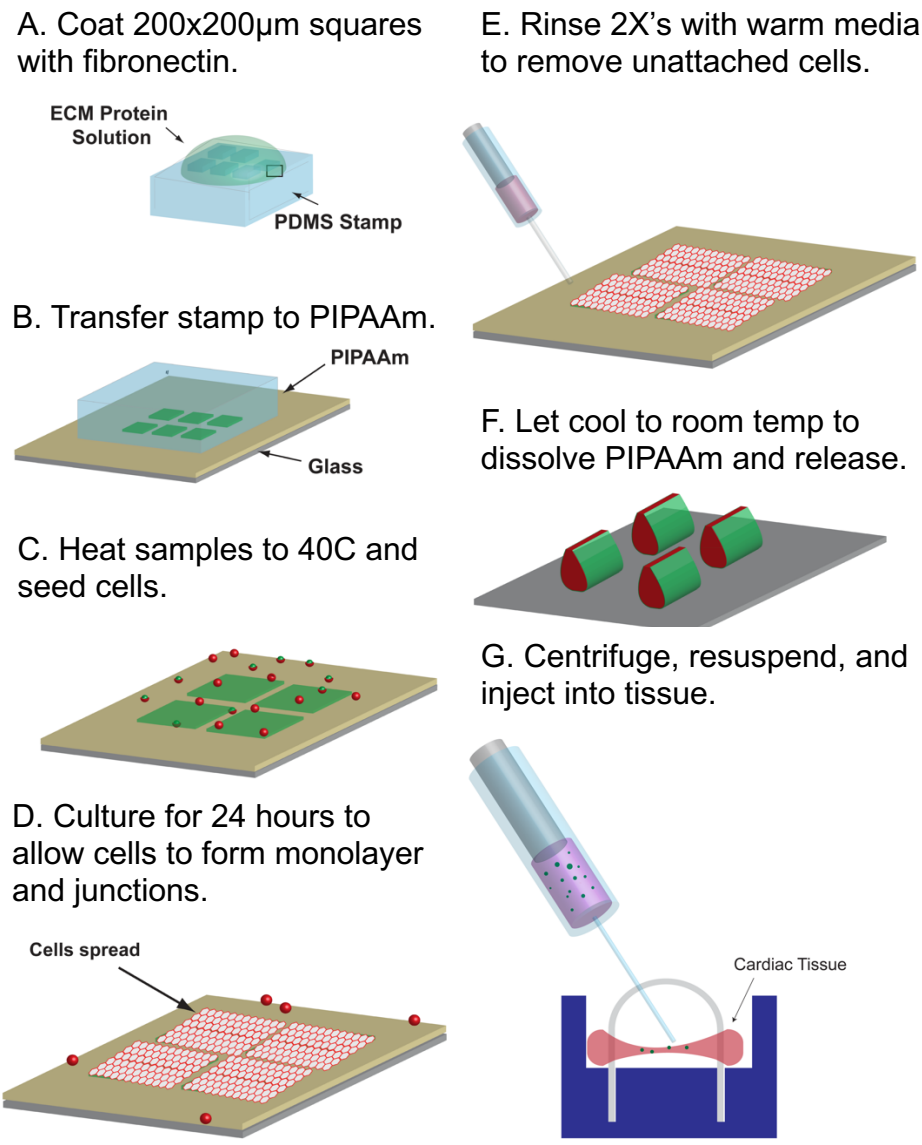

Fig 8.1: Schematic of Cellular Shrink-Wrapping. (A) Stamps are coated with 50 µg/mL fibronectin solution. Stamps are fabricated to have raised features consisting of arrays of squares (200 µm x 200 µm). **(B)** Stamps are then brought into conformal contact with a PIPAAm coated coverslip to transfer the pattern. **(C)** Patterned coverslips are heated to about ~39°C to prevent dissolution of PIPAAm during cell seeding. **(D)** Cells are seeding on the patterned coverslips and incubated for 24 hours to form monolayer and establish certain junctions. **(E)** Prior to release, cells are rinsed with warmed media to remove any unattached or floating cells. **(F)** To release, the substrates are cooled to room temperature triggering PIPAAm dissolution and release of fibronectin and cells from the surface. **(G)** Shrink-wrapped cells can be centrifuged, resuspended, and either injected or delivered into tissues. Figure modified from Dr. Rachelle Palchesko.

Cells are then seeded on these patterned coverslips and are allowed to adhere for 24 hours (Figure 8.1C-D). Unattached cells are rinsed with warmed media prior to PIPAAm release (Figure 8.1E). Cells on the patterned coverslips are then brought to room temperature to trigger PIPAAm dissolution resulting in release of fibronectin from the surface and subsequent shrink-wrapping of cells (Figure 8.1F). Finally, these shrink-wrapped cells can then be centrifuged, resuspended, and delivered to tissues (Figure 8.1G).

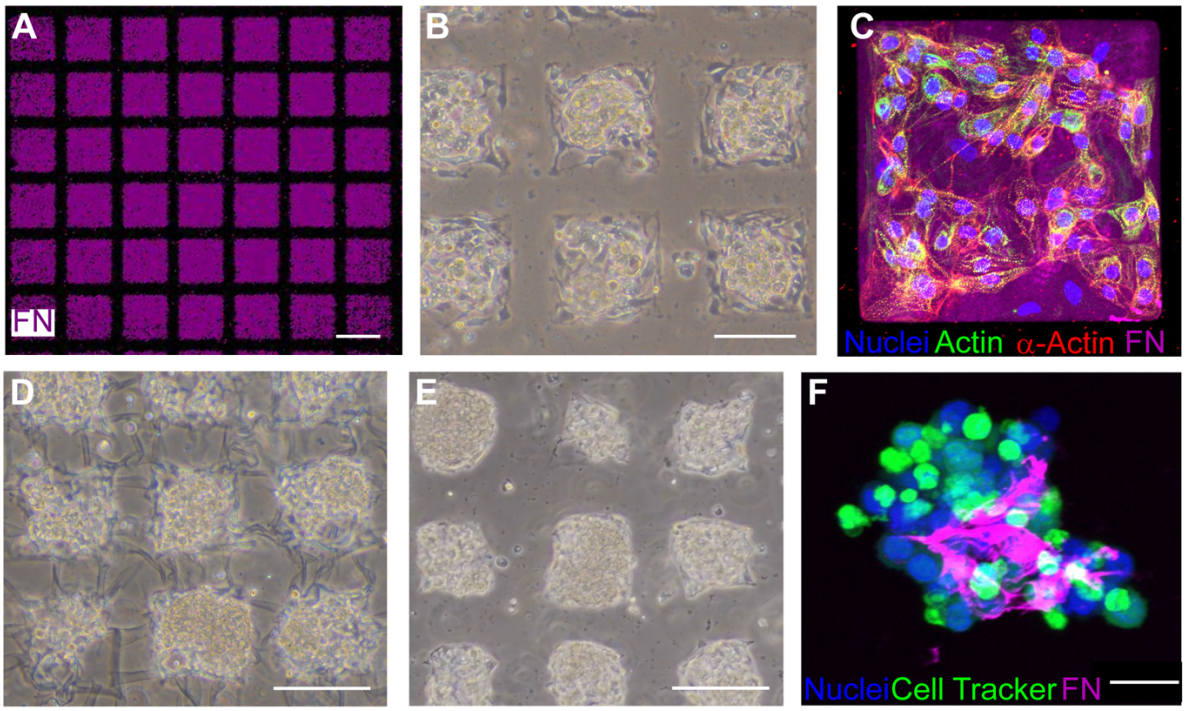

Fig 8.2. Shrink-Wrapped Cell Structure. (A) Fluorescently labelled fibronectin squares patterned on PIPAAm coated coverslips. Scale bar is 200 µm. **(B)** Brightfield image of cardiomyocytes attached to fibronectin squares. Scale bar is 200 µm. **(C)** Confocal microscopy image of cardiomyocytes seeded on a fibronectin (FN) square on PDMS. **(D)** Brightfield image of cells being released from the surface following PIPAAm dissolution. Dissolution of PIPAAm is triggered by lowering the temperature of culture. Scale bar is 200 µm. **(E)** Brightfield image of shrink-wrapped cardiomyocytes. Scale bar is 200 µm. **(F)** Confocal image of release shrink-wrapped cardiomyocyte cluster. Scale bar is 25 µm. Figure and data prepared by Jacqueline Bliley and Kristina Kim.

8.3.2 Shrink-Wrapped Cell Cluster Structure

With this method, I found that we could reliably pattern fibronectin squares onto the PIPAAm substrate (Figure 8.2A). Both C2C12 and cardiomyocytes attached to these fibronectin

patterns (Figure 8.2B). By stamping the fibronectin squares onto PDMS, I was also able to visualize the cellular structure that would be observed prior to release from the PIPAAm (Figure 8.2C). Cardiomyocytes were spread on the fibronectin squares and displayed sarcomeric striations based on the presence of α-actinin expression at the z-lines. When fibronectin squares are patterned onto the PIPAAm surface, they can also be released by lowering the temperature of the media (Figure 8.2D-E). Following release, the fibronectin partially wraps around the cells to create a shrink-wrapped cellular cluster (Figure 8.2F).

8.3.3. Cellular Delivery and Integration Into Tissues

To determine if shrink-wrapped cells could integrate into tissues, I manufactured skeletal muscle tissues and then injected shrink-wrapped clusters into the tissue using a beveled Nanofil syringe (Figure 8.3A).

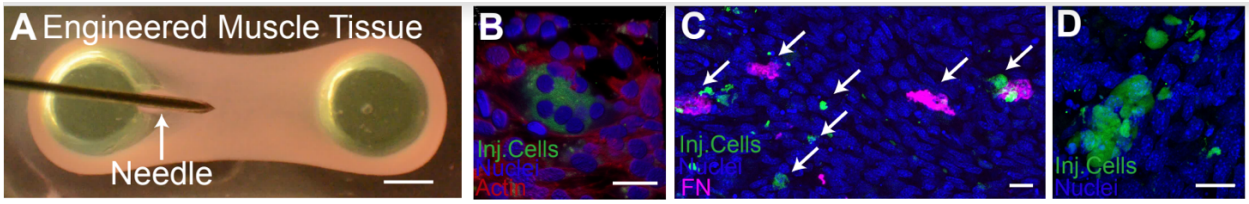

Figure 8.3. Cellular Delivery and Integration into Engineered Muscle Tissues. (A) Brightfield image of needle positioning prior to injection of shrink-wrapped cells. Scale bar is 1 mm. **(B)** High magnification confocal image of injected shrink-wrapped cells (green) immediately after injection. Scale bar is 20 µm. **(C)** Larger area tile scan showing the presence of numerous injected shrink-wrapped clusters into skeletal muscle tissue after 3 days of culture. Scale bar is 25 µm. **(D)** High magnification of integrated shrink-wrapped cluster after 3 days of culture. Scale bar is 25 µm. Figure and data prepared by Jacqueline Bliley and Kristina Kim.

Tissues were fixed and stained immediately following injection to see if the clusters could be delivered and 3 days after injection to observe integration. Immediately after injection shrink-wrapped clusters were present (Figure 8.3B). Following 3 days of culture, numerous shrink-wrapped cells were present on the tissue as well as residual fibronectin fragments (Figure 8.3C). High magnification confocal images of the tissue also appear to show shrink-wrapped cell

integration into the tissue (Figure 8.3D).

8.3.4. Creating a Model of Localized Tissue Damage

Once I had verified that injected cells could be delivered, our next step was to create a model to reliably damage tissues in order to repair them later on. To do this, I used a cryoablation technique by cooling a probe with liquid nitrogen and immediately pressing it on the tissue. LIVE/DEAD stain was used to confirm the presence of live and dead cells on the tissue after staining. Unsurprisingly, engineered tissues that were not damaged had mostly live cells on their surface (Figure 8.4A-D). Application of the cooled probe led to a localized region of death on the tissue surface and area of tissue death seemed to be increased with longer application times of the cooled probe (Figure 8.4C-E).

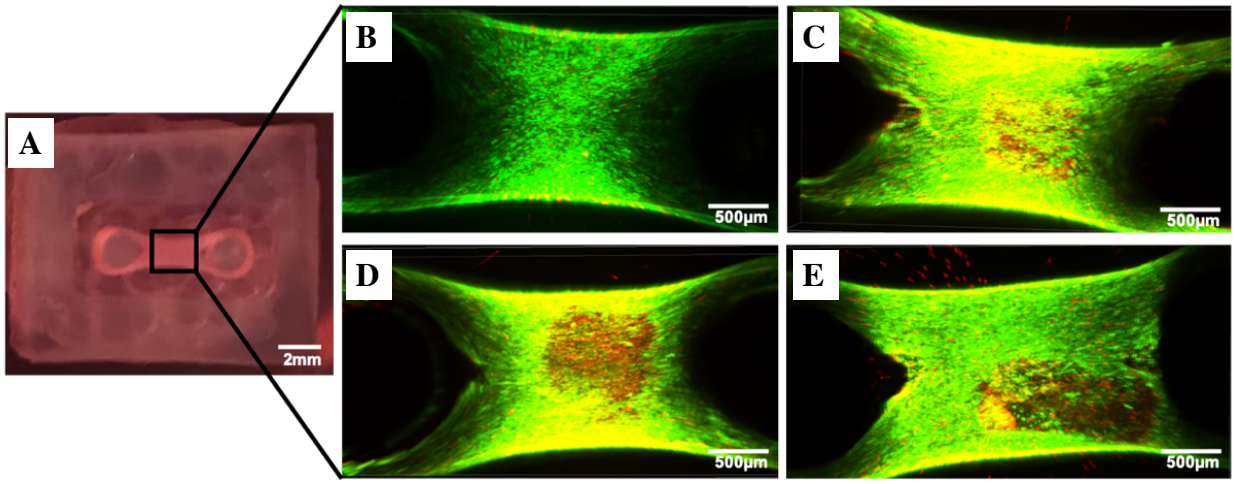

Figure 8.4. Verification of Cryoablation Technique. (A) Engineered skeletal muscle tissue and region used for imaging. (B) Confocal image of LIVE/DEAD staining of control, undamaged skeletal muscle tissue. **(C)** Confocal image of LIVE/DEAD staining of skeletal muscle tissue following 10 seconds of cryoablation. **(D)** Confocal image of LIVE/DEAD staining of skeletal muscle tissue following 20 seconds of cryoablation. **(E)** Confocal image of LIVE/DEAD staining of skeletal muscle tissue following 30 seconds of cryoablation. In all panels, the green color signifies live cells and the red color shows dead cells. Figure and data prepared by Jacqueline Bliley and Kristina Kim.

8.4 Discussion

In this chapter, I utilized an existing technique to shrink-wrap clusters of cells in fibronectin

in order to deliver them to damaged muscle. Previous work in our laboratory has investigated this technique in repairing corneal endothelium and found that shrink-wrapped cell clusters more readily integrate in comparison to injection of isolated cells alone[7]. Similar to our previous work, I found that we could pattern arrays of fibronectin squares onto PIPAAm and that both C2C12 myoblasts and cardiomyocytes could be seeded on fibronectin squares. Following a drop in temperature, the cells were also effectively shrink-wrapped within the fibronectin extracellular matrix. Interestingly, I also found that these shrink-wrapped cells readily attach to both engineered skeletal and heart muscle tissues and that they appear to integrate into the tissues within 3 days of culture. Finally, I created a model of localized tissue damage that we will later use to assess if shrink-wrapped cells can heal the injured area.

Future studies will be important in assessing the ability of shrink-wrapped cells to repair portions of engineered heart muscle tissue and compare these to single cells alone. Previous work has utilized both engineered heart muscle patches[3,8,10–12] and embryoid-body based cardiomyocyte injections[1,5] to repair damaged heart muscle. A current challenge larger engineered heart muscles face is their ability to mechanically and electrically integrate with the surrounding heart tissue. In contrast, cardiomyocytes derived from embryoid bodies appear to incorporate into surrounding heart muscle but also display a high incidence of arrhythmias. This suggests that size of the injected tissues may play a big role in the ability of the injected cardiomyocytes to integrate but also in the development of arrhythmias. Thus, this will be important to assess in future studies.

8.5 Conclusions

In conclusion, I developed a delivery technique where cells are shrink-wrapped inside a fibronectin extracellular matrix. I found that these shrink-wrapped cells readily attach and integrate into engineered tissues. In the future, it will be important to assess the ability of shrink-wrapped

cells to repair damaged muscle.

8.6 Acknowledgements

We would like to thank Dr. Rachelle Palchesko for developing the shrink-wrapping technique for corneal endothelium cells and helping us adapt this technique to be utilized with C2C12 myoblasts and cardiomyocytes. We would also like to thank the undergraduates who worked extensively on this project, including Madison Stiefbold and Kristina Kim.

8.7 References

1. Chong, J. J. H., X. Yang, C. W. Don, E. Minami, Y. W. Liu, J. J. Weyers, W. M. Mahoney, B. Van Biber, S. M. Cook, N. J. Palpant, J. A. Gantz, J. A. Fugate, V. Muskheli, G. M. Gough, K. W. Vogel, C. A. Astley, C. E. Hotchkiss, A. Baldessari, L. Pabon, H. Reinecke, E. A. Gill, V. Nelson, H. P. Kiem, M. A. Laflamme, and C. E. Murry. Human embryonic-stem-cell-derived cardiomyocytes regenerate non-human primate hearts. *Nature* 510:273–277, 2014.
2. Deng, M. Cardiac Transplantation. *Heart* 87:177–184, 2002.
3. Jackman, C. P., A. M. Ganapathi, H. Asfour, Y. Qian, B. W. Allen, Y. Li, and N. Bursac. Engineered cardiac tissue patch maintains structural and electrical properties after epicardial implantation. *Biomaterials* , 2018.doi:10.1016/j.biomaterials.2018.01.002
4. Katz, A. M. Maladaptive growth in the failing heart: The cardiomyopathy of overload. , 2002.doi:10.1023/A:1020604623427
5. Laflamme, M. A., K. Y. Chen, A. V. Naumova, V. Muskheli, J. A. Fugate, S. K. Dupras, H. Reinecke, C. Xu, M. Hassanipour, S. Police, C. O'Sullivan, L. Collins, Y. Chen, E. Minami, E. A. Gill, S. Ueno, C. Yuan, J. Gold, and C. E. Murry. Cardiomyocytes derived from human embryonic stem cells in pro-survival factors enhance function of infarcted rat hearts. *Nat. Biotechnol.* 25:1015–1024, 2007.
6. Palchesko, Rachelle N., et al. Shrink Wrapping Cells in a Defined Extracellular Matrix to Modulate the Chemo-Mechanical Microenvironment. *Cell. Mol. Bioeng.* 23:1–7, 2014.
7. Palchesko, R. N., Y. Du, M. L. Geary, S. D. Carrasquilla, D. J. Shiwarski, I. Khandaker, J. L. Funderburgh, and A. W. Feinberg. Injury-Free In Vivo Delivery and Engraftment into the Cornea Endothelium Using Extracellular Matrix Shrink-Wrapped Cells. *bioRxiv* , 2021.
8. Stevens, K. R., L. Pabon, V. Muskheli, and C. E. Murry. Scaffold-free human cardiac tissue patch created from embryonic stem cells. *Tissue Eng. - Part A* , 2009.doi:10.1089/ten.tea.2008.0151
9. Tzahor, E., and K. D. Poss. Cardiac regeneration strategies: Staying young at heart. *Science (80-.).* 356:1035–1039, 2017.
10. Weinberger, F., K. Breckwoldt, S. Pecha, A. Kelly, B. Geertz, J. Starbatty, T. Yorgan, K. H. Cheng, K. Lessmann, T. Stolen, S. C. Marielle, G. Smith, H. Reichenspurner, A. Hansen, and T. Eschenhagen. Cardiac repair in Guinea pigs with human engineered heart tissue from induced pluripotent stem cells. *Sci. Transl. Med.* , 2016.doi:10.1126/scitranslmed.aaf8781
11. Zimmermann, W. H., M. Didié, G. H. Wasmeier, U. Nixdorff, A. Hess, I. Melnychenko, O. Boy, W. L. Neuhuber, M. Weyand, and T. Eschenhagen. Cardiac grafting of engineered heart tissue in syngenic rats. *Circulation* , 2002.doi:10.1161/01.cir.0000032876.55215.10
12. Zimmermann, W. H., I. Melnychenko, G. Wasmeier, M. Didié, H. Naito, U. Nixdorff, A. Hess, L. Budinsky, K. Brune, B. Michaelis, S. Dhein, A. Schwoerer, H. Ehmke, and T. Eschenhagen. Engineered heart tissue grafts improve systolic and diastolic function in infarcted rat hearts. *Nat. Med.* ,

2006.doi:10.1038/nm1394

Appendix B:

3D Bioprinted Collagen Tubes Support Tissue Viability

9.1 Introduction

Death or damage to the heart muscle can occur due to a number of insults, including lack of blood supply after a coronary artery occlusion (myocardial infarction) or due to exposure to toxic drugs, like certain chemotherapeutics. This is a significant concern because the heart has limited regenerative capacity[1] and is unable to repair the damage, leading to a progressive decline in pump function. While medication and lifestyle changes can limit such a decline in heart function, many patients will ultimately develop heart failure, a condition where the heart cannot pump enough blood to meet the body's demands. Heart transplantation is one solution, but unfortunately, there are not enough available donor organs for all those who need them[3], and the surgery plus required lifelong postoperative immunosuppression, are daunting challenges for transplant recipients.

Advances in tissue engineering have made it possible to create patient-derived contractile, heart muscle tissues[13,14], but it is difficult to create viable, large volume (>1cm^3) cardiac muscle because many of these tissues lack a vasculature needed to supply necessary nutrients. Previous work fabricating large diameter (1-6 mm diameter) vascular tubes to repair damaged blood vessels has demonstrated moderate success, but fabrication strategies to create complex architectures capable of supporting nutrient delivery to large volumetric tissues has proved challenging[16]. 3D printing can potentially be used as a tool to fabricate the vasculature required to support the viability of large volume tissues. However, it is difficult to print soft biomaterials (including type

I collagen) that comprise the *in vivo* vasculature. Several 3D printing strategies have been employed to create vasculature within engineered tissues, including casting tissues around sacrificial 3D printed filaments that can later be removed to create vessels with patent lumens[7,8]. While this strategy has greater control over architecture compared to traditional casting approaches, it is limited, in that it is unable to form the structural wall of the vessel. This wall structure is important for vascular cell attachment as well as forming a niche that supports the function of the main vessel (for example, the smooth muscle cell layer found in arterioles capable of diverting blood flow to specific capillary beds).

Here, I utilize an alternative strategy to directly extrude the collagen filaments that make up the vessel walls by using a 3D printing technique termed Freeform Reversible Embedding of Suspended Hydrogels, or FRESH. Previous work has demonstrated our ability to 3D print complex vascular architectures out of type I collagen but we had yet to evaluate these printed vessels as a means to allow nutrient exchange to support tissue viability[5]. Thus, the purpose of this study was to evaluate the ability of 3D printed collagen tubes to support perfusion, allow the diffusion of nutrients, and support the viability of large volume tissues (~0.6cm^3).

9.2 Materials and Methods

9.2.1 Cell Culture

Murine C2C12 myoblasts were used for viability studies (CRL-1772, ATCC). The C2C12s were cultured at 37°C under 5% CO_2 with Dulbecco's modified Eagle's medium (DMEM) (15-013-CM, Corning) supplemented with 10% (v/v) Fetal Bovine Serum (FBS) (89510-186, VWR), 1% (v/v) L-glutamine (25030-081, Life Technologies), and 1% (v/v) penicillin-streptomycin (15140-122, Life Technologies). Media was exchanged every 2 days and C2C12s were passaged

prior to reaching 80% confluence.

9.2.2 Large Volume Tissue Casting

C2C12 tissues were cast in custom, 3D printed polylactic acid (PLA) wells. C2C12 were cast in a 3D hydrogel within the 3D printed PLA mold, consisting of 2.5 mg/mL rat tail collagen type I (354249, Corning), 1.7 mg/mL Matrigel (354234, Corning), 10% (v/v) 10X PBS, 2.3% (v/v) 1N NaOH, and 37.5 X 10^6 C2C12 cells/mL. A 600 µL volume of this cell and collagen mixture was pipetted into each well and gelled in the incubator at 37ºC for 1 hour.

To determine tissue viability, tissues were removed from the wells at 1, 2, and 5 days and rinsed with Tyrode's solution (T2145, Sigma-Aldrich) for 10 min on an orbital shaker. Tissues were then cross-sectioned with a scalpel and stained with 2 µM calcein AM and 4 µM ethidium homodimer (Live Dead Kit; L3224, Life Technologies) according to the manufacturer's protocol. Large area, tile-scan images of the entire tissue cross-section were performed using a Zeiss LSM 700 laser scanning confocal microscope with a 10x objective. Imaris image analysis software was used to quantify the number of live cells (calcein-positive) as a function of distance from the top surface of the construct (i.e., not touching the sides of the well).

9.2.3 Design and Preparation of Perfusion Chambers and System

Long-term assessment of tissues surrounding the collagen tube was performed using custom-designed perfusion chambers under sterile culture conditions. Perfusion chambers designed to hold the collagen tube construct and interface it with inlet and outlet needles were fabricated using a multi-step process. First, the main chamber was printed with Dental SG resin (RS-F2-DGOR-01, Formlabs) on a Form 2 SLA printer (Formlabs). Next, a polylactic acid (PLA)

insert was 3D printed with a MakerBot Replicator 2X and placed on top of the perfusion chamber to form a temporary mold around which polydimethylsiloxane (PDMS) (Sylgard 184, Dow Corning) was cast and cured to form a rectangular well. Stainless steel, 310 μm ID, 1" long deposition needles (JG24-1.0HP, Jensen Global) were inserted into the side of the perfusion chamber and central PLA insert during PDMS curing to form through holes within the PDMS well for future perfusion needle placement. Prior to use, perfusion chambers were sterilized with an autoclave.

9.2.4 FRESH printing of Collagen Tubes

Perfusable collagen tubes were designed to approximate the scale of small arteries with a 2 mm outer diameter and a 300 μm wall thickness. The construct was FRESH printed with the tube oriented within the *xy* build plane, and the tube walls were printed as perimeters at a speed of 10 mm/s to ensure high print fidelity and lumen patency. Once printed, perfusion tube constructs were released from the FRESH support by heating to 37ºC, washed gently with 50 mM HEPES and sterilized under UV (PSD Pro Series, Novascan) for 15 min prior to use.

9.2.5 Diffusion Experiments Through Tube Walls

Fidelity, patency and wall integrity of the printed collagen tube was assessed by perfusion using fluorescently-labeled dextrans. Perfusion within the tube lumen and diffusion through tube wall was visualized using 10 kDa fluorescein dextran and 70 kDa rhodamine dextran, which flowed sequentially through the tube using a peristaltic pump (ISM934C, Ismatec). Epifluorescent time-lapse imaging was performed on a stereomicroscope (SMZ1500, Nikon) with a CMOS camera (Prime 95B, Photometrics) and X-cite lamp (Excelitas Technologies). A kymograph was

constructed from the time series in ImageJ and used to quantify relative dextran diffusion through the tube wall and into the surrounding tissue casting chamber.

9.2.6 Tissue Casting Around Collagen Tubes and Perfusion Experiments

For perfusion studies, collagen tube constructs were carefully transferred into the PDMS wells in the perfusion chambers. Stainless-steel needles were inserted for inflow and outflow. Next, C2C12s in a 3D hydrogel were cast around the collagen tube within the tissue casting chamber. The gel consisted of 2.5 mg/mL rat tail collagen type I (354249, Corning), 1.7 mg/mL Matrigel (354234, Corning), 10% (v/v) 10X PBS, 2.3% (v/v) 1N NaOH, and 37.5 X 10^6 C2C12 cells/mL. A 600 µL aliquot of this cell and collagen mixture was pipetted around each collagen tube and gelled in the incubator at 37ºC for 1 hour. Collagen tube constructs with cast C2C12s were then cultured as static controls (no perfusion) or perfused within the incubator. Briefly, 1/16" ID silicone tubing (EW-95802-02, Cole Parmer), male and female Luer connectors (51525K291 and 51525K141, McMaster Carr), perfusion needles (JG24-1.0HP, Jensen Global), and media bags (32C, St. Gobain) were autoclaved and then connected into a flow loop. Collagen tube constructs were perfused at a flow rate of 0.4 mL/min using a peristaltic pump (ISM934C, Ismatec) for 5 days at 5% CO_2 and 37ºC using DMEM (15-013-CM, Corning) with 10% (v/v) FBS (89510-186, VWR), 1% (v/v) L-glutamine (25030-081, Life Technologies), and 1% (v/v) penicillin-streptomycin (15140-122, Life Technologies). The non-perfused controls were cultured for 5 days in the perfusion chambers with 3 mL of medium on top of the construct with daily media exchanges.

To determine tissue viability, constructs were removed from the perfusion chambers at 5 days and rinsed with Tyrode's solution (T2145, Sigma-Aldrich) for 10 min on an orbital shaker.

Constructs were then cross-sectioned with a scalpel and stained with 2 μM calcein AM and 4 μM ethidium homodimer (L3224, Life Technologies) according to the manufacturer's protocol. Large area tile-scan images of the entire construct cross-section were performed using a Zeiss LSM 700 laser scanning confocal microscope with a 10X objective. Imaris image analysis software was used to quantify the number of live cells (calcein-positive) as a function of distance from the top surface of the construct (i.e., not touching the sides of the PDMS well in the perfusion chamber). A depth of 600 μm from the top surface of the construct was analyzed because the perfused constructs compacted much more than non-perfused controls.

9.2.7 Statistical Analysis

Statistical analysis was performed using Prism 6 (GraphPad Software) software, and appropriate statistical tests were chosen according to experimental conditions and data requirements.

9.3 Results

9.3.1 Large Volume Bulk Cast Tissues Display Largely Non-Viable Interior

To determine the extent and time course of cell death within large volume, static (non-perfused) tissues, I first cast tissues (600 μL) in custom 3D printed PLA molds (Figure 9.1A). Little tissue compaction was observed over the course of 5 days with the main amount of compaction being observed on the tissue surface closest to the media source (Figure 9.1B). Confocal images of the entire tissue cross-section revealed that tissue death is rapid with the majority of the tissue interior containing dead cells after only 1 day of culture (Figure 9.1C). This finding persists on days 2 and 5 with tissues demonstrating a small layer of viable cells of about

100-200 µm near the tissue surface closest to the media source (Figure 9.1D). These studies were important because they helped inform when media perfusion through the collagen tube should begin and that cast tissues at this volume and cellular density display little cell-driven tissue compaction enabling us to accurately quantify cell death as a function of distance from the tissue surface.

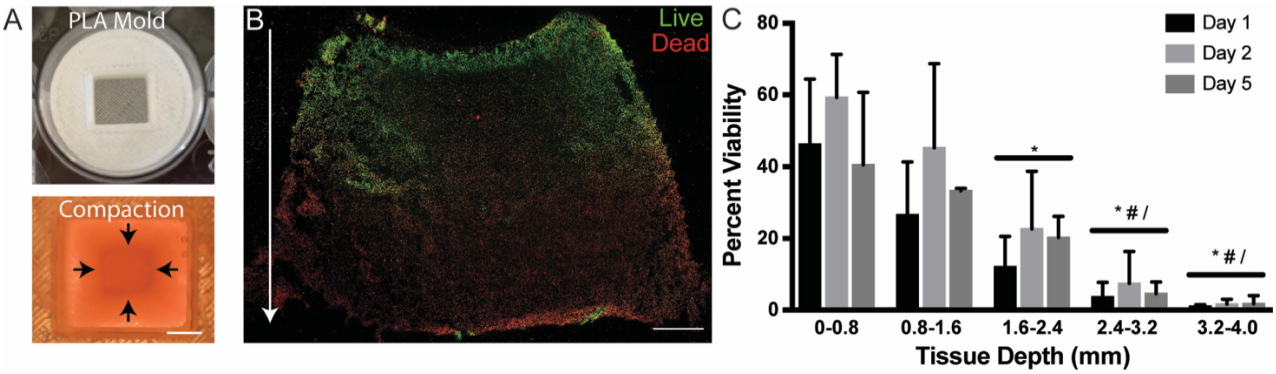

Figure 9.1: Determining live and dead cell distribution in cast large volume gels. **(A)** Image of PLA mold used for large volume tissue casting and image of tissue compaction. Arrows demonstrate that the tissue surface (closest to the media source) compacted much more than the bottom of the tissue. **(B)** Cross-section of tissue stained for LIVE/DEAD after one day of culture. White arrow indicates increasing tissue depth. **(C)** Percent viability as a function of tissue depth. Statistics based on 2 way ANOVA on ranks with independent variables being tissue depth and number of days in culture. n=4 tissues/group for day 1, n=5 tissues/group day 2, and n=3 tissues/group for day 5. * indicates statistical significance from 0-0.8 mm depth ($p<0.0001$). # indicates statistical significance from 0.8-1.6 mm depth ($p<0.05$). / indicates statistical significance from 1.6-2.4 mm depth ($p<0.05$). Figure and data prepared by Jacqueline Bliley.

9.3.2 Design and Preparation of Perfusion Chambers and System

As previously stated, the goal of this project was to assess the ability of 3D printed collagen tubes to support tissue viability. To do this, it was necessary to design a custom perfusion dish, where the collagen tube construct could sit and that allowed for media to be perfused through it. The CAD model of this custom perfusion dish is shown in Figure 9.2A. The perfusion dish was printed with a Form 2 stereolithographic printer which allowed high resolution printing of a fluid-tight, sealed, chamber (Figure 9.2B). Dental SG resin was used because previous work has demonstrated its biocompatibility[9] and ability to be autoclaved ensuring sterility during tissue

perfusion studies. Following printing, a PDMS well was created in the central region of the perfusion dish using a PLA insert (Figure 9.2C). The PLA insert was designed to clip into the perfusion chamber and interface with the perfusion needles. This created holes within the PDMS that allowed for future perfusion needle placement.

An image of the complete perfusion chamber is shown in Figure 9.2D, with the PDMS well (where the collagen tube construct would sit) and inserted perfusion needles (which would eventually attach the perfusion chamber to the media flow circuit). Once the perfusion chamber was complete, the collagen tube construct was placed in the PDMS well and perfusion needles were advanced into the lumen of the collagen tube (Figure 9.2E). Following collagen tube placement, the tissue was cast around the collagen tube and then leur connectors attached the perfusion dish (Figure 9.2F) to the perfusion system (Figure 9.2G). The perfusion system consisted of silicone tubing connecting a multichannel peristaltic pump and a sterile bag containing media (media reservoir).

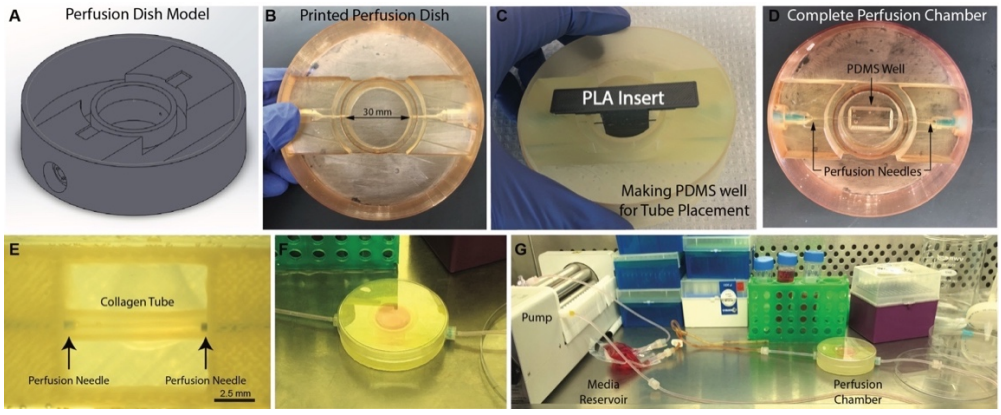

Figure 9.2: Perfusion setup for collagen tubes. (A) A CAD model of the perfusion chamber. **(B)** The perfusion chamber 3D printed using stereolithography. **(C)** The 3D printed perfusion chamber (clear yellow plastic) with the 3D printed polylactic acid (PLA) negative mold (gray plastic) placed on top. Polydimethylsiloxane (PDMS) is poured in between these pieces and cured to form a well to hold the collagen tube construct. **(D)** The complete perfusion chamber setup with a central PDMS well and perfusion needles inserted. **(E)** The FRESH printed collagen tube construct within the perfusion chamber showing insertion of perfusion needles through both ends. **(F)** The perfusion chamber with media added and lid placed for sterile culture. **(G)** The perfusion chamber circuit used for long term culture including a perfusion chamber with collagen tube construct, multichannel peristaltic pump and media reservoir. The entire setup is then placed within a cell culture incubator. Figure and data prepared by Jacqueline Bliley.

9.3.3 3D Printed Collagen Tube Design and Perfusability

The model consisted of a tube with a 1.4 mm inner diameter (ID) lumen, 0.3 mm wall thickness, and 9 mm freestanding length (Figure 9.3A). Each end of the tube was embedded within a block-like region of collagen to provide mechanical support for the freely-suspended region of the tube and for needle insertion during perfusion. 3D printed collagen tubes were robust and did not collapse under their own weight (Figure 9.3B). The central region of the construct consisted of a tissue casting chamber with a volume of 600 μL. A confocal reflectance image of the printed tube revealed a highly porous tube cross-section, which previous work in our laboratory has demonstrated is due to gelatin particles that become embedded during the printing process (Figure 9.3C).

Perfusion with the fluorescent dextran through the tube lumen demonstrated that printed tubes were patent and manifold along their length (Figure 9.3D). Perfusion with fluorescent dextrans was also used to assess diffusion of certain molecular weight (MW) substances through the collagen tube wall (Figure 9.3E). The higher MW fluorescent dextran (70 kDa) demonstrated reduced diffusion through the collagen tube walls compared to the lower MW fluorescent dextran (10 kDa) (Figure 9.3F). Diffusion of the lower MW dextran is significant because this size is on order of the size of a small growth factor suggesting these and other small nutrients (e.g. glucose) are able to diffuse across the tube wall.

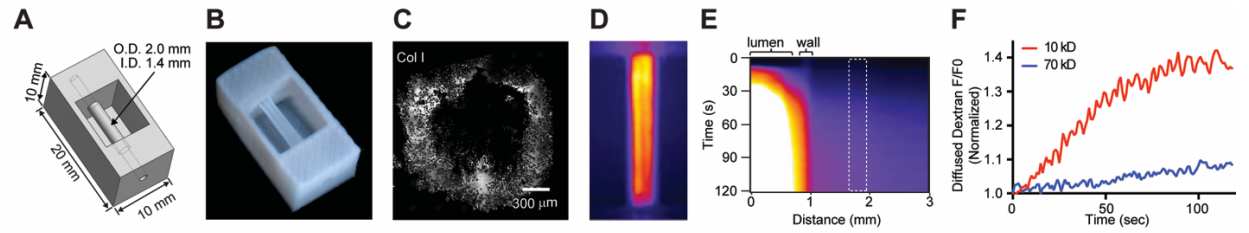

Figure 9.3: Tube Model Can Be Printed and Allows for Diffusion of Certain Molecular Weight Substances. (A) CAD model of tube structure consisting of tube suspended over a well where a tissue would eventually be cast. **(B)** Image of 3D printed collagen tube. **(C)** Confocal Reflectance microscopy image of tube cross-section. **(D)** Fluorescence image of 70 kDa fluorescent dextran flowing through tube lumen with attached perfusion circuit. **(E)** Kymograph of fluorescent intensity of 10 kDa fluorescent dextran perfusing through printed collagen tube wall into surround well where tissue would eventually be cast. Dotted line indicates region where relative fluorescent intensity measurements were taken. **(F)** Relative diffusion of 10 kDa and 70 kDa dextran through the tube wall from the kymograph (white box in E). Figure and data prepared by Jacqueline Bliley, Dan Shiwarski and Josh Tashman.

9.3.4 Perfusion Through 3D Printed Collagen Tubes Increases Tissue Compaction and Supports Tissue Viability

C2C12 cells within a collagen gel were cast around the printed collagen tube to evaluate the ability of diffusion of media through the tube to support volumetric tissue viability. The static non-perfused controls showed minimal compaction over 5 days (Figure 9.4A). A cross-section revealed dead cells throughout the interior volume with a layer of viable cells only at the surface (~100-200 µm) similar to previous results from control studies (Figure 9.4B). In contrast, after active perfusion for 5 days, C2C12 cells compacted the collagen gel around the collagen tube (Figure 9.4C), demonstrating viability and active remodeling of the gel through cell-driven compaction. The cross section showed cells alive throughout the entire area, which was measured to be 8.86 ±1.24 mm^2 (Figure 9.4D). Quantitative analysis using LIVE/DEAD staining confirmed high viability within the perfused vascular construct (Figure 9.4E).

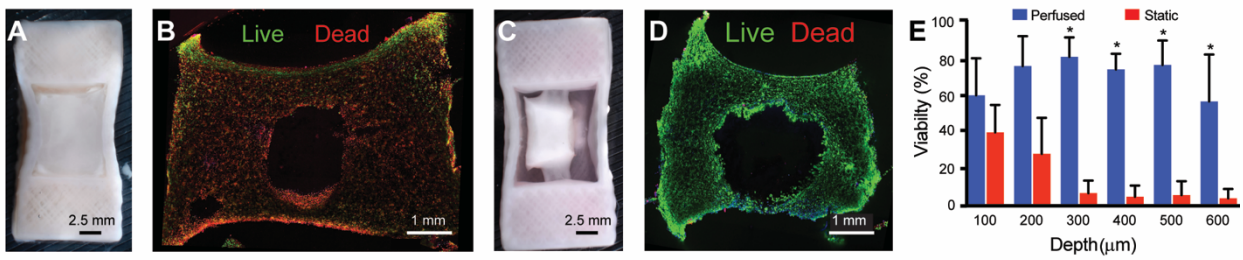

Figure 9.4: Perfused Collagen Tubes Support Tissue Viability. (A) C2C12 cell and collagen gel mixture cast around the collagen tube and static-cultured for 5 days. **(B)** Cross section of the statically-culture tissue stained for live (green) and dead (red) cells. **(C)** C2C12 cell and collagen gel mixture cast around the collagen tube and perfused for 5 days. **(D)** Cross section of the perfused tissue stained for live and dead cells. **(E)** Percent cell viability as a function of depth from the top surface of the tissues from the static and perfused collagen tube constructs [N = 3, data are means ± SD, *P < 0.05 (two-way ANOVA followed by Bonferroni multiple-comparisons post hoc test)]. Figure and data prepared by Jacqueline Bliley.

9.4 Discussion

In this chapter, I demonstrated that 3D printed collagen tubes can be perfused to support the viability of surrounding tissue. First, I established that large volume (600 µL), diffusion-limited tissues could be cast and reliably develop an internal core consisting mostly of dead cells. From these studies, I also demonstrated that the time course of this death is very rapid (within 24 hours), which informed my future studies, necessitating rapid media perfusion immediately after casting. It is important to note that although C2C12 tissues were cast at a high density (~40 million cells per mL), casting cells within a gel is limited because it is unable to recreate the high cellular density observed in many *in vivo* tissues and organs. For instance, the normal cellular density in heart muscle is approximately one billion cells per mL, which is nearly 2 orders of magnitude higher than the density of tissues utilized in these studies[4]. Future work should focus on creating tissues with higher cell density by using either packed embryoid body-based approaches[15] or stacked cellular sheets[4]. Despite these concerns, I was able to cast diffusion-limited tissues which demonstrated a reproducible core of dead cells.

Further, I was able to develop a perfusion system and chamber in-house which easily interfaced with the printed collagen tube structure. Though the perfusion system was able to

perfuse media continually through the tissues for 5 days, there are several improvements which could be made to the design. The system was designed to allow for media to be cultured on top of the tissue during the duration of the study, in addition to allowing perfusion through the tube lumen. Thus, tissues in this study would have been exposed to two nutrient sources: one flowing through the tube and the other bathing the external surface. This means the tissue did not survive on the media source flowing through the collagen tube alone. However, given the minimal contribution that static media bathing the surface of the tissue had on viability, I postulate that a large contribution of the increased cellular viability was actually due to the media source flowing through the collagen tube lumen. Another limitation of the perfusion system is that it did not increase oxygen availability that would also promote tissue viability. Typical oxygen saturation in tissue culture media is around 1-3% and it precipitously declines within a cast cellular construct[12]. This is especially important for cardiac tissues where cardiomyocytes have a high metabolic demand and are more reliant on oxygen for oxidative metabolism. Researchers have also developed several strategies to improve oxygen saturation in perfusion bioreactors in efforts to improve cellular viability by incorporating oxygen carriers (like perfluorocarbon beads) into the media[6] or using a long length of tubing within the flow circuit to enhance oxygen diffusion into the media[2].

One additional limitation of the perfusion system was the lack of a good seal between the collagen tube and the perfusion tubing. Due to the fact that the collagen was very fragile (on the order of a few kPa), I chose to interface the perfusion tubing using a perfusion needle situated in the center of the collagen tube. Future work should focus on creating a better seal between these two interfaces (the collagen tube and the perfusion tubing) to ensure that nutrients are only flowing through the tube. This would allow a better assessment of the efficacy of the collagen tube in

supporting tissue viability.

One interesting finding was that the cell death seemed to correlate with the amount of tissue compaction. In bulk cast statically cultured tissues, tissue compaction was very minimal with most of the compaction being observed at the tissue surface. This correlated with the location of live cells within tissue. A similar finding was observed within the static cultured tissues cast around the collagen tube where even less tissue compaction was observed. The surrounding collagen walls may have effectively increased the distance for nutrient diffusion on the side of the tissue. The presence of a perfused media source through the tube led to robust tissue compaction suggesting that not only were the cells alive, but their metabolic activity (measured via tissue compaction) was vastly increased.

Finally, given the resolution limit of our 3D printer, it would be very difficult to print the small capillaries and venules that comprise the vascular tree. However, since endothelial cells along with other vascular cells have the capacity to self-assemble into capillary and venule-like structures, printing of such small elements of the vascular tree, may not be required[11]. In addition, previous research suggests that our 3D prints have a unique capacity to enhance vascular cellular infiltration via the inherent porosity of the prints[10]. This will be a prime focus of future investigations.

9.5 Conclusions

In conclusion, I was able to create a simplified vascular tube using collagen 3D printing that allowed enough perfusion to support tissue viability. Future work will assess the ability of these 3D printed collagen tubes to get at our ultimate goal of supporting heart muscle tissue viability, which will be necessary as we transition to printing larger heart muscle tissue segments.

9.6 Acknowledgements

We would like to thank TJ Hinton for his help with designing the perfusion chamber. We would also like to thank Dan Shiwarski and Josh Tashman for their help with fluorescent dextran studies and tube photography.

9.7 References

1. Bergmann, O., R. D. Bhardwaj, S. Bernard, S. Zdunek, F. Barnabé-Heide, S. Walsh, J. Zupicich, K. Alkass, B. A. Buchholz, H. Druid, S. Jovinge, and J. Frisén. Evidence for cardiomyocyte renewal in humans. *Science (80-.).* 324:98–102, 2009.
2. Brown, M. A., R. K. Iyer, and M. Radisic. Pulsatile perfusion bioreactor for cardiac tissue engineering. *Biotechnol. Prog.* 24:907–920, 2008.
3. Girlanda, R. Deceased organ donation for transplantation: Challenges and opportunities. *World J. Transplant.* 6:451, 2016.
4. Guo, Y., X. Z. Zhang, Y. Wei, C. Guo, R. X. Li, Q. C. Zeng, and Y. J. Zhang. Culturing of ventricle cells at high density and construction of engineered cardiac cell sheets without scaffold. *Int. Heart J.* 50:653–662, 2009.
5. Hinton, T. J., Q. Jallerat, R. N. Palchesko, J. H. Park, M. S. Grodzicki, H. J. Shue, M. H. Ramadan, A. R. Hudson, and A. W. Feinberg. Three-dimensional printing of complex biological structures by freeform reversible embedding of suspended hydrogels. *Sci. Adv.* 1:, 2015.
6. Iyer, R. K., M. Radisic, C. Cannizzaro, and G. Vunjak-Novakovic. Synthetic oxygen carriers in cardiac tissue engineering. *Artif. Cells, Blood Substitutes, Biotechnol.* 35:135–148, 2007.
7. Jordan S. Miller, Kelly R. Stevens, Michael T. Yang, Brendon M. Baker, Duc-Huy T. Nguyen, Daniel M. Cohen, Esteban Toro, Alice A. Chen, Peter A. Galie, Xiang Yu, Ritika Chaturvedi, Sangeeta N. Bhatia, c, d, and C. S. C. Rapid casting of patterned vascular networks for perfusable engineered 3D tissues. *Nat. Mater.* 176:139–148, 2019.
8. Kolesky, D. B., K. A. Homan, M. A. Skylar-Scott, and J. A. Lewis. Three-dimensional bioprinting of thick vascularized tissues. *Proc. Natl. Acad. Sci. U. S. A.* 113:3179–3184, 2016.
9. Kurzmann, C., K. Janjić, H. Shokoohi-Tabrizi, M. Edelmayer, M. Pensch, A. Moritz, and H. Agis. Evaluation of Resins for Stereolithographic 3D-Printed Surgical Guides: The Response of L929 Cells and Human Gingival Fibroblasts. *Biomed Res. Int.* 2017:, 2017.
10. Lee, A., A. R. Hudson, D. J. Shiwarski, J. W. Tashman, T. J. Hinton, S. Yerneni, J. M. Bliley, P. G. Campbell, and A. W. Feinberg. 3D bioprinting of collagen to rebuild components of the human heart. *Science (80-.).* , 2019.doi:10.1126/science.aav9051
11. Moya, M. L., Y. H. Hsu, A. P. Lee, C. W. H. Christopher, and S. C. George. In vitro perfused human capillary networks. *Tissue Eng. - Part C Methods* 19:730–737, 2013.
12. Radisic, M., J. Malda, E. Epping, W. Geng, R. Langer, and G. Vunjak-Novakovic. Oxygen gradients correlate with cell density and cell viability in engineered cardiac tissue. *Biotechnol. Bioeng.* 93:332–343, 2006.
13. Ronaldson-Bouchard, K., S. P. Ma, K. Yeager, T. Chen, L. J. Song, D. Sirabella, K. Morikawa, D. Teles, M. Yazawa, and G. Vunjak-Novakovic. Advanced maturation of human cardiac tissue grown from pluripotent stem cells. *Nature* , 2018.doi:10.1038/s41586-018-0016-3
14. Shadrin, I. Y., B. W. Allen, Y. Qian, C. P. Jackman, A. L. Carlson, M. E. Juhas, and N. Bursac. Cardiopatch

platform enables maturation and scale-up of human pluripotent stem cell-derived engineered heart tissues. *Nat. Commun.* 8:, 2017.

15. Skylar-Scott, M. A., S. G. M. Uzel, L. L. Nam, J. H. Ahrens, R. L. Truby, S. Damaraju, and J. A. Lewis. Biomanufacturing of organ-specific tissues with high cellular density and embedded vascular channels. *Sci. Adv.* 5:, 2019.
16. Song, H. H. G., R. T. Rumma, C. K. Ozaki, E. R. Edelman, and C. S. Chen. Vascular Tissue Engineering: Progress, Challenges, and Clinical Promise. *Cell Stem Cell* 22:340–354, 2018.

Appendix C:

Publications, Presentations, Posters, Patents and Awards/Honors

PUBLICATIONS

1. James IB; Bourne DA; Minteer DM; Schusterman, MA; Wang S; **Bliley JM**; Donnenberg AD; Donnenberg V; Branstetter B; Haas GL; Simon P; Meyer EM; Marra KG; Coleman S; Rubin JP. **Comparing Telfa Rolling versus Centrifugation for Fat Grafting Craniofacial Deformities: A Clinical Study**. Plastic and Reconstructive Surgery. Mar 2021 (Under Preparation).
2. Bliley JM; Tashman J; Shiwarski D; Stang M; Lee A; Coffin B; Hinton TJ; Feinberg AW. **FRESH 3D Bioprinting a Contractile Heart Tube Using Human Stem Cell-Derived Cardiomyocytes**. Biofabrication. Mar 2021 (In Review).
3. Ng WH; Johnston E; Tan JJ; **Bliley JM**; Feinberg AW; Stolz D; Sung M; Hawkins F; Kotton D; Ren Xi. **Recapitulate Human Cardio-pulmonary Co-development Using Simultaneous Multilineage Differentiation of Pluripotent Stem Cells.** eLife. February 2021 (In Review).
4. Batalov I; Jallerat Q; Kim S; **Bliley JM**; Feinberg AW; **Engineering Aligned Human Cardiac Muscle Using Developmentally-Inspired Fibronectin Micropatterns**. Scientific Reports. November 2020 (Accepted).
5. Dipalo M; Rastogi S; Matino L; Garg R; **Bliley JM**; Iachetta G, Melle G, Shrestha R; Shen S; Santoro F; Feinberg AW; Barbaglia A; Cohen-Karni T; de Angelis F; **Intracellular action potential recordings from cardiomyocytes by ultra-fast pulsed laser irradiation of fuzzy graphene microelectrodes.** Science Advances. July 2020 (In Press).
6. Vermeer M; Bolling M#; **Bliley JM**#; Pavez-Giani M; Kramer D; Arevalo G; Romero-Herrera P; Diercks G; van den Berg M; Feinberg AW; Sillje H; van der Meer P; **Gain of Function Mutation in Ubiquitin-ligase KLHL24 causes Desmin Degradation and Dilated Cardiomyopathy**. The Journal of Clinical Investigation. May 2020 (Accepted).
7. Bliley JM#; Vermeer M#; Duffy R; Batalov I; Kramer D; Tashman J; Shiwarski D; Lee A; Teplenin A; Volkers L; Coffin B; Hoes M; Kalmykov A; Palchesko R; Sun Y; Jongbloed J; Bomer N; de Boer R; Suurmeijer A; Pijnappels D; Bolling M; van der Meer P; Feinberg AW. **Dynamic Loading of Human Engineered Heart Tissue Enhances Contractile Function and Drives Desmosome-linked Disease Phenotype.** Science Translational Medicine. May 2020 (Accepted).
8. Shiwarski DJ#; Tashman JW#; Tsamis A; **Bliley JM**; Blundon M; Aranda-Michel E; Jallerat Q; Szymanski J; McCartney B; Feinberg AW; Fibronectin-Based Nanomechanical Biosensors to Map 3D Strains in Live Cells and Tissues. Nature Communications. Feb 2020 (In Press).
9. Rastogi SK; **Bliley JM**; Matino L; Garg R; Santoro F; Feinberg AW; Cohen-Karni T; Three-dimensional fuzzy graphene ultra-microelectrodes for sub-cellular electrical recordings**.** Nano Research. Feb 2020.
10. Fadia NB #; **Bliley JM**#; DiBernardo, GA; Crammond DJ; Schilling BK; Sivak WN; Spiess AM; Washington KM; Waldner M; Tsung LH; James IB; Minteer DM; Tompkins-Rhoades C; Kim DY; Schweizer R; Bourne DA; Cottrill AR; Panagis GE; Schusterman MA; Egro FM; Campwala IK; Simpson T; Weber DJ; Gause T; Brooker JE; Josyula T; Guevara AA; Repko AJ; Mahoney CM; Marra KG; **Long-Gap Peripheral Nerve Repair Through Sustained Release of a Neurotrophic Factor in Non-Human Primates**. Science Translational Medicine. Jan 2019.
11. Lee A; Hudson A; Shiwarski DJ; Tashman JW; Hinton TJ; Yerneni S; **Bliley JM**; Campbell PG; Feinberg AW; **3D Bioprinting of Collagen to Rebuild Components of the Human Heart**. Science. Aug 2019.
12. Kalmykov A; Huang C; **Bliley JM**; Shiwarski D; Tashman J; Arif A; Rastogi K; Shukla S; Mataev E; Feinberg AW; Hsia JK; Cohen-Karni T; Organ on e-chip: Three dimensional self-rolled biosensor array for electrical interrogations of electrogenic spheroids. Science Advances. Aug 2019.
13. Bourne DA; **Bliley JM**; James I; Rubin J.P; **Changing the Paradigm of Craniofacial Reconstruction: A Prospective Clinical Trial of Autologous Fat Transfer for Craniofacial Deformities**. Annals of Surgery. Apr 2019.

14. Passipieri J; Dienes J; Frank J; Glazier J; Portell A; Venkatesh K; **Bliley JM**; Grybowsky D; Schilling B; Marra K; Christ G; Adipose Stem Cells Enhance Nerve Regeneration and Muscle Function in A Peroneal Nerve Ablation Model**.** Tissue Engineering Part A. May 2019.
15. Bourne D; Thomas RD; **Bliley JM**; Haas G; Wyse A; Donnenberg A; Doonnenberg VS; Chow I; Cooper R; Coleman S; Marra K; Pasquina P; Rubin JP; Amputation Site Soft Tissue Restoration Using Adipose Stem Cell Therapy**.** Plastic and Reconstructive Surgery. Nov 2018.
16. Waldner M; Wensheng Z; James I; Allbright K; Havis E; **Bliley JM**; Almadori A; Schweizer R; Plock J; Washington K; Gorantla V; Solari M; Marra KG; Rubin JP; Characteristics and Immunomodulating Functions of Adipose-Derived and Bone Marrow-Derived Mesenchymal Stem Cells Across Defined Human Leukocyte Antigen Barriers**.** Frontiers in Immunology. July 2018.
17. Rastogi SK; **Bliley JM**; Shiwarski DJ; Garg R; Feinberg AW**;** Cohen-Karni T; Graphene Microelectrode Arrays for Electrical and Optical Measurements of Human Stem Cell-Derived Cardiomyocytes*.* Cellular and Molecular Bioengineering. May 2018.
18. Allbright KO; **Bliley JM**; Havis E; Kim DY; Dibernardo GA; Grybowski D; Waldner M; James IB; Sivak WN; Rubin JP; Marra KG; **Delivery of adipose-derived stem cells in poloxamer hydrogel improves peripheral nerve regeneration.** Muscle and Nerve. Aug 2018.
19. Bliley JM; Rubin JP; Nomenclature of the Stromal Vascular Fraction. In book: Fat Injection: From Filling to Regeneration, pp. 67-81 (2018).
20. Bliley JM; Argenta AE; Satish L; McLaughlin MM; Marra KG; Rubin JP; **Administration of Adipose-Derived Stem Cells Enhances Vascularity, Induces Collagen Deposition, and Enhances Dermal Adipogenesis in Burn Wounds.** Burns. Sep 2016.
21. Unadkat J; Schnider J; Feturi F; Tsuji W; **Bliley JM**; Venkataramanan R; Gorantla V; Marra K; Solari M; Gorantla V; Spiess A; **Single Implantable FK506 Disk Prevents Rejection in Vascularized Composite Allotransplantation**. Plastic and Reconstructive Surgery. Feb 2017.
22. Bliley JM; Satish L; McLaughlin MM; Kling RE; Day JR; Grahovac TL; Kokai LE; Zhang W; Marra KG; Rubin JP; Imaging the Stromal Vascular Fraction During Soft Tissue Reconstruction. Plastic and Reconstructive Surgery (2015).
23. Bliley JM; Sivak WN; Minteer DM; Tompkins-Rhoades C; Day J; Williamson G; Liao HT; Marra KG; **Ethylene Oxide Sterilization Preserves Bioactivity and Attenuates Burst Release of Encapsulated Glial Cell Line Derived Neurotrophic Factor from Tissue Engineered Nerve Guides For Long Gap Peripheral Nerve Repair.** ACS Biomaterials Science and Engineering. Dec 2015.
24. Lannau B; **Bliley JM**; James I; Wang S; Sivak WN; Kang K; Johnson J; Fowler J; Spiess A. Long-term Patency of Primary Arterial Repair and the Modified Cold Intolerance Symptom Severity Questionnaire**.** Plastic and Reconstructive Surgery Global Open. Dec 2015.
25. Sivak, WN; **Bliley JM**; Marra, K.G; **Polymeric biomaterials for peripheral nerve regeneration: fabrication and use of a polycaprolactone guide**. In book: Axon Growth and Regeneration. Volume 1162 of the series Methods in Molecular Biology pp 139-148. (2014).
26. Sivak W; White J; **Bliley JM**; Tien L; Liao HT; Kaplan D; Marra K; Delivery of Chondroitinase ABC (ChABC) and Glial Cell-derived Neurotrophic Factor (GDNF) from Silk Fibroin Conduits Enhances Peripheral Nerve Regeneration. Journal of Tissue Engineering and Regenerative Medicine. (2014)
27. Bliley JM; Marra KG; **Polymeric Biomaterials as Tissue Scaffolds**. In book: Stem Cell Biology and Tissue Engineering in Dental Sciences, pp.149-161. Mar 2014.
28. Philips BJ; Grahovac, TL; Valentin JE; Chung CW; **Bliley JM**; Pfeifer ME; Roy SB; Dreifuss S; Kelmendi-Doko A; Kling R.E; Ravuri SK; Marra KG; Donnenberg VS; Donnenberg AD; Rubin JP; Prevalence of endogenous CD34+ adipose stem cells predicts human fat graft retention in a xenograft model**.** Plastic and reconstructive surgery. Oct 2013.
29. Bliley JM; Woodley SK; **The effects of repeated handling and corticosterone treatment on behavior in an amphibian (Ocoee salamander/ Desmognathus ocoee)**. Physiology and Behavior. Mar 2012.
30. Ricciardella LF; **Bliley JM**; Feth CC; Woodley SK; **Acute stressors increase plasma corticosterone and decrease locomotor activity in a terrestrial salamander (Desmognathus ochrophaeus)**. Physiology and Behavior. Apr 2010.

INVITED PRESENTATIONS

1. Bliley JM; Vermeer M; van der Meer P; Feinberg AW; **Dynamic Loading of Human Engineered Heart Tissue Enhances Contractile Function and Drives Desmosome-linked Disease Phenotype**. 2020 TERMIS SYIS AM & EU Webinar Series. November 3, 2020, Pittsburgh, PA.
2. Bliley JM; Vermeer M; van der Meer P; Feinberg AW; **Dynamic Loading of Human Engineered Heart Tissue Enhances Contractile Function and Drives Desmosome-linked Disease Phenotype**. Single Ventricle Series Webinar. October 14, 2020, Pittsburgh, PA.
3. Bliley JM; Vermeer M; Feinberg AW; **Mechanical Loading of Engineered Cardiac Tissues Induces a Disease Phenotype in Patient Specific Engineered Heart Muscle Tissues.** Bioengineered Organs Initiative Meeting, February 21, 2019, Pittsburgh, PA.
4. Bliley JM; Vermeer M; Feinberg AW; ***Cardiac Tissue Engineering: From In Vitro Disease Models to 3D Bioprinted Heart Scaffolds***. McGowan Institute Injury, Repair and Regenerative Medicine Seminar Series, December 5, 2017, Pittsburgh, PA.
5. *Bliley JM; Marra KG;* ***Regeneration of Long Gap Median Nerve Defects and Functional Reinnervation of the Abductor Pollicis Brevis Muscle Using Novel Tissue Engineered Nerve Guides in a Non-Human Primate Model.*** McGowan Institute Injury, Repair and Regenerative Medicine Seminar Series, February 2, 2016, Pittsburgh, PA.

ORAL PRESENTATIONS

1. Bliley JM; Vermeer M; van der Meer P; Feinberg AW; **Modeling Load-Induced Disease Phenotypes in Human Engineered Cardiac Tissues with Patient-Specific Desmoplakin Mutations**. World Biomaterials Congress. Glasgow, Scotland (Virtual). Dec 2020.
2. Bliley JM; Vermeer M; van der Meer P; Feinberg AW; **Modeling Load-Dependent Heart Failure in Patient-Derived Engineered Cardiac Tissues**. Biomedical Engineering Society Meeting. San Diego, CA (Virtual). October 2020.
3. Bliley JM; Lee A; Hinton TJ; Hudson A; Shiwarski D; Tashman J; Yerneni S; Campbell PG; Feinberg AW; **Perfused 3D Printed Collagen Tubes Support Tissue Viability**. Biomaterials Day. Case Western Reserve University. Cleveland OH. Oct 2019.
4. Bliley JM; Lee A; Hinton TJ; Hudson A; Shiwarski Dl Tashman J; Yerneni S; Campbell PG; Feinberg AW; **Perfused 3D Printed Collagen Tubes Support Tissue Viability**. McGowan Retreat. Pittsburgh PA. Mar 2019
5. Bliley JM; Lee A; Hinton TJ; Hudson A; Shiwarski D; Tashman J; Yerneni S; Campbell PG; Feinberg AW; **3D Printed Collagen Tubes as Scaffolds for Engineering Functional Human Muscle**. Biomedical Engineering Society Meeting. Atlanta GA. Oct 2018.
6. Bliley JM; Duffy R; Batalov I; Vermeer M; Kalmykov A; van der Meer P; Feinberg A; **Cardiac Microtissues with Integrated Force Sensors for Non-Invasive Readout of Contractile Function**. Society for Biomaterials Annual Meeting. Minneapolis, MN. Apr 2017.
7. Bliley JM; Bourne D; Havis E; James IB; Schroth R; Dees A; DiBernardo G; Grybowski D; Wang S; Kokai L; Kelmendi-Doko A; Mahoney C; Sivak W; Marra K; Rubin JP; **The Effects of Cold Storage And Poloxamer 188 Treatment on Stromal Vascular Fraction Viability And Volume Retention of Fat Grafts**. Robert H. Ivy Society of Plastic Surgeons at Omni Bedford Springs Resort and Spa. Pittsburgh, PA. Apr 2016.
8. Bliley JM; Satish L; McLaughlin MM; Kling RE; Day JR; Grahovac TL; Kokai LE; Zhang W; Marra KG; Rubin JP; **Imaging the Stromal Vascular Fraction During Soft Tissue Reconstruction**. 58th Ohio Valley Society of Plastic Surgeons meeting, Covington, KY. May 2015.
9. Bliley JM; Bourne D; James I; Sivak W; Wang S; Schroth Rl Marra KG; Rubin JP; **Reconstruction following craniofacial trauma with stromal vascular fraction enriched fat grafts: Correlating in vitro findings with clinical outcomes**. International Federation for Adipose Therapeutics and Science. New Orleans, LA. Nov 2015.
10. Bliley JM; Bourne D; James I; Kostereva N; Waldner M; Grybowski D; Sivak WN; Schweizer R; Schroth RN; Minteer DM; Simpson T; Tompkins-Rhoades C; Taylor A; Dees A; Washington KM; Spiess AM; Crammond DJ; Marra KG; **Regeneration of Long Gap Median Nerve Defects and Functional Reinnervation of the Abductor Pollicis Brevis Muscle Using Novel Tissue Engineered Nerve Guides in a Non-Human Primate Model**. TERMIS. Boston, MA. Sep 2015.

11. Bliley JM; Sivak WN; Minteer DM; Schweizer R; Bourne D; James I; Kostereva N; Schroth RN; Simpson T; Tompkins-Rhoades C; Taylor A; Washington KM; Spiess AM; Crammond DJ; Marra KG; **Interim Analysis of Long Gap Median Nerve Regeneration Through Novel Tissue Engineered Nerve Guides in a Non-Human Primate Model**. Regenerative Medicine: Technologies Enabling Novel Therapies. Hilton Head, South Carolina. Mar 2015.
12. Bliley J.M; Bourne D; James I; Kostereva N; Waldner M; Grybowski D; Sivak WN; Schweizer R; Schroth RN; Minteer DM; Simpson T; Tompkins-Rhoades C; Taylor A; Dees A; Washington KM; Spiess AM; Crammond DJ; Marra KG; **Regeneration of Long Gap Median Nerve Defects and Functional Reinnervation of the Abductor Pollicis Brevis Muscle Using Novel Tissue Engineered Nerve Guides in a Non-Human Primate Model**. UPMC Plastic Surgery Resident Research Day. Pittsburgh, PA. June 2015.
13. Bliley JM; Argenta A; Satish L; McLaughlin M; Marra K; Rubin JP; **Use of Adipose derived stem cells for the improvement of burn wound healing**. Robert H. Ivy Society of Plastic Surgeons at Omni Bedford Springs Resort and Spa. Bedford, PA. May 2014.
14. Bliley JM; Sivak WN; Minteer DM; Liberatore R; Schroth RN; Liao HT; Schweizer R; Gause T; Simpson T; Hokanson J; Tompkins-Rhoades C; Washington K.M; Spiess AM; Weber D; Crammond DJ; Marra KG**; Interim Analysis of Long Gap Median Nerve Regeneration Through Novel Tissue Engineered Nerve Guides in a Non-Human Primate Model**. UPMC Plastic Surgery Resident Research Day. Pittsburgh, PA. Jun 2014.
15. Bliley JM; Grahovac TL; McLaughlin MM; Kling RE; Philips BJ; Day JR; Satish L; Marra KG; Rubin JP; **Identification of the Minimum Cell Dose Necessary to Increase Fat Graft Retention**. University of Pittsburgh Plastic Surgery Resident Research Day. Pittsburgh, PA. Jun 2013.
16. Bliley JM; Grahovac TL; McLaughlin MM; Kling RE; Philips BJ; Day JR; Satish L; Marra KG; Rubin JP**; Identification of the Minimum Cell Dose Necessary to Increase Fat Graft Retention**. International Federation of Adipose Therapeutics and Science. New York City, NY. Nov 2013.
17. Bliley JM; Grahovac TL; Nayar HS; Philips BJ; Courcoulas AP; Marra KG; Rubin JP; **Correlating Body Mass Index (BMI) to Adipose Stem Cell Functionality and Fat Graft Retention**. University of Pittsburgh Plastic Surgery Resident Research Day. Pittsburgh, PA. Jul 2012.
18. Bliley JM; Grahovac TL; Nayar HS; Philips BJ; Courcoulas AP; Marra KG; Rubin JP; **Correlating Body Mass Index (BMI) to Adipose Stem Cell Functionality and Fat Graft Retention**. International Federation of Adipose Therapeutics and Science. Quebec, Canada. Oct 2012.
19. Bliley JM; Feth CC; Woodley SK; **Acute Stress Response as an Adaptive Mechanism in Salamanders**. Duquesne University Summer Research Symposium. Pittsburgh, PA. Jul 2009.

POSTER PRESENTATIONS

1. Bliley JM; Duffy R; Batalov I; Vermeer M; Kalmykov A; van der Meer P; Feinberg A; **Dynamic Mechanical Loading Induces a Disease Phenotype in Diseased Engineered Cardiac Tissues**. ISSCR. Los Angeles, CA. Jun 2019.
2. Bliley JM; Duffy R; Batalov I; Vermeer M; Kalmykov A; van der Meer P; Feinberg A; **Dynamic Mechanical Loading Induces a Disease Phenotype in Diseased Engineered Cardiac Tissues**. American Heart Association Fellows Day. Pittsburgh, PA. Jan 2019.
3. Bliley JM; Duffy R; Batalov I; Vermeer M; Kalmykov A; van der Meer P; Feinberg A; **Dynamic Mechanical Loading Induces a Disease Phenotype in Disease Engineered Cardiac Tissues**. Biomaterials Day. Pittsburgh, PA. Nov 2018.
4. Bliley JM; Duffy R; Batalov I; Vermeer M; Kalmykov A; van der Meer P; Feinberg A; **Cardiac Microtissues with Integrated Force Sensors for Non-Invasive Readout of Contractile Function**. Keystone Conference: Molecular Mechanisms of Heart Development. Keystone, CO. Mar 2017.
5. Bliley JM; Bourne D; James I; Kostereva N; Waldner M; Grybowski D; Sivak WN; Schweizer R; Schroth RN; Minteer DM; Simpson T; Tompkins-Rhoades C; Taylor A; Dees A; Washington KM; Spiess AM; Crammond DJ; Marra KG; **Evaluation of Clinical Alternatives to Nerve Autograft in Long Gap Median Nerve Defects**. Regenerative Medicine: Technologies Enabling Novel Therapies. Hilton Head, South Carolina. Mar 2016.
6. Bliley JM; Bourne D; Havis E; James IB; Schroth R; Dees A; DiBernardo G; Grybowski D; Wang S; Kokai L; Kelmendi-Doko A; Mahoney C; Sivak W; Marra K; Rubin JP; **The Effects of Cold Storage And Poloxamer 188 Treatment on Stromal Vascular Fraction Viability And Volume Retention of Fat**

Grafts. McGowan Institute for Regenerative Medicine Retreat. Nemacolin Woodlands Resort, PA. Mar 2016.

7. Bliley JM; Bourne D; James I; Kostereva N; Waldner M; Grybowski D; Sivak WN; Schweizer R; Schroth RN; Minteer DM; Simpson T; Tompkins-Rhoades C; Taylor A; Dees A; Washington KM; Spiess AM; Crammond DJ; Marra KG; **Evaluation of Clinical Alternatives to Nerve Autograft in Long Gap Median Nerve Defects**. McGowan Institute for Regenerative Medicine Retreat. Nemacolin Woodlands Resort, PA. Mar 2016.

8. Bliley JM; Sivak WN; Minteer DM; Schweizer R; Bourne D; James I; Kostereva N; Schroth R.N; Simpson T; Tompkins-Rhoades C; Taylor A; Washington KM; Spiess AM; Crammond DJ; Marra KG; **Interim Analysis of Long Gap Median Nerve Regeneration Through Novel Tissue Engineered Nerve Guides in a Non-Human Primate Model**. McGowan Institute for Regenerative Medicine Retreat. Nemacolin Woodlands Resort, PA. Mar 2015.

9. Bliley JM; Bourne D; James I; Kostereva N; Sivak WN; Schweizer R; Schroth RN; Minteer DM; Simpson T; Tompkins-Rhoades C; Taylor A; Dees A; Washington KM; Spiess AM; Crammond DJ; Marra KG; **Regeneration of Long Gap Median Nerve Defects and Function Reinnervation of the Abductor Pollicis Brevis Muscle Using Novel Tissue Engineered Nerve Guides in a Non-Human Primate Model**. Military Health System Research Symposium. Fort Lauderdale, FL. Aug 2015.

10. Bliley JM; Sivak WN; Crammond DJ; Minteer D; McLaughlin MM; Liberatore R; Schroth RN; Liao HT; Simpson T; Hokanson J; Williamson G; Tompkins-Rhoades C; Washington K; Spiess A; Weber D; Marra KG; **An Interim Analysis of Outcomes following 5-cm Median Nerve Defect Repair in Non-Human Primates**. Plastic Surgery Research Council. New York City, NY. Mar 2014.

11. Bliley JM; Sivak WN; Minteer DM; McLaughlin MM; Liberatore R; Schroth RN; Liao HT; Gause T; Simpson T; Hokanson J; Tompkins-Rhoades C; Williamson G; Washington KM; Spiess AM; Weber D; Crammond DJ; Marra KG**; Interim Analysis of Long Gap Median Nerve Regeneration Through Novel Tissue Engineered Nerve Guides in a Non-Human Primate Model**. Military Health System Research Symposium. Fort Lauderdale, Fl. Aug 2014.

12. Bliley JM; Minteer DM; McLaughlin MM; Sivak W; Washington KM; Spiess AM; Crammond DJ; Rubin JP; Marra KG**; Establishing a pre-clinical 5-centimeter median nerve defect in a *Rhesus macaque* model**. McGowan Institute for Regenerative Medicine Retreat. Nemacolin Woodlands Resort, PA. Mar 2013.

13. Bliley JM; Minteer DM; McLaughlin MM; Sivak W; Washington KM; Spiess AM; Crammond DJ; Rubin JP; Marra KG; **Establishing a pre-clinical 5-centimeter median nerve defect in a *Rhesus macaque* model**. Regenerative Medicine: Technologies Enabling Novel Therapies. Hilton Head, South Carolina. Mar 2013.

14. Bliley JM; Grahovac TL; Nayar HS; Philips BJ; Courcoulas AP; Marra KG; Rubin JP; **Correlating Body Mass Index (BMI) to Adipose Stem Cell Functionality and Fat Graft Retention**. University of Pittsburgh Surgery Resident Research Day. Pittsburgh, PA. May 2013.

15. Bliley JM; Lin YC; Minteer DM; Oh S; Kaplan DL; Van Dyke M; Smith T; Pixley S; Rubin JP; Marra KG; **Strategies for Enhanced Peripheral Nerve Repair**. Boston University Science and Engineering Day. Boston, MA. Mar 2012.

16. Bliley JM, Lin YC; Minteer DM; McLaughlin MM; Oh S; Kaplan DL; Van Dyke M; Smith T; Pixley S; Rubin JP; Marra KG; **Strategies for Enhanced Peripheral Nerve Repair**. McGowan Institute for Regenerative Medicine Retreat. Nemacolin Woodlands Resort, PA. Mar 2012.

17. Bliley JM; Grahovac TL; Nayar HS; Philips BJ; Courcoulas AP; Marra KG; Rubin JP; **Correlating Body Mass Index (BMI) to Adipose Stem Cell Functionality and Fat Graft Retention**. Plastic Surgery Research Council. Ann Arbor, MI. Jun 2012.

18. Bliley JM; Lin YC; Minteer DM; McLaughlin MM; Oh S; Kaplan DL; Van Dyke M; Smith T; Pixley S; Rubin JP; Marra KG; **Strategies for Enhanced Peripheral Nerve Repair**. Annual Symposium on Regenerative Rehabilitation. Pittsburgh, PA. Nov 2012.

19. Bliley JM; Lin YC; Minteer DM; McLaughlin MM; Oh S; Kaplan DL; Van Dyke M; Smith T; Pixley S; Rubin JP; Marra KG; **Strategies for Enhanced Peripheral Nerve Repair**. Vision Restoration: Regenerative Medicine in Opthamology, Pittsburgh, PA. May 2012.

20. Bliley JM; Woodley SK; **Acute Effects of Corticosteroids in Salamanders**. Duquesne University Undergraduate Research and Scholarship Symposium. Pittsburgh, PA. Feb 2010.

21. Bliley JM; Woodley SK; **The Effects of Chronic Stress on Salamander Behavior and Body Condition**. Western Pennsylvania Undergraduate Symposium at Geneva College. Beaver Falls, PA. Apr

2010.
22. Bliley JM; Feth CC; Woodley SK; **Acute Stress Response as an Adaptive Mechanism in Salamanders**. Duquesne University Undergraduate Summer Research Symposium. Pittsburgh, PA. Jul 2009.
23. Bliley JM; Feth CC; Woodley SK; **Effects of Chemosensory Cues on Locomotor Activity in the Salamander**. Duquesne University Undergraduate Research and Scholarship Symposium. Pittsburgh, PA. Apr 2009.

PATENTS

1. PCT/US2018/000165. "3D Microtissues with Integrated Mechanical Loading and Non-invasive Readout of Tissue Generated Stress and Strain".
2. PCT/US2018/060788. "Systems And Methods For Reconstruction Of Nerve Defects"

ACADEMIC AWARDS, FELLOWSHIPS & HONORS

- **Tissue Engineering Special Interest Group Student Abstract Award.** World Biomaterials Congress (virtual). Dec 2020.
- **Presidential Fellowship**. College of Engineering**,** Carnegie Mellon University. Pittsburgh, PA. Jan 2020-Dec 2021.
    - Fellowship awarded for producing an impactful body of work leading to a research paper, either published or submitted.
- **1st Place Oral Presentation Award**. Biomaterials Day, Case Western Reserve University. Cleveland, OH. Oct 2019.
- **Outstanding Teaching Assistant Award**. Department of Biomedical Engineering, Carnegie Mellon University. Pittsburgh, PA. May 2019.
- **3rd Place Best Basic Science Award**. American Heart Association Fellows Day, Pittsburgh, PA. Jan 2019.
- **1st Place Poster Award**. Biomaterials Day, Carnegie Mellon University/University of Pittsburgh. Pittsburgh PA. Nov 2018.
- **Dowd Fellowship**. Carnegie Mellon University. Pittsburgh, PA. Sep 2018-Sep 2019.
    - Fellowship awarded by Philip and Martha Dowd following submission of a grant proposal for a "high risk, high reward" research project.
- **STAR (Student Travel Award Recognition) Award**. Society for Biomaterials Annual Meeting. Minneapolis, MN. Apr 2017.
    - Travel award to attend Society For Biomaterials Meeting based on abstract scoring.
- **Best Oral Presentation Student and Young Investigator Section**. Tissue Engineering and Regenerative Medicine International Society (TERMIS) World Congress. Boston, MA. Sep 2015.
- **National Science Foundation Travel Award.** Regenerative Medicine: Technologies Enabling Novel Therapies. Hilton Head, SC. Mar 2015.
    - Travel award to attend Regenerative Medicine: Technologies Enabling Novel Therapies Meeting based on abstract scoring.
- **From "Benchtop to Bedside" Translational Medicine Certificate**. University of Pittsburgh. Pittsburgh, PA. May 2013.
    - Certificate awarded for completing classes and workshops aimed at commercializing a nerve conduit developed in the Marra laboratory.
- **Boston University Professional Development Award**. Boston University. Boston, MA. April 2011.
    - Travel Award used to attend and present research at the Boston University Science and Engineering Day.
- **Outstanding Health Management Systems Student Award**. Duquesne University. Pittsburgh, PA. May 2010.
- **Duquesne University Undergraduate Research Dean's Fellowship**. Duquesne University. Pittsburgh, PA. May 2009.
    - Fellowship award to perform undergraduate research over the summer of 2009.

- **Duquesne University Felding Scholarship.** Duquesne University. Pittsburgh, PA. Sep 2008-May 2010.
    - Merit-Based Pre-medical Scholarship
- **Duquesne University Academic Scholarship.** Duquesne University. Pittsburgh, PA. Sep 2006-May 2010.
    - Merit-Based Scholarship